

FACULDADE DE ENGENHARIA DA UNIVERSIDADE DO PORTO

A Homogenisation Technique for Multiscale Analysis of Bone Tissue Combined With Advanced Discretisation Techniques

Marco da Costa Marques



FEUP FACULDADE DE ENGENHARIA
UNIVERSIDADE DO PORTO

Programa Doutoral em Engenharia Biomédica

Supervisor: Professor Doutor Jorge Américo Belinha

Co-supervisor: Professor Doutor António Fonseca Oliveira

April 27, 2020

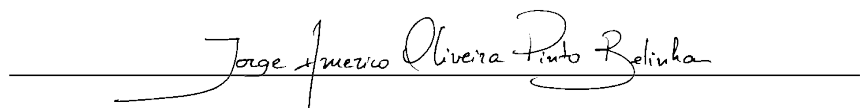
A Homogenisation Technique for Multiscale Analysis of Bone Tissue Combined With Advanced Discretisation Techniques

Marco da Costa Marques

Programa Doutoral em Engenharia Biomédica

Approved by:

Supervisor: Professor Doutor Jorge Américo Belinha

A handwritten signature in black ink, reading "Jorge Américo Oliveira Pinto Belinha", is written over a horizontal line.

April 27, 2020

Resumo

O osso, um tecido complexo e dinâmico, tem um papel essencial na fisiologia e anatomia humana, possuindo a capacidade intrínseca de regeneração e remodelação. Estes processos biológicos são fundamentais para que o tecido ósseo se renove como resultado de diferentes necessidades fisiológicas ao longo da vida. O processo de remodelação é um dos muitos processos biológicos modelados por engenheiros e cientistas, que de forma a os conseguir descrever e compreender melhor. Usando ferramentas computacionais, como são os métodos numéricos, e utilizando a formulação de equações e leis constitutivas, é possível descrever este processo e, assim, expandir a sua compreensão. Os modelos de remodelação óssea evoluíram desde os modelos mais simples, em que apenas eram considerados os estímulos mecânicos como fator influenciadores, até modelos que consideram fatores biológicos e mecânicos, e em diferentes escalas. O objetivo desta tese foi alargar o conhecimento relativo ao processo de remodelação óssea, entender os métodos numéricos, como o método dos elementos finitos e os métodos sem malha, e usá-los para desenvolver ferramentas que permitam estudar a remodelação óssea. Para isso, foi explorado o uso do método dos elementos finitos e de métodos sem malha no estudo de estruturas biológicas para verificar e validar que estas metodologias eram comparáveis e eficientes com este tipo de análise. Uma das características incorporadas nos modelos matemáticos de remodelação óssea que consideram os estímulos mecânicos são as propriedades mecânicas ósseas. Assim, nesta tese, foi desenvolvida uma metodologia de homogeneização que utiliza o conceito de *fabric tensor*, que é capaz de definir as propriedades mecânicas ósseas, tendo em consideração a informação da morfologia óssea existente em imagens médicas. Esta metodologia, desenvolvida para distribuições bidimensionais (2D) e tridimensionais (3D), é capaz de representar um domínio ósseo altamente heterogéneo, utilizando um domínio homogeneizado que contém as informações do domínio heterogéneo. Para o desenvolvimento da metodologia do *fabric tensor* em 2D foi usada uma abordagem em que são usadas técnicas de processamento de imagem, enquanto que a metodologia usada para definir o *fabric tensor* em 3D usa uma abordagem algébrica e geométrica. As duas metodologias foram avaliadas e posteriormente validadas. Nesta validação foram usados o método dos elementos finitos e os métodos sem malha, de forma a comparar se o comportamento mecânico das estruturas homogéneas definidas usando a metodologia desenvolvida eram equivalentes às estruturas heterogéneas. Foi também verificado a existência de um decréscimo do custo computacional quando é utilizada a metodologia proposta para definir as propriedades mecânicas materiais homogeneizadas, uma vez que é necessária uma menor discretização do domínio ósseo para se conseguir um comportamento mecânico equivalente ao do domínio altamente heterogéneo do osso. Os métodos numéricos computacionais provaram ser uma ferramenta importante em biomecânica e, neste trabalho em particular, mostraram resultados fundamentais para validação e aplicação da metodologia de homogeneização desenvolvida.

Abstract

Bone, a complex and dynamic tissue, plays an essential role in human physiology and anatomy, possessing the intrinsic capacity of regeneration and remodelling. These biological processes are fundamental for bone tissue to be renewed as a result of different physiological needs throughout life. The remodelling process is one of many biological processes that arouse interest to engineers and scientists. Using computational tools, such as numerical methods, and using the equation formulations and constitutive laws, it is possible to describe this process and thus expand its understanding. Bone remodelling models evolved from the simplest models, in which only mechanical stimuli were considered, to models that consider biological and mechanical factors, and at different scales. The objective of this thesis was to expand the knowledge related to the bone remodelling process, understand numerical methods, such as finite element methods and meshless methods, and use them to develop tools to study bone remodelling. Exploring the use of the finite element method and meshless methods in the study of biological structures was possible to verify and validate that these methodologies were equivalent and efficient with this type of analysis. One of the parameters incorporated in the study of bone using numerical methods and mathematical modelling of bone remodelling, where is consider mechanical stimuli, is the bone mechanical properties. In this thesis was developed a homogenization methodology that uses the concept of *fabric tensor*, which is capable to define bone mechanical properties taking into account the information of bone morphology existing in medical images. This methodology, developed for two-dimensional (2D) and three-dimensional (3D) distributions, is capable of representing a highly heterogeneous bone domain, using a homogenized domain that contains information from the heterogeneous domain. For the development of the methodology of *fabric tensor* in 2D were used image processing approaches, while the methodology used to define the *fabric tensor* in 3D uses an algebraic and geometric approach. Both methodologies were evaluated and later validated. In this validation, the finite element method and the meshless methods were used to compare whether the mechanical behaviour of the homogeneous structures defined using the developed methodology developed was equivalent to heterogeneous structures. It was also verified the existence of a decrease in computational cost using the proposed methodology to define the mechanical properties of homogenized material. This occurs since is necessary a lower bone domain discretization to achieve a mechanical behaviour equivalent to the bone highly heterogeneous domain. Computational numerical methods proved to be an important tool in biomechanics and, in this particular work, showed fundamental results for validation and application of the homogenization methodology developed.

Acknowledgments

Na reta final desta etapa, não podia deixar de agradecer a todas as pessoas que, indiretamente ou diretamente, me ajudaram a definir o caminho a seguir e que me ajudaram nestes quatro anos, na realização e finalização com sucesso deste trabalho. Em primeiro lugar agradeço ao Professor Doutor Jorge Belinha, a oportunidade que me deu, aquando da ajuda para obter financiamento junto da FCT para frequentar o Programa Doutoral em Engenharia Biomédica. Agradeço também por todo o apoio, interesse, incentivo, disponibilidade constante, que me dispensou em todo o processo de investigação no âmbito do doutoramento. Não posso também deixar de agradecer todas as oportunidades que me concedeu ao poder entrar em contacto com novos temas, novas ideias, alunos e investigadores, mesmo que fora do âmbito da tese. Pela paciência e por muitas vezes me indicar o norte. O meu muito Obrigado!

Não posso deixar de agradecer também ao meu co-orientador Professor Doutor António Fonseca Oliveira pela disponibilidade apresentada quando necessário. Agradeço ao Professor Renato Natal, ao Professor Marco Parente, pela partilhas de conhecimento, as conversas casuais que muitas vezes aconteciam em corredor, que resultavam na solução de problemas, pela amizade, ao longo destes anos. Quero expressar um agradecimento especial ao Professor Renato por me ter dado a oportunidade de fazer parte da UCVE quando em 2015 expressei que gostaria de vir trabalhar em biomecânica e me indicar o professor Jorge Belinha quando pensei em fazer o Doutorado. Agradeço todos que indiretamente me proporcionaram novas experiências no Laboratório de Desenvolvimento de Produtos e Serviços da FEUP, em especial ao Professor Doutor Jorge Lino e o Professor Doutor António Augusto Fernandes.

Aos meus amigos na luta que é a investigação que sei que também sentem as alegrias e as tristezas da coisas que para outros parecem absurdas. À Ana, à Carla, à Dulce, ao Daniel, à Elisabete, à Joana, à Margarida, à Nilza, ao Sergio (obrigado por todos os aviso para almoços e cafés), ao Andre Brandão e ao Leonardo, pela partilha de conhecimento e interesse na impressão 3D, ao João Ferreira, pela trocas de ideias que por vezes resultavam em soluções, pela companhia nos cafés, almoços, desabafos, risadas e devaneios. Aos meus amigos pelas palavras de incentivo e pelos momentos de descontração que me proporcionaram.

Aos meus pais porque esta reta final é o resultado de um percurso longo e de muita dedicação, orientação e muito amor. Sem dúvida, sem vocês nunca conseguiria ter chegado tão longe. Obrigado! À minha irmã Marta e ao Nuno, por mesmo longe, me perguntarem sempre como corria e por me darem força. Ao irmão Miguel por mesmo à distância me estar sempre a mandar despachar e acabar, mesmo quando não tinha ideia do que falava. Aos meus sobrinho Beatriz e Tomás que não percebem o meu trabalho mas entendem que é algo muito importante para mim. Aos meus avós que não tiveram a oportunidade de me ver concluir o doutoramento, e em especial ao meu avô Albano, que sei, que teria um orgulho imenso em dizer que tem um neto com Doutorado.

A ti Rita, pelo teu amor incondicional. Sem dúvida que só consegui alcançar esta etapa porque tu estiveste sempre comigo. Obrigado pelo empurrão que me deste quando perguntei se achavas que devia falar com o Professor Renato, porque gostava de trabalhar em biomecânica. Olha no

que resultou. Obrigado pela paciência e amor a todos os momentos, pelas horas que me ouviste a desabafar, que me fizeste acreditar em mim, e que me deste força e coragem para nunca desistir. Sem dúvida que esta tese é dedicada aos meus pais e, principalmente, a Ti!

Marco Marques

Institutional Acknowledgments

The author acknowledges the funding by Ministério da Ciência, Tecnologia e Ensino Superior - Fundação para a Ciência e a Tecnologia, Portugal and POCH, by Fundo Social Europeu and MCTES under research grant SFRH / BD / 11047 / 2015. Regarding the work conditions, the author truly acknowledges the conditions provided by the department of mechanical engineering (DEMec) of Faculty of Engineering of the University of Porto (FEUP), by INEGI - Instituto de Ciência e Inovação em Engenharia Mecânica e Engenharia Industrial and LAETA - Associated Laboratory for Energy, Transports and Aeronautics through the Unity of Conception and Experimental Validation (UCVE), and by the MIT - Portugal project "MIT - EXPL / ISF / 0084 / 2017", funded by Massachusetts Institute of Technology (USA) and "Ministério da Ciência, Tecnologia e Ensino Superior - Fundação para a Ciência e a Tecnologia" (Portugal). Additionally, the authors gratefully acknowledge the funding of Project NORTE - 01 - 0145 - FEDER - 000022 - SciTech - Science and Technology for Competitive and Sustainable Industries, cofinanced by Programa Operacional Regional do Norte (NORTE2020), through Fundo Europeu de Desenvolvimento Regional (FEDER). Furthermore, the author acknowledges the inter-institutional collaboration with the orthopedics service of Central Hospital of Porto - Hospital de Santo António - and its director, Prof.Dr. António Fonseca Oliveira. Finally, the author acknowledges the synergetic collaboration with the collaborators of "Computational Mechanics Research Laboratory CMech-Lab" (ISEP / FEUP / INEGI), and its director, Prof.Dr. Jorge Belinha, and its senior advisors, Prof.Dr. Renato Natal Jorge and Prof.Dr. Lúcia Dinis.

Contents

1	Introduction	1
1.1	Motivation	1
1.2	Goals	1
1.3	Thesis Outline	2
2	Background Literature Review	7
2.1	Bone	7
2.1.1	Bone Structure and Functions	7
2.1.2	Bone Morphology	8
2.1.3	Bone Structural Classification	9
2.2	Bone Cells	12
2.2.1	Osteoprogenitors	12
2.2.2	Osteoblasts	12
2.2.3	Bone-lining cells	13
2.2.4	Osteocytes	13
2.2.5	Osteoclasts	13
2.3	Bone Remodelling	14
2.3.1	Bone Remodelling Process	15
2.3.2	Bone Remodelling: Up to Mechanobiological Models	17
2.4	Homogenisation Techniques	20
2.4.1	3D Homogenisation Technique	23
2.5	Numerical Methods	25
2.5.1	Finite Elements Method	26
2.5.2	Meshless Methods	27
3	Original Developed Work	39
3.1	Introductory Remarks	39
3.2	Contribution I: A new numerical approach to mechanically analyse biological structures.	40
3.3	Contribution II: A brain impact stress analysis using advanced discretisation meshless techniques.	71
3.3.1	Highlights of Contribution: 3.3	71
3.4	Homogenisation Technique	105
3.5	Contribution III: A multiscale homogenisation procedure using the fabric tensor concept.	105
3.5.1	Highlights of Contribution: 3.5	105
3.6	Contribution IV: Combining the radial point interpolation meshless method with a new homogenisation technique for trabecular bone multiscale structural analyses.	118

3.6.1	Highlights of Contribution: 3.6	118
3.7	Contribution V: A multiscale homogenisation procedure combining the fabric tensor with a natural neighbour meshless method.	140
3.7.1	Highlights of Contribution: 3.7	140
3.8	Contribution VI: A 3D trabecular bone homogenization technique. (Submitted)	188
3.8.1	Highlights of Contribution: 3.8	188
3.9	Contribution VII. Application of an enhanced homogenization technique to the structural multiscale analysis of a femur bone. (Submitted)	213
3.9.1	Highlights of Contribution: 3.9	213
3.10	Book Chapters	231
3.10.1	Contribution VIII: "Meshless, Bone Remodelling and Bone Regeneration Modelling."	231
3.10.2	Contribution IX: Advances in Biomechanics and Tissue Regeneration: 10. Determination of the Anisotropic Mechanical Properties of Bone Tissue.	259
4	Conclusion	297
4.1	General Discussion	297
4.2	Conclusion and Future Work	299

List of Figures

2.1	Bone morphology example adapted from [1].	8
2.2	Cortical and trabecular bone schematics, adapted from [1]	9
2.3	Cortical bone schematics, adapted from [1]	10
2.4	Osteon schematics, adapted from [2]	11
2.5	Trabecular bone schematics, adapted from [1]	11
2.6	Bone cells schematics	12
2.7	I_s representative of trabecular bone	22
2.8	Images of parallel lines rotation I_t with an angle increment of 45° , within the interval of $t = [0, 180]$	23
2.9	Grid Lines Rotation Interceptions of Fig. 2.7	23
2.10	2.10a: Polar plot of ODF data, the red points, from figure 2.7; and 2.10b correspondent fitted ellipse.	24
2.11	RVE and orthogonal planes. Orthogonal direction 1 - red; Orthogonal direction 2 - Black; Orthogonal direction 3 - blue.	24
2.12	2.12a - ODF data for figure 2.11 orthogonal direction 1; 2.12b - ODF data for figure 2.11 orthogonal direction 2; 2.12c - ODF data for figure 2.11 orthogonal direction 3; 2.12d - ODF merged data; 2.12e ODF data fitted with ellipsoid.	24
2.13	2.13a - Example of a RVE with an obliquely principal direction; 2.13b - inaccurate ellipsoid fitting ODF data from obliquely principal direction	24
2.14	A: \mathbf{n}_0 Neighbour nodes; B: Provisional Voronoï cell, \mathbf{V}_0^* ; C: Voronoï cell, \mathbf{V}_0 ; D: Voronoï diagram	31
2.15	A: First and second degree natural neighbours in NNRPIM.; B and C: Delaunay Tessellation; D: Generated quadrilaterals; E: Sub-cell.	32
3.1	Contribution I convergence study results: A - 2D; B - 3D.	41
3.2	Contribution II convergence study results.	72
3.3	Contribution II: computational cost results.	72
3.4	Contribution III numerical convergence comparing structural analysis using heterogeneous models and the equivalent homogeneous ,defined using the developed methodology.	106
3.5	Contribution III computational time.	106
3.6	Contribution IV convergence study results.	119
3.7	Contribution IV computational time.	119
3.8	Contribution V: Rotation validation data.	141
3.9	Contribution V: Scale validation data: 3.9a - data from a trabecular bone RVE; and 3.9b - data from a created periodic benchmark.	142
3.10	Contribution V: FEM vs NNRPIM methodology and homogenous and heterogeneous models convergence.	142

3.11 Contribution V: Computational cost.	143
3.12 3.12a - Homogenised stiffness K for the mechanical simulation results performed using the first set of boundary conditions; 3.12b - Homogenised stiffness K value for the mechanical simulation results performed using the second set of boundary conditions.	189
3.13 Computational cost of the models defined with the homogenised methodology versus the computational cost of the heterogenous models.	190
3.14 Computational cost of the models defined with the homogenised methodology versus the computational cost of the heterogenous models.	214

Abbreviations

ATP	Adenosine Triphosphate
BMP	None Morphogenic Proteins
BMU	Bone Remodeling Unit
CSF	Cerebrospinal Fluid
CSF-1	Colony Stimulating Factor 1
CT	Computed Tomography
DEM	Diffuse Element Method
EFG	Element Free Galerkin
FDM	Finite Difference Method
FEA	Finite Element Analysis
FEM	Finite Element Method
micro-CT	Micro Computed Tomography
MIL	Mean Intercept Length
MLPG	Meshless Local Petrov–Galerkin
NNRPIM	Natural Neighbour Radial Point Interpolation Method
ODF	Orientation Distribution Function
OPG	Osteoprotegerin
PIM	Point Interpolation Method
PTH	Parathyroid Hormone
RANK	Receptor Activator of Nuclear Factor Kappa- β
RANKL	Receptor Activator of Nuclear Factor Kappa- β Ligand
RBF	Radial Basis Functions
RPI	Radial Point Interpolators
RPIM	Radial Point Interpolation Method
RVE	Representative Volume Element
SED	Strain Energy Density
SPH	Smooth Particle Hydrodynamics
TC	Tropocollagen
TGF- β	Transforming Growth Factor β

Chapter 1

Introduction

1.1 Motivation

The bone is a living-dynamic biomaterial tissue active during its lifetime that possesses relevant structural properties and a remarkable remodelling capacity. Being medical science evolving to individualised solutions, dictated by the distinct physiology of each patient, this study will allow to better predict the bone mechanical proprieties, a key factor used in many studies that allow predicting bone healing time up to the design of suitable implants for the patient unique bone properties, obtained by CT or X-ray images. This ultimately allows to improve patient life quality in a bone healing process, due to fracture/implants. Biomechanics is an area of increasing interest within the scientific community. Currently, the exciting improvements of experimental techniques allow researchers to obtain a considerable amount of data at several spatial scales. Supplied by the accuracy of these experimental measurements and the novelty of the observed phenomena, mathematical modelling of living matter begins to be a very attractive research field.

1.2 Goals

Based on all the reported facts, besides the biomechanical and bone remodelling research, the main goal of this study was to extend the knowledge of bone tissue by exploring the use of homogenisation multiscale methodologies combined with advanced discretisation methodologies to mechanically characterise bone. This goals to produce a methodology that can be used, in the future, combined with the bone remodelling research.

To understand and contextualise this problem, the following specific objectives were defined:

- Literature review of the biomechanical models of the bone remodelling process;
- Literature review of numerical tools as FEM, RPIM and NNRPIM;
- Validate the application of numerical tools as FEM, RPIM and NNRPIM to evaluate the behaviour of biological structures;
- Consider new application methodologies in biological structure in order to numerically analyse their response;
- Contribute to a better knowledge related with bone remodelling methodologies;
- Further develop tools to better study bone remodelling;
- Publication of the research outputs in international journals.

1.3 Thesis Outline

This structure of this thesis is based on the published/submitted journal papers and book chapters, is organised in 4 main Chapters.

Chapter 1 introduces the thesis subject. It is divided into 3 sections. Section 1.1 describes motivation for the development of the work. The objectives of the work are presented in the section 1.2. The last section, section 1.3, shows the thesis outline.

Chapter 2 provides a literature introduction on bone and bone cells. Afterwards, it is introduced the bone remodelling as the biological processes, but also, as its study and application in the modelling point of view. The fourth section of this chapter briefly introduces the homogenisation methodology developed in this thesis, once the methodology is explored in the contributions in Chapter 3. At last, numerical methods are introduced. In this chapter, section are presented the Finite Element Method and the meshless methods.

Chapters 3 is composed of the articles and book chapters written during the project. This chapter is designed to achieve the main purpose of this thesis. The sequence of articles is organised as follows:

Section 3.2 - Article 1:

- **Title:** A new numerical approach to mechanically analyse biological structures;
- **Authors:** M. Marques, J. Belinha, L. M. J. S. J. S. Dinis, and R. M. Natal Jorge;

- **Published in:** Computer Methods in Biomechanics and Biomedical Engineering;
- **Year:** 2019;
- **DOI:** <https://doi.org/10.1080/10255842.2018.1538413>

Section 3.3 - Article 2:

- **Title:** A brain impact stress analysis using advanced discretization meshless techniques;
- **Authors:** M. Marques, J. Belinha, L. M. J. Dinis, and R. Natal Jorge;
- **Published in:** Proceedings of the Institution of Mechanical Engineers, Part H: Journal of Engineering in Medicine;
- **Year:** 2018;
- **DOI:** <https://doi.org/10.1177/0954411917751559>

Section 3.5 - Article 3:

- **Title:** A multiscale homogenization procedure using the fabric tensor concept;
- **Authors:** M. Marques, J. Belinha, A. F. Oliveira, M. C. Manzanares Céspedes, and R. N. Jorge;
- **Published in:** Science and Technology of Materials;
- **Year:** 2018;
- **DOI:** <https://doi.org/10.1016/j.stmat.2018.01.002>;

Section 3.6 - Article 4:

- **Title:** Combining radial point interpolation meshless method with a new homogenization technique for trabecular bone multiscale structural analyses;
- **Authors:** M. Marques, J. Belinha, A. Fonseca Oliveira, M. C. C. Manzanares Céspedes, and R. M. N. Jorge;
- **Published in:** Acta of Bioengineering and Biomechanics;
- **Year:** 2018;
- **DOI:** <https://doi.org/10.5277/ABB-01300-2019-02>;

Section 3.7 - Article 5:

- **Title:** A multiscale homogenization procedure combining the fabric tensor with a natural neighbour meshless method;
- **Authors:** M. Marques, J. Belinha, A. Fonseca Oliveira, M. C. C. Manzanares Céspedes, and R. M. N. Jorge;

- **Published in:** Engineering Analysis with Boundary Elements;
- **Year:** 2019;
- **DOI:** <https://doi.org/10.1016/j.enganabound.2018.05.007>;

Section 3.8 - Article 6:

- **Title:** A 3D trabecular bone homogenization technique;
- **Authors:** M. Marques, J. Belinha, A. Fonseca Oliveira, M. C. C. Manzanares Céspedes, and R. M. N. Jorge;
- **Submitted in:** Acta of Bioengineering and Biomechanics;
- **Year:** 2020;

Section 3.9 - Article 7:

- **Title:** Application of an enhanced homogenization technique to the structural multiscale analysis of a femur bone;
- **Authors:** M. Marques, J. Belinha, A. Fonseca Oliveira, M. C. C. Manzanares Céspedes, and R. M. N. Jorge;
- **Submitted in:** Computer Methods in Biomechanics and Biomedical Engineering;
- **Year:** 2020;

Section 3.8 - Book Chapter 1:

- **Title:** Meshless, Bone Remodelling and Bone Regeneration Modelling;
- **Authors:** M. Marques, J. Belinha, R. M. N. Jorge and A. Fonseca Oliveira;
- **To be published in:** The Computational Mechanics of Bone Tissue - Biologic behaviour, remodelling algorithms and numerical applications;
- **Year:** 2019;
- **DOI:** <https://doi.org/10.1007/978-3-030-37541-6>;
- **ISBN:** 978-3-030-37540-9

Section 3.8 - Book Chapter 2:

- **Title:** Determination of the Anisotropic Mechanical Properties of Bone Tissue;
- **Authors:** M. Marques, J. Belinha, A. Fonseca Oliveira and R. M. N. Jorge
- **Published in:** Advances in Biomechanics and Tissue Regeneration;
- **Year:** 2019;
- **DOI:** <https://doi.org/10.1016/B978-0-12-816390-0.00010-8>

- **ISBN:** 978-0-12-816390-0

Chapter 4 explore the main conclusions and possible future research.

Chapter 2

Background Literature Review

2.1 Bone

Bone is a structure mainly defined by the bone matrix and by bone cells. Bone cells are responsible to produce the bone matrix. These cells create the bone matrix and reabsorb it, allowing the replacement of the old bone matrix by a newer one. The bone matrix is normally made by 35% organic and 65% inorganic material, being the inorganic material mainly calcium phosphate crystal, called hydroxyapatite $Ca_{10}(PO_4)_6(OH)_2$. The organic bone matrix is mainly made of type I collagen (88%) and the remaining 12% are divided in 10% of non-collagenous proteins (osteocalcin, osteonectin, bone sialoprotein and various proteoglycans) and 2% of lipids and glycosaminoglycans. [3]

2.1.1 Bone Structure and Functions

All the bones in the human body make the skeletal system. This system has support, protection, movement, storage and blood cell production functions. Being bone a rigid and strong structure, it is suited to support the body weight. Bones also allow the protection of organs by enclosing them, being, for example, the brain and the spinal cord enclosed in the skull and in the vertebrae for protection. Bones are connected to the muscles by tendons, which permits that when a muscle contract a bone moves, producing body movements. Bones also have other functions as mineral and energy repository. Mineral since they storage calcium and phosphorus, and energy since

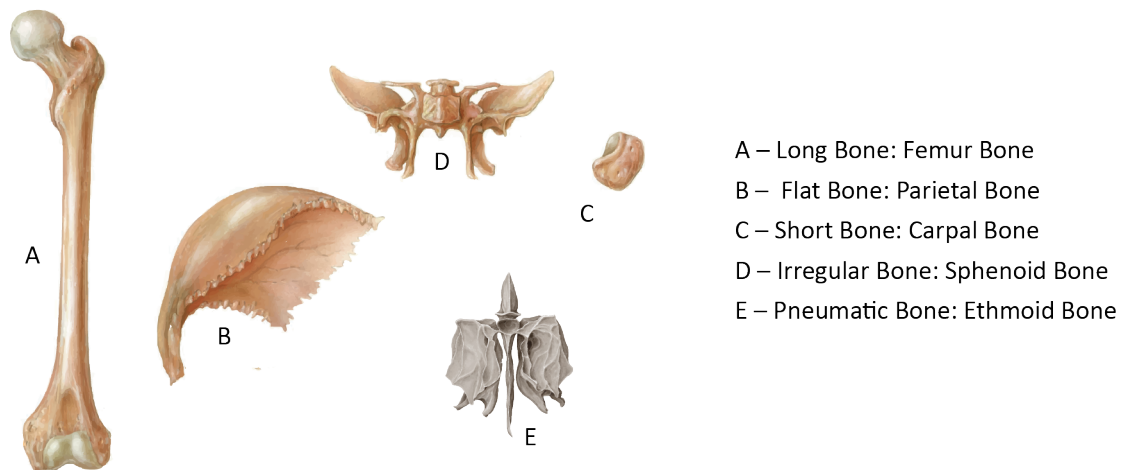


Figure 2.1: Bone morphology example adapted from [1].

yellow marrow fat cells are present in bones. Usually, long bones contain cavities filled with red bone marrow, responsible for the creation of the blood cells and platelets. [1,2,4]

2.1.2 Bone Morphology

Bones can be classified according to its morphology, existing 5 classifications, the long, short, flat, irregular and pneumatic bones, as can be seen in figure 2.1

Long bones have an elongated shaft, the diaphysis, and two expanded ends, the epiphyses, one on either side of the shaft. Normally, the epiphyses are smooth and articular and the diaphysis has a central medullary cavity where the bone marrow exists. Long bones are used for a greater range of motion. Femur, humerus, metacarpals, metatarsals, and phalanges are examples of long bones. Short bones have as main function providing support and stability with small movement. These bones have a larger width than length. They are found mainly in the feet and hands, carpal and tarsal bones, but also other anatomic areas, as the scaphoid and trapezoid bones. Flat bones are flat and have two prominent surfaces known as the anterior and posterior surfaces, made from compact bone to provide strength for protection, and their core consists of trabecular bone. Flat bones main function is to provide protection to the body vital organs and to provide a base for muscular attachment. Cranial bones, as frontal and temporal, are an example of flat bones. Irregular bones consist primarily of trabecular bone, with a thin outer layer of compact bone. Typical examples of irregular bones are the vertebrae, sacrum, and bones in the base of the skull Pneumatic bones, or hollow bones, have the unique and different characteristic of having in it large void spaces,

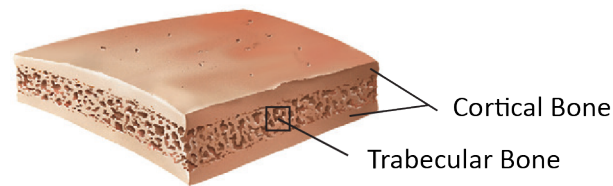


Figure 2.2: Cortical and trabecular bone schematics, adapted from [1]

which makes them lightweight. Pneumatic bones form the major portion of the skull to making it light in weight. Pneumatic bones also contribute to the resonance of sound and function as air-conditioning chambers for inspired air. [1,2,4]

2.1.3 Bone Structural Classification

Bone can be classified by its structure at different microscopic and macroscopic level. At a microscopic level, bone can be classified as reticular or lamellar and at a macroscopic level it can be classified as cortical or trabecular, Figure 2.2.

2.1.3.1 Microscopic Level Bone: Reticular

Reticular or woven bone is immature bone, that contain collagen fibres in a not stress orientation. Eventually reticular bone is converted to lamellar bone, except in adults, for whom it is only present in a few places, such as the sutures of the flat bones of the skull, tooth sockets, and at the insertion sites of some tendons. In adult, if present in other than this places reticular bone is considered pathological. Compared to lamellar bone, reticular bone has more osteocytes per unit of volume, providing a higher rate of turnover, and has smaller amounts of mineral substance making it weaker and more flexible than lamellar bone. [1,2,4]

2.1.3.2 Microscopic Level Bone: Lamellar

Lamellar bone having its origin in reticular bone, is organised and stress oriented, being stronger and less flexible than reticular bone. This is a normal type of adult mammalian bone composed of thin plates (lamellae). Being cortical or trabecular bone, it is composed by parallel lamellae former and concentric around a vascular canal. [1,2,4]

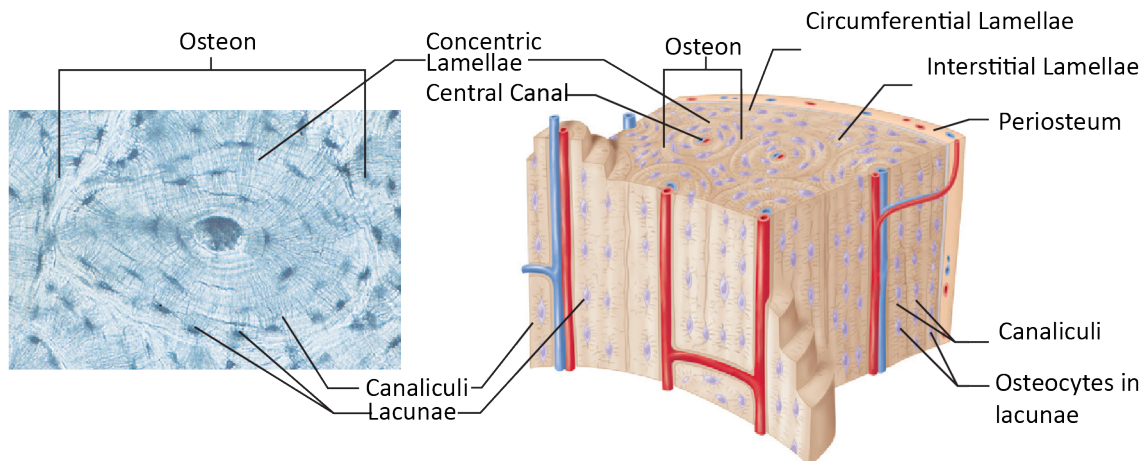


Figure 2.3: Cortical bone schematics, adapted from [1]

2.1.3.3 Macroscopic Level Bone: Cortical Bone

Cortical or compact bone is the denser and harder type of bone and constitutes 80% of the skeletal bone mass. Cortical bone is the hard material that makes the shaft of long bones and the outside surfaces of other bones. [4] Figure 2.3 and Figure 2.4 have represented some of the most relevant entities of the cortical bone.

The basic functional unit of cortical bone is the osteon, also known as the Havers system, which consists of 4–20 concentric layers of bony lamellae surrounding a central Haversian canal, that can contain blood vessels, nerves and loose connective tissue. The existence of perforating canals, called Volkmann's canals, which run perpendicular to the long axis of the bone, allow blood vessels from the periosteum or medullary cavity to enter the bone and the connection of the osteons with each other, allowing the conduction of blood vessels through the bone.

In the between of the lamellar rings are present the osteocytes. The osteocytes communicate with each other by projecting throughout the lamellae very thin and long cytoplasmic extensions along the tiny canals called canaliculi. It is through the canaliculi that electro-chemical information flows, the nutrients and minerals reach all points of the bone matrix but also the waste products are removed. In long bones, besides the osteons, the outer surfaces of compact bone are formed by circumferential lamellae, spawned by the inner layer of the periosteum. [1, 2] In general, the Young's modulus of compact bone is about 18 GPa and its porosity ranges from 5% to 30%. [4]

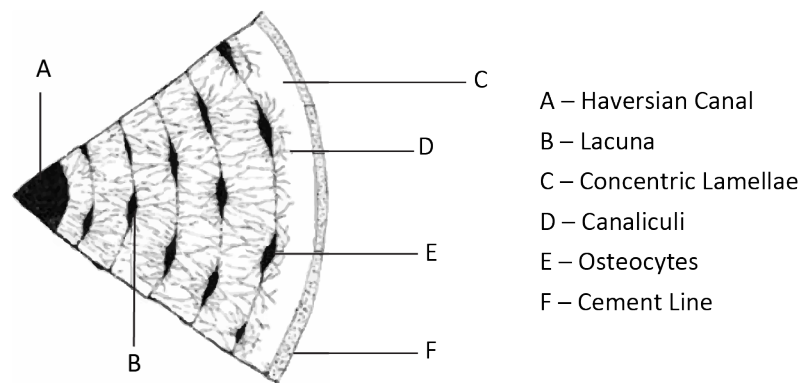


Figure 2.4: Osteon schematics, adapted from [2]

2.1.3.4 Macroscopic Level Bone: Trabecular Bone

The trabecular bone, or spongy bone, is composed of mature lamellar bone and consists of inter-connecting rods or plates of bone, a meshwork called trabeculae, Figure 2.5.

Trabeculae consist of thin, irregularly shaped plates arranged in an openwork framework. In the case of a long bone, the trabecular bone is typically located at the proximal ends, where the arrangement of the trabeculae is relatively regular, reflecting the mechanical loads to which this kind of bone is subjected. Existing a variation of this load patter, the bone has the capability of realigning the trabecular pattern with the new lines of stress created by the new load pattern. Trabecular bone constitutes 20% of the skeletal bone mass, but due to the trabeculae vast specific-surface, the surface-to-volume ratio is ten times higher than the cortical bone, reflecting why metabolic bone diseases have a greater effect on trabecular bone than on cortical bone. Most trabeculae are thin, 50–400 microns, and consist of several lamellae with osteocytes located in lacunae between the lamellae. The trabeculae surfaces are covered with a layer of cells consisting mostly of osteoblasts with a few osteoclasts. These osteocytes trapped between calcified lamellae

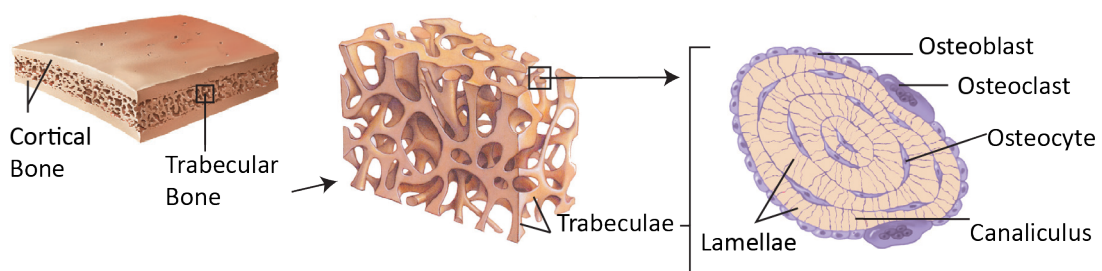


Figure 2.5: Trabecular bone schematics, adapted from [1]

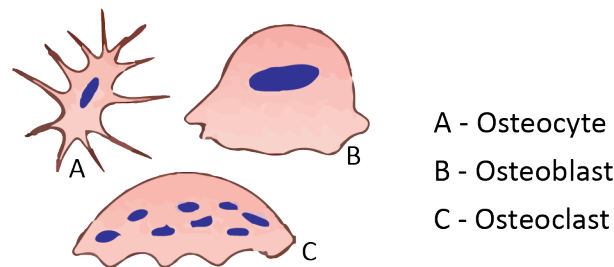


Figure 2.6: Bone cells schematics

are connected to each other through canaliculi. Being trabecula only a few cell layers thick, the osteocyte can exchange nutrients with nearby blood vessels through their canaliculi. Despite its relatively small volume and high apparent porosity, trabecular bone is well adapted to resist and conduct compressive loads. Trabecular bone Young's modulus is about 1 GPa and have a porosity between 30% and 90%. [2,4]

2.2 Bone Cells

Bone cells are found within the bone tissue and are responsible for many different metabolic processes. These cells are included in the processes such as the development of new bones, bone remodelling and in other processes such as homeostatic regulation of minerals in the body. The bone cells are, Osteoprogenitors, Osteoblasts, Bone-lining cells, Osteocytes and Osteoclasts. In Figure 2.6 is represented a schematic of the osteocyte, osteoblast and osteoclast.

2.2.1 Osteoprogenitors

The osteoprogenitors are non-specialised cells which differentiate to origin the osteoblasts. [5] These cells are in the origin of all bone structures during the development process and are generated in the bone marrow, or in other connective tissues. This cells can be found in the interior layers of the periosteum, in the endosteum and in the Haversian's and Volkman's canals. [1,2,4]

2.2.2 Osteoblasts

The osteoblasts are mononuclear bone-forming cells responsible for bone formation and for the mineralization of the osteoid matrix. Osteoblasts are produced in the periosteum, bone outer

surface, endosteum, bone inner surface, and in the bone marrow and can be found in the bone endosteum and in bone periosteum, in a laminar distribution. These cells are responsible for the collagen and proteoglycans production but also for the release of matrix vesicles, that contains concentrate Ca^{2+} and PO_4^{3-} that originate hydroxyapatite crystals. Being the hydroxyapatite crystals released from the matrix vesicles, they stimulate hydroxyapatite formation and mineralization of the matrix. [1,2,4]

2.2.3 Bone-lining cells

The bone-lining cells are inactive elongated and thin osteoblasts that remain inactive in the bone surface once the bone formation, or the bone remodelling, has finished. These cells, can however be reactivated in response to mechanobiological stimulus. [1,2,4]

2.2.4 Osteocytes

The osteocytes are cells that mature from the osteoblasts. Osteocytes are relatively inactive, compared with most osteoblasts, but still, they are able to produce the components needed to maintain the bone matrix. Osteocytes occupy spaces inside the mineralised bone matrix, the lacunae. These chambers are connected to each other by long cytoplasmic extensions, the canaliculi, that allow osteocytes to conserve the connection with the outer osteoblasts. This leads to the preservation of the surrounding mineralised bone matrix vitality. Canaliculi are used to pass through nutrients and gases through the small amount of fluid surrounding the cells in the canaliculi and lacunae. These canals also allow the creation of a vast network of cells that connect each other through GAP connection. This vast network of osteocytes is connected to the outer cell, making osteocytes work as a local sensor of the mechanical and chemical state of the bone and if needed initiates the reabsorption process from the surface. [1,2,4,6,7]

2.2.5 Osteoclasts

Osteoclasts are the cells responsible for the reabsorption and/or elimination of Ca^{2+} and of PO_4^{3-} . This process is done through the demineralisation of the mineralised bone matrix and the destruction of the bone organic matrix. This reabsorption allows the usage of Ca^{2+} and of PO_4^{3-} in many

metabolic processes. Osteoclasts are multinucleated cells that originate within the red bone marrow monocyte/macrophage lineage and are matured into functional osteoclasts by direct contact with osteoblasts. Osteoclasts cells are located in superficial depressions (Howship lacunae) which identify the bone reabsorption zones. The bone reabsorption process begins when the osteoblasts present in the connective tissue around bone activate the movement of mature osteoclasts into a bone remodelling area. Once the osteoclasts come in contact with the bone surface, they form attachment structures via interactions with cell-surface proteins called integrins. After this, a set of structures are formed, podosomes, creating a sealed section under the osteoclast. The osteoclast forms a called ruffled border, that is a highly folded cell membrane. Acidic vesicles fuse of the ruffled border and ATP-powered H^+ pumps, and protein-digesting enzymes are inserted into the membrane of the ruffled border. The secretion of H^+ within the sealed section causes decalcification of the bone matrix, and the protein-digestion enzymes that are secreted into the sealed compartment digest the organic, protein component of the bone matrix. The degradation products are removed by a transcytosis mechanism, where products enter the osteoclast through the sealed side and move across the cytoplasm to the other side. These products are then secreted into the extracellular space and enter the blood flow, is available for metabolic processes. [1,2,4]

2.3 Bone Remodelling

Bone remodelling is the biological process whereby living bone tissue renews itself in the course of life. [8] In general growth, reinforcement, and resorption are collectively termed as remodelling. This remodelling is progressive and is induced in order to adapt the bone morphology to any new external load. The concept strain/stress-induced bone remodelling was firstly reported by Wolff in 1886. [9] Later in 1892, Wolff found that the orientation of trabecular bone coincides with the direction of the stress trajectories. With this, Wolff proposed that bone loading is somehow sensed by the bone. This principle of functional adaptation is known as Wolff's law. In 1939 Wolff's law was firstly described in vitro by Glucksmann in 1939. [10] In 1965 by Pauwels, was created the first mathematical formulation that described the process described by Wolff. [11] This mathematical formulation assumed that exist an optimal mechanical stimulus that balanced the bone tissue resorption and deposition. [12]

2.3.1 Bone Remodelling Process

Bone remodelling is a complex process performed by the coordinated activities of the osteoclasts, that resorb the bone, osteoblasts that replace the bone, the osteocytes within the bone matrix, the bone lining cells that covering the bone surface and the capillary blood supply. Together, osteoclasts and the osteoblasts cells form temporary anatomical structures, called bone remodelling units (BMUs), which execute bone remodelling. The interactions between osteoblasts and osteoclasts, that guarantees a proper balance between bone gain and loss, is known as coupling. [13] All the millions BMU present in the skeleton are in different stages, being the life span of individual cells that create a BMU much shorter than that BMU itself. [14–16] These BMUs are constantly remodelling bone tissue in growing adult and senescent skeleton, preventing premature deterioration and maintaining its overall strength. If there is an interruption of this bone remodelling process due to a biochemical or cellular link cut, such as osteoporosis or hyperparathyroidism, might be disrupted a metabolic bone disease. Normal bone remodelling occurs in discrete bone locations taking 2 to 5 years for a discrete location to complete one bone remodelling cycle. [17] This constant care of the bone matrix prevents its premature deterioration and maintains its overall strength. Bone remodelling can be classified as targeted remodelling, or by random remodelling. If a specific region of the bone is induced to remodel due to a, for example, a structural microdamage, is said to occur a targeted remodelling. [18, 19] In this case remodelling permits to restore the microdamage caused by fatigue and/or by shock. Being bone remodelling a main process with a role in the mineral homeostasis, by providing calcium and phosphate, and being these calcium and phosphate removed from random locations from the skeleton, in this case, it occurs a random remodelling. [18, 19] Bone balance is defined as the amount of bone removed and of new bone restored in the bone remodelling process. While the interactions between osteoblasts and osteoclasts are rarely affected by outer factors, bone balance can be easily modified by diseases, hormonal factors and even by external mechanical stimulus. Being bones a major reservoir of body calcium, bone is under the hormonal control of parathyroid hormone (PTH), the most important hormone regulating calcium homeostasis and bone remodelling. [20] The modification of the bone remodelling behaviour, that has a direct influence in the bone mass is affected by the effect of PTH, in which a continuous increase of the PTH levels decreases bone mass and discontinuous PTH administration leads to an increase of bone mass. [21–24]

Also, long-term physical activity on a regular basis plays a particularly important role in bone remodelling. The mechanical stimulus-induced by physical exercise can maintain or increase bone strength by increasing bone mass or by changing bone structures at micro and macro levels. Two main types of exercise are beneficial to bone health: weight-bearing, exercise performed while a person is standing so that gravity is exerting a force, and resistance exercise, exercises involving lifting weights with arms or legs. Long-term physical activity on a regular basis plays a particularly important role in maintaining healthy bones. Exercise can maintain and increase bone strength by increasing bone mass or by changing bone structures at micro and macro levels [25]. More recently, it was reported that as the presence of external loads lead to bone remodelling, also the absence of load that occurs in conditions of disuse, such as during immobility, space flight, and long-term bed rest lead to the same processes, having the opposite result, bone loss and mineral changes. [4,26,27] Bone remodelling can be divided into five distinct phases that occur in a coordinate and sequential way. This five phases are the activation, resorption, reversal, formation and the termination. The activation phase is characterised by being a continuum process that occurs in the boundaries of the BMU where it is detected the presence of an inducing remodelling signal, that can be of mechanical or hormonal nature [17]. Bone cells are exposed to a dynamic environment of biophysical stimuli that includes strain, stress, shear, pressure, fluid flow, streaming potentials and acceleration, having these parameters independently the ability to regulate the cellular responses and influence the bone remodelling. The osteocytes located in the cortical bone have the ability to sense this biophysical stimulus that through the canaliculi network activate the regulation of the proteins sclerostin and receptor activator of nuclear factor kappa- β ligand (RANKL), that has a major role in bone remodelling, by other bone cells. [25,28] The resorption phase is characterised by the formation and activity of osteoclasts that, as explained before, create a sealed section where the resorption process occurs. This formation and activity of osteoclasts is controlled by osteoblast cells that activate the movement of mature osteoclasts into a bone remodelling site with the expression of Colony Stimulating Factor 1 (CSF-1), RANKL, Osteoprotegerin (OPG) and by PTH. [1, 2, 4, 17, 29, 30] The reversal phase lasts around 9 days and occurs when the maximum eroded depth is achieved, between 60-40 μm . This phase is characterized by the transition of the activity from osteoclast to osteoblast. [15] The osteoclasts start the process of apoptosis and at the same time the bone-lining cells enter the lacuna and clean bone matrix remains. This clean up

allows the deposition of a proteins (collagenous) layer in the resorption pits forming a cement line (glycoprotein) which helps in the attachment of preosteoblasts that begin to differentiate. [31,32] The formation phase is characterized by the formation of new bone. Once osteoclasts resorbed the cavity of the bone, they are replaced by cells of the osteoblast lineage, that initiate the bone formation, the preosteoblast. The preosteoblast are attracted by the growth factors liberated from the matrix that act as chemotactic and in addition stimulate its proliferation. The preosteoblasts synthesise a cementing substance upon which the new tissue is attached and express bone morphogenic proteins (BMP) responsible for differentiation. The bone resorption liberates TGF- β from the matrix, which is a key protein for recruiting mesenchymal stem cells to sites of bone resorption. This recruitment of mesenchymal stem cells and the presence of the BMP lead to the differentiation of preosteoblasts to osteoblasts. The already differentiated osteoblasts synthesise the osteoid matrix and also secrete collagen, that accumulated contributes to the cessation of cell growth. Having the osteoid, the non-mineralised organic portion of the bone matrix, it has to be mineralised with hydroxyapatite to create a mature bone tissue. [25,33]

The termination phase is characterized when occurs the terminal differentiation of the osteoblast. Some of the osteoblast transform to lining cells, that cover the newly formed bone surface while others osteoblast differentiate into osteocytes and remain in the matrix. [25,28,33]

2.3.2 Bone Remodelling: Up to Mechanobiological Models

Bone remodelling is a process that has been continuously studied, resulting in the developing of semi-empirical mathematical descriptions of this process. This mathematical modelling resulted in the creation of mathematic models that allow to study the process, providing a tool to simulate and predict experimental results using computer science. Since the understanding of bone remodelling, the scientific community is continuously developing semi-empirical mathematical descriptions of this process to gain a better understanding of the nature of bone remodelling. This way, mathematical modelling provides a powerful tool for computational simulation and to predict experimental results. The first mathematical formulation that described the ‘Wolff’s law’, assumed the existence of an optimal mechanical stimulus balancing the bone tissue resorption and deposition and it was developed in 1965 by Pauwels. [11] In 1964 Frost presented the "Curvature Model" describing that the remodelling process was controlled by strain actions . [34] In 1976, Cowin and

co-workers presented the “Adaptive Elasticity” model that described the theory of bone internal remodelling defined as the sum of chemical reactions between the bone matrix and the extra-cellular fluids. [35–38] Later in 1987, the "self-optimisation" concept was introduced by Carter and co-workers, disclosing the functional adaptation of a mathematical law for the bone trabecular structure. [39–42] The algorithm proposed by Carter assumes that the mechanical stimulus is proportional to the effective stress field and permits to consider several mechanical cases. Also in 1987, Huiskes et al, developed a method to predict stress-related adaptive bone remodelling, where the Strain Energy Density (SED) was used as a feed-back control variable to determine shape or bone density adaptations, whereby homeostatic SED distribution was assumed as the remodelling objective. [43] Later, Reiter et al. [44] and Pettermann et al [12], modifying Huiskes et al [43] model introduced the effects of overstrain necrosis and usage of anisotropic material behaviour, respectively. Harrigan and Hamilton introduced the strain energy density for stress-induced remodelling as mechanical stimuli, using "Adaptive Elasticity" concept. [45–47] In 2012, Belinha et al [48, 49], developed a material law that permits to correlate the bone apparent density with the obtained level of stress. With this new material law, Belinha et al developed a biomechanical model for predicting bone density distribution, based on the assumption that the bone structure is a gradually self-optimising anisotropic biological material that maximises its own structural stiffness. This model, an adaptation of Carter’s model [39–42], assumes that mechanical stimulus acts as the principal driving force in the bone tissue remodelling process [48, 49].

Since the majority of the proposed models only concern the bone remodelling induced by mechanical stimuli at a non-cellular level, more recently have been developed and proposed mathematical models that mathematically reconstruct the process of bone remodelling at the cellular level. [50–54] These models focus on how biomechanical stress induces bone formation [50–54] or how biological factors affect bone resorption. [55] Martin and Buckland-Wright, 2004 developed a mathematical model that predicted the depth of erosion and duration of the resorption phases in healthy adult cancellous bone-based wholly on biological information. This model uses Michaelis-Menten-like feedback mechanics to affect bone resorption. [55] Lemaire in 2004, developed the first mathematical model that includes the RANKL/Receptor Activator of Nuclear Factor Kappa- β (RANK)/OPG pathway, that affects the bone remodelling process. This model based on the idea that the relative proportions of immature and mature osteoblasts control the degree of osteoclas-

tic activity. [51] Pivonka et al, 2008 [53] proposed a model based on the Lemaire's model [51], adding four new parameters: 1: rate equation describing changes in bone volume with time; 2: a rate equation describing the release of TGF- β from the bone matrix; 3: the expression of OPG and RANKL on osteoblastic cell lines; 4: modified activator/repressor functions. [53] Komarova et al, 2003 [50] developed a mathematical model that described the population dynamics of bone cells, with the number of osteoclasts and osteoblasts at a single BMU. The interactions of autocrine and paracrine among osteoblasts and osteoclasts allowed the authors to calculate cell population dynamics and changes in bone mass at a discrete site of bone remodelling. [50] To summarise the net effect of local factors on the rates of cell production, this model uses a power-law approximation that was developed by Savageau [56] as effective tools for analysis of highly nonlinear biochemical systems. In this model, all factors leading to a cell response are taken together in a single exponential parameter. [50]

In an attempt to integrate both the mechanical and the biological components simulating the remodelling process at a cellular level, mechanobiology, a discipline at the edge of biology and engineering, started to gain importance. The used strategy to study bone cell remodelling restricted to biochemical factors or to mechanical stimuli became to be considered reductionist, and so, bone remodelling models start to consider the entire cell microenvironment, being now accepted that mechanical forces are also involved in the development, physiological and pathological processes. [57] Examples of mechanobiology are present in the mechanobiological models developed by Yi et al 2015, [58] Hambli 2014, [59] and by Lerebours et al, 2015. [60] Yi et al 2015, developed a microscale bone remodelling model and corresponding governing equation. In this models were used the equivalent strain as the mechanical stimuli, that affect proliferation and differentiation of the osteoblast cells. The influence of the different physiological conditions, restricted by the Denosumab, a used drug for treating osteoporosis, on the formation/resorption rate was also considered. [58] Hambli, [59] developed a model that describes the bone remodelling process, taking into consideration biological and mechanical stimuli. In this model, the cellular behaviour is based on Komarova et al. (2003) dynamic law. [50] The mechanical behaviour of bone is defined by the bone material fatigue damage accumulation and mineralization. In this model are present strain–damage stimulus functions that relate the mechanical stimuli with the biological one, since the strain–damage stimulus function controls the level of autocrine and paracrine fac-

tors. Lerebours et al, 2016 [60] developed a multiscale mechanobiological model that describes the evolution of a human mid-shaft femur scan subjected in osteoporosis and mechanical disuse, two deregulating circumstances. In these models are included hormonal regulation and biochemical coupling of bone cell populations. These models also include a mechanical adaptation of the tissue and factors that influence the microstructure on the bone turnover rate. [60]

Mathematical models that describe and simulate bone remodelling have evolved from simple macroscale models with simplistic approaches to multiscale, multi-factor and complex models. The mechanobiological models used to simulate bone remodelling are quite much unexplored, thus, this new approach has enough space and high possibilities to evolve and to describe unexplored topics.

2.4 Homogenisation Techniques

Some of the models and methodologies previously presented consider bone has a hierarchical structure, where different structural levels can be identified from the macroscale (whole bone) to sub-nano scale (hydroxyapatite crystals, constituents of the inorganic phase of bone and Tropocollagen (TC) molecules). [61, 62] The macroscale and the microscale (the trabecular architecture level), can be defined by different physical properties due to its different functional requirements, such as bone density and corresponding mechanical properties. This means that the behaviour of the structure at its microscale significantly influences the behaviour of the structure observed at the macroscale. Finding the relation across scales, will allow to develop multiscale models capable to predict the behaviour of the macroscale using the microscale, and vice-versa. Homogenisation techniques allow to homogenise the mechanical properties of the heterogeneous material under study, thereby allowing to substitute this material with an equivalent homogeneous material. This homogenisation can be integrated into multiscale methods allowing to define, for example, the mechanical properties of highly complex microstructure as trabecular bone, and replace this microstructure by a simple structure with equivalent mechanical proprieties. This simplification allows to relate the multi scales and simplify the problem complexity, solving it at the macroscale. [63] Combining homogenisation technique (applied to the trabecular bone micro scale) with numerical methods, meshless or FEM, it is possible to achieve low-cost and ef-

efficient multiscale techniques. These homogenisation techniques allows to define the mechanical properties of a trabecular bone representative volume element (RVE), often using medical images generated by micro-computational tomography (micro-CT), allowing to acquire information of the trabecular bone morphology. The fabric tensor, a symmetric second rank tensor, started to be used to create homogenisation techniques. [64–66] The fabric tensor, that can be obtained using mechanical based or morphologic-based techniques, and it can mechanically characterise arrangement of a multiphase material by encoding the orientation and anisotropy of the material. Recalling that morphologic-based methods use the interface between phases of the material to estimate the fabric tensor and that bone morphology can be defined using a micro-CT (at the microscale) or a computational tomography (CT) (at the macroscale), it is possible to use medical images to define the fabric tensor, when considering bone. Most of the available techniques using morphologic-based methods to obtain the fabric tensor apply an orientation distribution function (ODF), to estimates an orientation-dependent feature of interest. In mechanics, and in biomechanics, the accurate determination/characterisation of the material's mechanical properties is a key parameter, which will allow to describe and predict numerically the behaviour of such materials for different scenarios. Naturally, there is a never-ending interest from the scientific community concerning the material characterisation, by developing/enhancing: constitutive laws, experimental procedures and computational tools/methodologies. The use of the fabric tensor often start by the definition of a region of interest able to define the material morphology that is intended to be studied, ex. figure 2.7. The methodology developed by Whitehouse [67] (considered a golden standard in this kind of application) requires the identification in the RVE of different phases characteristic of the material. [67–71] Whitehouse's methodology requires image processing tools. In Whitehouse methodology, the Mean Intercept Length (MIL) methodology, the number of interceptions between a parallel family line in direction ι , with the interface between both phases of the material is counted, $\text{Int}(\iota)$. The length of the parallel lines family, h , is also considered. The relation between the parameters h , ι and $\text{Int}(\iota)$, equation (2.1), allow to define the ODF needed to define the fabric tensor.

$$\text{MIL}(\iota) = \frac{h}{\text{Int}(\iota)} \quad (2.1)$$

Figure 2.8a represents an example of an image containing a family of parallel lines I_ι , in this



Figure 2.7: I_s representative of trabecular bone

case, with $\iota = 0^\circ$. Counting the interceptions of those parallel lines with changes of phase of RVE, represented by the boundaries of the I_s , it is possible to obtain the orientation-dependent feature. For different ι , between 0° and 180° , it is possible to obtain the ODF of the I_s . The generated data for ι between $]180^\circ, 360^\circ[$ is a $[0^\circ, 180^\circ]$ data repetition, since the orientation-dependent feature is not influenced by the direction. For example, Fig. 2.8 represent the rotation of I_t between 0° and 180° with a ι increment of 45° .

To better understand how the ODF data is acquired using I_s and I_t , figure 2.9 is presented. Each sub-image makes reference ι between 0° and 180° , using an increment of 45° . In each one of the images, five pixel colours: black, blue, cyan, red and pink are presented, as a result of the combination of multiple images information. The blue pixels represent the correspondent white pixels from the I_s image. The black pixels represent the background of the I_s image. This information is constant in each set of images with origin in the same I_s image. The only pixels that changes in these images are the pixels in red, cyan and pink. The red pixels represent the I_t . The creation of this I_t results in five different images, as can be observed in 2.9. The union of the pink pixels with the cyan pixels represent the intersection of I_s with each one of the I_t images. The methodology to acquire the ODF data only needs the information of the material phase change, and for this reason, only the cyan pixels are used to obtain the ODF data. Counting the number of cyan pixels that result from combining I_s with each I_t , and considering the length of the parallel family lines, equation (2.1), the resulting ODF data is plotted in figure 2.10a. Fitting an ellipse into this data, it is possible to obtain the material orientation of the trabecular RVE. In figure 2.10b is representer the fitted ellipses to the corresponding ODF data. Considering Wolff's Law, it is understandable that this ellipse is aligned with the RVE preferential trabecular

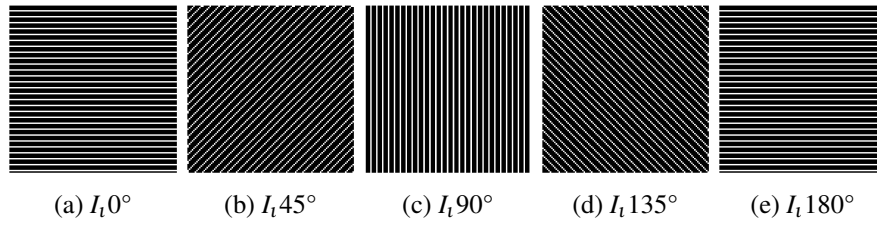


Figure 2.8: Images of parallel lines rotation I_t with an angle increment of 45° , within the interval of $t = [0, 180]$

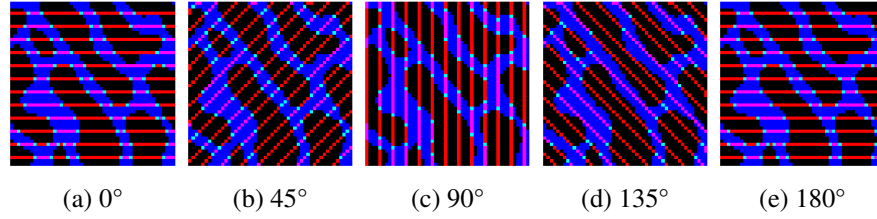


Figure 2.9: Grid Lines Rotation Interceptions of Fig. 2.7

2.4.1 3D Homogenisation Technique

The 3D homogenisation technique can be developed using the same principles of the 2D methodology. In this work were attempted different approaches to extrapolate the 2D methodology to 3D. One of attempt was to develop the 3D methodology using exactly the same approach used in the 2D methodology, where to each slice of the 3D image was applied the 2D methodology. Thus, when validating the results, it was verified that the used approach was not accurate. In this failed attempt, the 3D RVEs, a set of piled 2D images acquired from a micro-CT or CT image, was used. To each layer of each orthogonal plane of this 3D image was applied the 2D methodology, as showed in figure 2.11. This methodology has the expected result if the principal directions of the material was normal to any of the 3 orthogonal planes of the image. In figure 2.12, is presented as example a RVE with the principal direction normal to one of the orthogonal directions. In this cases, the ODF data from each layer of each orthogonal direction, figure 2.12a, 2.12b and 2.12c, was able to encode the RVE principal direction. Merging the ODF data off all RVE layers, figure 2.12d, it was possible to define an ellipsoid that encodes the RVE principal direction, figure 2.12e. On the other hand, when the principal diction of the RVE was not normal to any of the orthogonal planes, figure 2.13a, the methodology was no able to define an ellipsoid with the RVE principal direction encoded, figure 2.13b. In figure, 2.13a the red line represents the RVE principal direction, that is oblique to all the orthogonal planes.

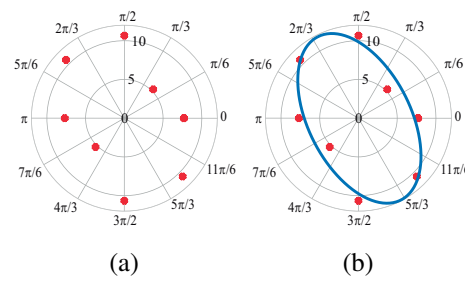


Figure 2.10: 2.10a: Polar plot of ODF data, the red points, from figure 2.7; and 2.10b correspondent fitted ellipse.

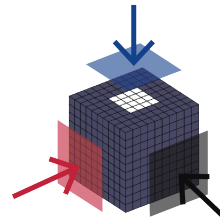


Figure 2.11: RVE and orthogonal planes. Orthogonal direction 1 - red; Orthogonal direction 2 - Black; Orthogonal direction 3 - blue.

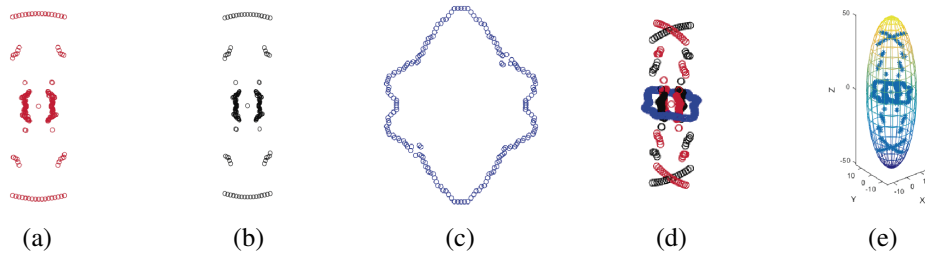


Figure 2.12: 2.12a - ODF data for figure 2.11 orthogonal direction 1; 2.12b - ODF data for figure 2.11 orthogonal direction 2; 2.12c - ODF data for figure 2.11 orthogonal direction 3; 2.12d - ODF merged data; 2.12e ODF data fitted with ellipsoid.

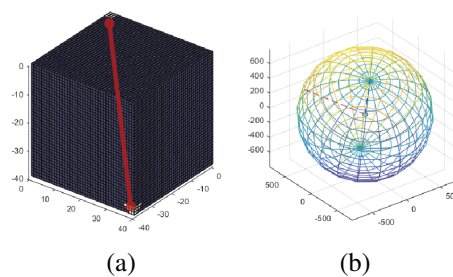


Figure 2.13: 2.13a - Example of a RVE with an obliquely principal direction; 2.13b - in-accurate ellipsoid fitting ODF data from obliquely principal direction

After the development of these inaccurate methodologies, it was seeking other methodology

able to define accurately the 3D fabric tensor, in order to further develop the 3D homogenisation technique to define bone mechanical properties. With this, the methodology used to define the 3D fabric tensor was developed with the hypothesis of a search sphere, that contains a set of vectors with well-defined directions, that iteratively change its centre, within the RVE geometrical space, and the interceptions of each vector is counted, in each iteration with the RVE bone zones. Contribution VI [3.8](#), explore the development of this methodology as well as its validation and application on a structural analysis.

2.5 Numerical Methods

One of the most central activities performed by engineers and scientists is to model natural phenomena in order to study and simulate them. Much of the physical phenomena studied, particularly those related to continuum theory and time variable, can be formulated in terms of algebraic, ordinary or partial differential and/or integral equations, and referred to a particular area. This conceptual and mathematical models simulate physical events, whether they are biological, chemical, geological, or mechanical, are based on laws of physics. The constitutive model from the physical law allows to build a set of integro-differential equations after the application of energy and mass conservation principles. Such equations form an equilibrium system of equations, allowing to obtain the aimed variable field (displacement, temperature, velocity, etc.). In order to obtain the problem's solutions, one has to characterise the problem boundary conditions (or border) and (or) initial conditions. There are many phenomena often associated with different branches, that can obtain using the same mathematical model and consequently the same differential equations. [\[72\]](#) Most real engineering problems cases are characterised by very complex equations modelled on geometrically complicated regions and defined by equations with nonlinear nature, making it generally impossible to obtain an analytical solution. For these cases, it can be used numerical approximation methods to obtain the solutions. The development of computers in recent decades has made possible from these methods, the solution of many problems heretofore unsolvable and allowed the development of new formulations and new algorithms for solving many others. With the massive usage of computers, the development and use of numerical methods has increased. In this work, it is understood as numerical simulation, the solution of governing equations of one mathe-

mathematical model using a numerical method and a computer. Numerical methods typically transform differential equations to algebraic equations that are easily and quickly solved using computers, making them an extremely powerful tools for engineering analysis. Even linear problems may not admit exact solutions due to geometric and material complexities, but it is relatively easy to obtain approximate solutions using numerical methods. Finite difference methods, finite element methods, meshless methods, and their variants, are the most used numerical methods in the analysis of practical engineering problems. These methods are created on the idea that every system is created by different parts and hence its solution may be represented in parts.

2.5.1 Finite Elements Method

The finite element methods are based on the idea that every system is physically a continuum but may be represented in parts. With this, the problem domain is discretised as a collection of geometrically simple subdomains, called finite elements, that although discretising the domains, it keeps the domain connectivity, and can differ from each other in shape, material properties and physical behaviour. These finite elements express the unknown field variables by approximating functions, the shape functions, within each element. These shape functions approximate the unknown field variables by linear combinations of algebraic polynomials and undetermined parameters, and algebraic relations among the parameters often in a weighted-integral sense, in all elements. The undetermined parameters represent the values of the field variable at a finite number of preselected points, the so-called nodes, [72, 73] Finite element method usually follows the following pipeline:

- Selection of suitable field variables and elements.
- Discretisation of the continua.
- Selection of interpolation functions.
- Define elements properties.
- Assemble element properties to obtain global properties.
- Impose the boundary conditions, natural and essential.
- Solve the system equations to obtain the nodal unknown field variable.

2.5.2 Meshless Methods

One of the most popular numerical tools is the Finite Element Method (FEM), but in the last few years meshless methods, such as Smooth Particle Hydrodynamics (SPH) Method [74], Radial Point Interpolation Method (RPIM) [75–77], and as Natural Neighbour Radial Point Interpolation Method (NNRPIM) [78], came into the focus of interest. The first meshless method to be developed dates from 1977, when Gingold et al 1977 proposed the smooth particle hydrodynamics (SPH) method, that had a kernel approximation for a single function $u(x)$ in a domain Ω . This method was used for modelling astrophysical phenomena without boundaries, such as exploding stars and dust clouds. [74] From 1997 to now many different methods were developed, using different approaches: generalised finite difference method (FDM) (Liszka et al, 1980) [79], diffuse element method (DEM) (Nayroles et al., 1992) [80], element free Galerkin (EFG) method (Belytschko et al, 1994) [81], meshless local Petrov–Galerkin (MLPG) method (Atluri et al, 1998) [82], point interpolation method (PIM) (Liu et al, 2001, 2001, 2001) [75–77] and RPIM (Wang et al, 2002, 2002), [83, 84]. The point interpolation method (PIM) was developed using Galerkin weak form and shape functions that are constructed based only on a group of nodes arbitrarily distributed in a local support domain by means of interpolation. [75–77] The major advantage of PIM is that the shape functions created to possess the Kronecker delta function property, which allows simple enforcement of essential boundary conditions as in the conventional finite element method. PIM can use two types of shape functions: polynomial basis functions and radial basis functions (RBFs), being termed RPIM when using the RBFs. [83, 84] More recently were developed new methods, such as the NNRPIM (Dinis et al 2007), [78] that is based on the combination of the natural neighbour finite element method with the radial point interpolation method, and Natural Radial Element Method (NREM) (Belinha, J. et al 2013), [85] that combines the simplicity of low-order finite elements connectivity with the geometric flexibility of meshless methods.

The main advantage of the meshless methods is that they do not require elements to discretise the problem domain [2]. In meshless methods, the problem domain is discretised using an unstructured nodal mesh. In biomechanics, this discretisation flexibility is advantageous, since it permits to discretise the problem domains using directly medical images. Meshless methods can be divided in approximation meshless methods [80–82, 86] and interpolation meshless meth-

ods [75, 83, 85, 87, 87, 88]. The major advantage of using interpolator meshless methods is the possibility to impose directly the essential and natural boundary conditions, since the constructed test functions possess the delta Kronecker property. They can also be separated in meshless methods that use the strong form solution, that uses directly the partial differential equations governing the studied physical phenomenon, and others that use the weak form solution. The weak form stands by a formulation that uses the variational principle to minimise the residual weight of the differential equations ruling a phenomenon, where the residual is obtained replacing the exact solution by an approximated one, affected by a test function. The meshless methods start with the problem domain being discretised by a regular or irregular node set. These nodal set are not considered a mesh since the meshless method does not require any previous information about the nodes in order to create the approximation or interpolation functions to the unknown variable field function. In meshless methods, the nodal spatial distribution and nodal density discretisation affects the performance of the method. Usually having a denser nodal distributions result in more accurate results, however, the increase of the density of the dense distributions results in a growth of the computational costs. As unbalanced nodal distribution leads to a lower accuracy, where location with predictable concentration of stress should have a higher nodal density when compared with locations with a smooth distribution of stress. After having the domains discretised by a set of nodes is created a background integration mesh, that can be nodal dependent or nodal independent. This background mesh allows to numerically integrate the weak form of the equation that governs the problem. The most used integration meshes are created using the Gauss-Legendre quadrature technique, resulting in a fitter Gaussian integration mesh or in a general Gaussian integration mesh, independent nodal integration meshes, and can be also created using the Voronoï approach that results in the creation of nodal dependent background integration mesh. Having the nodal distribution and the integration mesh, meshless methods have to guarantee the nodal connectivity, that are not predefined by elements as in FEM. With this, in meshless methods, for each point of interest must be defined areas or volumes that act as influence-domains. The meshless methods and the FEM are discrete numerical methods, and so, both need to discretise the problem-domain. The FEM discretise the problem-domain using nodes and elements, where the finite element concept assures the nodal connectivity. In the meshless methods, the problem's domain is discretised using nodes and points, and consequently, there are no elements, as in the

FEM assuring that the nodes belong to the same element interact directly between each other and with the boundary nodes of neighbour finite elements. Herewith in the meshless methods in order to obtain the influence-domains is necessary to first define areas or volumes, respectively for the 2D and 3D problem, containing a certain number of nodes.

2.5.2.1 Radial Point Interpolation Method

RPIM is a meshless method that evolved from the Point Interpolation Method (PIM) [75], which uses a group of arbitrarily distributed points to build polynomial interpolants. With the inclusion of a RBF a distinction occurred between PIM and RPIM, since this inclusion allowed to stabilise the construction procedure of the shape function. [2] RPIM uses the concept of influence-domain instead of global domain, which allows to generate sparse and banded stiffness matrices, more adequate to complex geometry problems. RPIM evolved and today it can be found several variations of the original RPIM, such as the Natural Neighbour RPIM [78, 89, 90], the nodal integration RPIM [91], the linearly conforming RPIM [92], the cell-based smoothed RPIM [93] and the Natural Radial Element Method. [85, 87, 87] RPIM is an interpolator meshless method that uses the concept of influence-domain to force the nodal connectivity. RPIM requires a background integration mesh, which can be constructed using integration cells and the Gauss-Legendre quadrature rule. The meshless methods and the FEM are discrete numerical methods, and so, both need to discretise the problem-domain. The FEM discretise the problem-domain using nodes and elements, where the finite element concept assures the nodal connectivity. In meshless methods, the problem's domain is discretised using nodes and points, and consequently, there are no elements, as in the FEM, assuring that the nodes belong to the same element interact directly between each other and with the boundary nodes of neighbour finite elements. Herewith in the meshless methods in order to obtain the influence-domains, it is necessary to first define areas or volumes, respectively for the 2D and 3D problem, containing a certain number of nodes. In order to obtain the influence-domains, RPIM uses a radial search to find the nodes inside the area or volume. Overlapping the influence-domain of each node allows to obtain the nodal connectivity. [2, 81–83, 86, 94] This is a simple method, however, the size, shape of the influence-domain, and the existence of irregular domain-boundaries or node clusters, can lead to unbalanced influence-domains affecting the performance and the meshless method final solution. [2] The weak formulation uses a variational

principle (the Galerkin weak form) to determine the system of equations and to minimise the residual weight of the integrodifferential equations ruling the studied physical phenomenon. In order to obtain the integral of the residual weight of the differential equations, it is necessary to select an integration scheme. In the FEM the integration mesh is built from a lattice of integration cells coincident with the element mesh and following the Gauss-Legendre quadrature rule. Since the FEM shape functions are known polynomial functions, the number of integration points per integration cell can be pre-determined using accurate well-known relations. [95, 96] Otherwise, in meshless methods the shape function degree is generally unknown, being impossible to define a priori the background integration mesh, that allows to perform the numerical integration. In RPIM the background integration mesh can be created, using an analogy with the FEM, being nodal dependent, or nodal independent [2]. In a nodal independent background integration, the problem-domain can be divided into a regular grid forming quadrilateral integration cells, being, each grid-cell filled with integration points, respecting the Gauss-Legendre quadrature rule. [2] In the RPIM shape functions are obtained using the Radial Point Interpolators (RPI), that combine radial basis functions with polynomial basis functions, where the support-domain, a small set of field nodes in the vicinity of the interest point, is coincident with the influence-domain.

2.5.2.2 Natural Neighbours Radial Point Interpolation Method

The NNRPIM is a combination of the RPI with the concept of the Natural Neighbours, [97] the Voronoï Diagrams [98] and the Delaunay tessellation [99], to create the influence-cells and the background integration mesh, completely dependent on the nodal mesh. In NNRPIM the interpolation functions, possessing the delta Kronecker property, are used in the Galerkin weak form and are constructed using RPI. The RBF used in the RPI is the multi-quadric RBF. [100].

Discretization

Firstly, the problem domain is discretised in a nodal computational mesh, then using the Natural Neighbour concept [97], similar to the RPIM that created an influence-domain, the NNRPIM uses the influence-cell concept, which are influence-domains dependent on the nodal mesh organisation. This influence-cells are created based on geometric and spatial relations between Voronoï

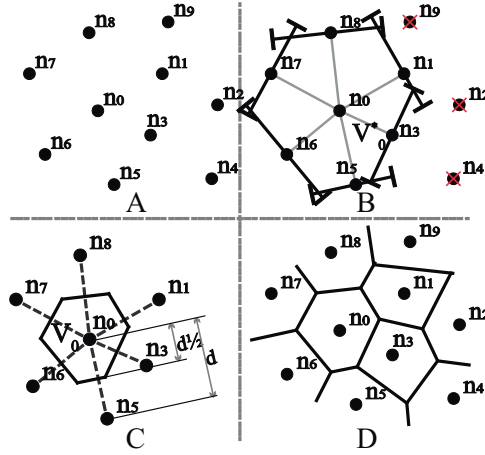


Figure 2.14: A: n_0 Neighbour nodes; B: Provisional Voronoï cell, V_0^* ; C: Voronoï cell, V_0 ; D: Voronoï diagram

cells and the Delaunay triangulation [2, 98]. Considering the nodal set $\mathbf{N} = \{n_1, n_2, \dots, n_N\}$ discretising the space domain $\Omega \subset \mathbb{R}^d$ with $\mathbf{X} = \{\mathbf{x}_1, \mathbf{x}_2, \dots, \mathbf{x}_N\} \in \Omega$. The Voronoï diagram of \mathbf{N} is the partition of the function space discretised by \mathbf{X} in closed and convex sub-regions, V_i . Each V_i sub-region is associated to the node n_i in a way that no other point in the interior of V_i is closer to n_i than any other node $n_j \in \mathbf{N} \wedge j \neq i$. The set of Voronoï cells V define the Voronoï diagram, $V = \{V_1, V_2, \dots, V_N\}$. The Voronoï cell is defined by, $V_i = \{x_1 \in \Omega \subset \mathbb{R}^d : \|x_1 - x_i\| < \|x_1 - x_j\|, \forall i \neq j\}$, being \mathbf{x}_1 an interest point of the domain and $\|\cdot\|$ the Euclidian metric norm. Thus, the Voronoï cell V_i is the geometric place where all points are closer to n_i than to any other node. Considering that a nodal set is used create the Voronoï cell V_0^* of node n_0 , being some nodes chosen as potential neighbours of n_0 . Then one of the nodes is selected as potential neighbour, for example node n_1 , and the vector u_{10} is determined, $\mathbf{u}_{10} = \frac{(x_0 - x_1)}{\|x_0 - x_1\|}$, being $\mathbf{u}_{10} = \{u_{10}, v_{10}, w_{10}\}$. Using the normal vector u_{10} it is possible to defined plane p_{10} , and if the node do not respect the following condition, $u_{10}x + v_{10}y + w_{10}z \geq (u_{10}x_1 + v_{10}y_1 + w_{10}z_1)$, is discarded as natural neighbours of n_0 . This process is repeated for each one of the initial nodal set. Being V_0^* a provisional Voronoï, they are modified by equation (2.2), resulting in V_0 .

$$d_{0i}^* = \frac{d_{0i}}{2} = \frac{\|x_0 - x_i\|}{2} \quad (2.2)$$

Doing this process to all de nodes in the nodal set, the result is the Voronoï diagram, 2.14

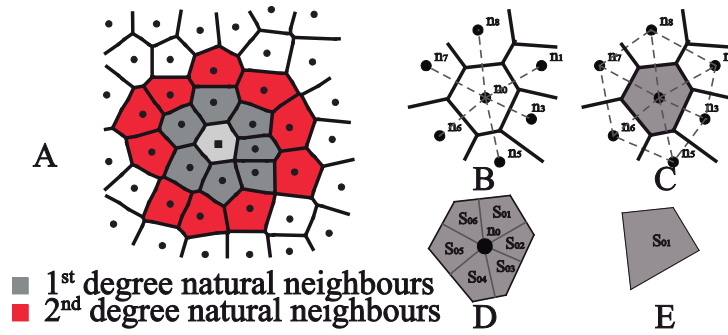


Figure 2.15: A: First and second degree natural neighbours in NNRPIM.; B and C: Delaunay Tessellation; D: Generated quadrilaterals; E: Sub-cell.

The influence-cell can have two degrees, Figure 2.15A. The first degree contains the first-degree natural neighbours of a certain influence-cell. In the second-order influence-cell, the influence-cell considers those with first-degree natural neighbour plus the natural neighbours of the first-degree influence-cells. The Delaunay triangulation is the geometrical dual of the Voronoi diagram and it is constructed by connecting the nodes whose Voronoi cells have common boundaries. An important property of the Delaunay triangles is the empty circumcircle criterion where, if a set of nodes $\mathbf{N}_{set} = \{n_j, n_k, n_l\} \in \mathbf{N}$ forms a Delaunay triangle, then the circumcircle formed by the triangle \mathbf{N}_{set} contains no other nodes of the global nodal set \mathbf{N} . In the context of the natural neighbour interpolation, these circles are known as natural neighbour circumcircles. The Voronoi diagram is used to create the influence-cells, which enforce the connectivity between the nodes discretising the problem domain, \mathbf{N} . On the other hand, the duality between the Voronoi cells and the Delaunay triangles is used in order to construct a nodal dependent background integration mesh. Following the construction of the Voronoi diagram, it is possible to obtain a nodal dependent integration mesh-based purely on the nodal distribution spatial information. [2] This is done by taking the previously obtained Voronoi diagram and dividing each of its Voronoi cells into smaller sub-areas, using the Delaunay tessellation. The nodes of Voronoi cells sharing common boundaries are connected, figure 2.15B, and the overlap of both the Delaunay tessellation and the influence-cell boundaries leads to a smaller sub-cell, figure 2.15C. [2] As result, as demonstrated in figure 2.15D, it is possible to divide each Voronoi cell, V_I into n sub-cells S_{Ii} , being n the total number of natural neighbours of a particular Voronoi cell, V_I . Having the sub-cells for all Voronoi cells, being each sub-area isoparameterised and filled with integration points using the Gauss-Legendre integration scheme the domain integration mesh is obtained, figure 2.15E.

2.5.2.3 Shape Functions

In order to construct the shape functions, the NNRPIM uses the RPI technique, which requires a RBF and a complete polynomial basis. [97] Still, previous works on the NNRPIM showed that if the shape parameters of the RBF are chosen carefully, the polynomial basis can be removed from the formulation and substituted by a constant unity basis. [78, 101] Consider the function $u(\mathbf{x})$ defined in the domain $\Omega \subset \mathbb{R}^d$ and an interest point $\mathbf{x}_I \in \Omega$, possessing an influence-cell containing n nodes: $\mathbf{X}_I = \{\mathbf{x}_1, \mathbf{x}_2, \dots, \mathbf{x}_n\} \in \Omega \wedge \mathbf{x}_i \in \mathbb{R}^d$. It is assumed that only the nodes within the influence-cell of the interest point \mathbf{x}_I have effect on $u(\mathbf{x}_I)$. Thus, the value of function $u(\mathbf{x}_I)$ can be defined with equation (2.5.2.3).

$$u(\mathbf{x}_I) = \sum_{i=1}^n [R_i(\mathbf{x}_I) \cdot a_i(\mathbf{x}_I)] + C_u \cdot b(\mathbf{x}_I) = \mathbf{R}(\mathbf{x}_I) \cdot \mathbf{a}(\mathbf{x}_I) + C_u \cdot b(\mathbf{x}_I) \quad (2.3)$$

In equation (2.5.2.3) $R_i(\mathbf{x}_I)$ is the RBF and $a_i(\mathbf{x}_I)$ are non-constant coefficients of $R_i(\mathbf{x}_I)$. The parameter C_u is the unity basis, being $C_u = 1$ and $b(\mathbf{x}_I)$ is a non-constant coefficient of C_u . In this work it is used the multi-quadric (MQ) RBF function, $R_i(\mathbf{x}_I) = R(r_{Ii}) = (r_{Ii}^2 + c^2)^p$ in which r_{Ii} is the distance between the relevant node \mathbf{x}_I and the neighbour $r_{Ii} = |\mathbf{x}_i - \mathbf{x}_I|$, and c and p are two shape parameters [100]. It was found that c should be close to zero, $c \cong 0$, and p should be close to one, $p \cong 1$, [78]. Applying equation (2.5.2.3) to the node inside the influence-cell domain, considering each node as the interest point, and including an extra equation $\sum_{i=1}^n a_i(\mathbf{x}_I) = 0$, to guarantee the unique solution [102], it is possible to obtain the following equation system (2.4),

$$\begin{bmatrix} u_1 \\ u_2 \\ \vdots \\ u_n \\ 0 \end{bmatrix} = \begin{bmatrix} R(r_{11}) & R(r_{12}) & \dots & R(r_{1n}) & 1 \\ R(r_{21}) & R(r_{22}) & \dots & R(r_{2n}) & 1 \\ \vdots & \vdots & \ddots & \vdots & \vdots \\ R(r_{n1}) & R(r_{n2}) & \ddots & R(r_{nn}) & 1 \\ 1 & 1 & \dots & 1 & 0 \end{bmatrix} \begin{bmatrix} a_1(\mathbf{x}_I) \\ a_2(\mathbf{x}_I) \\ \vdots \\ a_n(\mathbf{x}_I) \\ b(\mathbf{x}_I) \end{bmatrix} \Leftrightarrow \begin{bmatrix} \mathbf{u}_s \\ 0 \end{bmatrix} = \begin{bmatrix} \mathbf{R} & C_u \\ C_u & 0 \end{bmatrix} \begin{bmatrix} \mathbf{a} \\ b \end{bmatrix} \quad (2.4)$$

where $\mathbf{u}_s = \{u_1, u_2, \dots, u_n\}^T$ is the vector for the nodal function values for the nodes on the influence-cell. Therefore, reorganising equation (2.4) it is possible to obtain the non-constant

coefficients,

$$\begin{bmatrix} \mathbf{a} \\ b \end{bmatrix} = \begin{bmatrix} \mathbf{R} & \mathbf{C}_u \\ \mathbf{C}_u & 0 \end{bmatrix}^{-1} \begin{bmatrix} \mathbf{u}_s \\ 0 \end{bmatrix} \Rightarrow \begin{bmatrix} \mathbf{a} \\ b \end{bmatrix} = \mathbf{M}^{-1} \begin{bmatrix} \mathbf{u}_s \\ 0 \end{bmatrix} \quad (2.5)$$

Substituting in equation , the result from equation , it is possible to obtain the interpolation function $\Phi(\mathbf{x}_I) = \{\varphi_1(\mathbf{x}_I), \varphi_2(\mathbf{x}_I), \dots, \varphi_n(\mathbf{x}_I), \psi_c\}$ for an interest point \mathbf{x}_I .

$$u(\mathbf{x}_I) = \left\{ R_1(\mathbf{x}_I) \quad R_2(\mathbf{x}_I) \quad \dots \quad R_n(\mathbf{x}_I) \quad C_u \right\} \mathbf{M}^{-1} \begin{Bmatrix} \mathbf{u}_s \\ 0 \end{Bmatrix} = \Phi(\mathbf{x}_I) \begin{Bmatrix} \mathbf{u}_s \\ 0 \end{Bmatrix} \quad (2.6)$$

The last term of the interpolation function, ψ_c , comes from the constant term C_u and it does not possess useful physical meaning. Thus, only the n first components of $\Phi(\mathbf{x}_I)$ are relevant and form the interpolation function [85]. The partial derivative of $\Phi(\mathbf{x}_I)$ with respect to a variable ξ is defined as equation (2.7),

$$\Phi_{\xi}(\mathbf{x}_I) = \left\{ R_1(\mathbf{x}_I) \quad R_2(\mathbf{x}_I) \quad \dots \quad R_n(\mathbf{x}_I) \quad C_u \right\}_{\xi} \mathbf{M}^{-1} \quad (2.7)$$

Notice that since C_u is a constant scalar, then $C_{u,\xi} = 0$. The partial derivatives of the MQ-RBF with respect to a variable ξ are obtained with equation (2.8),

$$R_{,\xi}(r_{ij}) = 2p(r_{ij}^2 + c^2)^{p-1}(\xi_j - \xi_i) \quad (2.8)$$

The NNRPIM shape functions possess several important numerical properties, such as the unit partition property and the delta Kronecker property, which permits to impose the essential and natural boundary conditions using direct imposition methods. In the literature, it is possible to find complete studies regarding its numerical properties. [2,98]

2.5.2.4 Discrete System of Equations

Consider the body described by the domain $\Omega \subset \mathbb{R}^2$ and bounded by Γ , where $\Gamma \in \Omega : \Gamma_u \cup \Gamma_t = \Gamma \wedge \Gamma_u \cap \Gamma_t = \emptyset$, being Γ_u the essential boundary and Γ_t the natural boundary. The equilibrium equations governing the linear elastostatic problem are defined as $\nabla \Lambda + \mathbf{b} = 0$ in Ω . Being ∇ the gradient operator; Λ the Cauchy stress tensor for a kinematic admissible displacement field \mathbf{u} and

\mathbf{b} the body force per unit volume. The boundary conditions are given by, $\Lambda \mathbf{n} = \bar{\mathbf{t}}$ on Γ_t and $\mathbf{u} = \bar{\mathbf{u}}$ on Γ_u , where $\bar{\mathbf{u}}$ is the prescribed displacement on the essential boundary Γ_u , $\bar{\mathbf{t}}$ is the traction on the natural boundary Γ_t and \mathbf{n} is the unit outward normal to the boundary of domain Ω . Using the Voigt notation and assuming the Galerkin procedure for linear elasticity, the weak form for the discrete problem can be written as equation (2.9),

$$\delta L = \int_{\Omega} \delta \boldsymbol{\varepsilon}^T \boldsymbol{\sigma} d\Omega - \int_{\Omega} \delta \mathbf{u}^T \mathbf{b} d\Omega - \int_{\Omega} \delta \mathbf{u}^T \bar{\mathbf{t}} d\Gamma_t = 0 \quad (2.9)$$

Where $\boldsymbol{\varepsilon}$ is the strain vector defined as $\boldsymbol{\varepsilon} = \mathbf{L}\mathbf{u}$, being \mathbf{L} a differential operator (2.10) and (2.11),

$$\mathbf{L}_{2D} = \begin{bmatrix} \frac{\partial}{\partial y} & 0 & \frac{\partial}{\partial y} \\ 0 & \frac{\partial}{\partial x} & \frac{\partial}{\partial y} \end{bmatrix}^T \quad (2.10)$$

$$\mathbf{L}_{3D} = \begin{bmatrix} \frac{\partial}{\partial x} & 0 & 0 & \frac{\partial}{\partial y} & 0 & \frac{\partial}{\partial z} \\ 0 & \frac{\partial}{\partial y} & 0 & \frac{\partial}{\partial x} & \frac{\partial}{\partial z} & 0 \\ 0 & 0 & \frac{\partial}{\partial z} & 0 & \frac{\partial}{\partial y} & \frac{\partial}{\partial x} \end{bmatrix}^T \quad (2.11)$$

It is possible to directly correlate the stress field with the strain field using the Hooke Law: $\boldsymbol{\sigma} = \mathbf{c}\boldsymbol{\varepsilon} = \mathbf{c}\mathbf{L}\mathbf{u}$. Being \mathbf{c} the material constitutive matrix, which can be obtained inverting the compliance elasticity matrix, $\mathbf{c} = \mathbf{s}^{-1}$. The compliance elasticity matrix \mathbf{s} for the general isotropic material case is defined by equation (2.12) for the 2D plane strain formulation and in equation (2.13) for the 3D classical formulation.

$$s_{2D} = \begin{bmatrix} \frac{1}{E_{xx}} & -\frac{\nu_{yx}}{E_{yy}} & 0 \\ -\frac{\nu_{xy}}{E_{xx}} & \frac{1}{E_{yy}} & 0 \\ 0 & 0 & \frac{1}{G_{xy}} \end{bmatrix} \quad (2.12)$$

$$s_{3D} = \begin{bmatrix} \frac{1}{E_{xx}} & -\frac{\nu_{yx}}{E_{yy}} & -\frac{\nu_{zx}}{E_{zz}} & 0 & 0 & 0 \\ -\frac{\nu_{xy}}{E_{xx}} & \frac{1}{E_{yy}} & -\frac{\nu_{zy}}{E_{zz}} & 0 & 0 & 0 \\ -\frac{\nu_{xz}}{E_{xx}} & -\frac{\nu_{yz}}{E_{yy}} & \frac{1}{E_{zz}} & 0 & 0 & 0 \\ 0 & 0 & 0 & \frac{1}{G_{xy}} & 0 & 0 \\ 0 & 0 & 0 & 0 & \frac{1}{G_{yz}} & 0 \\ 0 & 0 & 0 & 0 & 0 & \frac{1}{G_{zx}} \end{bmatrix} \quad (2.13)$$

Being E the elasticity modulus, ν material Poisson coefficient and G the distortion modulus. To easy the exposition, consider now just the 2D the plane strain assumption. Each node \mathbf{x}_i discretising the problem domain has two degrees of freedom: $\mathbf{u}_i = \mathbf{u}_i \mathbf{v}_i$. Thus, in order to interpolate the virtual displacement at the interest point \mathbf{x}_I equation (2.6) can be written as,

$$\begin{aligned} \delta \mathbf{u}(\mathbf{x}_I) = \delta \mathbf{u}_I &= \mathbf{I} \begin{Bmatrix} \Phi_I \\ \Phi_I \end{Bmatrix} \delta \mathbf{u}_s = \begin{bmatrix} \varphi_1(\mathbf{x}_I) & 0 & \dots & \varphi_n(\mathbf{x}_I) & 0 \\ 0 & \varphi_1(\mathbf{x}_I) & 0 & 0 & \varphi_n(\mathbf{x}_I) \end{bmatrix} \begin{Bmatrix} \delta \mathbf{u}_1 \\ \delta \mathbf{v}_1 \\ \vdots \\ \delta \mathbf{u}_n \\ \delta \mathbf{v}_n \end{Bmatrix} \\ &= \mathbf{H}_I \delta \mathbf{u}_s \end{aligned} \quad (2.14)$$

Being \mathbf{I} a 2×2 identity matrix. Substituting $\boldsymbol{\varepsilon} = \mathbf{L}\mathbf{u}$ in the first term of equation (2.9) and considering equation (2.14) it is possible to write,

$$\begin{aligned} \int_{\Omega} \delta \boldsymbol{\varepsilon}^T \boldsymbol{\sigma} d\Omega &= \int_{\Omega} (\mathbf{L}\delta \mathbf{u})^T \mathbf{c}(\mathbf{L}\mathbf{u}) d\Omega = \int_{\Omega} (\mathbf{L}\mathbf{H}_I \delta \mathbf{u}_s)^T \mathbf{c}(\mathbf{L}\mathbf{H}_I \mathbf{u}_s) d\Omega \\ &= \int_{\Omega} \delta \mathbf{u}_s^T \mathbf{B}_I^T \mathbf{c} \mathbf{B}_I \mathbf{u}_s d\Omega = \delta \mathbf{u}_s^T \int_{\Omega} \mathbf{B}_I^T \mathbf{c} \mathbf{B}_I d\Omega \mathbf{u} \end{aligned} \quad (2.15)$$

Being \mathbf{B}_I the resultant deformation matrix defined for the n nodes constituting the influence-cell of interest point \mathbf{x}_i ,

$$\mathbf{B}_I = \begin{bmatrix} \frac{\partial \varphi_1(\mathbf{x}_I)}{\partial x} & 0 & \frac{\partial \varphi_2(\mathbf{x}_I)}{\partial x} & 0 & \dots & \frac{\partial \varphi_n(\mathbf{x}_I)}{\partial x} & 0 \\ 0 & \frac{\partial \varphi_1(\mathbf{x}_I)}{\partial y} & 0 & \frac{\partial \varphi_2(\mathbf{x}_I)}{\partial y} & \dots & 0 & \frac{\partial \varphi_n(\mathbf{x}_I)}{\partial y} \\ \frac{\partial \varphi_1(\mathbf{x}_I)}{\partial y} & \frac{\partial \varphi_1(\mathbf{x}_I)}{\partial x} & \frac{\partial \varphi_2(\mathbf{x}_I)}{\partial y} & \frac{\partial \varphi_2(\mathbf{x}_I)}{\partial x} & \dots & \frac{\partial \varphi_n(\mathbf{x}_I)}{\partial y} & \frac{\partial \varphi_n(\mathbf{x}_I)}{\partial x} \end{bmatrix} \quad (2.16)$$

Using an analogous procedure for the second and third terms of equation (2.9), the following force vectors are obtained,

$$\int_{\Omega} \delta \mathbf{u}_s^T \mathbf{b} d\Omega = \int_{\Omega} (\mathbf{H}_I \delta \mathbf{u}_s)^T \mathbf{b} d\Omega = \delta \mathbf{u}_s^T \int_{\Omega} \mathbf{H}_I^T \mathbf{b} d\Omega \quad (2.17)$$

$$\int_{\Gamma_i} \delta \mathbf{u}^T \bar{\mathbf{t}} d\Gamma_t = \int_{\Gamma_i} (\mathbf{H}_I \delta \mathbf{u}_s)^T \bar{\mathbf{t}} d\Gamma_t = \delta \mathbf{u}_s^T \int_{\Gamma_i} \mathbf{H}_I^T \bar{\mathbf{t}} d\Gamma_t \quad (2.18)$$

Thus, equation (2.9) can be re-written as,

$$\delta L = \delta \mathbf{u}^T \int_{\Omega} \mathbf{B}_I^T \mathbf{c} \mathbf{B}_I d\Omega - \delta \mathbf{u}_s^T \int_{\Omega} \mathbf{H}_I^T \mathbf{b} d\Omega - \delta \mathbf{u}_s^T \int_{\Gamma_i} \mathbf{H}_I^T \bar{\mathbf{t}} d\Gamma_t = 0 \quad (2.19)$$

The equation system can be presented in the matrix form: $\mathbf{K}\mathbf{u} = \mathbf{f}$. Being \mathbf{K} the stiffness matrix, \mathbf{u} the displacement field vector and $\mathbf{f} = \mathbf{f}_b + \mathbf{f}_t$, the vector of applied forces. Since the RPI shape function possesses the delta Kronecker property, the essential boundary conditions can be directly applied in the stiffness matrix [78]. After the determination of the displacement field solving the linear equation system $\mathbf{K}^{-1}\mathbf{f} = \mathbf{u}$, the strain in an interest point $\mathbf{x}_I \in \Omega$ can be obtained using $\boldsymbol{\varepsilon}(\mathbf{x}_I) = \mathbf{L}\mathbf{u}(\mathbf{x}_I)$, and then, considering the Hooke Law, $\boldsymbol{\sigma}(\mathbf{x}_I) = \mathbf{c}(\mathbf{x}_I) \boldsymbol{\varepsilon}(\mathbf{x}_I)$, it is possible to determine the stress field. It is possible to obtain the three principal stresses $\sigma(\mathbf{x}_I)_i$ for each interest point \mathbf{x}_I , $\det(\boldsymbol{\Lambda}(\mathbf{x}_I) - \sigma(\mathbf{x}_I)_i \mathbf{I}) = 0$, and the three principal directions $\mathbf{n}(\mathbf{x}_I)_i : (\boldsymbol{\Lambda}(\mathbf{x}_I) - \sigma(\mathbf{x}_I)_i \mathbf{I})\mathbf{n}(\mathbf{x}_I)_i = 0$, being $\boldsymbol{\Lambda}(\mathbf{x}_I)$ the Cauchy stress tensor obtained for the interest point and \mathbf{I} the identity matrix. Using the three principal stresses $\sigma(\mathbf{x}_I)_i$ and equation (2.20), the von Mises effective stress of interest point \mathbf{x}_I is obtained.

$$\bar{\sigma}(\mathbf{x}_I) = \sqrt{\frac{1}{2} \left((\sigma(\mathbf{x}_I)_1 - \sigma(\mathbf{x}_I)_2)^2 + (\sigma(\mathbf{x}_I)_2 - \sigma(\mathbf{x}_I)_3)^2 + (\sigma(\mathbf{x}_I)_3 - \sigma(\mathbf{x}_I)_1)^2 \right)} \quad (2.20)$$

Comparing NNRPIM with other meshless methods, it has a higher re-meshing flexibility and a higher accuracy on the solution variable field. [90, 103] Another benefit of the NNRPIM compared to others meshless methods is its lower computational cost during the processing phase of the numerical analysis (after the construction of the nodal connectivity, integration mesh and shape functions), that can be relevant in demanding tasks as in non-linear and dynamic analysis. [78, 89, 101, 104–106] Being the nodal connectivity and integration mesh constructed only based on the nodal discretisation, this becomes an advantage in the biomechanical analysis, since it is possible

to analyse extremely irregular meshes and convex boundaries. [\[107\]](#)

Chapter 3

Original Developed Work

3.1 Introductory Remarks

In order to develop the proposed work, it was first required to perform a technical introduction to the used numerical tools and softwares. For that, it was developed a work concerning the usage of these softwares and numerical tool in biological structures. The softwares used in this works was FEMAS - Finite Element and Meshless Analysis Software, that in this case was only used to perform the numerical analyses, and Mimics Innovation Suite 19, that was used to create the biological structures geometrical models, through the usage of medical images. The first contribution, section 3.2, present a study where it was explored and confronted the usage of a numerical meshless method, the NNRPIM, with the FEM, in a biological structure, the brain. The second contribution, section 3.3, intended to explore and confront the numerical meshless method, the RPIM, with the FEM, in the brain. Contribution, 3.5, 3.6 and 3.7 explore the usage and validation of a 2D homogenisation technique, where it is used the fabric tensor concept in 2D, to define the mechanical properties of trabecular bone. In these publications were used the FEM, RPIM and NNRPIM to verify the methodology. Contribution 3.8 explores the homogenisation methodology in 3D to define bone mechanical properties, using the fabric tensor concept and a set of phenomenological laws. In contribution 3.9 the 3D homogenisation technique was applied to a femoral bone, allowing to analyse femur mechanical behaviour, using three different approaches to define the domain mechanical properties, being one of the methodologies the developed homogenisation technique.

3.2 Contribution I: A new numerical approach to mechanically analyse biological structures.

Highlights of Contribution: [3.2](#)

This contribution focused on the numerical simulation of biological structures, using the NNRPIM meshless method and the FE method.

Therefore, the main contents of this publication include:

- I. Literature review on brain impact mechanical models;
- II. NNRPIM methodology applications and formulation;
- III. A convergence study to demonstrate the differences between the FEM and the NNRPIM meshless methods;
- IV. One 2D and two 3D brain geometrical model were constructed with the resource to medical images, gathered from Lalys F, et al, with a 1024×1024 pixel resolution, using MIMICS Innovation Suite V19 software, [[108](#), [109](#)]. The 2D geometrical model was built using an image in the medial sagittal plane, where it was considered the skull, brain grey and white matter and the cerebrospinal fluid (CSF). Concerning the 3D geometrical models, one was constructed by extruding the 2D model, and the other was constructed using the medical images, allowing to create a half brain 3D model.
- V. Convergence study: NNRPIM shows a faster convergence when compared with the FEM method, in both 2D and 3D analysis, figure [3.1](#).
- VI. Conclusion: The performed convergence study compared the discretisation techniques and allowed to obtain the necessary awareness regarding the level of the discretisation required to obtain a reliable solution. It was concluded that commonly FEM analyses available in the literature did not consider the importance of the discretisation level. In many cases the discretisation level in commercial software is automatic and the lack of awareness regarding the value of the discretisation level can lead to invalid results. The results obtained with meshless methods are capable to produce smoother stress fields when compared with the FEM.

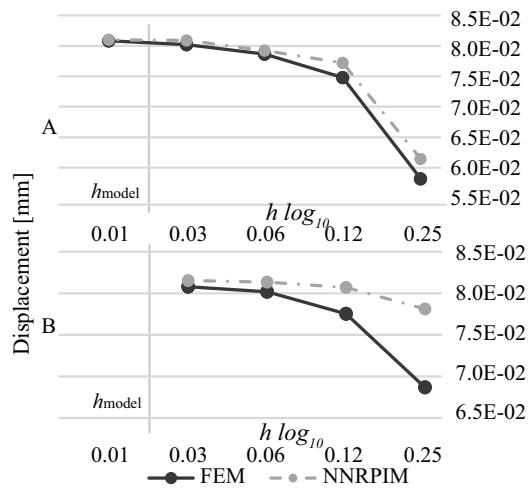


Figure 3.1: Contribution I convergence study results: A - 2D; B - 3D.

The complete document can be found in the next pages.

A New Numerical Approach to Mechanically Analyse Biological Structures

M. Marques^a, J. Belinha^{a, b*}, L.M.J.S. Dinis^{a, c}, R. M. Natal Jorge^{a, c}

^a *Institute of Science and Innovation in Mechanical and Industrial Engineering (INEGI), University of Porto, Portugal;*

^b *ISEP - School of Engineering, Polytechnic of Porto, Porto, Portugal;*

^c *Faculty of Engineering of the University of Porto (FEUP), Portugal*

In this work, an advanced discretization meshless technique is used to study the structural response of a human brain due to an impact load. The 2D and 3D brain geometrical models, and surrounding structures, were obtained through the processing of medical images, allowing to achieve a realistic geometry for the virtual model and to define the distribution of the mechanical properties accordingly with the medical images colour scale. Additionally, a set of essential and natural boundary conditions were assumed in order to reproduce a sudden impact force applied to the cranium. Then, a structural numerical analysis was performed using the Natural Neighbour Radial Point Interpolation Method (NNRPIM). The obtained results were compared with the finite element method (FEM) and a solution available in the literature. This work shows that the NNRPIM is a robust and accurate numerical technique, capable to produce results very close to other numerical approaches. In addition, the variable fields obtained with the meshless method are much smoother than the FEM corresponding solution.

Keywords: brain impact; meshless methods; natural neighbours; radial point interpolator;

1. Introduction

Head injury is a major health and socioeconomic problem, since it is frequent and severe in almost all types of traffic accidents that annually injures 20-50 million persons [1], [2]. The traumatic brain injuries (TBI) occur due to an abrupt mechanical stimulus applied

to the cranium affecting directly or indirectly the brain. This can cause temporary or permanent brain damage and dysfunction [3], [4]. Brain is one of the softest biologic materials. It shows nonlinear behaviour, which does not allow a straightforward prediction of its response to an applied mechanical stimulus. Being largely constituted by water, brain maintains its volume when pressures are applied slowly or transiently. However, because of its tissue characteristics when shearing forces are applied injuries may occur, which can be classified as focal or diffuse [5]. In the case of focal injuries, it occurs a bleeding within the brain, on the surface of the brain, or in the cortical gray matter, leading to the brain tissue necrosis and to the increase of the intracranial pressure. In the case of diffuse injuries (not localized to one area of the brain but more distributed throughout the brain), it occurs damage at the level of neuronal cells, leading to a widespread disruption of brain neuronal networks [6], [7]. These lesions can result in hospitalization, being estimated that one fifth of the hospitalized patients cannot return to a normal life [8]. Having the TBI devastating consequences and a significant incidence (1.4 million people in the US per year), considerable research has been devoted to understand and to prevent TBI [9], [10]. Herewith, the scientific community started to investigate this event conducting studies using cadaver heads, animal heads, physical head models, and in vitro models [11]. However, with the computational evolution, biomechanical computational simulation now provides powerful tools that allow a less expensive study of the TBI event. Most of the experimental mechanical tests available in biomechanics are only capable to detect external structural changes (measuring the surface deformation, for instances). The use of computational mechanics applied to bio-tissues allows to predict the full domain deformation. Thus, computational simulation permits to obtain a potential stress/strain field and thus, to understand how the material will respond to a given loading scenario, overcoming some inherent limitations of experimental tests. [12]. Such non-invasive methodology is very useful to study delicate tissues, as the brain tissue. The current usage of the computational simulation led to the development of the numerical head models, that evolved from simple anatomic representations to sophisticated models created through the usage of medical images [11].

One of the most popular numerical tools used in structural analysis is the Finite Element Method (FEM). However, in the last few years, meshless methods came into focus of interest. The main difference between the Finite Element Method and meshless methods is the procedure to impose the nodal connectivity. The two methodologies apply distinct

methodologies to impose how the nodes discretizing the problem's domain interact with each other. Furthermore, FEM and meshless methods use distinct techniques to build the background integration mesh and to construct their shape functions. In the finite element method, it is assumed a nodal connectivity using the finite element mesh, made by elements, where the nodes belonging to the same element interact directly between each other and with the boundary nodes of neighbour finite elements. In meshless methods the nodal connectivity has to be determined after the nodal distribution, using different methodologies accordingly to different meshless methods. The main advantage of the meshless method is they do not require elements to discretize the solid's domain [13], being the solid's domain discretized using an unstructured nodal mesh. In biomechanics this discretization flexibility is advantageous, since it permits to discretize the problem domains using directly medical images. Additionally, meshless methods have a high re-meshing efficiency, allowing the method to deal with large distortions, that commonly occur in soft materials or soft tissues, such as muscles, internal organs, skin, or to simulate fluid flow, with great importance for example in the hemodynamics.

Meshless methods can be divided in approximation meshless methods [14]–[17] and interpolation meshless methods [18]–[23]. The major advantage of using interpolation meshless methods is the possibility to impose directly the essential and natural boundary conditions, since the constructed test functions possess the delta Kronecker property. In this work, it was used the Natural Neighbour Radial Point Interpolation Method (NNRPIM) [24], that uses mathematical concepts, such as the Voronoï Diagrams [25] and the Delaunay tessellation [26], to create the influence-cells and the background integration mesh, both completely dependent on the nodal mesh. The NNRPIM shape functions are constructed using the Radial Point Interpolation technique, which permits to obtain shape functions possessing a virtual infinite continuity and the delta Kronecker property. The NNRPIM was extended to several biomechanical applications [13], such as bone tissue remodelling analysis [27]–[32], stress state transient analysis due to the insertion of implants [33]–[37], and the study of the inner ear [38], [39].

2. Meshless Method

In order to integrate the integro-differential equation from the Galerkin weak formulation, the discrete numerical method requires a background integration mesh. Additionally, in order to establish the algebraic system of equations, it is necessary to

substitute the test functions of the Galerkin weak form by the shape functions of the assumed numerical methodology. Furthermore, aiming to construct the shape functions it is necessary to obtain the nodal connectivity of each integration point. Therefore, a discrete approximation numerical technique based on the Galerking weak formulation requires three numerical entities: a background integration mesh, a technique to enforce the nodal connectivity and a methodology to construct the shape functions. This section presents these three entities for the NNRPIM. In addition, the implementation of the discrete system of equations is shown.

2.1 Nodal Connectivity and Numerical Integration

In the NNRPIM, both the nodal connectivity and the background integration mesh are constructed using the Natural Neighbour concept [40], which is explained with detail in the literature [13], [25] and briefly in the following paragraph.

Consider the nodal set $\mathbf{N} = \{n_1, n_2, \dots, n_N\}$ discretizing the problem's domain $\Omega \subset \mathbb{R}^d$, being $\mathbf{X} = \{\mathbf{x}_1, \mathbf{x}_2, \dots, \mathbf{x}_N\} \in \Omega$ are the corresponding nodal coordinates. The Voronoï diagram of \mathbf{N} is the partition of the function space discretized by \mathbf{X} in closed and convex sub-regions, V_i . Each V_i sub-region is associated to the node n_i in a way that no other point in the interior of V_i is closer to n_i than any other node $n_j \in \mathbf{N} \wedge j \neq i$. The set of Voronoï cells V define the Voronoï diagram, $\mathbf{V} = \{V_1, V_2, \dots, V_N\}$. The Voronoï cell is defined by, $V_i = \{\mathbf{x}_l \in \Omega \subset \mathbb{R}^d: \|\mathbf{x}_l - \mathbf{x}_i\| < \|\mathbf{x}_l - \mathbf{x}_j\|, \forall i \neq j\}$, being \mathbf{x}_l an interest point of the domain and $\|\cdot\|$ the Euclidian metric norm. Thus, the Voronoï cell V_i is the geometric place where all points are closer to n_i than to any other node.

After the construction of the Voronoï diagram, it is possible to enforce the nodal connectivity using the concept of the “influence-cell”, which is very similar with the “influence-domain” concept commonly used in meshless methods. However, the influence-cells are directly obtained from the Voronoï diagram, making the process much more organic and automatic. Generally, the influence-cells can have two degrees, Figure 1A. The first degree influence-cell of an interest point \mathbf{x}_l contains the first natural neighbours of \mathbf{x}_l . The second degree influence-cell of an interest point \mathbf{x}_l contains the first natural neighbours of \mathbf{x}_l and, in addition, it contains the natural neighbours of the first natural neighbours of \mathbf{x}_l , enlarging significantly the final influence-domain.

The Delaunay triangulation is constructed by connecting the nodes whose Voronoï cells have common boundaries. The duality between the Voronoï cells and the Delaunay triangles is used to construct a nodal dependent background integration mesh. [13], [25] Following the construction of the Voronoï diagram, it is possible to obtain a nodal dependent integration mesh based purely on the nodal distribution spatial information [13], [25]. This is done by taking the previously obtained Voronoï diagram and dividing each of its Voronoï cells into smaller sub-areas, using the Delaunay tessellation. The nodes of Voronoï cells sharing common boundaries are connected, Figure 1B, and the overlap of both the Delaunay tessellation and the influence-cell boundaries leads to a smaller sub-cell, Figure 1C [13], [25]. As result, as demonstrated in Figure 1D, it is possible to divide each Voronoï cell, V_I into n sub-cells S_{Ii} , being each sub-area isoparameterized and filled with integration points using the Gauss-Legendre integration scheme, the domain's integration mesh is finally obtained, Figure 1E.

2.2 Shape Functions

In order to construct the shape functions, the NNRPIM uses the Radial Point Interpolators (RPI) technique, which requires a radial basis function (RBF) and a complete polynomial basis [40]. Still, previous works on the NNRPIM showed that if the shape parameters of the RBF are chosen carefully, the polynomial basis can be removed from the formulation and substituted by a constant unity basis [24], [41].

In this work, a Multiquadric (MQ) RBF was used, $R_i(\mathbf{x}_I) = R(r_{Ii}) = (r_{Ii}^2 + c^2)^p$, with parameters c close to zero, $c \cong 0$, and p close to one, $p \cong 1$, being \mathbf{x}_I , the point of interest and r_{Ii} [24], [42]. The NNRPIM shape functions possess several important numerical properties, such as the unit partition property and the delta Kronecker property. In the literature, it is possible to find complete studies regarding its numerical properties [13], [25]. Since the NNRPIM shape functions are interpolating functions (due to the delta Kronecker property), the essential and natural boundary conditions can be imposed using the direct imposition method (the same methodology used to impose the boundary conditions in the FEM). Additionally, the literature describes with detail the development of the system of equation for an elasto-static problem (as the one here presented) and the imposition of the essential and natural boundary conditions, see the work of Belinha [13].

3. Materials and Methods

In this study, a mechanical simulation was done to evaluate the TBI. This study was performed using a meshless method - the NNRPIM - and the conventional FEM. Firstly, in order to demonstrate the differences between the FEM and the meshless methods a convergence study was performed. Afterwards, a 2D elasto-static simulation the TBI was studied considering the 2D plane strain assumption. At last, a 3D analysis was performed.

3.1 Convergence Study

This section presents the 2D and 3D models used to perform the convergence study. Regarding the 2D study, a $10m \times 10m$ square was discretized with 5 distinct nodal distributions, which are indicated in Table 1. For the 3D study, a $10m \times 10m \times H$ regular hexahedron was considered. The 3D solid was discretized with four regular nodal distributions, Table 1. In order to maintain a regular nodal spacing, respecting the nodal average distance h in all directions, the thickness H varies with the nodal mesh, Table 1. The h parameter is obtained with the expression: $h = \min(h_{ij}), \forall \{i, j\} \in \mathbb{N}: \{i, j\} \leq N \wedge i \neq j$, being N the number of node discretizing the problem domain. In both 2D and 3D models, all the nodes in coordinate $y = 0$ are constrained. In the 2D model those nodes are fixed with $\{u, v\} = \{0, 0\}$ and in the 3D models they are fixed with $\{u, v, w\} = \{0, 0, 0\}$. For the nodes at $y = 10$, it was applied a distributed shear force of $1N/m$, coplanar with Oxz plane, as represented in Figure 2. Additionally, for this preliminary study the following mechanical properties were assumed: Elastic modulus: $E = 1GPa$; and a Poisson ratio: $\nu = 0.45$.

3.2 Traumatic Brain Injuries Analysis

The TBI was simulated using a 2D numerical model and assuming a 2D plane strain linear elastic analysis. The 2D geometrical model was built from medical images, gathered from Lalys F, *et al*, with a 1024×1024 pixel resolution, using MIMICS Innovation Suite V19 software [43], [44], providing a high detail geometry, that represents a slice of the brain in a medial sagittal plane, Figure 4. The discretization mesh was obtained using triangular elements, having 1653 nodes and 3165 elements. Regarding the h parameter, the 2D model presents $h=0.0222$.

Afterwards, two 3D numerical models were constructed. One was constructed by extruding the previously built 2D model in the O_z direction with a thickness of 16mm, the 3D slice model, Figure 6A-1 and Figure 6A-2, and the other was constructed using the medical images, allowing to create a half brain 3D model, Figure 5A. Although the authors were able to construct the complete 3D brain model, the authors decided to construct the 3D model from the 2D model in order to fully control the mesh generation and to create a 3D model similar with the 2D models, and also due to hardware limitations, the authors decided just to create a 3D half brain geometrical model. The obtained 3D slice model has 8265 nodes and 12660 tetrahedral elements, leading to a h parameter: $h=0.0221$. For the 3D half brain model, the number of nodes (9790) and the number of elements (56005), correspond to 29370 degrees of freedom.

The mechanical properties considered in this study were gathered from the literature [10], [45]. Four distinct mechanical properties were assumed, being applied to the four distinct assumed anatomic structures, correspondingly. These anatomic structures were segmented using the MIMICS software and are in accordance with the medical images information. Thus, the models contain: the skull bone with a 1210 Kg/m³ density, a 8000 MPa elastic modulus and a 0,22 Poisson's ratio; the cerebrospinal fluid (CSF) with a 1130 Kg/m³ density, a 12 MPa elastic modulus and a 0,45 Poisson's ratio; and the brain grey matter with a 1040 Kg/m³ density, a 34 MPa elastic modulus and a 0,45 Poisson's ratio; and the brain white matter with a 1040 Kg/m³ density, an 41 MPa elastic modulus and a 0,45 Poisson's ratio. To simplify the model and the analysis, since CSF is a fluid, its mechanical properties were replaced by the dura mater meninges mechanical properties.

Regarding the essential boundary conditions, the 2D model assumed the skull completely constrained: $\bar{u} = 0 \wedge \bar{v} = 0$, as represented in Figure 6A-1. For the 3D slice model, in addition to the previous mentioned constrains, in the top and bottom plane ($z = 0 \wedge z = 16$), the nodes were fixed along O_z direction ($\bar{w} = 0$), in order to create a symmetry plane, Figure 6A-2. For the half brain 3D model, in order to enforce the symmetry of the model, it was assumed that all nodes belonging to the symmetry plane of the head model (plane O_{xy} with $z = 0$) are fixed along the O_z direction ($\bar{w} = 0$). In addition, all the nodes belonging to the skull surface were fixed in the three directions: O_x , O_y and O_z ($\{\bar{u}, \bar{v}, \bar{w}\} = \{0,0,0\}$).

In the 2D and 3D models, it was applied to all nodes of the model an acceleration of 2000m/s^2 along direction O_y , corresponding to the peak head acceleration found in the literature, Figure 6A-1 and Figure 6B. [10]

4. Results

In this section, the results for the 2D and 3D convergence studies are presented. Additionally, the results regarding the 2D and 3D analyses of the brain, using the NNRPIM and FEM, are shown. A new graphical technique suited to evaluate the stress values in the brain is introduced by showing only the results regarding the brain domain.

4.1 - Convergence Results

Regarding the convergence study, the results to be acquired were the total displacement, $|u|$, at the coordinates $\{x, y, z\} = \{10, 10, 0\}$. The $|u|$ was acquired for all models, 2D and 3D, using two different discrete methods, FEM and NNRPIM. In Figure 3A, for the 2D model, it is visible that NNRPIM shows a faster convergence when compared with the FEM method. This can be concluded, since all the methods converge to a very similar displacement value when the h parameter of the mesh is $h=0.015625$. Notice, that for high values of h the NNRPIM solution is closer to the final converged solution than the FEM for the same values of h . As Figure 3A shows, using a mesh possessing $h=0.03125$, the NNRPIM is capable to obtain a solution very close to the final converged solution, since the results are very similar with the results obtained with $h=0.015625$. Concerning the 3D analysis, Figure 3B shows that once more the NNRPIM converges faster than the FEM. Notice that with $h=0.0625$ both methods present the same magnitude for $|u|$ and with $h=0.25$ the FEM shows a much lower value of $|u|$ when compared to the meshless method. Figure 3B shows that considering $h=0.03125$ both methods have already converged to a solution very close to the expected final converged solution, since the results are very close to those obtained with $h=0.015625$.

4.2 - 2D Models Results

In order to perform a comparative analysis of the stress field in the brain tissue, a division of the brain in standardized layers was performed. The technique is inspired in the Gruen zones, a common clinical division adopted for the femur. Thus, a geometrical division of the brain was performed, in which 6 divisions were assumed, all with the

same height and perpendicular to the imposed acceleration, as represented in Figure 7, being zone 1 the more proximal and zone 6 the more distal. In Figure 7A, it is represented the average von Mises effective stress obtained in each corresponding division, and in Figure 7B the average principal stress σ_{11} found in each division.

The behaviours of NNRPIM and FEM are similar, which can be confirmed by the results presented in Figure 7. Both Table 2 and Figure 7B, in which are presented the σ_{11} average values for each division, show that the difference between the FEM and the NNRPIM solution is less than 5% (with the exception of division 4). In Figure 9, the principal stress, σ_{11} , σ_{22} , and the von Mises effective stress are represented in colour maps. The σ_{11} stress map shows that in the impact proximal zone are found mainly compressive stresses (since σ_{11} is negative). The distal impact zone, in which σ_{11} is mostly positive, is under the action of tension stresses.

4.3 - 3D Slice Model Results

Following the technique adopted for the 2D analysis, a division of the 3D domain of the brain was performed. In Figure 8A is represented the corresponding average values of von Mises effective stress for each division, and in Figure 8B the average principal stress σ_{11} for each division are represented. Once more, the NNRPIM and FEM solutions are very close, as shown in Figure 8A and Figure 8C. Comparing the results obtained with the two numerical techniques, Table 2 indicates that the difference between the NNRPIM solution and the FEM solution does not overcome 8%. Figure 8C supports this last statement. The divisions showing lower average values for the von Mises effective stress and principal stress σ_{11} are the central one: 2, 3 and 4. As in the 2D, the distal slice has the highest stress values.

In Figure 9, relevant stress fields are presented. The results allow to sustain that the FEM values are higher than the NNRPIM, which corroborates the results of the average stress values presented in Figure 8A and Figure 8B.

4.4 - 3D Half Brain Model Results

Following the technique adopted for the 2D and for the 3D slice model analysis, in the created half brain 3D model, the same six Gruen zones were considered and it was calculated their local average principal stresses σ_{11} , σ_{22} and the von Mises stress, for both FEM and NNRPIM analyses, as shown in Table 3. As can be seen from Table 3, the

results between different methodologies are very similar. Still, comparing the results of the 2D model and 3D model with the half brain 3D model, it is possible to visualize that the results are different. Nevertheless, regardless it is being used a slice of the half brain model (represented in Figure 5B) to obtain the stress values, this difference was expected, since the geometrical models are very different. Thus, concerning the effective stress, σ_{11} , σ_{22} and the von Mises stress results obtained using the FEM and the NNRPIM, there is an average difference of 5,9% with a SD of 1%. The σ_{11} Gruen zone values show that in the impact proximal zone are found mainly compressive stress (since σ_{11} is negative), and that in the distal impact zone, in which σ_{11} is mostly positive, is under the action of tension stresses. This is coherent with the results obtained with the analysis of the 2D model.

5. Discussion

In this work, it was used a methodology that allowed the construction of a 2D and two 3D brain models from medical images. From these medical images, using the software Mimics, the mechanical properties (obtained from the literature) were attributed to the identified anatomic regions, according to the segmented anatomical zones. Using the impact acceleration found in the literature, the constructed models were analysed using NNRPIM and FEM. It was also performed a convergence study to compare the discretization techniques that allowed to obtain the necessary awareness regarding the level of the discretization required to obtain a reliable solution. It was shown that the quality of the discretization level can be gauged by the h parameter.

The usage of the h parameter permits to understand the discretization level and to decide regarding the necessity to increase or to reduce such level, allowing to optimize the discretization. In our 2D model and in the 3D slice model the selected h parameter is more than capable to produce accurate results, as seen in Figure 3A and Figure 3B. This is an important issue in approximation techniques. Unfortunately, most of FEM analysis available in the literature did not consider such parameter. In many cases the discretization level in commercial software is automatic and the lack of awareness regarding the value of the discretization level can lead to invalid analyses. The convergence study confirm that meshless methods have a faster converge rate when compared with the FEM, allowing to meshless methods to use sparser meshes and still produce valid results. Due to the authors' hardware limitations, it was not possible to

analyse a full 3D brain with a nodal mesh density comparable to the 2D brain model and to the 3D brain slice model. Due to hardware limitations, this 3D half brain model does not possess a sufficient discretization level, capable to discretize with detail the brain structures.

From the obtained stress fields, it can be concluded that meshless and FEM results are very similar, in magnitude and in its spatial distribution. Comparing the 2D model and the 3D slice model, since the acceleration was applied only in one direction, the results are comparable using the σ_{11} field. The von Mises stress fields cannot be used to compare the 3D model with 2D, since the 2D analysis principal stress component σ_{33} is null ($\sigma_{33} = 0$), making the results incomparable. Comparing the σ_{11} fields of the NNRPIM and FEM, it is perceived that the results are very similar. The average value of the principal stresses σ_{11} is relevant, since it indicates the higher compressive and traction zones. As anticipated, the average stress values in each division, show that the higher values are present in the proximal and distal impact zone divisions. It is notorious that the values of σ_{11} , are higher than σ_{22} in both numerical methods, which is an expected result since the impact force was considered along the Oy -axis direction.

Concerning the results of the 3D half brain model, σ_{11} , σ_{22} and the von Mises stress, obtained for each zone, the two numerical approaches give very similar results. As previously said, in order to objectively compare the results obtained with the 2D model and the 3D slice model, with the 3D half brain model, a brain slice with the same thickness of the 3D slice model was selected from the half brain 3D model. Despite this, it is possible to visualize comparing the results from Table 2 and Table 3 that the results are different. Nevertheless, this difference was expected because, as said before, in contrast to the 2D model and the 3D slice model, the 3D half brain model is not capable to define with detail all the structures defining the brain.

Being FEM a widely used method, possessing several available commercial packages, it has the advantage of being more evolved and optimized. FEM has the advantage of being faster when compared to the meshless methods since its shape functions can be pre-established before the beginning of the numerical analysis. Additionally, the FEM shape functions are simpler to compute due to its lower intrinsic connectivity. In FEM, the triangular and tetrahedral elements are widely used due to their ability to adjust virtually

to any geometry. However, as this work has shown, these elements present a weaker numerical performance when compared with meshless methods.

Regarding the stress distribution, the results show that meshless methods are capable to produce smoother stress fields. As figure 9 shows, meshless methods allow to obtain stress levels similar to the FEM. However, notice that the stress field produced by meshless methods does not show as many field discontinuities as the FEM solution. This smoothness comes from the higher nodal connectivity of meshless method. Thus, an interest point (belonging to a material domain) will interact with distant nodes (which can belong to another material domain). This creates a natural gradient material homogenization that smooths the variable fields, such as the displacement field, the stress field, the strain field, etc.

If the numerical model is constructed through imaging techniques, meshless methods have the advantage to permit the allocation of the material properties directly to the nodes, using the pixel/voxel information. They also have the benefit of allowing the construction of complex geometrical models, without any special concern about the mesh geometry and element discretization created by the CAD programs.

The methodology of creating divisions in the brain to evaluate the stress fields revealed itself to be useful and standardizable, which will permit to future research works a solid and robust comparison basis. Although the main objective of the present study was to show the potential of meshless methods combined with imaging techniques, this study presents some limitations. First, regarding the 3D analyses, it was used a 3D brain model constructed from the extrusion of the 2D model, resulting in the lost the anatomical real reproduction, and afterwards, a 3D half brain model was built possessing an insufficient mesh discretization level. Furthermore, the study was performed considering a linear elastic regime, neglecting the viscoelastic mechanical properties of the brain. Additionally, it was also used in substitution of the CSF, a fluid, a mechanical propriety of the dura mater with $\nu=0.45$. In addition, although the impact analysis demands a dynamic and transient regime, all the analyses here presented assumed the corresponding static assumptions.

Acknowledgments

The authors truly acknowledge the funding provided by Ministério da Ciência, Tecnologia e Ensino Superior - Fundação para a Ciência e a Tecnologia (Portugal), under Grants SFRH/BD/110047/2015, and by project funding MIT-EXPL/ISF/0084/2017. Additionally, the authors gratefully acknowledge the funding of Project NORTE-01-0145-FEDER-000022 - SciTech - Science and Technology for Competitive and Sustainable Industries, co-financed by Programa Operacional Regional do Norte (NORTE2020), through Fundo Europeu de Desenvolvimento Regional (FEDER).

References

- [1] R. O. Mujalli, G. López, and L. Garach, “Bayes classifiers for imbalanced traffic accidents datasets,” *Accid. Anal. Prev.*, vol. 88, pp. 37–51, Mar. 2016.
- [2] B. Roozenbeek, A. I. R. Maas, and D. K. Menon, “Changing patterns in the epidemiology of traumatic brain injury.,” *Nat. Rev. Neurol.*, vol. 9, no. 4, pp. 231–6, Apr. 2013.
- [3] A. F. De Andrade, W. S. Paiva, R. L. O. De Amorim, E. G. Figueiredo, E. Rusafa Neto, and M. J. Teixeira, “Mecanismos de lesão cerebral no traumatismo cranioencefálico,” *Rev. Assoc. Med. Bras.*, vol. 55, no. 1, pp. 75–81, 2009.
- [4] J. M. Taylor, M. H. Montgomery, E. J. Gregory, and N. E. J. Berman, “Exercise preconditioning improves traumatic brain injury outcomes,” *Brain Res.*, vol. 1622, pp. 414–429, Oct. 2015.
- [5] D. F. Meaney and D. H. Smith, “Biomechanics of Concussion,” *Clin. Sports Med.*, vol. 30, no. 1, pp. 19–31, Jan. 2011.
- [6] S. Khoury and R. Benavides, “Pain with traumatic brain injury and psychological disorders,” *Prog. Neuro-Psychopharmacology Biol. Psychiatry*, vol. 87, pp. 224–233, Dec. 2018.
- [7] D. F. Meaney, B. Morrison, and C. Dale Bass, “The Mechanics of Traumatic Brain Injury: A Review of What We Know and What We Need to Know for Reducing Its Societal Burden,” *J. Biomech. Eng.*, vol. 136, no. 2, p. 021008, Feb. 2014.
- [8] C. R. Summers, B. Ivins, and K. A. Schwab, “Traumatic brain injury in the United States: An epidemiologic overview,” *Mt. Sinai J. Med.*, vol. 76, no. 2, pp. 105–

110, Apr. 2009.

- [9] Z. Liang and Y. Luo, "A QCT-Based Nonsegmentation Finite Element Head Model for Studying Traumatic Brain Injury," *Appl. Bionics Biomech.*, vol. 2015, pp. 1–8, 2015.
- [10] B. Yang *et al.*, "Development of a finite element head model for the study of impact head injury.," *Biomed Res. Int.*, vol. 2014, p. 408278, Jan. 2014.
- [11] H. Mao *et al.*, "Development of a Finite Element Human Head Model Partially Validated With Thirty Five Experimental Cases," *J. Biomech. Eng.*, vol. 135, no. 11, p. 111002, Nov. 2013.
- [12] X. Yue, L. Wang, and R. Wang, "Tissue Modeling and Analyzing with Finite Element Method: A Review for Cranium Brain Imaging," *Int. J. Biomed. Imaging*, vol. 2013, pp. 1–12, 2013.
- [13] J. Belinha, *Meshless Methods in Biomechanics: Bone Tissue Remodelling Analysis*, vol. 2. Dordrecht: Springer Netherlands, 2014.
- [14] B. Nayroles, G. Touzot, and P. Villon, "Generalizing the finite element method: Diffuse approximation and diffuse elements," *Comput. Mech.*, vol. 10, no. 5, pp. 307–318, 1992.
- [15] T. Belytschko, Y. Y. Lu, and L. Gu, "Element-free Galerkin methods," *Int. J. Numer. Methods Eng.*, vol. 37, no. 2, pp. 229–256, Jan. 1994.
- [16] W. K. Liu, S. Jun, and Y. F. Zhang, "Reproducing kernel particle methods," *Int. J. Numer. Methods Fluids*, vol. 20, no. 8–9, pp. 1081–1106, Apr. 1995.
- [17] S. N. Atluri and T. Zhu, "A new Meshless Local Petrov-Galerkin (MLPG) approach in computational mechanics," *Comput. Mech.*, vol. 22, no. 2, pp. 117–127, Aug. 1998.
- [18] G. R. Liu and Y. T. Gu, "A point interpolation method for two-dimensional solids," *Int. J. Numer. Methods Eng.*, vol. 50, no. 4, pp. 937–951, Feb. 2001.
- [19] E. Cueto, N. Sukumar, B. Calvo, M. a. Martínez, J. Cegoñino, and M. Doblaré, "Overview and recent advances in natural neighbour galerkin methods," *Arch. Comput. Methods Eng.*, vol. 10, no. 4, pp. 307–384, Dec. 2003.
- [20] J. G. Wang and G. R. Liu, "A point interpolation meshless method based on radial

- basis functions,” *Int. J. Numer. Methods Eng.*, vol. 54, no. 11, pp. 1623–1648, Aug. 2002.
- [21] J. Belinha, L. M. J. S. Dinis, and R. M. Natal Jorge, “The natural radial element method,” *Int. J. Numer. Methods Eng.*, vol. 93, no. 12, pp. 1286–1313, Mar. 2013.
- [22] J. Belinha, L. M. J. S. Dinis, and R. M. N. Jorge, “Composite laminated plate analysis using the natural radial element method,” *Compos. Struct.*, vol. 103, pp. 50–67, Sep. 2013.
- [23] J. Belinha, L. M. J. S. Dinis, and R. M. Natal Jorge, “Analysis of thick plates by the natural radial element method,” *Int. J. Mech. Sci.*, vol. 76, no. 12, pp. 33–48, Nov. 2013.
- [24] L. M. J. S. Dinis, R. M. Natal Jorge, and J. Belinha, “Analysis of 3D solids using the natural neighbour radial point interpolation method,” *Comput. Methods Appl. Mech. Eng.*, vol. 196, no. 13–16, pp. 2009–2028, Mar. 2007.
- [25] G. Voronoi, “Nouvelles applications des paramètres continus à la théorie des formes quadratiques. Deuxième mémoire. Recherches sur les paralléloèdres primitifs,” *J. für die Reine und Angew. Math.*, vol. 1908, no. 134, pp. 198–287, 1908.
- [26] B. Delaunay, “Sur la sphère vide. A la memoire de Georges Voronoï,” *Bull. l’Academie des Sci. l’URSS. Cl. des Sci. Math. na*, vol. 7, pp. 793–800, 1934.
- [27] J. Belinha, L. M. J. S. M. J. S. Dinis, and R. M. M. Natal Jorge, “The analysis of the bone remodelling around femoral stems: A meshless approach,” *Math. Comput. Simul.*, vol. 121, pp. 64–94, Mar. 2016.
- [28] J. Belinha, L. M. J. S. Dinis, and R. M. N. Jorge, “The Meshless Methods in the Bone Tissue Remodelling Analysis,” *Procedia Eng.*, vol. 110, pp. 51–58, 2015.
- [29] M. Marques, J. Belinha, A. F. F. Oliveira, M. C. C. Manzanares Céspedes, and R. M. M. Natal Jorge, “A multiscale homogenization procedure combining the fabric tensor with a natural neighbour meshless method,” *Eng. Anal. Bound. Elem.*, vol. 100, no. August 2017, pp. 211–224, Mar. 2019.
- [30] J. Belinha, *Meshless Methods in Biomechanics*, Vol.16., vol. 16. Cham: Springer International Publishing, 2014.

- [31] J. Belinha, R. M. M. Natal Jorge, and L. M. J. S. Dinis, “Bone tissue remodelling analysis considering a radial point interpolator meshless method,” *Eng. Anal. Bound. Elem.*, vol. 36, no. 11, pp. 1660–1670, Nov. 2012.
- [32] M. M. A. Peyroteo, J. Belinha, S. Vinga, L. M. J. S. Dinis, and R. M. Natal Jorge, “Mechanical bone remodelling: Comparative study of distinct numerical approaches,” *Eng. Anal. Bound. Elem.*, Feb. 2018.
- [33] H. M. S. Duarte, J. R. Andrade, L. M. J. S. Dinis, R. M. N. Jorge, and J. Belinha, “Numerical analysis of dental implants using a new advanced discretization technique,” *Mech. Adv. Mater. Struct.*, vol. 23, no. 4, pp. 467–479, Apr. 2016.
- [34] H. M. S. Duarte, J. Rafael Andrade, L. M. J. S. Dinis, R. M. Natal Jorge, and J. Belinha, “Mechanics of Advanced Materials and Structures Numerical analysis of dental implants using a new advanced discretization technique Numerical analysis of dental implants using a new advanced discretization technique,” 2016.
- [35] S. F. Moreira, J. Belinha, L. M. J. S. Dinis, and R. M. Natal Jorge, “A global numerical analysis of the ‘central incisor/local maxillary bone’ system using a meshless method,” *MCB Mol. Cell. Biomech.*, vol. 11, no. 3, pp. 151–184, Sep. 2014.
- [36] C. S. S. Tavares, J. Belinha, L. M. J. S. Dinis, and R. M. N. Jorge, “The Elastoplastic Response of the Bone Tissue Due to the Insertion of Dental Implants,” *Procedia Eng.*, vol. 110, pp. 37–44, 2015.
- [37] S. F. Moreira, J. Belinha, L. M. J. S. Dinis, and R. M. Natal Jorge, “A Global Numerical Analysis of the ‘Central Incisor / Local Maxillary Bone’ System using a Meshless Method,” *Mol. Cell. Biomech.*, vol. 11, no. 3, pp. 151–184, 2014.
- [38] C. F. Santos, J. Belinha, F. Gentil, M. Parente, and R. N. Jorge, “The free vibrations analysis of the cupula in the inner ear using a natural neighbor meshless method,” *Eng. Anal. Bound. Elem.*, vol. 92, pp. 50–63, Jul. 2018.
- [39] C. F. Santos, J. Belinha, F. Gentil, M. Parente, and R. N. Jorge, “The free vibrations analysis of the cupula in the inner ear using a natural neighbor meshless method,” *Eng. Anal. Bound. Elem.*, vol. 92, pp. 50–63, Jul. 2018.
- [40] R. Sibson, “A Brief Description of Natural Neighbor Interpolation,” in *Interpolating Multivariate Data*, V. Barnett, Ed. Wiley, Chichester, 1981, pp. 21–

36.

- [41] L. M. J. S. Dinis, R. M. Natal Jorge, and J. Belinha, “Analysis of plates and laminates using the natural neighbour radial point interpolation method,” *Eng. Anal. Bound. Elem.*, vol. 32, no. 3, pp. 267–279, Mar. 2008.
- [42] R. L. Hardy, “Theory and applications of the multiquadric-biharmonic method 20 years of discovery 1968-1988,” *Comput. Math. with Appl.*, vol. 19, no. 8–9, pp. 163–208, Jan. 1990.
- [43] “Mimics® Medical Image Segmentation for Engineering on Anatomy™.” Materialise NV, Leuven, Belgium.
- [44] F. Lalys, C. Haegelen, J. C. Ferre, O. El-Ganaoui, and P. Jannin, “Construction and assessment of a 3-T MRI brain template,” *Neuroimage*, vol. 49, no. 1, pp. 345–354, Jan. 2010.
- [45] C. Giordano, R. J. H. Cloots, J. A. W. van Dommelen, and S. Kleiven, “The influence of anisotropy on brain injury prediction,” *J. Biomech.*, vol. 47, no. 5, pp. 1052–1059, Mar. 2014.

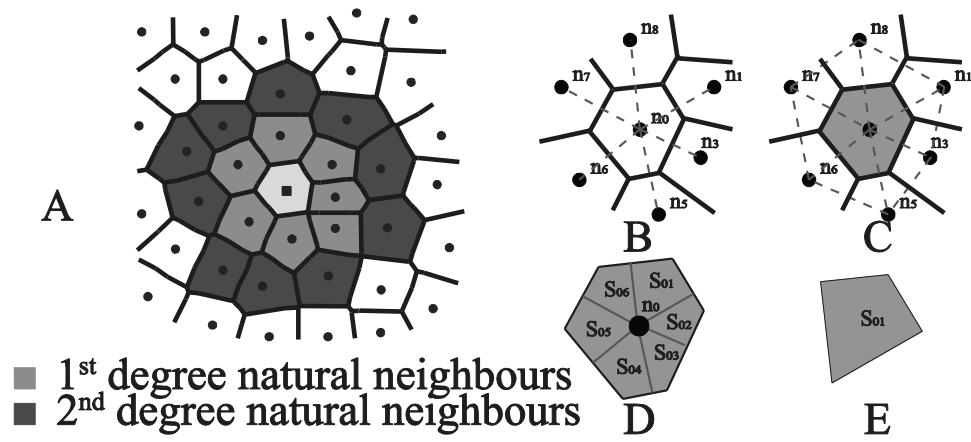


Figure 1 – A: First and second degree natural neighbours in NNRPIM.; B and C: Delaunay Tessellation; D: Generated quadrilaterals; E: Sub-cell.

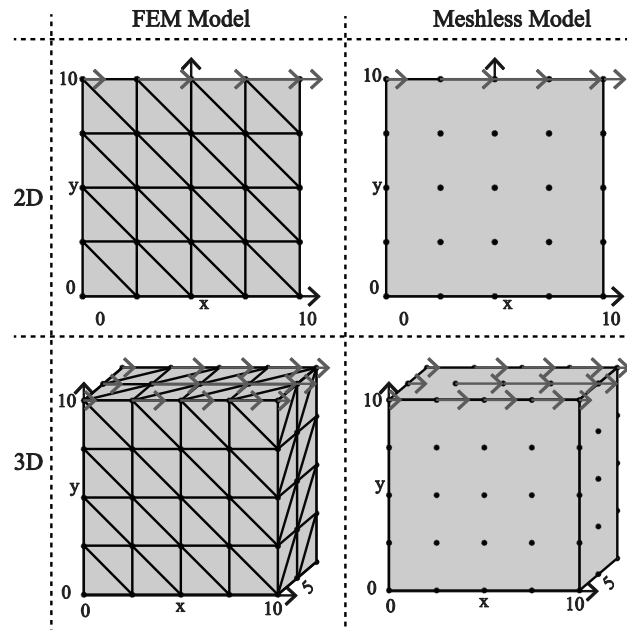


Figure 2 – 2D and 3D models, for meshless and FEM analysis, with h parameter = 0.25, and with applied natural boundary condition, dimensions in [m].

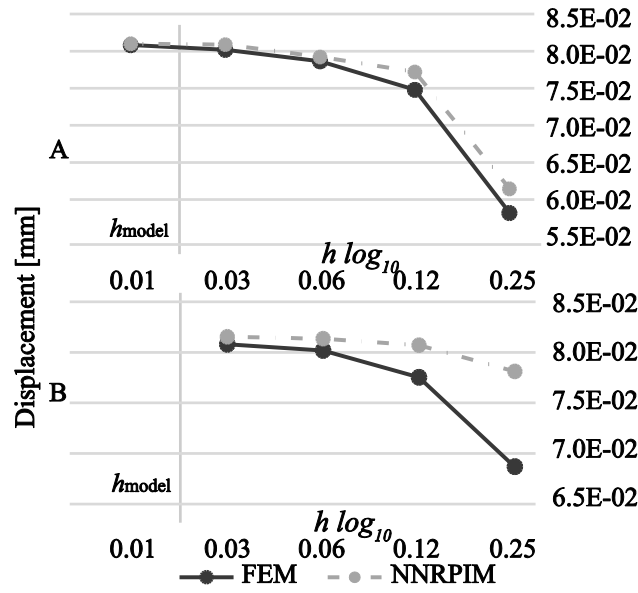


Figure 3 – A: convergence results for the 2D model, $h_{\text{model}}= 0,0222$; B: convergence results for the 3D model, $h_{\text{model}}= 0,0221$. In both images, the vertical bar, (—), indicates the h value for the 2D and 3D brain model. x axis in Log_{10} scale.

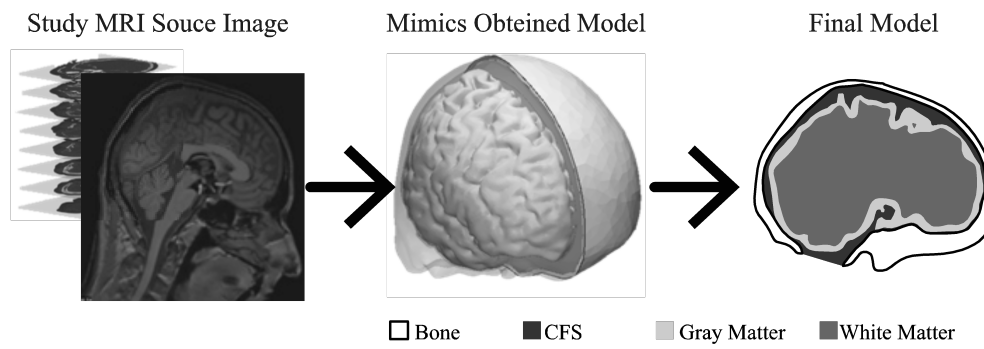


Figure 4 – Geometrical head model obtained from a MRI, through the Mimics® software. [43].

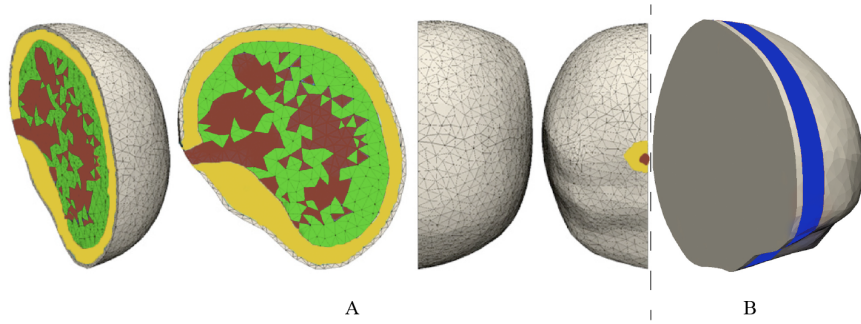


Figure 5 – A: Images of the half brain 3D model; B: image with representation of the 3D half brain model slice used to acquire the σ_{11} , σ_{22} and von Mises stress values.

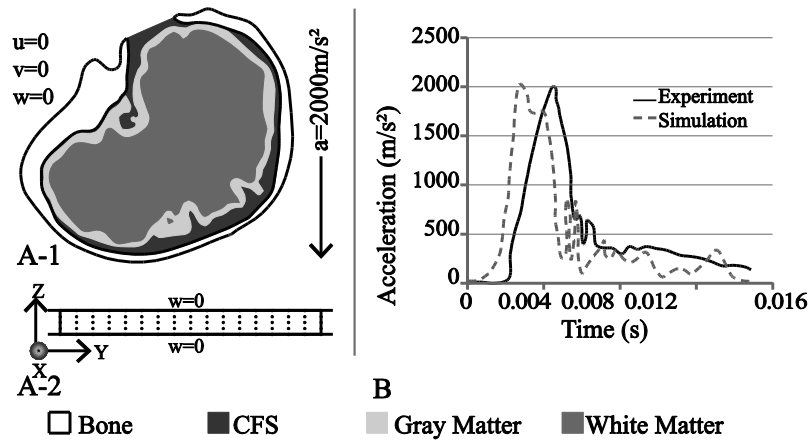


Figure 6 – A-1: 2D model with $\mathbf{u} = \mathbf{0} \wedge \mathbf{v} = \mathbf{0} \wedge \mathbf{w} = \mathbf{0}$ constrains in the skull and with an acceleration with y component of 2000m/s^2 ; A-2: Symmetry condition applied to the top and bottom slice of the 3D slice model, for $\mathbf{z} = \mathbf{0} \wedge \mathbf{z} = \mathbf{16}$: $\mathbf{w} = \mathbf{0}$; B: Curve regarding the head peak acceleration from Yang et al 2014 [10].

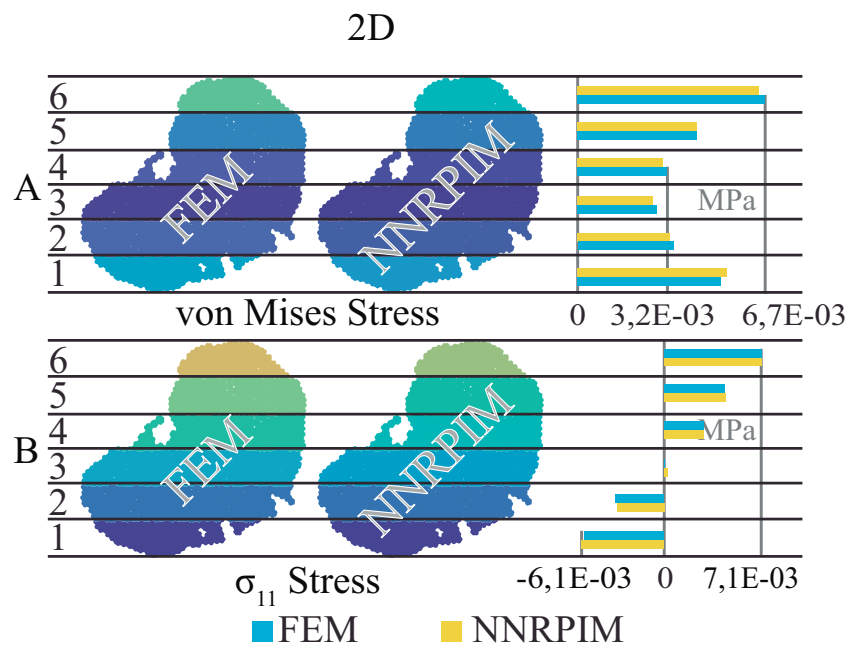


Figure 7 – A: 2D model division average von Mises stress and representative column graphic for NNRPIM.; B: 2D model's division average σ_{11} stress and representative column graphic for FEM and NNRPIM.

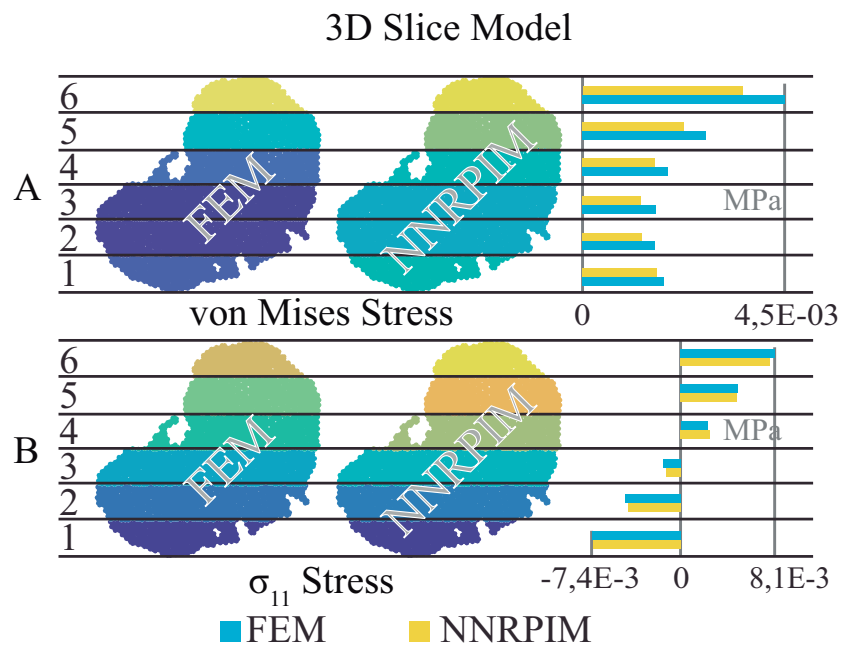


Figure 8 – A: 3D model division average von Mises stress and representative column graphic for NNRPIM.; B: 3D model's division average σ_{11} stress and representative column graphic for FEM and NNRPIM.

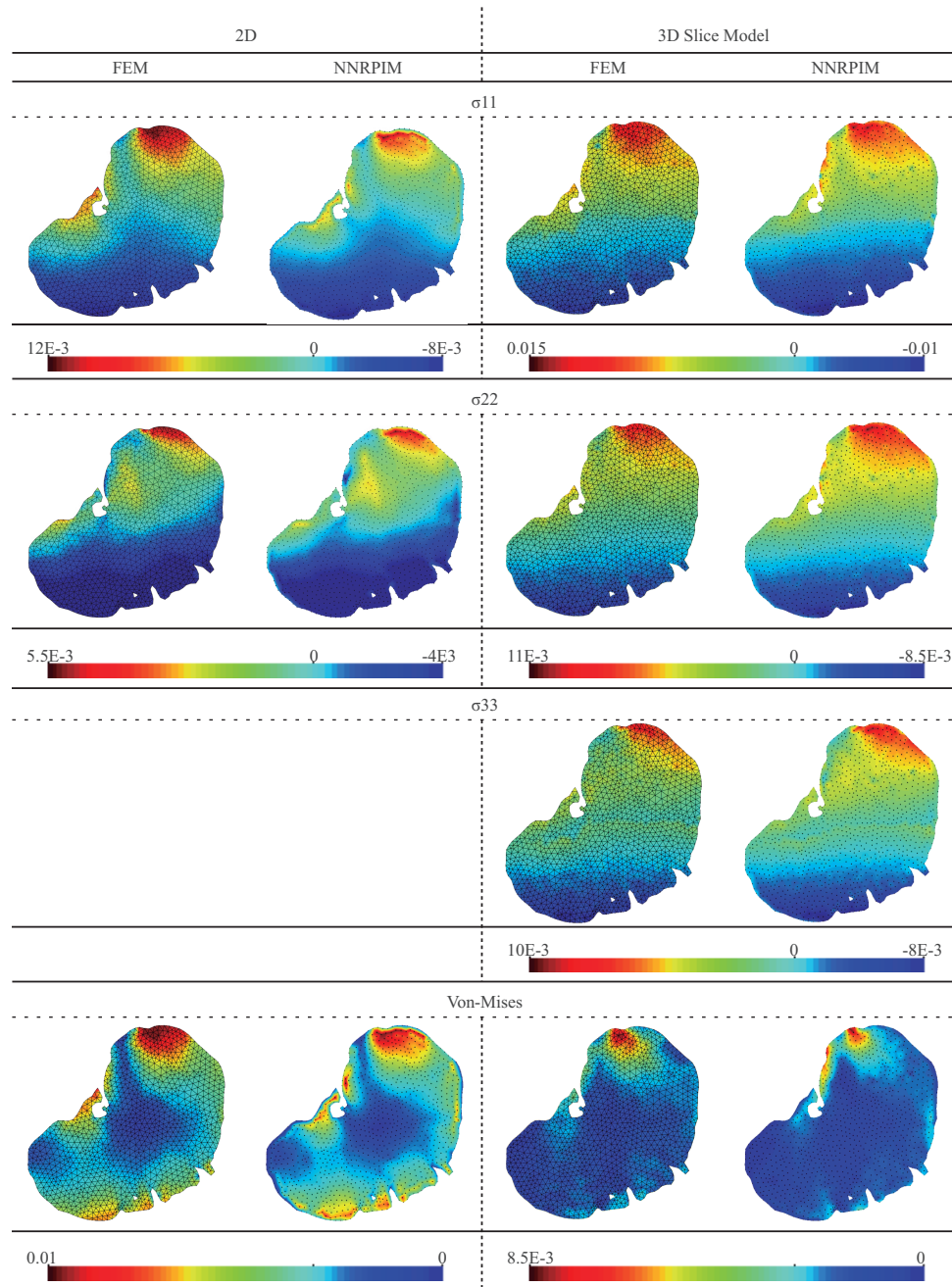


Figure 9 – Principals stress field, σ_{11} and σ_{22} , and von Mises stress field for 2D FEM and NNRPIM and principals stress field, σ_{11} , σ_{22} and σ_{33} for the FEM and NNRPIM 3D slice models.

2D discretization				3D discretization				
Mesh	Nodal	Nodes	h	Mesh	Nodal	Nodes	h	Thickness H
A	5x5	25	0,25	F	5x5x3	125	0,25	0,25
B	9x9	81	0,125	G	9x9x3	243	0,125	0,125
C	17x17	289	0,0625	H	17x17x3	867	0,0625	0,0625
D	33x33	1089	0,03125	I	33x33x3	3267	0,03125	0,03125
E	65x65	4225	0,015625					

Table 1 – Different discretization and correspondent h value.

Division	2D		3D Slice Model	
	FEM	NNRPIM	FEM	NNRPIM
1	-6,0E-03	-6,1E-03	-7,6E-03	-7,5E-03
2	-3,6E-03	-3,5E-03	-4,7E-03	-4,5E-03
3	6,2E-05	2,8E-04	-1,5E-03	-1,2E-03
4	3,0E-03	3,0E-03	2,3E-03	2,5E-03
5	4,5E-03	4,5E-03	5,0E-03	4,9E-03
6	7,2E-03	7,2E-03	8,1E-03	7,7E-03

Table 2 – Principals average stress field, σ_{11} , for the 3D slice model and for the 2D model, using FEM and NNRPIM, for each Gruen division [MPa].

3D Half Brain Model Gruen zones.						
Division	σ_{11}		σ_{22}		von Mises Stress	
	FEM	NNRPIM	FEM	NNRPIM	FEM	NNRPIM
1	-7,6E-02	-7,4E-02	-7,9E-02	-7,9E-02	2,2E-02	2,4E-02
2	-4,1E-02	-4,0E-02	-4,5E-02	-4,5E-02	1,9E-02	2,0E-02
3	-4,4E-03	-4,2E-03	-1,1E-02	-1,2E-02	1,5E-02	1,6E-02
4	2,9E-02	2,7E-02	2,0E-02	1,8E-02	1,2E-02	1,3E-02
5	7,1E-02	6,5E-02	5,5E-02	5,0E-02	1,9E-02	2,0E-02
6	1,2E-01	1,1E-01	8,9E-02	8,2E-02	3,0E-02	2,8E-02

Table 3 – Principals average stress field, σ_{11} , σ_{22} and von Mises stress, for the 3D half brain FEM and NNRPIM models, in each Gruen division [MPa].

3.3 Contribution II: A brain impact stress analysis using advanced discretisation meshless techniques.

3.3.1 Highlights of Contribution: 3.3

This contribution focused on the numerical simulation of biological structures, using the RPIM meshless method and the FE method.

Therefore, the main contents of this publication include:

- I. Literature review on brain impact mechanical models and meshless methods;
- II. RPIM methodology applications and formulation;
- III. A convergence study to demonstrate the differences between the FEM and the RPIM meshless methods, whereas also compared the FEM results using Abaqus and FEMAS.
- IV. One 2D and two 3D brain geometrical models were constructed with the resource to medical images, gathered from Lalys F, et al, with a 1024×1024 pixel resolution, using MIMICS Innovation Suite V19 software, [108, 109]. The 2D geometrical model was built using an image in the medial sagittal plane, where it was considered the skull, brain grey and white matter and the CSF. Concerning the 3D geometrical models, one was constructed by extruding the 2D model, and the other was constructed using the medical images, allowing to create a half brain 3D model.
- V. Convergence study: RPIM shows a faster convergence when compared with the FEM method, figure 3.2. ABAQUS FEM and FEMAS FEM results in the convergence study are almost coincident, validating the FEM formulation implemented in the academic software FEMAS. Regarding the computational cost, the meshless formulation shows a computational time very similar to the FEM, figure 3.3.
- VI. Conclusion: The convergence study developed in this study enhanced the importance of the discretisation level to obtain a reliable solution when working with numerical methods. The convergence study showed that RPIM has a faster converge rate than the FEM, allowing the usage of sparse meshes, still capable of providing valid results. RPIM and FEM results are very similar, in magnitude and in spatial distribution, being meshless methods capable of producing smoother results. The methodology of dividing the brain domain in standard

sections allowed to compare efficiently the RPIM and the FEM results. Additionally, this technique could permit future works to compare future results following a standardised system, inspired in the Gruen zones, a standardised system widely used to evaluate stress upon the use of prostheses in the femoral bone. [110, 111]

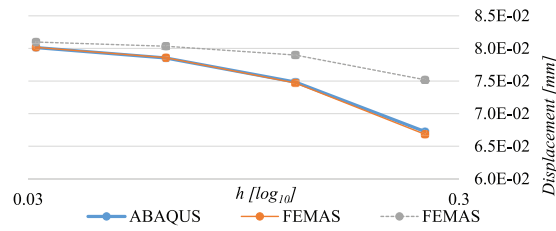


Figure 3.2: Contribution II convergence study results.

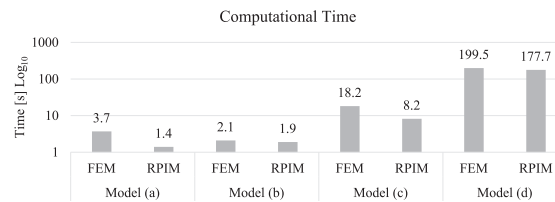


Figure 3.3: Contribution II: computational cost results.

The complete document can be found in the next pages.

A brain impact stress analysis using advanced discretization meshless techniques

Marco Marques¹, Jorge Belinha^{*,1,2}, L.M.J.S. Dinis^{1,2}, Renato Jorge^{1,2}

¹ Institute of Mechanical Engineering and Industrial Management (INEGI), University of Porto, Portugal

² Faculty of Engineering of the University of Porto (FEUP), Portugal

(*) corresponding author: jbelinha@fe.up.pt

Abstract

This work has the objective to compare the mechanical behaviour of a brain impact using an alternative numerical meshless technique. Thus, a discrete geometrical model of a brain was constructed using medical images. This technique allows to achieve a discretization with realistic geometry, allowing to define locally the mechanical properties accordingly with the medical images colour scale. After defining the discrete geometrical model of the brain, the essential and natural boundary conditions were imposed to reproduce a sudden impact force. The analysis was performed using the Finite Element Analysis (FEM) and the Radial Point Interpolation Method (RPIM), an advanced discretization technique. The results of both techniques are compared. When compared with the FEM, it was verified that meshless methods possess a higher convergence rate and that they are capable to produce smoother variable fields.

Keywords: computational biomechanics; meshless methods; radial point interpolation method; finite element analysis; brain impact.

1. Introduction

Head injury is a major health and socioeconomic problem, since it is frequent and severe in almost all types of traffic accidents that annually injury approximately 24 million individuals [1]. Head injury is also very common in contact sports, such as American

football, boxing, ice hockey, football and others [2]. In particular, the traumatic brain injuries (TBI) occurs in the presence of an abrupt mechanical stimulus (due to an external factor) into the brain or to the cranium. This sudden action cause temporary or permanent brain damage and dysfunction, and can result in a diffuse lesion, if there are rotational and deceleration forces, or can result in a focal lesion, result of the direct contact forces [3,4]. These lesions can result in the hospitalization of the subject, and it is estimated that one fifth of the hospitalized persons cannot return to a normal life [5]. Having the TBI devastating consequences and a significant incidence, 2–5 million people in the US per year, considerable research efforts have been devoted to understand and to prevent TBI [6–8]. Due to the significant incidence of TBI, the scientific community interest started to grow. Driven by unprecedented technological developments, computational mechanics evolved and now it is possible to simulate in-silico several physical phenomena, such as TBI. The early research works of TBI used in-vitro models, such as cadaver human heads [9,10], animal heads and physical head models that have evolved from simple anatomic representations to highly complex models constructed from medical images [11–13]. With the technological developments, today, using computational mechanics, it is possible to study the TBI virtually, using geometric models representative of the head, that allow to short the total time of the research (since computational analysis are faster and more predictable than experimental analysis) and with a very low economic cost (because the computational procedure is much cheaper than the complete experimental process).

Due to its robustness and reabilitate, in computational mechanics, the most widely used discrete numerical technique is the Finite Element Method (FEM). Nevertheless, in recent years, meshless methods come into focus within the computational mechanic's research community. Meshless methods possess some relevant advantages when compared with the FEM. For instances, meshless methods allow to discretize the physical domain using only a cloud of points or nodes, without the need to build an element mesh [14]. The meshless concept comes from the fact that the points, or nodes, of the computational cloud do not have any pre-established connection between them. Thus, the nodal discretization of the domain can be completely unstructured, fitting exactly the domain geometry of complex shapes, such are the biological structures. Thus, in computational biomechanics, the discretization flexibility of meshless methods is a true asset, since it permits to discretize the problem domains using directly the pixels/voxels of the medical images.

There are several meshless methods available in the literature, each one with its own particular characteristics, however all have common features [14]. A meshless method for the analysis of a mechanical problem requires: a technique to impose the nodal connectivity; a methodology to build the background integration grid and; a numerical technique to construct the shape functions. This work uses a very popular meshless method, the radial point interpolation method (RPIM) [15]. The RPIM is a meshless method that evolved from the point interpolation method (PIM) [16], which uses a polynomial basis function to construct the interpolation shape functions but is not capable to produce stable results when the nodes are perfectly aligned (regular nodal grids). Therefore, Wang and Liu [15] included a radial basis function (RBF) in the formulation allowing the stabilization of the procedure. RPIM evolved and today it is possible find several variations of the original RPIM, such as the Natural Neighbour RPIM [17–19], the nodal integration RPIM [20], the linearly conforming RPIM [21,22], the cell-based smoothed RPIM [23] and the Natural Radial Element Method [24–26]. As mentioned before, being the RPIM a meshless method, it allows to discretize the physical domain using only a cloud of points or nodes, that do not have any pre-established connection between them, eliminating the need to build an element mesh [14]. Thus, using the RPIM, the nodal discretization of the domain can be completely unstructured, fitting exactly the domain geometry of complex shapes, such are the biological structures, which is not possible using the FEM conventional method. Presently, the RPIM is validated in several computational mechanics applications, such as the analysis of composite laminated plates [27], determination of stress intensity factors for fatigue crack growth [28] or numerical analysis of piezoelectric ceramics [29].

In this work, the mechanical response of a human head model was simulated in order to evaluate the effects of a TBI. This study was performed using the RPIM and then, for comparison purposes, using the Finite Element Method (FEM). Firstly, in order to understand and document the discretization effects, a convergence study is performed. Afterwards, a 2D head model and a 3D model are analysed with both numerical techniques. The results are compared and discussed and in the end the most relevant conclusions are mentioned.

In order to allow an accurate and comprehensive comparison between methodologies, the authors have fully developed a complete RPIM and FEM computational framework for the analysis of a human head. The developed software allows to read the discrete models

built in the imaging software MIMICS© [30,31]. In this work, the RPIM is compared with the triangular finite element and with the tetrahedron finite element formulations, because these two elements types are the most commonly used finite elements for 2D and 3D analyses, respectively.

2. Methodology

In this section, it is presented the methodology used in the study. Then, it was performed a convergence study in order to understand the convergence rate of the proposed technique and to obtain the suitable mesh size that allows to perform robust analyses. In addition, this convergence study permitted to compare the FEM and RPIM performances. Afterwards, a 2D analysis and a 3D analysis of the TBI was performed. Thus, in order to compare the FEM and RPIM solutions, it was used a technique inspired in the Gruen zones, a common technique that allows to evaluate the stress shielding in the femoral bone. In Gruen zone analysis the femur bone is divided in medial and lateral patches and an average stress values for each patch is calculated [32].

The RPIM is an interpolator meshless method that uses the concept of influence-domain to force the nodal connectivity. Recall that the FEM discretizes the problem-domain using nodes and elements, and the finite element concept assures the nodal connectivity: nodes belonging to the same element interact directly between each other and with the boundary nodes of neighbour elements. In opposition, an influence-domain consists in a set of neighbour nodes surrounding an interest point (commonly an integration point). Generally, these nodes are found by radial search [14]. Overlapping the influence-domain of each node allows to obtain the nodal connectivity [14,15,33–36]. This is a simple concept used by several meshless techniques [14]. The use of local influence-domains, instead of global influence-domains, allows to generate sparse and banded stiffness matrices, more adequate to complex geometry problems. As already mentioned, a meshless method requires the construction of a background grid of integration points. The weak formulation uses a variational principle (the Galerkin weak form) to determine the system of equations and to minimize the residual weight of the integro-differential equations ruling the studied physical phenomenon. In order to obtain the integral of the residual weight of the differential equations it is necessary to select an integration scheme. In meshless methods, generally, the integration points are obtained using a background

grid, in which each grid-cell is filled with integration points via the Gauss-Legendre quadrature rule [14]. RPIM shape functions are obtained using the Radial Point Interpolators (RPI), that combine radial basis functions with polynomial basis functions, where the support-domain, a small set of field nodes in the vicinity of the interest point, is coincident with the influence-domain [14].

However, previous works have shown that the polynomial basis of the RPI is unnecessary if shape parameters of the RBF are chosen carefully [14]. This is an important innovation since it increases the computational efficiency of these methods. So, considering the function $h(\mathbf{x}_I)$ defined in the domain $\Omega \subset \mathbb{R}^2$, the value of function $h(\mathbf{x}_I)$ at the point of interest \mathbf{x}_I is defined by,

$$h(\mathbf{x}_I) = \sum_{i=1}^n R_i(\mathbf{x}_I) \cdot a_i(\mathbf{x}_I) = \mathbf{R}(\mathbf{x}_I) \cdot \mathbf{a}(\mathbf{x}_I) \quad (1)$$

where $R_i(\mathbf{x}_I)$ is the RBF, n is the number of nodes in the influence-cell of \mathbf{x}_I . The coefficients $a_i(\mathbf{x}_I)$ and $b_j(\mathbf{x}_I)$ are the non-constant coefficients of $R_i(\mathbf{x}_I)$ and $p_j(\mathbf{x}_I)$, respectively. The monomials of the polynomial basis are defined by $p_j(\mathbf{x}_I)$ and m is the basis monomial number. The variable r_{ij} is the distance between the relevant node $\mathbf{x}_i = \{x_i, y_i\}^T$ and the neighbor node $\mathbf{x}_j = \{x_j, y_j\}^T$, $r_{ij} = \sqrt{(x_j - x_i)^2 + (y_j - y_i)^2}$. Several known RBFs are well studied and developed in [14]. This work uses the Multiquadric (MQ) function $R(r_{ij}) = (r_{ij}^2 + c^2)^p$, where c and p are two parameters that need to be optimized, since they affect the performance of the RBFs.

Notice that each integration weight should possess its own c parameter. Thus, for integration point I with an integration weight $\hat{\omega}_I$, the shape parameter c is obtained with: $c_I \cong \gamma \hat{\omega}_I$. This spatial dependence of the RBF's shape parameter is demonstrated in research works available in the literature [14]. Previous works on the NNRPIM found that parameter γ should be close to zero, $\gamma \cong 0$, and p should be close to one, $p \cong 1$ [14]. However, these values cannot be $\gamma = 0$ and $p = 1$. The use of the exact integer value for p leads to a singular moment matrix and assuming a null γ leads to singular moment matrix. Furthermore, previous works [14] have shown that values of p very close to the unit allow to obtain the most accurate solutions (regardless the analysed problem). Thus,

the authors have decided to use $p = 1.0001$ or $p = 0.9999$. Additionally, as shown in [14], the parameter γ should be very close to zero, because as its value grows, the RPI shape functions lose its interpolation properties. Thus, the authors have selected $\gamma = 0.0001$ in order to “maximize” the RPI interpolation properties.

Commonly, the polynomial basis has to possess a low degree to guarantee that the interpolation matrix of RBF is invertible. Thus, in this work the constant polynomial basis is used: $\mathbf{p}^T(\mathbf{x}) = \{1\}$; $m = 1$. The polynomial basis has to satisfy an extra requirement in order to obtain an unique solution [14],

$$\sum_{i=1}^n p_j(\mathbf{x}_i) a_i(\mathbf{x}_i) = 0, \quad j = 1, 2, \dots, m \quad (2)$$

in which n represents the number of nodes inside the influence-cell of interest point \mathbf{x}_I . Therefore, applying Eq.(1) and Eq.(2) to every node forming the influence-cell of interest point \mathbf{x}_I , a new equation system can be written,

$$\begin{Bmatrix} \mathbf{u}_s \\ 0 \end{Bmatrix} = \begin{bmatrix} \mathbf{R}_Q & \mathbf{P}_m \\ \mathbf{P}_m^T & 0 \end{bmatrix} \begin{Bmatrix} \mathbf{a} \\ \mathbf{b} \end{Bmatrix} = \mathbf{G} \begin{Bmatrix} \mathbf{a} \\ \mathbf{b} \end{Bmatrix} \quad (3)$$

where \mathbf{u}_s are the variable values at the nodes inside the influence-cell of interest point \mathbf{x}_I . It must be noted that the geometric matrix \mathbf{G} is a symmetric matrix because the distance is directional independent, i.e., $R(r_{ij}) = R(r_{ji})$. By solving Eq.(3) and substituting its solution into Eq. (1), the shape function $\boldsymbol{\varphi}(\mathbf{x}_I)$ is obtained,

$$\begin{aligned} \{\boldsymbol{\varphi}(\mathbf{x}_I), \boldsymbol{\psi}(\mathbf{x}_I)\} &= \{\mathbf{R}^T(\mathbf{x}_I), \mathbf{p}^T(\mathbf{x}_I)\} \mathbf{G}^{-1} \\ &= \{\{\varphi_1(\mathbf{x}_1), \varphi_2(\mathbf{x}_2), \dots, \varphi_n(\mathbf{x}_1)\}, \{\psi_1(\mathbf{x}_1), \psi_2(\mathbf{x}_2), \dots, \psi_m(\mathbf{x}_1)\}\} \end{aligned} \quad (4)$$

Notice, that the shape function $\boldsymbol{\varphi}(\mathbf{x}_I)$ is only formed by the first n terms, $\{\varphi_1(\mathbf{x}_1), \varphi_2(\mathbf{x}_2), \dots, \varphi_n(\mathbf{x}_1)\}$. The last m terms $\{\psi_1(\mathbf{x}_1), \psi_2(\mathbf{x}_2), \dots, \psi_m(\mathbf{x}_1)\}$ are not included in the shape function vector because they are a by-product of Eq.(4), with no relevant physical meaning associated.

In order to obtain the equilibrium equations, the principle of virtual work is applied,

$$\int_{\Omega} \delta \boldsymbol{\varepsilon}^T \boldsymbol{\sigma} d\Omega + \int_{\Omega} \delta \mathbf{u}^T \mathbf{b} d\Omega - \int_{\Gamma_t} \delta \mathbf{u}^T \mathbf{t} d\Gamma = 0 \quad (5)$$

Where \mathbf{u} is the displacement field, \mathbf{b} is the body force vector and \mathbf{t} the traction on the natural boundary, Γ_t . The strain vector $\boldsymbol{\varepsilon}$ is defined as $= \mathbf{L} \mathbf{u}$, where \mathbf{L} is the differential operator defined as:

$$\mathbf{L} = \begin{bmatrix} \frac{\partial}{\partial x} & 0 \\ 0 & \frac{\partial}{\partial y} \\ \frac{\partial}{\partial y} & \frac{\partial}{\partial x} \end{bmatrix} \quad (6)$$

The linear constitutive relations are given with $= \mathbf{c} \boldsymbol{\varepsilon}$. Being $\boldsymbol{\sigma}$ the stress tensor and \mathbf{c} the material matrix defined as

$$\mathbf{c} = \mu_1 \begin{bmatrix} 1 & \nu & 0 \\ \nu & 1 & 0 \\ 0 & 0 & \mu_2 \end{bmatrix} \quad (7)$$

being $\mu_1 = E/(1 - \nu^2)$ and $\mu_2 = E/(2 + 2\nu)$, where E is the Young's modulus and ν is the Poisson's ratio. In general, the first term of Eq. (9) can be presented as

$$\int_{\Omega} \delta \boldsymbol{\varepsilon}^T \boldsymbol{\sigma} d\Omega = \delta \mathbf{u} \left[\int_{\Omega} \mathbf{B}^T \mathbf{c} \mathbf{B} d\Omega \right] \mathbf{u} = \delta \mathbf{u} \left[\int_{\Omega} \mathbf{B}^T \mathbf{c} \mathbf{B} d\Omega \right] \quad (8)$$

where \mathbf{B} is the deformation matrix,

$$\mathbf{B}(\mathbf{x}_I)_i^T = \begin{bmatrix} \frac{\partial \varphi_i}{\partial x} & 0 & \frac{\partial \varphi_i}{\partial y} \\ 0 & \frac{\partial \varphi_i}{\partial y} & \frac{\partial \varphi_i}{\partial x} \end{bmatrix} \quad (9)$$

The force vectors are defined by developing the second and third terms of Eq. (9),

$$\mathbf{F}_t = \int_{\Gamma_t} \mathbf{H}^T \mathbf{t} d\Gamma_t \quad \text{and} \quad \mathbf{F}_b = \int_{\Omega} \mathbf{H}^T \mathbf{b} d\Omega \quad (10)$$

Matrix \mathbf{H} is an interpolation matrix, $\mathbf{H}_I = \boldsymbol{\varphi}(\mathbf{x}_I)\mathbf{I}$, being \mathbf{I} the identity matrix with size 2×2 for 2D formulations and 3×3 for 3D formulations. Thus, the stiffness matrix can be defined as: $\mathbf{K} = \int_{\Omega} \mathbf{B}^T \mathbf{c} \mathbf{B} d\Omega$. Both vectors can be combined, $\mathbf{F} = \mathbf{F}_t + \mathbf{F}_b$. The essential boundary conditions can be directly imposed in the mass matrix and in the stiffness matrix as in the FEM, since the RPIM interpolation function possesses the delta Kronecker property. Thus, the equilibrium equations governing the linear dynamic response, neglecting the damping effect, can be represented in the matrix form $\mathbf{K}\mathbf{U} = \mathbf{F}$.

The mechanical properties used in this work are linear elastic properties, since the main focus of the study is to evaluate the performance of the FEM and RPIM formulations. However, other more complex and realistic material models that characterizes the brain and skull could be considered, such as viscoelastic and hyperelastic material models assuming large-strains [37–46]. These models would allow to obtain more accurate strain fields, expectedly higher than the ones obtained with linear elasticity, and a structural response depending on time. Nevertheless, these non-linear analyses (assuming large deformations and hyperelastic or viscoelastic models) possess a much higher computational cost than the small-strains linear analysis. Additionally, in this study, it was considered a quasi-static analysis. The main aim of this work is to show the potentialities of a new numerical technique (the RPIM meshless method), combined with imaging techniques, in the structural simulation of the brain. Thus, the authors have selected from the literature a reproducible case, such as an impact study. From the impact study it was possible to obtain the peak acceleration occurring during a head impact. Thus, with the peak acceleration it is possible to perform a quasi-static study, which in the authors' opinion is enough to show the potentialities of the RPIM.

2.1 Convergence

In order to understand the refinement level that has to be achieved and, additionally, to demonstrate the differences between the FEM and the meshless methods, a convergence study was performed. It was also performed a cross-validation study in which the solution obtained with the software developed by the authors is compared with the solution of a well-known and widely used commercial FEM software: ABAQUS.

A regular parallelepiped with $L \times D \times H \text{ mm}^3$ was considered for this study, as **Figure 1** shows. The dimensions L and D (the dimensions along Ox and y , respectively) are defined as: $L = 10\text{mm}$ and $D = 10\text{mm}$. The dimension H represents the thickness of the parallelepiped (dimensions along direction Oz). In order to maintain a uniform nodal discretization, the number of division along the thickness of the 3D model (direction Oz) is always 2 (corresponding to 3 nodes along direction Oz) and the model thickness varies.

Thus, the solid is discretized with four regular nodal distributions of $m \times m \times 3$ nodes, in which four values for m were considered: $m = \{5, 9, 17, 33\}$, leading to four nodal distributions with $\{75, 243, 867, 3267\}$ nodes respectively, each one with its own thickness $H = \{5, 2.5, 1.25, 0.625\}$ and h parameter $h = \{0.25, 0.125, 0.0625, 0.03125\}$. In this work, the discretization level is indicated by a h parameter, which is obtained with the expression: $h = (\min(h_i)) / (\max(L, D, H)), \forall \{i, j\} \in \mathbb{N}: \{i, j\} \leq N \wedge i \neq j$, being N the number of node discretizing the problem domain and (L, D, H) are the maximum dimension of the domain along Ox , Oy and Oz , respectively. As the expression indicates, sparse meshes present high values for h and refined meshes present low values for h . Thus, as **Figure 1** shows, with the mentioned discretization it is possible to discretize the solid domain using evenly distributed nodes (in the 3 dimensional directions Ox , Oy and Oz).

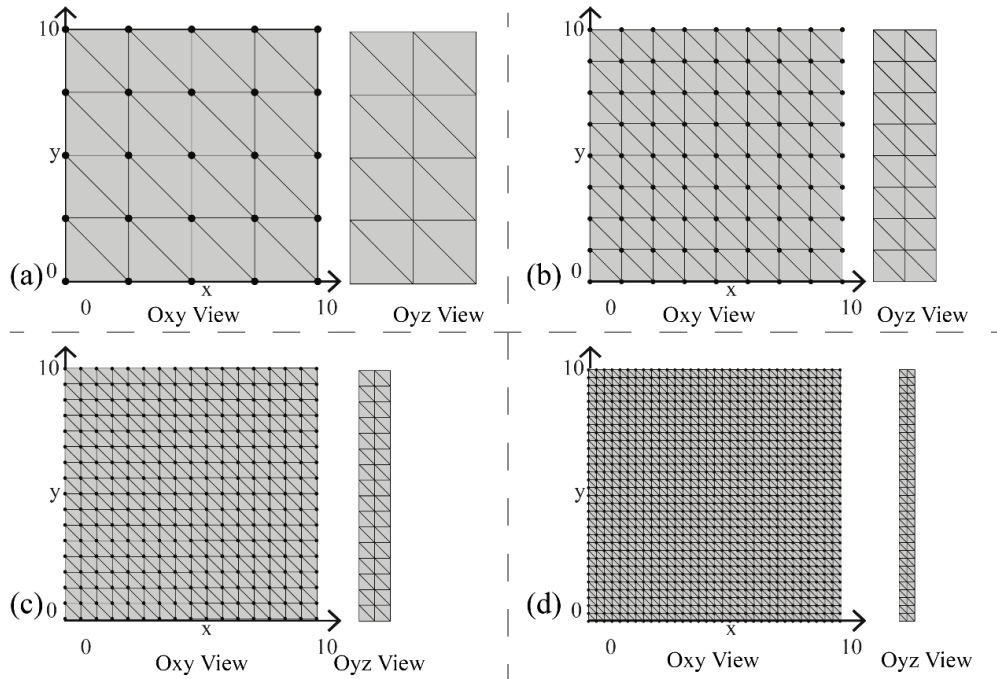


Figure 1. Created geometrical models to be used in the convergence study, using meshless and FEM method, using ABAQUS and the developed software.

In order to clarify the dimensions, the geometric features of each model presented in **Figure 1** are shown in **Table 1**. It is notorious that the number of elements and nodes increases as the number of divisions of the models increases.

Model	(a)	(b)	(c)	(d)
Dimensions	10 x 10 x 5	10 x 10 x 2.5	10 x 10 x 1.25	10 x 10 x 0.625
Sides Divisions	4 x 4x 2	8x8x2	16x16x2	32x32x2
Number of nodes	94	286	991	3590
Number of elements	307	1029	3824	14284

Table 1 - Geometrical features of each model analysed (a,b,c,d)

Regarding the essential boundary conditions, all nodes with $y = 0$ possess a constrain displacement: $\bar{u} = 0 \wedge \bar{v} = 0 \wedge \bar{w} = 0$. Notice that $\{u, v, w\}$ are the displacement along the axis directions Ox, Oy and Oz, respectively. An example of the natural boundary conditions applied to the models is represented in **Figure 2**. For the convergence models, in the surface boundary $y = 10\text{mm}$ it was applied a shear uniform distributed pressure of 1N/mm^2 .

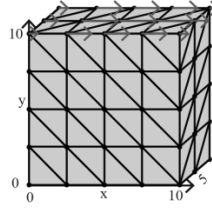


Figure 2. Example of the natural boundary conditions applied to models, in this case for model (a).

In this convergence study, the material of the model is assumed isotropic and homogeneous, possessing the mechanical properties indicated in **Table 2**.

Young's modulus [E]	1000 MPa
Poisson's ratio [ν]	0.3

Table 2 – Mechanical proprieties of the material

2.2 Traumatic Brain Injuries Analysis

In this work, the TBI was analysed using two distinct approaches, a 2D analysis and a 3D analysis. The 2D analysis assumes the plane strain linear elastic formulation with small strains. The 3D analysis assumes the classical 3D deformation theory with small strains. The 2D geometrical model of the human head was obtained from anonymized medical images, providing a highly detailed and accurate geometry. Two distinct 3D models were constructed. One was obtained by extrusion of the 2D model, allowing to obtain a 3D slice model by means of an extrusion of 16mm from the 2D model. The other 3D model was obtained from anonymized medical images, and it represents half of a brain.

The mechanical proprieties considered in this work were gathered from the literature [7,47]. Regarding the boundary conditions, the skull bone was fixed, and an acceleration was applied to all nodes of the model.

2.2.1 2D model

Firstly, it was created a 2D model possessing the skull bone, the cerebrospinal fluid (CSF), and the brain (with grey and white matter division). This model represents a slice of the brain in a medial sagittal plane. This 2D model was created using MIMICS© software, which allows to easily perform the segmentation of the zones of interest,

according to the MRI different grey values. Notice that the distinct grey zones represent different anatomical zones. This procedure permits to create a realistic model [30,31].

The domain was initially discretized using triangular elements, since the element mesh can be used for both FEM (assuming the standard 3-node constant strain triangular element) and meshless analysis (the meshless analysis neglects the element and only assumes the nodes). The final 2D model possessed 3165 triangular elements with a total of 1653 nodes. since in the 2D plane strain analysis each node possesses two degrees of freedom, this 2D model possesses a total of 3306 degrees-of-freedom. The 2D model has a parameter $h=0.0222$. As already mentioned, the h parameter permits to understand the level of the discretization and to make an inform decision regarding the necessity to increase or to reduce the level of discretization, allowing to optimize the discretization process. Unfortunately, most of the FEM analysis available in the literature do not take into account such parameter.

In this study, accordingly to each anatomical zone, four distinct mechanical proprieties were assumed. To simplify the model and the analysis, since CSF is a fluid, its mechanical proprieties were replaced by the meninges mechanical proprieties, more specifically from the dura mater. The used mechanical proprieties obtained from the literature are represented in **Table 3** [7,47].

Anatomical Region	Density [Kg/m ³]	Young's Modulus [MPa]	Poisson's Ratio
Bone	1210	8000	0,22
Grey Matter	1040	34	0,45
White Matter	1040	41	0,45
CSF	1130	12	0,45

Table 3. Model mechanical properties

In this study, the nodes belonging to the skull were constrained in both directions: $\bar{u} = 0 \wedge \bar{v} = 0$, as represented in **Figure 3-A-1**. Additionally, it was applied to all the nodes of the model an acceleration of 2000m/s^2 along direction Oy , corresponding to the peak head acceleration occurring during sudden impact, as [7] recommends,. The acceleration value and the direction of the impact is documented in the literature [7,12]. Notice that the work developed by Yang et al. [7], deals with a general problem of a head impact, in which the peak impact occurs with a total acceleration of 2000m/s^2 . Thus, the authors have decided to use this acceleration peak as a typical acceleration occurring in a standard impact case.

The acceleration was applied to all model nodes, assuming that in the instant before the impact, every part of the domain possesses the same acceleration. The impact is simulated by constraining all degrees of freedom of the skull. This way, the free nodes (brain and cerebrospinal fluid) will be compressed against the rigid skull.

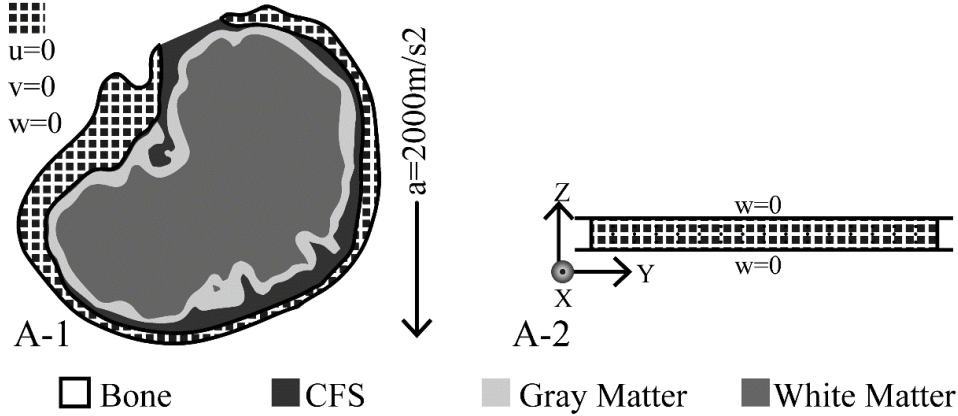


Figure 3. A-1: 2D model with $u=0 \wedge v=0$ constraints in the skull and with an acceleration with y component of 2000m/s^2 [7]; A-2 Symmetry condition applied to the top and bottom slice of the 3D model, for $z = 0 \wedge z = 16$: $w = 0$;

As already mentioned, since the 2D model has a much smaller thickness than its dimension along Ox or Oy and the displacement (and the deformation) along the Oz directions is null, due to a physical imposition, the plane strain formulation was assumed.

2.2.2 3D model

In this work, as mentioned before, the two 3D models were obtained by two distinct processes. One of the 3D models was obtained by extrusion of the 2D model along the Oz direction, creating a 3D slice with 16mm and 5 nodes distributed along the thickness. The other 3D model was constructed using anonymized medical images, which allowed to create an half brain 3D model.

Nevertheless, despite having the complete 3D brain model, due to hardware limitations, the authors decided to analyse the 3D slice and a half brain geometrical model. This approach allows a higher control in the mesh generation and the construction of a 3D model more suitable to be compared with the 2D model. From **Figure 3-A-2**, it is possible to understand how the 3D slice model was obtained. Since the 3D slice model was obtained by extrusion of a triangular mesh of a 2D model, the created 3D triangular prism elements (linear finite elements with 6 nodes) from the linear extrusion were then divided

each one in three tetrahedral elements (linear tetrahedral finite element with 4 nodes). In the end, the final 3D slice model possess 12660 elements, 8265 nodes and, consequently, 24795 degrees-of-freedom. The obtained 3D slice model has a h parameter $h=0.0221$. The mechanical properties of the several materials considered in the analysis are described in **Table 3**.

Additionally, the 3D slice model is constrained in the orthogonal directions of the plane of the slices, the direction O_z , not allowing displacement or strains in that direction ($\varepsilon_{zz} = 0, \gamma_{zx} = 0, \gamma_{zy} = 0$). This condition is in accordance with the plain strain assumptions considered in the 2D model. Thus, both the 2D model and the 3D slice model can be directly compared.

For the half brain model, for each biological structure the material mechanical properties (already mentioned in **Table 3**) were once again considered. Additionally, the number of nodes and the number of elements of the half brain model are the ones present in **Table 4**, corresponding to 29370 degrees-of-freedom. The half brain model geometry is presented in **Figure 4**.

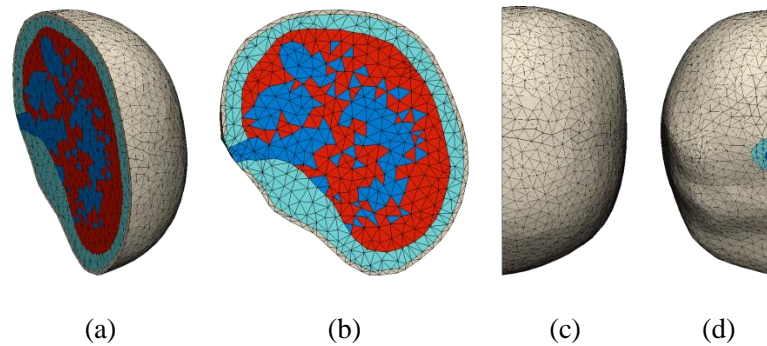


Figure 4. Image of the half brain 3D model with different views: (a) - isometric; (b) – side; (c) – front (d) – back.

	Nodes	Elements
Full Model	9790	56005
Skull	3937	11721
White Matter	3684	6806
Grey Matter	4796	20185
CSF	4987	17293

Table 4 - Geometrical characteristics of the 3D brain model.

The boundary conditions of the 3D slice model (as **Figure 3-A-1** shows) are the following: in the top and bottom plane ($z = 0 \wedge z = 16$), the nodes were fixed along Oz direction ($\bar{w} = 0$), in order to create a symmetry plane, **Figure 3-A-2**. Once again, the skull was completely constrained, $\{\bar{u}, \bar{v}, \bar{w}\} = \{0,0,0\}$. In order to simulate the peak force, an acceleration of 2000m/s^2 along direction Oy was assumed, **Figure 3-B**, as documented in the literature [7,12], and as previous explain in the 2D analysis

For the half brain 3D model, in order to enforce the symmetry of the model, it was assumed that all nodes belonging to the symmetry plane of the head model (plane Oxy with $z= 0$) are fixed along the Oz direction($\bar{w} = 0$). In addition, all the nodes belonging to the skull surface were fixed in the three directions: Ox, Oy and Oz ($\{\bar{u}, \bar{v}, \bar{w}\} = \{0,0,0\}$).

3. Results

In this section, the results for the convergence study are presented for both 2D and 3D analyses, using RPIM and FEM. Additionally, 2D and 3D analyses of brain models are performed and the obtained RPIM and FEM results are compared. Notice that, despite the brain models distinguishes the brain, the CSF and the skull bone domains, in this section only the results regarding the brain domain are evaluated and shown.

3.1 Convergence Results

Concerning the convergence study, the four models, (a), (b), (c) and (d), shown in **Figure 1**, were analysed with the commercial software ABAQUS and with the academic software fully developed by the authors. In ABAQUS, the 3D models were analysed using linear strain tetrahedral elements, ABAQUS FEM, and in the academic software the 3D models were analysed using the same kind of linear element, linear strain tetrahedral elements, FEMAS FEM, and also for the RPIM formulation, FEMAS RPIM. In each analysis, the displacement at node $\mathbf{x}_i = \{10,10,0\}^T$ along direction Ox is acquired. The obtained results are shown in **Figure 5**. Thus, in **Figure 5**, the Y-axis contains the obtained displacement in Ox direction and the X-axis contains the variable h , which represents the average nodal distance of the model.

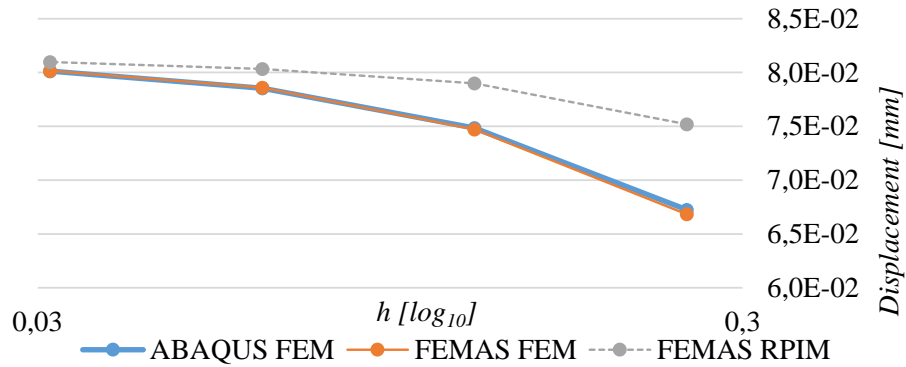


Figure 5. B: Convergence results for the (a), (b), (c) and (d) 3D model. Displacement value at node $x_i = \{10, 10, 0\}^T$. The x axis in Log_{10} scale.

Notice that the solutions ABAQUS FEM and FEMAS FEM are almost coincident, validating the FEM formulation implemented in the academic software.

Regarding the results from the meshless formulation, as expected, the obtained results are significantly different. As is shown in **Figure 5**, the meshless formulation converges much faster than the FEM solution

In order to perform a comparative study regarding the computational cost, the computational time of each analysis was documented. Thus, in **Figure 6**, it is possible to visualize the time necessary to perform the analysis of each model. Surprisingly, the meshless formulation shows a computational time very similar with the FEM. In the less discretize models, models (a) and (b), the obtained computational cost is not representative of the true analysis cost. The analysis is very fast, and the majority of the computational cost is due to intrinsic MATLAB functions, such as opening and closing results figures.

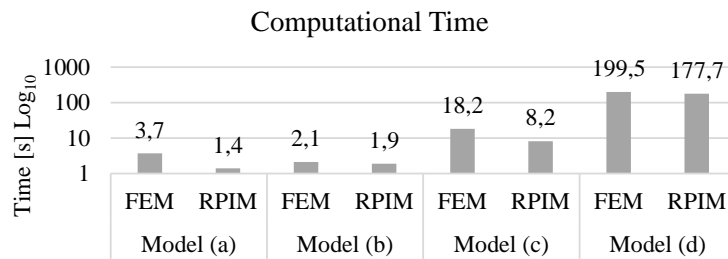


Figure 6. Computational time for the convergence models (a), (b), (c) and (d), used in the convergence study.

3.2 2D Brain Model Results

In order to perform a comparative analysis of the stress field in the brain tissue, a division of the brain domain in standardized layers was performed, a technique inspired in the Gruen zones [32]. Thus, a geometrical division of the brain domain was performed, in which 6 sections were assumed, all with the same height and orthogonal to the imposed acceleration, as represented in **Figure 7-A** and **Figure 7-B**. In **Figure 7-A** is represented the average von Mises effective stress for each section, and in **Figure 7-B** the average principal stress σ_{11} for each section.

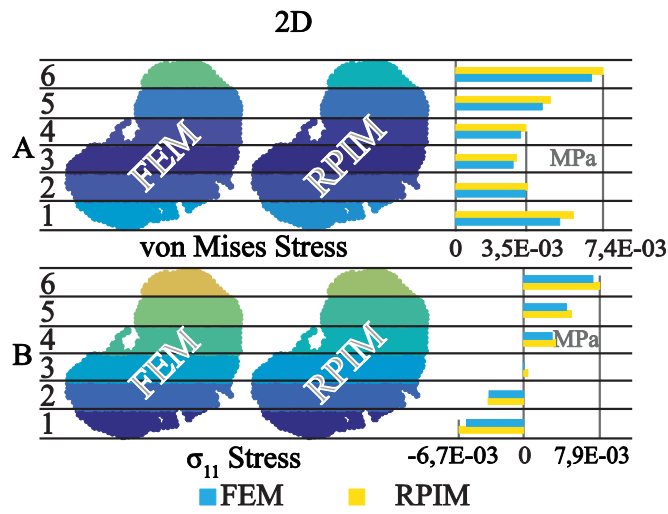


Figure 7. A: Average von Mises stresses in the 2D sections and representative column graphic for FEM and RPIM [MPa]; B: Average σ_{11} stress in the 2D sections and representative column graphic for FEM and RPIM [MPa].

The results obtained with the RPIM and the FEM are similar, as demonstrated in **Figure 7-A** and **Figure 7-B**. From **Figure 8** and **Figure 7-B**, where are represented the σ_{11} average values for each section, it can be found that RPIM, compared with FEM, has a difference of 10%, except in the fourth section where this difference is higher. The average value of the principal stresses σ_{11} is relevant, since it will indicate the higher compressive and traction zones.

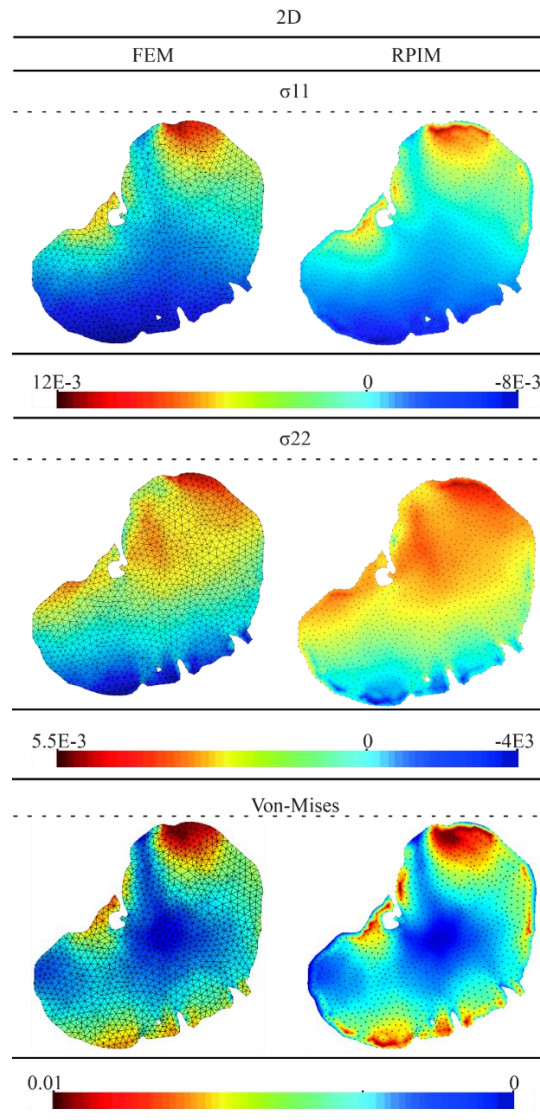


Figure 8. Principals stress field, σ_{11} and σ_{22} , and Von Mises stress field for 2D FEM and RPIM [MPa].

As expected, the average stress values in each section, show that the higher values can be found in the proximal and distal impact zones.

In **Figure 8** are represented the σ_{11} and σ_{22} , principal stresses and the von Mises effective stress. The σ_{11} stress map shows that in the impact proximal zone are mostly found compressive stress, as the σ_{11} is negative. In the distal impact zone, having σ_{11} positive values, it is possible to find mostly traction stresses. It is notorious, that the values of the σ_{11} are higher than the σ_{22} in both RPIM and FEM, as it what was expected since the impact force was applied along the Oy -axis direction. Concerning the RPIM results, it is

relevant to mention that some images show an abrupt variation of the stress value at the surroundings of the boundary. This phenomenon occurs due to the influence-domain concept. In FEM, each element is associated with a material (for example, bone, grey matter, white matter, etc.). Thus, since the integration points (in which the strains and stresses are evaluated) are built within each element, the integration point inherit the material of their parent-element. Additionally, in FEM, the interpolation is made for each element. Thus, the shape functions and respective partial derivatives are constructed for each integration point using the nodes forming the parent-element of the integration point. Thus, an integration point inside element 'j' (representing the material 'k') constructs the shape functions and its partial derivatives using the nodes of element 'j' (all nodes represent also material 'k').

In opposition, in meshless methods, there are no elements. Thus, in the model construction phase, to each node it will be associated a material (depending on its geometric position) and to each integration point will be associated also a material (depending on its geometric position). Due to the influence-domain concept, an integration point will search for 'n' nodes within its vicinity. Those nodes will form the influence-domain of that integration point. Notice now that an integration point representing material 'k', can possess inside its influence-domain nodes that are so distant that represent other materials. Thus, in meshless methods, an integration point (representing a material 'k') constructs the shape functions and its partial derivatives using, possibly, the nodes representing other materials than 'k'.

When the number of nodes is very large, this effect is desirable and produce smooth variations on the stress gradient. However, when the number of nodes is reduced, it causes abrupt material variations (such as the ones found near the boundary) and the approximation can be less smooth on those locations.

In **Figure 9** is represented the hydrostatic pressures for the 2D model, for the used numerical method, FEM and RPIM. As can be seen in **Figure 9**, in the impact proximal zone have the hydrostatic pressure presents negative values, caused by compression, and in the distal zone the hydrostatic pressure has positive values caused by the traction.

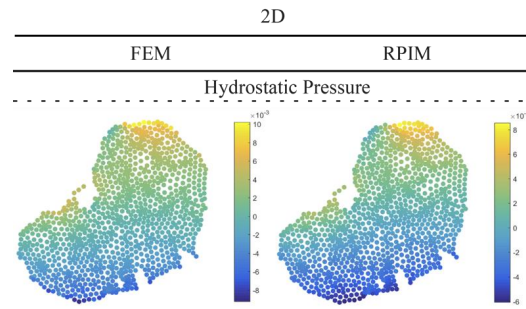


Figure 9. Hydrostatic Pressure field, for the 2D FEM and RPIM [MPa].

3.3 3D slice Brain Model

As in the 2D analysis, a Gruen division of the 3D domain of the brain was performed. In **Figure 10-A** are represented the average values of von Mises effective stress for each section, and in **Figure 10-B** are represented the σ_{11} average stress values also for each section.

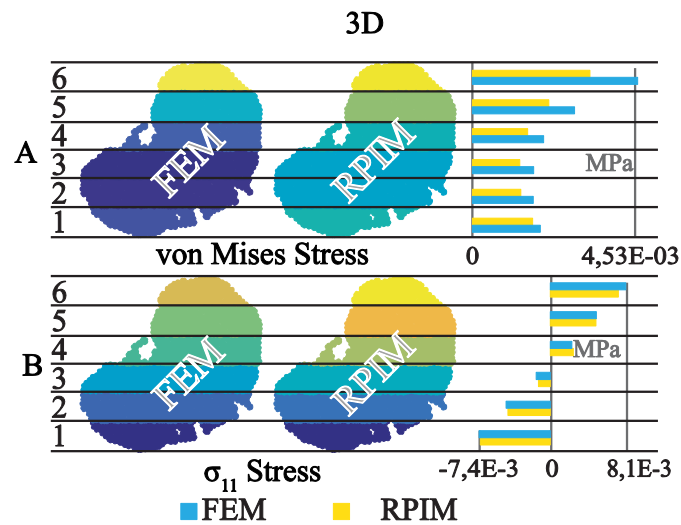


Figure 10. A: Average von Mises stress obtained in each 3D section and corresponding column graphic for FEM and RPIM [MPa]; B: Average σ_{11} stress in each 3D section and corresponding column graphic for FEM and RPIM [MPa].

Once again, the behaviour of RPIM and the FEM is similar, as shown in **Figure 10-A** and by **Figure 10-B**. As **Table 5** reports, comparing the average percentage difference between the σ_{11} values in the same section, but with different numerical methods, the difference does not overcome 8%. This observation is validated with the graph in **Figure 10-B**.

Section	2D		3D	
	FEM	RPIM	FEM	RPIM
6	-5,9554E-03	-6,7273E-03	-7,6364E-03	-7,5242E-03
5	-3,6333E-03	-3,7150E-03	-4,7459E-03	-4,5347E-03
4	6,1787E-05	4,1555E-04	-1,5196E-03	-1,2892E-03
3	2,9799E-03	3,3191E-03	2,3195E-03	2,4834E-03
2	4,4886E-03	4,9600E-03	4,9504E-03	4,8925E-03
1	7,1690E-03	7,9450E-03	8,1350E-03	7,3606E-03

Table 5. Average principal stresses, σ_{11} , for 2D and 3D obtained with the FEM and RPIM models in each division [MPa].

The sections with lower von Mises effective stress or lower σ_{11} stresses are the middle ones, zones 2,3 and 4. As in the 2D, the distal zone has the higher stress values.

In **Figure 11**, relevant stress fields are presented. The results allow to sustain that the FEM values are higher than RPIM, which corroborates the results of the average stress values presented in **Figure 10-A** and **Figure 10-B**.

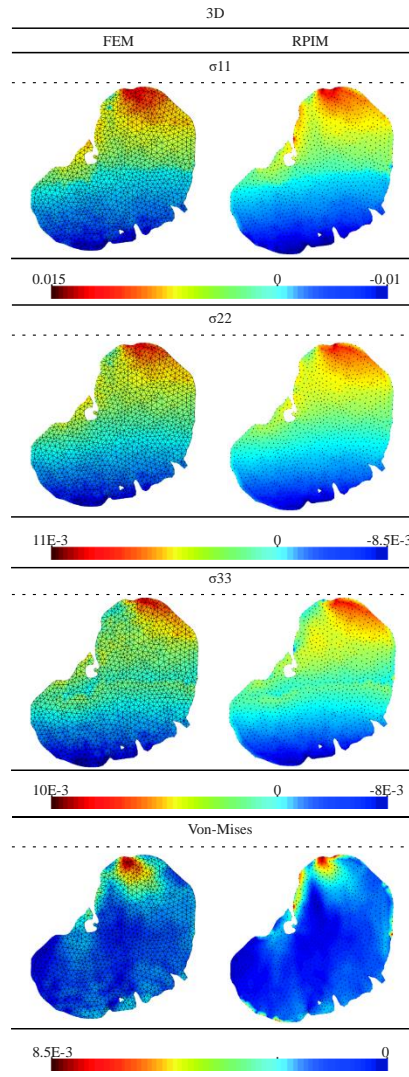


Figure 11. Principals stress field, σ_{11} , σ_{22} , and σ_{33} , and von Mises effective stress field for 3D FEM and RPIM [MPa].

3.4 3D Half Brain Model

In the created half brain 3D model, the same 6 Gruen zones were considered and their local average principal stresses σ_{11} were calculated.

For comparison purposes in **Table 6** are represented the obtained average values of σ_{11} for all the 6 zones of the 3D model obtained by extrusion of the 2D model, for both FEM and RPIM analyses. Also for comparison purposes, in **Table 7** are shown the average values of σ_{11} for the same 6 zones obtained with the 2D model, for both FEM and RPIM analyses.

3D Slice Brain Model - σ_{11}		
Section	FEM	RPIM
6	-7,6364E-03	-7,5242E-03
5	-4,7459E-03	-4,5347E-03
4	-1,5196E-03	-1,2892E-03
3	2,3195E-03	2,4834E-03
2	4,9504E-03	4,8925E-03
1	8,1350E-03	7,3606E-03

Table 6. σ_{11} obtained values for the FEM and RPIM formulation using the developed software for the different six sections, for the 3D model obtained with the extrusion of the 2D.

2D Brain Model - σ_{11}		
Section	FEM	RPIM
6	-5,9554E-03	-6,7273E-03
5	-3,6333E-03	-3,7150E-03
4	6,1787E-05	4,1555E-04
3	2,9799E-03	3,3191E-03
2	4,4886E-03	4,9600E-03
1	7,1690E-03	7,9450E-03

Table 7. σ_{11} obtained values for the FEM and RPIM formulation using the developed software for the different six sections, for the 2D model.

Concerning the half brain 3D model, in Table 8 and Table 9 are represented the average σ_{11} and σ_{22} stress values of each zone previously mentioned, respectively. In this case, the 3D model was analysed with the developed software using the FEM and RPIM methodology, and also with ABAQUS software using the linear strain tetrahedral finite elements.

3D Half Brain Model - σ_{11}			
Section	FEM	RPIM	Abaqus
6	-7,6418E-02	-7,1221E-02	-7,5084E-02
5	-4,0565E-02	-3,7638E-02	-4,1784E-02
4	-4,3978E-03	-2,7899E-03	-9,5437E-03
3	2,8753E-02	2,8861E-02	2,0582E-02
2	7,1482E-02	6,9915E-02	5,3468E-02
1	1,1675E-01	1,1704E-01	8,1727E-02

Table 8. σ_{11} obtained values for the FEM and RPIM formulation using the developed software for the different six sections, for the 2D model.

3D Half Brain Model - σ_{22}			
Section	FEM	RPIM	ABAQUS
6	-7,8270E-02	-7,6825E-02	-9,3783E-02

5	-4,4932E-02	-4,2249E-02	-5,3389E-02
4	-1,0981E-02	-9,9260E-03	-1,4131E-02
3	2,0126E-02	1,8905E-02	2,6471E-02
2	5,4800E-02	5,2332E-02	6,9180E-02
1	8,6878E-02	8,6280E-02	1,0566E-01

Table 9. σ_{22} obtained values for the FEM and RPIM formulation using the developed software, and for FEM formulation using Abaqus, for the different six sections, for the complete 3D model.

In order to allow a fair comparison with the results obtained with the 2D model and the 3D slice model, a brain slice with the same thickness of the 3D slice model, was selected from the half brain 3D model. In Figure 12, it is shown the selected slice.

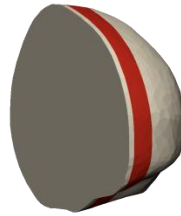


Figure 12. Used slice from the 3D model to obtain s_{11} and s_{22} results - isometric view.

As can be seen in **Table 6** to **Table 9** the results between different methodologies are very similar. Still, comparing the results of the 2D model and 3D model with the half brain 3D model, it is possible to visualize that the results are different. Nevertheless, this difference was expected.

Presently, due to the authors' hardware limitations, it is not possible to analyse a full 3D brain (or even a half brain 3D model) with a nodal mesh density comparable to the 2D brain model and to the 3D brain slice model. Nonetheless, it was built a 3D geometric model of the brain and adjacent structures with the maximum number of nodes allowed by the hardware limitations. In this 3D model it is not possible to define with detail all the structures defining the brain. For instances, this 3D sparse model does not allow to distinguish the brain white and grey matter.

With the construction and consequent analysis of the 3D half brain model, the analysis of this 3D half brain model intended to validate the implemented FEM and RPIM formulations against ABAQUS using a more complex 3D model.

The results from **Table 8** and **Table 9** show that the implemented FEM and RPIM formulations allows to obtain results very close with the ones obtained with ABAQUS.

Therefore, the difference observed between the results of **Table 6** (or **Table 7**) and **Table 8** does not have its origin in the software.

The observed difference is mainly due to the discretization level of the complete 3D model, which is not capable to accurately capture the details of the biological structures involved in the analysis. As **Figure 3** with the increase of the discretization level the solution tends to a theoretical converged solution. Unfortunately, the discretization level of the complete 3D model has not yet reached a sufficient refinement level. Thus, possibly, the obtained solution is still far from the theoretical converged solution. Nevertheless, these results are very important, since they reveal the relevance of selecting/constructing a proper finite element mesh capable of producing a solution near the theoretical converged solution.

In Figure 13 is represented the hydrostatic pressures of the 3D half brain model obtained with the FEM and RPIM formulation. The obtained FEM and RPIM values, as can be seen in Figure 13, are very similar.

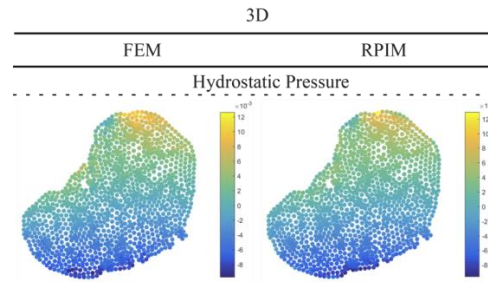


Figure 13. Hydrostatic Pressure field, for the 3D FEM and RPIM [MPa].

4. Conclusions

In this work, it was used a methodology that allowed the construction and the structural analysis of 2D and 3D brain models obtained directly from medical images. From these medical images, using the commercial software Mimics®, the mechanical properties were obtained according to the segmented anatomical zones. Using the impact acceleration found in the literature, corresponding to the head peak acceleration in case of an impact, the created models were analysed using RPIM and FEM. Furthermore, it was also performed a convergence study to compare both discretization techniques.

The presented convergence study allowed to understand the importance of the discretization level, which is vital to obtain a reliable solution. It was shown that the

quality of the discretization level can be gauged by the h parameter. This is an important issue in approximation techniques. In many cases, the discretization level in a commercial software is selected automatically and the unawareness of a proper discretization level can lead to invalid analysis. The convergence study, where the h parameter was analysed, show that RPIM has a faster converge rate than the FEM, allowing the usage of sparse meshes, still capable to provide valid results.

Being FEM a widely-used discretization method, with various commercial packages available, it has the advantage of being more evolved and optimized. FEM has the advantage of being faster when compared to meshless methods because its shape functions are simpler to compute due to its lower intrinsic connectivity. Additionally, in FEM, the triangular and tetrahedral elements are widely used due to its ability to adjust virtually to any geometry. However, as this work has shown, these elements present a weaker numerical performance when compared with the RPIM.

From the obtained stress fields, it is possible to conclude that meshless and FEM results are very similar, in magnitude and in spatial distribution. Regarding the 3D results, it is visible that the meshless method is capable to produce smoother results when compared to the FEM results.

Comparing the 2D and the 3D slice model solutions, since the acceleration was applied only in one direction, the results are comparable using the σ_{11} field. The von Mises effective stress field cannot be used to compare the 3D model with 2D, since for the 2D analysis the principal stress component σ_{33} is null ($\sigma_{33}=0$). Comparing the σ_{11} fields of the RPIM and FEM, it is perceived that the results are very similar in both discretization methods. In addition, the average values of σ_{11} in each section obtained with the RPIM are very close with the ones obtained with the FEM.

This study allowed to conclude that the RPIM is capable to produce variable fields smoother than the FEM, especially in the 3D analyses.

The methodology of dividing the brain domain in standard sections allowed to compare efficiently the RPIM and the FEM results. Additionally, this technique will permit to compare future results following a standardized system. This is also an advantage since, being the brain a region with different mechanical proprieties and different anatomical geometries, using the full model average values could lead to a wrong interpretation of

the results, but this approach allows to do a simultaneous local and overall results interpretation.

Since the authors built an original RPIM and FEM software, it is possible to understand the main differences between both numerical techniques. In biomechanics, the numerical model is constructed through imaging techniques. Since meshless methods allow to allocate the material properties directly to the nodes, using the pixel/voxel information, meshless methods are suitable techniques for biomechanics. It was also found that meshless methods also have the benefit of allowing the construction of complex geometrical models, without any special concern about the mesh geometry and element discretization created by the CAD programs. The literature shows that the most disadvantageous feature of the RPIM is the computational cost, which in 3D analyses can be 1.5 times slower than the FEM [14]. Nevertheless, in this work, the opposite was shown. The RPIM were actually faster than the FEM.

This study has several limitations. First, it was used a 3D brain model constructed from the extrusion of the 2D model, resulting in the lost the anatomical real reproduction. In addition, the created half brain 3D model was not capable to accurately capture the details of the biological structures involved in the analysis due to the discretization level, leading to the observed differences. Nevertheless, the obtained results are important to emphasise the relevance of selecting/constructing a proper finite element mesh capable of producing a solution near the theoretical converged solution. Moreover, the study was performed considering a linear elastic regime, neglecting the viscoelastic mechanical properties of the brain. Additionally, it was also used in substitution of the CSF, a fluid, a mechanical property of the dura mater with $\nu=0.45$. Furthermore, although the impact analysis demands a dynamic and transient regime, all the studies here presented were analysed assuming a quasi-static analysis.

Conflict of Interest Statement

There is not any financial and personal relationship with other people or organizations that could inappropriately influence this work.

Acknowledgments

The authors truly acknowledge the funding provided by Ministério da Ciência, Tecnologia e Ensino Superior—Fundação para a Ciência e a Tecnologia (Portugal), under Grants SFRH/BD/110047/2015 and SFRH/BPD/111020/2015, and by project funding

UID/EMS/50022/2013 (funding provided by the inter-institutional projects from LAETA). Additionally, the authors gratefully acknowledge the funding of Project NORTE-01-0145-FEDER-000022 - SciTech - Science and Technology for Competitive and Sustainable Industries, co-financed by Programa Operacional Regional do Norte (NORTE2020), through Fundo Europeu de Desenvolvimento Regional (FEDER).

References

- [1] World Health Organization. Global status report on road safety 2015. World Health Organization; n.d.
- [2] Blennow K, Hardy J, Zetterberg H. The Neuropathology and Neurobiology of Traumatic Brain Injury. *Neuron* 2012;76:886–99. <https://doi.org/10.1016/j.neuron.2012.11.021>.
- [3] Andrade AF De, Paiva WS, Amorim RLO De, Figueiredo EG, Rusafa Neto E, Teixeira MJ. Mecanismos de lesão cerebral no traumatismo cranioencefálico. *Rev Assoc Med Bras* 2009;55:75–81. <https://doi.org/10.1590/S0104-42302009000100020>.
- [4] Taylor JM, Montgomery MH, Gregory EJ, Berman NEJ. Exercise preconditioning improves traumatic brain injury outcomes. *Brain Res* 2015;1622:414–29. <https://doi.org/10.1016/j.brainres.2015.07.009>.
- [5] Summers CR, Ivins B, Schwab KA. Traumatic brain injury in the United States: An epidemiologic overview. *Mt Sinai J Med* 2009;76:105–10. <https://doi.org/10.1002/msj.20100>.
- [6] Liang Z, Luo Y. A QCT-Based Nonsegmentation Finite Element Head Model for Studying Traumatic Brain Injury. *Appl Bionics Biomech* 2015;2015:1–8. <https://doi.org/10.1155/2015/837585>.
- [7] Yang B, Tse K-M, Chen N, Tan L-B, Zheng Q-Q, Yang H-M, et al. Development of a finite element head model for the study of impact head injury. *Biomed Res Int* 2014;2014:408278. <https://doi.org/10.1155/2014/408278>.
- [8] Guilmette TJ, Paglia MF. The public's misconceptions about traumatic brain injury: a follow up survey. *Arch Clin Neuropsychol* 2004;19:183–9. [https://doi.org/10.1016/S0887-6177\(03\)00025-8](https://doi.org/10.1016/S0887-6177(03)00025-8).
- [9] Shailesh Govind G. Mechanics Of Blast Loading On Post-Mortem Human And Surrogate Heads In The Study Of Traumatic brain Injury (TBI) Using Experimental And Computational Approaches. The University of Nebraska, 2013.

- [10] Sharma S, Zhang L. Prediction of Intracranial Responses from Blast Induced Neurotrauma using a Validated Finite Element Model of Human Head. *Inj. Biomech. Symp.*, 2011.
- [11] Mao H, Zhang L, Jiang B, Genthikatti V V., Jin X, Zhu F, et al. Development of a Finite Element Human Head Model Partially Validated With Thirty Five Experimental Cases. *J Biomech Eng* 2013;135:111002. <https://doi.org/10.1115/1.4025101>.
- [12] Tse KM, Tan L Bin, Lee SJ, Lim SP, Lee HP. Development and validation of two subject-specific finite element models of human head against three cadaveric experiments. *Int j Numer Method Biomed Eng* 2014;30:397–415. <https://doi.org/10.1002/cnm.2609>.
- [13] Bar-Kochba E, M. Gutttag SS, Franck JA, McNamara K, Crisco JJ, Blume J, et al. Finite element analysis of head impact in contact sports. *SIMULIA Community Conf.*, Providence, RI, USA: SIMULIA: 2012.
- [14] Belinha J. *Meshless Methods in Biomechanics: Bone Tissue Remodelling Analysis.* vol. 2. Dordrecht: Springer Netherlands; 2014. <https://doi.org/10.1007/978-94-007-4174-4>.
- [15] Wang JG, Liu GR. A point interpolation meshless method based on radial basis functions. *Int J Numer Methods Eng* 2002;54:1623–48. <https://doi.org/10.1002/nme.489>.
- [16] Liu GR, Gu YT. A point interpolation method for two-dimensional solids. *Int J Numer Methods Eng* 2001;50:937–51. [https://doi.org/10.1002/1097-0207\(20010210\)50:4<937::AID-NME62>3.0.CO;2-X](https://doi.org/10.1002/1097-0207(20010210)50:4<937::AID-NME62>3.0.CO;2-X).
- [17] Dinis LMJSJS, Natal Jorge RM, Belinha J. Analysis of 3D solids using the natural neighbour radial point interpolation method. *Comput Methods Appl Mech Eng* 2007;196:2009–28. <https://doi.org/10.1016/j.cma.2006.11.002>.
- [18] Dinis LMJS, Natal Jorge RM, Belinha J. A natural neighbour meshless method with a 3D shell-like approach in the dynamic analysis of thin 3D structures. *Thin-Walled Struct* 2011;49:185–96. <https://doi.org/10.1016/j.tws.2010.09.023>.
- [19] Dinis LMJS, Jorge RMN, Belinha J. A 3D shell-like approach using a natural neighbour meshless method: Isotropic and orthotropic thin structures. *Compos Struct* 2010;92:1132–42. <https://doi.org/10.1016/j.compstruct.2009.10.014>.
- [20] Liu GR, Zhang GY, Wang YY, Zhong ZH, Li GY, Han X. A nodal integration technique for meshfree radial point interpolation method (NI-RPIM). *Int J Solids*

- Struct 2007;44:3840–60. <https://doi.org/10.1016/j.ijsolstr.2006.10.025>.
- [21] Zhao X, Liu GR, Dai KY, Zhong ZH, Li GY, Han X. Free-vibration analysis of shells via a linearly conforming radial point interpolation method (LC-RPIM). *Finite Elem Anal Des* 2009;45:917–24. <https://doi.org/10.1016/j.finel.2009.09.002>.
- [22] Zhao X, Liu GR, Dai KY, Zhong ZH, Li GY, Han X. A linearly conforming radial point interpolation method (LC-RPIM) for shells. *Comput Mech* 2008;43:403–13. <https://doi.org/10.1007/s00466-008-0313-z>.
- [23] Liu GR, Jiang Y, Chen L, Zhang GY, Zhang YW. A singular cell-based smoothed radial point interpolation method for fracture problems. *Comput Struct* 2011;89:1378–96. <https://doi.org/10.1016/j.compstruc.2011.03.009>.
- [24] Belinha J, Dinis LMJS, Natal Jorge RM. The natural radial element method. *Int J Numer Methods Eng* 2013;93:1286–313. <https://doi.org/10.1002/nme.4427>.
- [25] Belinha J, Dinis LMJS, Natal Jorge RM. Analysis of thick plates by the natural radial element method. *Int J Mech Sci* 2013;76:33–48. <https://doi.org/10.1016/j.ijmecsci.2013.08.011>.
- [26] Belinha J, Dinis LMJSJS, Jorge RMNN. Composite laminated plate analysis using the natural radial element method. *Compos Struct* 2013;103:50–67. <https://doi.org/10.1016/j.compstruct.2013.03.018>.
- [27] Belinha J, Araújo AL, Ferreira AJMM, Dinis LMJSJS, Natal Jorge RM. The analysis of laminated plates using distinct advanced discretization meshless techniques. *Compos Struct* 2016;143:165–79. <https://doi.org/10.1016/j.compstruct.2016.02.021>.
- [28] Farahani B V., Tavares PJ, Moreira PMGP, Belinha J. Stress intensity factor calculation through thermoelastic stress analysis, finite element and RPIM meshless method. *Eng Fract Mech* 2017;183:66–78. <https://doi.org/10.1016/j.engfracmech.2017.04.027>.
- [29] Ma J, Wei G, Liu D, Liu G. The numerical analysis of piezoelectric ceramics based on the Hermite-type RPIM. *Appl Math Comput* 2017;309:170–82. <https://doi.org/10.1016/j.amc.2017.03.045>.
- [30] Bushberg et al JT. *The essential physics of medical imaging*. Lippincott Williams & Wilkins; 2012.
- [31] Mimics® Medical Image Segmentation for Engineering on Anatomy™ n.d.
- [32] Gruen TA, McNeice GM, Amstutz HC. “Modes of failure” of cemented stem-type

- femoral components: a radiographic analysis of loosening. *Clin Orthop Relat Res* 1979;17–27.
- [33] Belytschko T, Lu YY, Gu L. Element-free Galerkin methods. *Int J Numer Methods Eng* 1994;37:229–56. <https://doi.org/10.1002/nme.1620370205>.
- [34] Liu WK, Jun S, Zhang YF. Reproducing kernel particle methods. *Int J Numer Methods Fluids* 1995;20:1081–106. <https://doi.org/10.1002/fld.1650200824>.
- [35] Atluri SN, Zhu T. A new Meshless Local Petrov-Galerkin (MLPG) approach in computational mechanics. *Comput Mech* 1998;22:117–27. <https://doi.org/10.1007/s004660050346>.
- [36] Nguyen VP, Rabczuk T, Bordas S, Duflot M. Meshless methods: A review and computer implementation aspects. *Math Comput Simul* 2008;79:763–813. <https://doi.org/10.1016/j.matcom.2008.01.003>.
- [37] Boccia E, Gizzi A, Cherubini C, Nestola MGC, Filippi S. Viscoelastic computational modeling of the human head-neck system: Eigenfrequencies and time-dependent analysis. *Int j Numer Method Biomed Eng* 2017;1–16. <https://doi.org/10.1002/cnm.2900>.
- [38] Eeg-Olofsson M, Stenfelt S, Taghavi H, Reinfeldt S, Håkansson B, Tengstrand T, et al. Transmission of bone conducted sound - Correlation between hearing perception and cochlear vibration. *Hear Res* 2013;306:11–20. <https://doi.org/10.1016/j.heares.2013.08.015>.
- [39] Nayak D, Roth TL, Mcgavern DB. *HHS Public Access* 2014;15:367–402. <https://doi.org/10.1146/annurev-immunol-032713-120240>. Microglia.
- [40] Mao H, Unnikrishnan G, Rakesh V, Reifman J. Untangling the Effect of Head Acceleration on Brain Responses to Blast Waves. *J Biomech Eng* 2015;137:124502. <https://doi.org/10.1115/1.4031765>.
- [41] Pérez-García V. Delay effects in the response of low grade gliomas. *Math Med Biol* 2015;TBA:1–26. <https://doi.org/10.1093/imammb/dqnxxx>.
- [42] Miller K, Wittek A, Joldes G. Biomechanics of the brain for computer-integrated surgery. *Acta Bioeng Biomech* 2010;12:25–37.
- [43] Ilic S, Hackl K, Gilbert R. Application of the multiscale FEM to the modeling of cancellous bone. *Biomech Model Mechanobiol* 2010;9:87–102. <https://doi.org/10.1007/s10237-009-0161-6>.
- [44] Velardi F, Fraternali F, Angelillo M. Anisotropic constitutive equations and experimental tensile behavior of brain tissue. *Biomech Model Mechanobiol*

- 2006;5:53–61. <https://doi.org/10.1007/s10237-005-0007-9>.
- [45] Ji S, Zhao W, Li Z, McAllister TW. Head impact accelerations for brain strain-related responses in contact sports: a model-based investigation. *Biomech Model Mechanobiol* 2014;13:1121–36. <https://doi.org/10.1007/s10237-014-0562-z>.
- [46] Lang GE, Vella D, Waters SL, Goriely A. Mathematical modelling of blood–brain barrier failure and oedema. *Math Med Biol* 2016;TBA:dqw009. <https://doi.org/10.1093/imammb/dqw009>.
- [47] Giordano C, Cloots RJH, van Dommelen JAW, Kleiven S. The influence of anisotropy on brain injury prediction. *J Biomech* 2014;47:1052–9. <https://doi.org/10.1016/j.jbiomech.2013.12.036>.

3.4 Homogenisation Technique

The following contributions focus on the definition of a multiscale homogenisation technique, where it was used the fabric tensor concept. The methodology was firstly explored in the 2D dimension, where the methodology was evaluated concerning its robustness upon changes in the RVE size and rotation. In these works, the FEM and the meshless methods were explored in order to validate the equivalence of the homogeneous mechanical properties obtained using the methodology with trabecular mechanical properties obtained from the literature. After the development of the 2D methodology, it was developed the 3D methodology, where the same concepts were used, but expanded to 3D.

2D Homogenisation Technique

3.5 Contribution III: A multiscale homogenisation procedure using the fabric tensor concept.

3.5.1 Highlights of Contribution: 3.5

This contribution focused on the bone mechanical properties definition using a homogenisation technique, defined by the fabric tensor concept.

Therefore, the main contents of this publication include:

- I. Literature review on multiscale homogenisation techniques;
- II. Literature review on the fabric tensor concept;
- III. Application of a homogenisation technique, defined using a morphologically based fabric tensor and a phenomenological material law method;
- IV. Validate of the homogenisation methodology using numerical tests involving size and rotation analyses;
- V. Applied a structural analysis using FEM, where it was created a metric able to compare heterogeneous and equivalent homogeneous domains.

VI. Conclusion: The methodology introduced in this contribution allowed to define the mechanical properties trabecular bone just using of a micro-CT information. As demonstrated in figure 3.4, by using the developed methodology a homogenous domain, with a less discretised mesh, is mechanically equivalent to a highly discretised heterogeneous domain. Thus, the methodology, as demonstrated in figure 3.5, provide models defined with the homogeneous domains and mechanical properties that have a lower computational cost, when compared to the equivalent heterogeneous models.

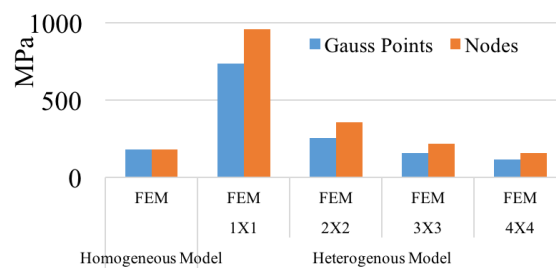


Figure 3.4: Contribution III numerical convergence comparing structural analysis using heterogeneous models and the equivalent homogeneous ,defined using the developed methodology.

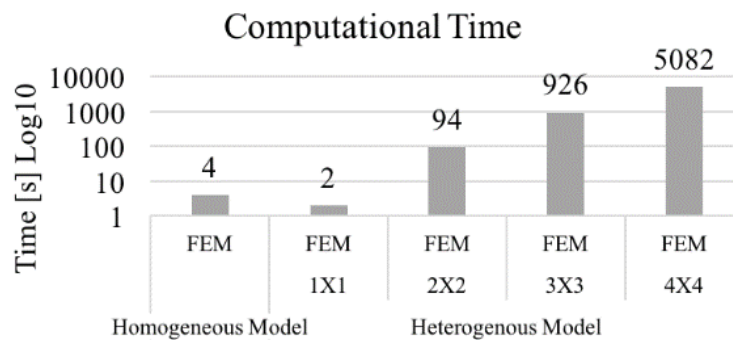


Figure 3.5: Contribution III computational time.

The complete document can be found in the next pages.

A multiscale homogenization procedure using the fabric tensor concept

Marco Marques^a, J. Belinha^{a,b*}, A.F. Oliveira^c, M.C. Manzanares Céspedes^d, Renato Natal Jorge^a

^aINEGI- Institute of Science and Innovation in Mechanical and Industrial Engineering, Porto, Portugal

^bFEUP - Faculty of Engineering of University of Porto, Porto, Portugal

^cICBAS - Institute of Biomedical Sciences Abel Salazar, Porto, Portugal

^dMuscular and Skeletal Pathology Research, Human Anatomy and Embryology Unit, Universitat de Barcelona, Barcelona, Spain

Abstract

Bone is a heterogeneous material in which structural levels can be identified, from the microscale to macroscale. Multiscale models enable to model the material using homogenization techniques. In this work, an innovative homogenization technique for trabecular bone tissue is proposed. The technique combines the fabric tensor concept and a bone phenomenological material law, linking the apparent density with the trabecular bone mechanical properties. The proposed methodology efficiently homogenizes the trabecular bone highly heterogeneous medium, allowing to define its homogenized microscale mechanical properties and to reduce the analysis computational cost (when compared with classical homogenization techniques).

In order to verify the efficiency of the technique, several examples were solved using a confined square patch of trabecular bone under compression. In the end, the results obtained with a classic homogenization technique and the proposed methodology were compared.

Keywords: Fabric Tensor; homogenization; multiscale.

1. Introduction

Bone biomechanics, one of the main biomechanics field of study, is based on the idea that load bearing bone tissues are structurally optimized for their mechanical function [1,2]. It is normal to classify bone as a hierarchical structure, where different structural levels can be identified as belonging to a macroscale or a microscale level [3]. The entire bone (macroscale) and the trabecular architecture level (microscale), can be defined by different physical properties due to its different functional requirements. At the trabecular level, microscale, it is possible to recognize the bone trabecular non-homogeneous structure, which after being homogenized allows to define local anisotropic homogeneous mechanical properties, such as apparent density and directional elastic moduli.

Bone is a tissue that renews itself by a biological process called bone remodelling [4]. This bone remodelling is progressive and induces adaptation of bone morphology to any new external stimulus. Wolff in 1886 reported that strain/stress induces bone remodelling [5]. Thus, Wolff documented that the orientation of trabecular bone coincides with the direction of the stress trajectories, proposing that external loads were, somehow, sensed by the bone. This principle is known as Wolff's law. In 1939 Wolff's law was firstly described in vitro by Glucksmann in 1939 [6] and it was described mathematically in 1965 by Pauwels et al. [7]. Later, this formulation was computationally implemented by Pettermann et al. [8]. In their bone remodelling algorithms, many authors have considered bone as an isotropic material, a simplistic approach on the behaviour of trabecular bone, disregarding the importance of orientation in the remodelling process [9–12].

Meanwhile other models were created linking material density and orientation with its anisotropic mechanical properties, allowing to overcome the material isotropy simplification. These remodelling models not only avoid any a priori assumption on material but also take into account the trabecular architecture [13–16]. More recent models start to consider biological and mechanical factors based on bone cell activity, resulting in mechanobiological models, which allow to simulate the evolution of bone tissue considering both mechanical and biological stimuli [17–20].

Bone started to be characterized mechanically using the fabric tensor concept [21,22]. The Fabric tensor is a symmetric second rank tensor that characterizes the arrangement of a multiphase material, encoding the orientation and anisotropy of the material. Back in 1985, Cowin [23] developed a relation between the elasticity tensor \mathbb{C}_{ijkl} and a fabric tensor \mathbf{A} , proving that an ellipsoid may be associated with the variation of material symmetries observed in many natural materials. The fabric tensor can be acquired by two different techniques, the mechanical based techniques and by the morphologic-based. In morphologic-based methods, the fabric tensor is estimated using the interface between phases of the material. The bone morphology is usually obtained using a micro-CT (at the microscale) or a CT (at the macroscale). Most of the available techniques, using morphologic-based methods, obtain the fabric tensor applying an orientation distribution function (ODF), which is estimated from an orientation-dependent feature of interest.

In mechanics, and in biomechanics, the accurate determination/characterization of the material's mechanical properties is a key parameter, which will allow to describe and predict numerically the behaviour of such materials for different scenarios.

Discrete numerical methods allow to study and analyse in silico the behaviour of materials and structures, being the finite element method (FEM) one of the most popular discrete numerical method [24].

2. Homogenization technique

In this section, the used homogenization technique is fully described. Firstly, 2D images (thin slices) were selected. The images correspond to the cuboid bone and describe locally the bone morphology at its microscale. Then, it was applied the fabric tensor concept in order to determine the material orientation to the selected square microscale images. Additionally, a bone tissue phenomenological law was used to obtain the homogenized material properties of the microscale patch. This homogenization allowed to define the anisotropic mechanical properties of the trabecular bone. Fig. 1 represents the algorithm describing the proposed homogenization technique.

2.1. Fabric tensor morphologic based method

By defining a relevant micro-CT slice image and then identifying a square region of interest with relevant information (the binary image represented in the left-upper image of Fig. 1), it was possible to define the morphologic based fabric tensor. This square patch, a grey scale image, was then binarized, resulting in a binary image I_s that contained the characteristic morphology of the (local) trabecular bone.

To define the fabric tensor it was used a methodology developed by Whitehouse [25], in which the number of interceptions between a parallel family line set, with direction ι , with the interface between both phases of the material were counted, $Int(\iota)$. The length of the parallel lines family, h , for the ι direction was also obtained. Knowing h and ι , it was possible to define the ODF, which in this case is called Mean Intercept Length (MIL), represented in equation (1).

$$MIL(\iota) = h/Int(\iota) \quad (1)$$

Whitehouse's methodology is considered a golden standard to predict mechanical properties of trabecular bone since exists a large amount of works that sustain its appropriateness [25–29]. The literature shows that when the ODF data is disposed on a polar plot and fitted in an ellipse, the corresponding ellipse parameters can be correlated with the material orientation (its anisotropy), in particular the trabecular bone [30].

The dimensional information of I_s was used to define the size of an image containing the family of parallel lines with $\iota = 0^\circ$. Counting the interceptions of those parallel lines with the boundaries of the binary image square patch, it was possible to obtain the orientation-dependent feature.

By rotating the family of parallel lines image with ι between 0° and 180° , and then counting the interception of the family of parallel lines with the square patch binary image I_s , it was possible to obtain the ODF of the I_s . The created data for ι between $]180^\circ, 360^\circ]$ is a $]0^\circ, 180^\circ]$ data repetition, since the orientation-dependent feature depends only on the orientation and it is not influenced by the direction.

The created ODF data was then plotted in polar coordinates, where it was fitted into an ellipse, from which it was possible to obtain the material orientation of the trabecular micropatch (see both central boxes of Fig. 1).

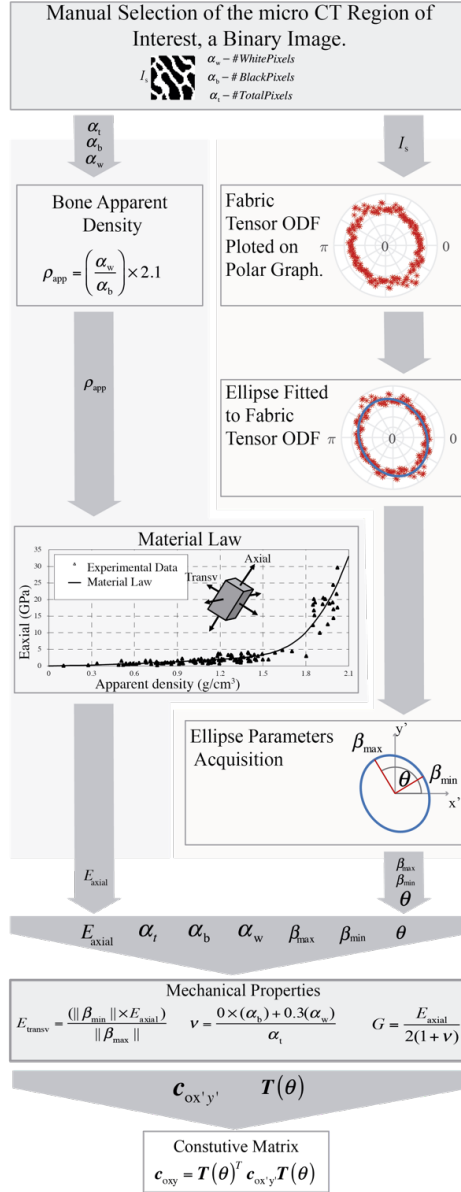


Fig. 1 - Microscale homogenization technique.

From the fitted ellipse, three parameters were extracted: the ellipse minor axis length, β_{min} ; the major axis length, β_{max} ; and the θ , the angle of ellipse major axis with the polar plot horizontal axis.

2.2. Phenomenological material law method

Using the fitted ellipse information and the average apparent density of the binary image I_s it was possible to define the homogenized anisotropic mechanical properties of I_s . Thus, first it was necessary to define the average apparent density,

ρ_{app} , of the binary image I_s . As equation 2 shows, the apparent density, ρ_{app} , was obtained using the number of white pixels, α_w and black pixels, α_b , of I_s . In this work, the cortical bone apparent density was assumed as $\rho_{app}^{cortical} = 2.1\text{g/cm}^3$

$$\rho_{app} = (\alpha_w/\alpha_b)\rho_{app}^{cortical} \quad (2)$$

Using the ρ_{app} and the phenomenological material law [31], the axial elastic modulus E_{axial} could be defined.

If $\rho_{app} \leq 1.3$, equation 3 is applied, otherwise, it should be used equation 4 [31]. Coefficients a_j and b_j can be found in Table 1

$$E_{axial} = \sum_{j=0}^3 a_j \rho_{app} \text{ if } \rho_{app} \leq 1.3 \quad (3)$$

$$E_{axial} = \sum_{j=0}^3 b_j \rho_{app} \text{ if } \rho_{app} > 1.3 \quad (4)$$

Table 1 - Coefficients for the assumed phenomenological material law [31].

	$j = 0$	$j = 1$	$j = 2$	$j = 3$
a_j	0.0E+00	7.216E+02	8.059E+02	0.0E+00
b_j	-1.770E+05	3.861E+05	-2.798E+05	6.836E+04

The transverse elastic modulus E_{transv} was defined using the relation between the ellipse minor axis length, β_{min} , and major axis length, β_{max} , and the axial elastic modulus E_{axial} as equation 5 shows.

$$E_{transv} = (\|\beta_{min}\|E_{axial})/\|\beta_{max}\| \quad (5)$$

The Poisson's coefficient, ν , was calculated according the mixture theory, using the relation between white and black pixels, as represented in equation 6, being α_t the total number of pixels of the binary image I_s .

$$\nu = (0.0\alpha_b + 0.3\alpha_w)/(\alpha_t) \quad (6)$$

The shear modulus, G , was expeditiously calculated using equation 7.

$$G = E_{axial}/(2(1 + \nu)) \quad (7)$$

As Fig. 1 shows, using the homogenized material properties (E_{axial} , E_{transv} , ν and G) the constitutive matrix was defined $\mathbf{c}_{oxy'}$, for the $ox'y'$ local coordinate system (oriented with the material principal axis, following the material principal directions 'axial' and 'transverse'). To define this matrix in global axis, it is used the angle θ obtained from the ellipse fitting, and then it is applied a rotation matrix \mathbf{T} , equation 8. Thus, it is possible to define the material constitutive matrix in global axis, \mathbf{c}_{oxy} , equation 9. Notice that $\mathbf{c} = \mathbf{s}^{-1}$, being the anisotropic compliance matrix \mathbf{s} defined by equation 10.

$$\mathbf{T}(\theta) = \begin{bmatrix} \cos(\theta) & -\sin(\theta) & 0 \\ \sin(\theta) & \cos(\theta) & 0 \\ 0 & 0 & 1 \end{bmatrix} \quad (8)$$

$$\mathbf{c}_{oxy} = \mathbf{T}(\theta)^T \mathbf{c}_{oxy'} \mathbf{T}(\theta) = \begin{bmatrix} \mathbf{c}_{11} & \mathbf{c}_{12} & \mathbf{c}_{13} \\ \mathbf{c}_{21} & \mathbf{c}_{22} & \mathbf{c}_{23} \\ \mathbf{c}_{31} & \mathbf{c}_{32} & \mathbf{c}_{33} \end{bmatrix} \quad (9)$$

$$\mathbf{s} = \begin{bmatrix} \frac{1-\nu_{zx}\nu_{xz}}{E_{xx}} & \frac{-\nu_{yz}-\nu_{zx}\nu_{yz}}{E_{yy}} & 0 \\ \frac{-\nu_{xy}-\nu_{zy}\nu_{xz}}{E_{xx}} & \frac{1-\nu_{zy}\nu_{yz}}{E_{yy}} & 0 \\ 0 & 0 & \frac{1}{G_{xy}} \end{bmatrix} \quad (10)$$

3. Numerical Examples

To validate the homogenization methodology, some numerical tests were performed involving size and rotation analyses of predefined I_s binary images.

Thus, to confirm the robustness of the proposed technique, a benchmark binary image (with a known preferential material orientation) was analysed. Then, the input image was rotated and it was verified if the fitted ellipse (from the fabric tensor based methodology) was aligned with the material orientation of the image. Furthermore, in order to verify the behaviour of the proposed homogenization technique, it was performed a structural FEM analysis using two distinct geometrical models (a homogeneous model and a heterogeneous model).

3.1. Validation of MIL methodology

The validation of the MIL methodology was assessed with two distinct studies. The first study verified the influence of the size of the representative volume element (RVE) in the determination of the anisotropic constitutive matrix. In the second study, the consistency of the methodology was tested, by imposing a known material orientations to the model.

3.1.1. RVE size

In order to understand the influence of the size of the RVE in the proposed methodology, two distinct models were constructed, figure Fig. 2a) and figure Fig. 2b). The model presented in figure Fig. 2a) is a benchmark fabricated unitary binary image showing a well-defined material orientation (90°). This model was repeated $r_n \times r_n$, being r_n the number of repetitions of the RVE. For illustration purposes, Fig. 2c) represents a 10×10 repetition.

Alternatively, the model shown in figure Fig. 2b) is a unitary binary image representing a realistic trabecular square patch obtained from a micro-CT image. Similarly to the benchmark fabricated unitary binary image, this patch was repeated $r_n \times r_n$, being the 10×10 repetition shown in figure Fig. 2d).

The propose homogenization methodology was applied to each one of the RVEs (fabricated benchmark and realistic square patch) and their several corresponding repetitions $r_n \times r_n$, being $r_n = \{1, 2, 3, \dots, 10\}$.

Following the described homogenization methodology, it was possible to obtain all the components of the constitutive tensor $\mathbf{c}_{\alpha\beta\gamma\delta}$, as can be seen in Fig. 3a), for the the realistic trabecular RVE, and in Fig. 3b) for the fabricated benchmark RVE. In both figures, it is possible to visualize the evolution of the components of the constitutive matrix, c_{ij} , with respect to the number of repetitions of the corresponding basic unit RVE. For both RVEs types (benchmark and realistic), it is perceptible that the value of each component of the constitutive matrix, c_{ij} , do not vary significantly with the number of repetitions, r_n .

Notice that for the fabricated benchmark RVE, as expected, θ does not vary significantly (the average value is 45° with a standard deviation of 0°). Similar, for the realistic trabecular RVE the number of repetitions do not relevantly change the material orientation angle of the basic unit RVE being the obtained average value: 115.7° with a standard deviation of 1.0° .

3.1.2. RVE rotation

To verify if the developed methodology was capable to deliver accurate material orientations, both, the benchmark fabricated RVE, figure Fig. 2a), and the realistic trabecular RVE, figure Fig. 2b) were rotated. The RVEs were rotated in relation to their initial position following increment angles of 20° between the interval $[0^\circ, 180^\circ]$. Fig. 4 and Fig. 5 show the results of a single analysis for the exposed case. It was possible to visualize the orientation/size of the produced ellipse and the corresponding angle of the material. In Fig. 6 are represented the material orientation angles θ of the fitted ellipse, and the expected ones for a 20° rotation. The difference between the expected orientation and the obtained material orientation θ (coming from the proposed MIL algorithm) can be explained by the change of the source image upon the rotation process, performed using a MATLAB 2016b function. This leads to the change of the number of white pixels of the image, a parameter closely related with the calculation of the fabric tensor.

4. Structural application

In this section it was verified if a homogenized RVE, with homogenized anisotropic mechanical properties obtained with proposed methodology, was capable to produce a homogenize von Mises effective stress field similar with the one obtained with a heterogeneous RVE. To evaluate the efficiency of the proposed homogenization technique, it was performed a structural analysis of the realistic trabecular RVE, figure Fig. 2b), and its $r_n \times r_n$ repetitions, and the results were compared with the ones obtained with a homogeneous RVE.

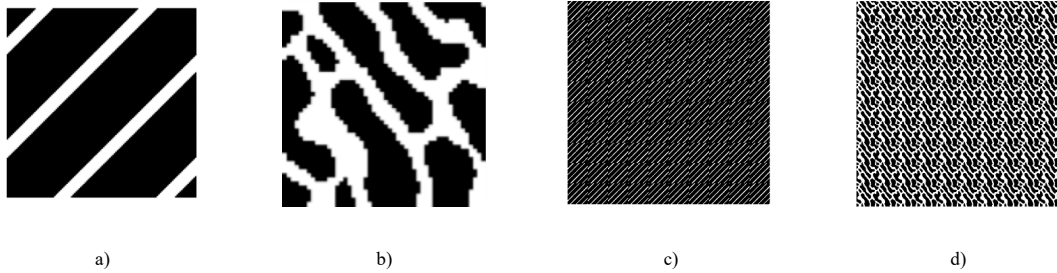


Fig. 2 - Binary images used to verify the MIL dependence on the RVE size. (a) Benchmark fabricated unitary image, (b). Realistic binary image from a micro-CT. To analyse the effect of using different RVE sizes, the binary images were repeated up to a 10×10 repetitions, c) 10×10 repetitions of benchmark fabricated unitary image and d) 10×10 repetitions realistic binary image.

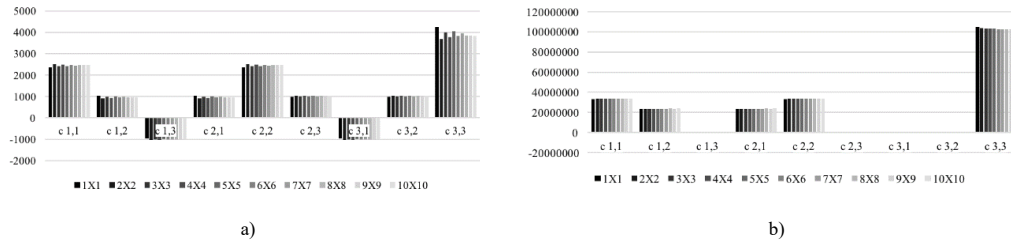


Fig. 3 - Constitutive matrix values obtained using a unitary image and up to 10×10 repetitions. (a) Results for the trabecular square patch obtained using the micro-CT image. (b) Results for the created image.

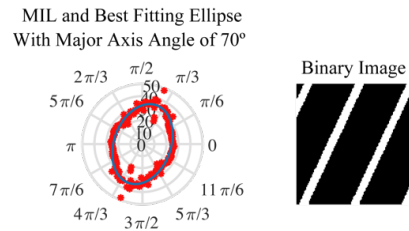


Fig. 4 - Benchmark fabricated RVE rotation results, for the 20° case.

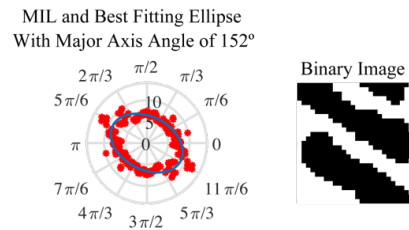


Fig. 5 – Realistic trabecular RVE rotation results, for the 20° case.

The same essential and natural boundary conditions were applied to all the RVEs. Being all the RVEs squares micro patches with dimensions $L \times L$, it was imposed a displacement of $0.1 \times L$ at the nodes of the top layer, $y = L$. The nodes at $x = 0$ and $x = L$ where constrained on Ox direction, $u = 0$, and the nodes at $y = 0$ and $y = L$ where constrained on Ox and Oy direction, $u = 0$ and $v = 0$. This constrains are exemplified in Fig. 7.

The homogeneous RVE is typically discretized by a set of $n \times n$ nodes uniformly distributed within the RVE domain, Fig. 8a). All the integration points of the homogeneous RVEs models possess the same homogenized material properties, while the heterogeneous RVEs (the realistic trabecular RVE) is formed by trabecular bone and void space, the discretization of such complex domain is exemplified in Fig. 8b).

Applying the proposed homogenization technique to the RVE it was possible to obtain the anisotropic material properties presented

Table 2, column "Homogeneous RVE". Thus, every integration point of the homogeneous RVEs assumed these materials properties.

Since the realistic trabecular RVEs are binary images, containing bone or void space, it was necessary to assume mechanical properties for these two materials, as indicated in

Table 2, trabecular bone and void space.

Following the literature, the mechanical properties of the trabecular bone were defined as isotropic [32].

Since the geometrical information coming from the micro-CT forces the existence of the void space in between the trabeculae, it was necessary to define this 'material' as solid, hence, the material was defined as a soft material that would not (significantly) interfere with the global structural response of the RVE, being attributed an elastic modulus with a much lower magnitude when compared with the trabecular bone.

Two homogeneous RVEs were analysed, one with 11×11 nodes and another with 21×21 nodes. The von Mises effective stress maps obtained with FEM, presented in Fig. 9a) and Fig. 9b).

In order to compare the stress field obtained with the homogeneous RVE with the heterogeneous RVE, the concept of homogenized stress was used. The RVE's von Mises effective stress field (or any other RVE's stress/strain field) can be summarized in one scalar value, the homogenized von Mises effective stress, which can be defined with equation 11, being n_Q the number of integration points discretizing the problem domain and not belonging to the vicinity of the domain boundary.

Table 2 - Mechanical properties used in the structural analysis.

Mechanical Properties					
	Homogenized RVE		Trabecular bone		Void Space
E_{axial}	2366.08 MPa	E	11600 MPa	E	100 MPa
E_{transv}	1035.86 MPa				
G	4239.87 MPa				
θ	62°				
ν	0.12	ν	0.36	ν	0.45

$$\sigma_{eff}^h = 1/n_Q (\sum_{i=1}^{n_Q} \sigma(x_i)_{eff}) \quad (11)$$

In Fig. 10 blue dots represent the integration points that were included to calculate σ_{eff}^h and in red the integration points that were excluded from equation 11.

This homogenization excludes only 2% of the integration points forming the integration mesh. This exclusion was necessary to avoid the (inaccurate) stress concentrations that appear near the domain boundary, as can be seen in Fig. 9. Thus, Fig. 11 shows the homogenized von Mises effective stress, σ_{eff}^h obtained for each analysed RVE, using FEM. In this figure, besides the homogenized von Mises effective stress obtained in the integration points, it is also shown the σ_{eff}^h extrapolated to the nodes. The stress at the nodes was obtained by linear extrapolation using the element information.

Notice that four heterogeneous RVE were considered: a 1×1 heterogeneous RVE (corresponding to the one represented in Fig. 9c), a 2×2 heterogeneous RVE (corresponding to the one represented in Fig. 9d), a 3×3 and a 4×4 heterogeneous RVEs following the same repetition rule. It is visible in Fig. 11 that increasing the level of detail and the size of the heterogeneous RVE, which are governed by the number of repetitions (the 1×1 RVE has a lower detail than the 4×4 RVE), the value of the homogenized stress decreases. Thus, when the analysis considers a

heterogeneous model following a 4×4 repetition, the obtained homogenized stress is very close with the homogenized stress obtained with the homogeneous RVE.

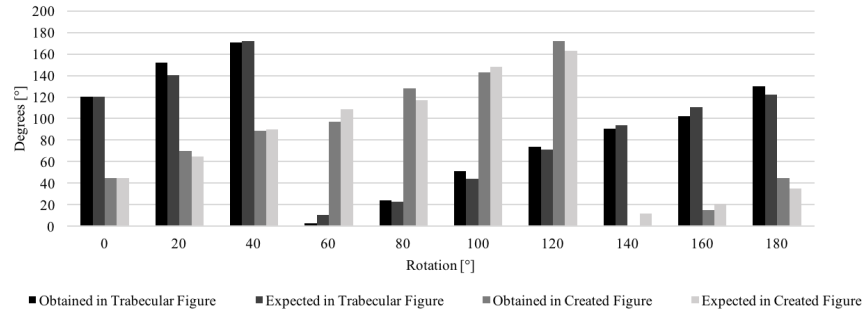


Fig. 6 - Obtained material orientation angles θ of the fitted ellipse versus the expected ones for the benchmark fabricated RVE and the realistic trabecular RVE.

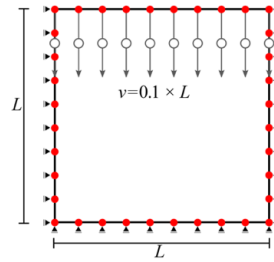


Fig. 7 -Boundary conditions applied to all RVEs.



Fig. 8 – a) Discretized homogeneous RVE; b) Example of a discretized heterogeneous RVE created using micro-CT image information.

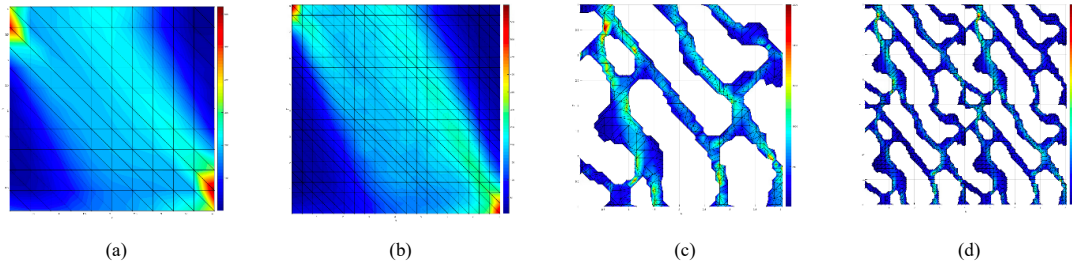


Fig. 9 – Effective Stress for the homogeneous model, a) 1×1 and b) 2×2, and for heterogeneous model, c) 1×1 and d) 2×2.

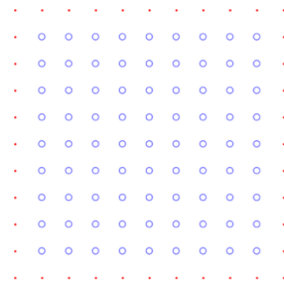


Fig. 10 - Integration points used to calculate the homogenized von Mises effective stress. The blue points represent valid integration points, the red points represent excluded integration points. Integration mesh of the homogenized RVE for FEM analysis;

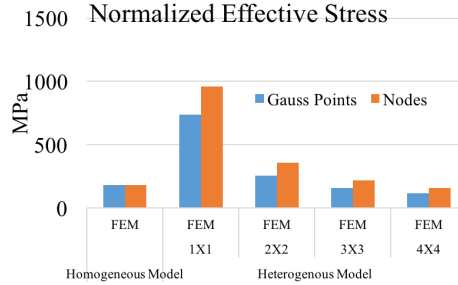


Fig. 11 - Homogenized von Mises effective stress σ_{eff}^h obtained with FEM methodology.

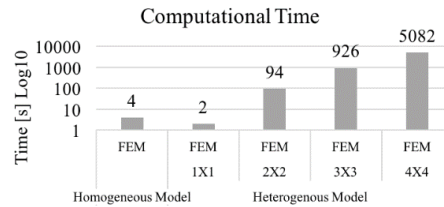


Fig. 12 - Computational cost (in seconds) of each analysis.

This indicates that the homogenization technique proposed in this work is capable to accurately obtain the homogenized anisotropic material properties of a trabecular patch. Each one the analyses has its own computational cost. In Fig. 12

are shown the time-lapse of each structural analysis. Observing the computational cost of each analysis, it is possible to understand that the analysis of the homogenized RVE is much faster than heterogeneous RVEs (with $r_n \times r_n$, $r_n = \{1,2,3,4\}$). In Fig. 11 it was shown that the 4×4 heterogeneous RVE produces results very close with the homogeneous RVE. However, the 4×4 heterogeneous RVE took 5000s to analyse and the homogeneous RVE only required 4 – 6s.

Generally, the multiscale techniques use highly discretized RVEs, with a high computational cost associated. As this example shows, the proposed homogenization methodology is capable to reduce the computational cost of the multiscale analysis, enabling more demanding simulations.

5. Conclusions

The methodology introduced in this work allowed to define the mechanical properties of a micro-CT trabecular bone square patch without any a-priory knowledge. The obtained data using the MIL methodology, enabled to define the material orientation using a distribution function. This function was approximated by a ellipse function, as described by Moreno et al. [30], that can define a tensor (a 2×2 matrix) that represents the bone trabeculae distribution/density. With this, it was possible to define the material mechanical properties, directly related with the trabeculae anisotropy encoded in the fabric tensor and with a phenomenological material law [31]. The studies performed to evaluate the behaviour of the methodology (both RVE scale and rotation studies), revealed that this methodologies are stable and provide solid results. In this work, it was verified that with the homogeneous RVE (whose material properties were obtained using the proposed homogenisation technique) it was possible to produce similar results with the ones obtained with highly heterogeneous RVE (the heterogeneous RVE).

Nevertheless, it was shown that an elasto-static analysis using the homogeneous RVE only takes 4 – 6s to perform and the same analysis with the 4×4 heterogeneous RVE takes about 5000s, 1000× more.

Since usually multiscale techniques use highly discretized RVEs, it is expected that the homogenization technique here proposed will be capable to reduce the cost of the multiscale analyses, allowing to simulate more complex problems.

Acknowledgements

The authors truly acknowledge the funding provided by Ministério da Ciência, Tecnologia e Ensino Superior - Fundação para a Ciência e a Tecnologia (Portugal), under Grants SFRH/BD/110047/2015 and SFRH/BPD/111020/2015, and by project funding MIT-EXPL/ISF/0084/2017 and UID/EMS/50022/2013. Additionally, the authors gratefully acknowledge the funding of Project NORTE-01-0145-FEDER-000022 - SciTech - Science and Technology for Competitive and Sustainable Industries, cofinanced by Programa Operacional Regional do Norte (NORTE2020), through Fundo Europeu de Desenvolvimento Regional (FEDER).

References

- [1] Carter DR, Van Der Meulen MC, Beaupré GS. Mechanical factors in bone growth and development. *Bone* 1996;18:5S–10S. doi:10.1016/8756-3282(95)00373-8.
- [2] Mow VC, Ratcliffe A, Poole AR. Cartilage and diarthrodial joints as paradigms for hierarchical materials and structures. *Biomaterials* 1992;13:67–97.
- [3] Lucchinetti E. Composite Models of Bone Properties. *Bone Mech. Handbook*, Second Ed., CRC Press; 2001, p. 12-1-12–9. doi:10.1201/b14263-16.
- [4] Wnek GE, Bowlin GL. *Encyclopedia of Biomaterials and Biomedical Engineering*. New York: Informa Healthcare USA; 2008.
- [5] Wolff J. The Law of Bone Remodelling. *J Anat* 1986;155:217. doi:10.1097/00006534-198810000-00036.
- [6] Glucksmann A. Studies on Bone mechanics in vitro. *Anat Rec* 1939;73:39–55. doi:10.1002/ar.1090730105.
- [7] Pauwels F. *Gesammelte Abhandlungen zur funktionellen Anatomie des Menschen*. Springer. Springer 1965:543.
- [8] Pettermann HE, Reiter TJ, Rammerstorfer FG. Computational simulation of internal bone remodeling. *Arch Comput Methods Eng* 1997;4:295–323. doi:10.1007/BF02737117.
- [9] Hart RT, Davy DT, Heiple KG. A Computational Method for Stress Analysis of Adaptive Elastic Materials With a View Toward Applications in Strain-Induced Bone Remodeling. *J Biomech Eng* 1984;106:342. doi:10.1115/1.3138503.

- [10] Huiskes R, Weinans H, Grootenboer HJ, Dalstra M, Fudala B, Slooff TJ. Adaptive bone-remodeling theory applied to prosthetic-design analysis. *J Biomech* 1987;20:1135–50. doi:10.1016/0021-9290(87)90030-3.
- [11] Carter DR, Fyhrie DP, Whalen RT. Trabecular bone density and loading history: Regulation of connective tissue biology by mechanical energy. *J Biomech* 1987;20:785–94. doi:10.1016/0021-9290(87)90058-3.
- [12] Beaupré GS, Orr TE, Carter DR. An approach for time-dependent bone modeling and remodeling-theoretical development. *J Orthop Res* 1990;8:651–61. doi:10.1002/jor.1100080506.
- [13] Jacobs CR, Simo JC, Beaupré GS, Carter DR. Adaptive bone remodeling incorporating simultaneous density and anisotropy considerations. *J Biomech* 1997;30:603–13. doi:10.1016/S0021-9290(96)00189-3.
- [14] Fernandes P, Guedes JM, Rodrigues H. Topology optimization of three-dimensional linear elastic structures with a constraint on “perimeter.” *Comput Struct* 1999;73:583–94. doi:10.1016/S0045-7949(98)00312-5.
- [15] Doblaré M, García JM. Application of an anisotropic bone-remodelling model based on a damage-repair theory to the analysis of the proximal femur before and after total hip replacement. *J Biomech* 2001;34:1157–70. doi:10.1016/S0021-9290(01)00069-0.
- [16] Doblaré M, García JM. Anisotropic bone remodelling model based on a continuum damage-repair theory. *J Biomech* 2002;35:1–17. doi:10.1016/S0021-9290(01)00178-6.
- [17] García-Aznar JM, Rueberg T, Doblaré M. A bone remodelling model coupling microdamage growth and repair by 3D BMU-activity. *Biomech Model Mechanobiol* 2005;4:147–67. doi:10.1007/s10237-005-0067-x.
- [18] Hazelwood SJ, Bruce Martin R, Rashid MM, Rodrigo JJ. A mechanistic model for internal bone remodeling exhibits different dynamic responses in disuse and overload. *J Biomech* 2001;34:299–308. doi:10.1016/S0021-9290(00)00221-9.
- [19] Taylor D, Lee TC. Microdamage and mechanical behaviour: predicting failure and remodelling in compact bone. *J Anat* 2003;203:203–11. doi:10.1046/j.1469-7580.2003.00194.x.
- [20] Hernandez CJ, Beaupré GS, Carter DR. A model of mechanobiologic and metabolic influences on bone adaptation. *J Rehabil Res Dev* 2000;37:235–44.
- [21] Hazrati Marangalou J, Ito K, van Rietbergen B. A novel approach to estimate trabecular bone anisotropy from stress tensors. *Biomech Model Mechanobiol* 2015;14:39–48. doi:10.1007/s10237-014-0584-6.
- [22] Moreno R, Smedby Ö, Pahr DH. Prediction of apparent trabecular bone stiffness through fourth-order fabric tensors. *Biomech Model Mechanobiol* 2016;15:831–44. doi:10.1007/s10237-015-0726-5.
- [23] Cowin SC. The relationship between the elasticity tensor and the fabric tensor. *Mech Mater* 1985;4:137–47. doi:10.1016/0167-6636(85)90012-2.
- [24] Zienkiewicz OC, Taylor RL. *The Finite Element Method*. 4th ed. London: McGraw-Hill; 1994.
- [25] Whitehouse WJ. The quantitative morphology of anisotropic trabecular bone. *J Microsc* 1974;101:153–68. doi:10.1111/j.1365-2818.1974.tb03878.x.
- [26] Cowin SC, Doty SB. *Tissue Mechanics*. Springer Science; 2007.
- [27] Mizuno K, Matsukawa M, Otani T, Takada M, Mano I, Tsujimoto T. Effects of structural anisotropy of cancellous bone on speed of ultrasonic fast waves in the bovine femur. *IEEE Trans Ultrason Ferroelectr Freq Control* 2008;55:1480–7. doi:10.1109/TUFFC.2008.823.
- [28] Odgaard A. Three-dimensional methods for quantification of cancellous bone architecture. *Bone* 1997;20:315–28. doi:10.1016/S8756-3282(97)00007-0.
- [29] Zysset PK. A review of morphology–elasticity relationships in human trabecular bone: theories and experiments. *J Biomech* 2003;36:1469–85. doi:10.1016/S0021-9290(03)00128-3.
- [30] Moreno R, Borgia M, Smedby O. Techniques for Computing Fabric Tensors - A Review. *Math. Vis.*, vol. 5, 2014, p. pp 271-292. doi:10.1007/978-3-642-54301-2_12.
- [31] Belinha J, Jorge RMN, Dinis LMJS. A meshless microscale bone tissue trabecular remodelling analysis considering a new anisotropic bone tissue material law. *Comput Methods Biomech Biomed Engin* 2012;5842:1–15. doi:10.1080/10255842.2012.654783.
- [32] Natali AN, Carniel EL, Pavan PG. Constitutive modelling of inelastic behaviour of cortical bone. *Med Eng Phys* 2008;30:905–12. doi:10.1016/j.medengphy.2007.12.001.

3.6 Contribution IV: Combining the radial point interpolation meshless method with a new homogenisation technique for trabecular bone multiscale structural analyses.

3.6.1 Highlights of Contribution: 3.6

This contribution focused on the bone mechanical properties definition using a homogenisation technique, defined by the fabric tensor concept, combined with the RPIM meshless method.

Therefore, the main contents of this publication include:

- I. Literature review on multiscale homogenisation techniques;
- II. Literature review on the fabric tensor concept;
- III. Application of a homogenisation technique, defined using a morphologically based fabric tensor and a phenomenological material law method;
- IV. Validate of the homogenisation methodology using numerical tests involving size and rotation analyses;
- V. Applied a structural analysis using FEM and RPIM, where it was used a metric able to compare heterogenous and equivalent homogeneous domains.
- VI. The RPIM meshless method results are very similar to the FEM methods, reinforcing the applicability of meshless methods in biomechanical applications.
- VII. Conclusion: The methodology introduced in this contribution allowed to define the mechanical properties of trabecular bone by using medical images information. As demonstrated in figure 3.6, by using the developed methodology a homogenous domain, with a less discretised mesh, is mechanically equivalent to a highly discretised heterogeneous domain. Thus, the methodology, as demonstrated in figure 3.7, provides models defined with the homogeneous domains and mechanical properties representing a lower computational cost, when compared to the equivalent heterogeneous models.

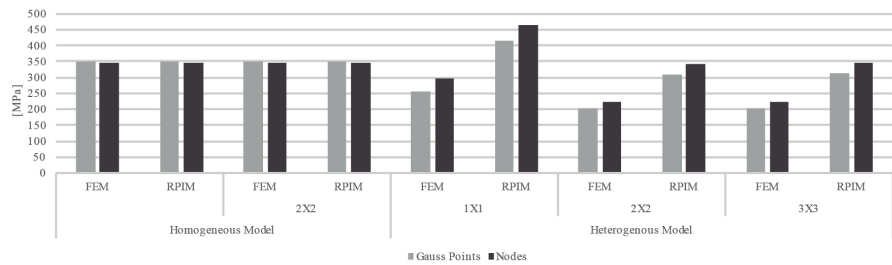


Figure 3.6: Contribution IV convergence study results.

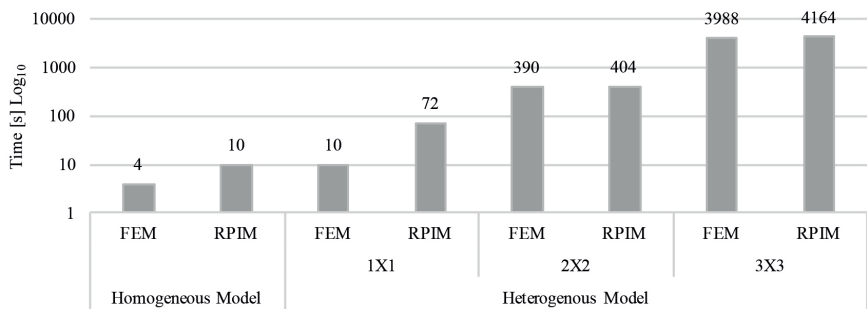


Figure 3.7: Contribution IV computational time.

The complete document can be found in the next pages.

Title: Combining radial point interpolation meshless method with a new homogenization technique for trabecular bone multiscale structural analyses

Abstract:

Purpose: Bone tissue is a dynamic tissue, possessing different functional requirements at different scales. This layered organization indicates the existence of a hierarchical structure, which can be characterized to distinguish macro-scale from micro-scale levels. Structurally, both scales can be linked by the used of classic multiscale homogenization techniques. Since in bone tissue each micro-scale domain is distinct from its neighbour, applying a classic multiscale homogenization technique to a complete bone structure could represent an inadmissible computational cost. Thus, this work proposes a homogenization methodology that is computationally efficient, presenting a reduced computational cost, and capable to define the homogenized microscale mechanical properties of the trabecular bone highly heterogeneous medium.

Methods: The methodology uses the fabric tensor concept in order to define the material principal directions. Then, using an anisotropic phenomenological law for bone tissue correlating the local apparent density with directional elasticity moduli, the anisotropic homogenized material properties of the micro-scale patch are fully defined. To validate the developed methodology, several numerical tests were performed, measuring the sensitivity of the technique to changes in the micro-patch size and preferential orientation.

Results: The results show that the developed technique is robust and capable to provide a consistent material homogenization. Additionally, the technique was combined with two discrete numerical techniques: the finite element method and radial point interpolation meshless method.

Conclusions: Structural analyses were performed using real trabecular patches, showing that the proposed methodology is capable to accurately predict the micro-scale patch mechanical behavior in a fraction of the time required by classic homogenization techniques.

Keywords: Meshless Methods, Radial Point Interpolation Method, Fabric Tensor, Homogenization Technique, Multiscale

1. Introduction

Bone is a mineralized biological structure defined by bone matrix and by bone cells. Among many other functions, bone is designed to structurally support soft tissues in the

body. The renew of bone occurs by a biological process called bone remodeling [20]. In addition to its morphology adaptation, bone also changes its macro-scale mechanical properties to fulfill and optimize the specific physiological function of structural support [6]. In order to understand bone structure and biological and mechanical functions bone can be classified in different hierarchical structures, constituted of many scale levels with specific interactions and with very complex architectures [10]. Some authors classify bone with different structural levels from the macroscale (whole bone) to sub-nanoscale (hydroxyapatite crystals, constituent of the inorganic phase of bone and TC molecules) [1]. Since the bone has different functional requirements at different scales, to analyze the equivalent (homogenized) mechanical behavior of bone material it is necessary to investigate the mechanical properties of its distinct components and the structural relationships between such components at different scales [13]. Many researchers have addressed the study of bone mechanical behavior by developing analytical and numerical models. Thus, to describe the mechanical behavior of bone at certain scale levels, some models apply multiscale approaches and other use homogenization techniques combined with distinct discretization approaches, such as finite element methods (FEM). Today, it is generally accepted that bone remodeling is mainly caused by the transient nature of its strain/stress fields (induced by the external loads applied in its physical boundary). This simple concept was proposed first by Wolff in 1886 [21]. Wolff reported that the directions of the external applied loads directly influences the direction of the trabecular bone, since bone cell sense the applied loads and change their physical disposition and distribution (modifying the local and global bone morphology).

The study of bone remodeling using numerical approaches evolved significantly since the first simplistic models, which considered bone as an isotropic-elastic material only sensitive to mechanical stimuli [5,11]. Year after year, the complexity of bone models starts to increase. Some authors started to consider the trabecular orientation (material anisotropy), and others developed bio-mechanical models assuming both mechanical and biological stimuli. More recently, multiscale models were successfully developed.

Trabecular bone is the major responsible for the bone metabolic activity, in which is included the remodeling process. The typically trabecular bone architecture leads to a highly heterogeneous medium, showing anisotropic material properties. Thus, some authors, started to characterize bone mechanical properties, considering and encoding the orientation and anisotropy of the material [16]. These authors used the fabric tensor

concept \mathbf{A} , a symmetric second rank tensor that characterizes the arrangement of a multiphase material. Back in 1985, Cowin [7], described the relation between the fabric tensor and the fourth rank elasticity tensor \mathbf{C}_{ijkl} . Cowin also shown that the fabric tensor provides an ellipsoid that can be associated with the varieties of material symmetries observed in many natural materials. Presently, two different techniques are available to estimate the fabric tensor, the mechanical based techniques and the morphologic-based techniques (morphologic-based use the interface between phases of the material to estimate the fabric tensor). Thus, naturally, morphologic-based techniques are commonly used to define the fabric tensor of bone tissue. Most of the available techniques, using morphologic-based methods, obtain the fabric tensor applying an orientation distribution function (ODF), which is estimated from an orientation-dependent feature of interest. In the literature it is shown that when the ODF data is disposed on a polar plot and fitted in an ellipse the corresponding ellipse parameters can be correlated with the material orientation/anisotropy. [8,15,19,22]. Material mechanical properties can be estimated experimentally (using mechanical tests) or virtually (using concepts as the fabric tensor). Such estimation is of high importance, since it feeds constitutive laws. Then, combining the constitutive laws with discrete numerical methods, it is possible to predict the material structural behavior. Thus, an accurate and robust model depends on three blocks: an accurate predictor of the material properties, a reliable constitutive law, and an accurate discrete numerical method.

Discrete numerical techniques allow to discretize the problem domain in small parts (elements in the FEM and nodes in meshless methods). Then, a variational principle (governing the physical phenomenon) is applied to obtain an algebraic system of equations. Solving such equation system permits to access the variable field of interest (such as the displacement or the strain/stress fields). The first discrete numerical technique applied to orthopedic biomechanics, in 1972, was the FEM and it was used to evaluate stresses in human bones [12]. In order to answer to some discretization drawbacks of FEM, other discretization techniques have been developed, such as meshless methods. In the literature it is possible to find several distinct meshless methods techniques [2,4,14,18].

The main objective of this work is to combine a new developed homogenization technique, in which is applied the fabric tensor concept in synergy with a previous

developed bone tissue material law, with the Radial Point Interpolation Method (RPIM) meshless method, aiming to achieve a low-cost and efficient multiscale technique.

2. Material and Methods

In this section the RPIM formulation is briefly presented. Also, the nodal connectivity, integration mesh, shape functions and elasto-static linear equations used in this formulation are explained. In this section is also fully presented the proposed homogenization technique.

2.1. Radial Point Interpolation Method Formulation

Meshless methods, unlike the FEM, do not use elements or any other lattice discretization to establish nodal/particle connectivity. With meshless methods, the problem domain is discretized using an unstructured nodal set where nodes can be distributed regularly or irregularly. These methods have advantages in the field of biomechanics, since they are capable of discretize highly complex problem domains using information gathered directly from medical images [2]. In meshless methods, the nodal discretization only requires the spatial coordinates of the nodes and, possibly, its individually material properties. The nodal connectivity (how each node interacts with its neighbor) is obtained using geometrical and mathematical constructions, allowing to define the influence-domain concept, the equivalent to the element concept in the FEM. In this work, meshless methods are combined with weak formulations to solve in integro-differential equations. Thus, it is mandatory the construction of a background integration mesh, which can be nodal-dependent or nodal-independent, to enable the numerical integration of such equations. Only the meshless methods that use nodal dependent constructions are called truly meshless methods, because they allow to directly define the spatial position and the integration weight of all integration points using only the spatial positions of the nodes [2]. Concerning the construction of shape functions, RPIM shape functions are obtained using the Radial Point Interpolators (RPI) technique. In this technique, a radial basis function is combined with a polynomial basis function [18]. Despite the classical RPI formulation uses polynomial basis functions, previous works have shown that they are unnecessary if RBF's shape parameters are chosen carefully [2]. This is an important innovation since it allows to increase its computational efficiency. Nonetheless, in this work, it is assumed the classical RPI formulation. Therefore, considering the function $h(\mathbf{x}_I)$ defined in the domain $\Omega \subset \mathbb{R}^2$ the value of function $h(\mathbf{x}_I)$ at the point of interest \mathbf{x}_I is defined by equation (1),

$$h(\mathbf{x}_I) = \sum_{i=1}^n R_i(\mathbf{x}_I) a_i(\mathbf{x}_I) + \sum_{j=1}^m P_j(\mathbf{x}_I) b_j(\mathbf{x}_I) = R(\mathbf{x}_I)^T a(\mathbf{x}_I) + P(\mathbf{x}_I)^T b(\mathbf{x}_I) \quad (1)$$

where $R_i(\mathbf{x}_I)$ is the RBF, n is the number of nodes in the influence-domain of \mathbf{x}_I . The coefficients $a_i(\mathbf{x}_I)$ and $b_j(\mathbf{x}_I)$ are the non-constant coefficients of $R_i(\mathbf{x}_I)$ and $p_j(\mathbf{x}_I)$, respectively. The monomials of the polynomial basis are defined by $p_j(\mathbf{x}_I)$ and m is the basis monomial number. The variable r_{ij} is the distance between the relevant node $\mathbf{x}_i = \{x_i, y_i\}^T$ and the neighbor node $\mathbf{x}_j = \{x_j, y_j\}^T$, $r_{ij} = \sqrt{(x_j - x_i)^2 + (y_j - y_i)^2}$. Several known RBFs are well studied and developed in [2]. This work uses the Multiquadric (MQ) function $R(r_{ij}) = (r_{ij}^2 + c^2)^p$, where c and p are two parameters that need to be optimized, since they affect the performance of the RBFs. Notice that each integration weight should possess its own c parameter. Thus, for integration point I with an integration weight $\hat{\omega}_I$, the shape parameter c is obtained with: $c_I \cong \gamma \hat{\omega}_I$. This spatial dependence of the RBF's shape parameter is demonstrated in research works available in the literature [2]. Previous works on the RPIM found that parameter γ should be close to zero, $\gamma \cong 0$, and p should be close to one, $p \cong 1$ [2]. However, these values cannot be $\gamma = 0$ and $p = 1$. The use of the exact integer value for p leads to a singular moment matrix and assuming a null γ leads to singular moment matrix. Furthermore, previous works [2] have shown that values of p very close to the unit allow to obtain the most accurate solutions (regardless the analyzed problem). Thus, the authors have decided to use $p = 1.0001$ or $p = 0.9999$. Additionally, as shown in [2], the parameter γ should be very close to zero, because as its value grows, the RPI shape function loses its interpolation properties. Thus, the authors have selected $\gamma = 0.0001$ in order to "maximize" the RPI interpolation properties. Commonly, the polynomial basis has to possess a low degree to guarantee that the interpolation matrix of RBF is invertible. Thus, in this work the constant polynomial basis is used: $p^T(\mathbf{x}) = \{1\}; m = 1$. The polynomial basis has to satisfy an extra requirement in order to obtain a unique solution [2],

$$\sum_{i=1}^n p_j(\mathbf{x}_i) a_j(\mathbf{x}_i) = 0, j = 1, 2, \dots, m \quad (2)$$

in which n represents the number of nodes inside the influence-domain of interest point \mathbf{x}_I . Comparing RPIM with other meshless methods, it has lower computational cost during the processing phase of the numerical analysis (after the construction of the nodal connectivity, integration mesh and shape functions) and shows a higher re-meshing flexibility and a higher accuracy on the solution variable field [9].

2.2. Homogenization Technique

The homogenization technique used in this work is fully described in this section. In this work, it was used a micro-CT from the cuboid bone. First, since this work is 2D, only a CT-slice was considered. Then, for the selected thin slice of bone tissue, a square Region of Interest (ROI) was identified. Afterwards, the fabric tensor concept was applied to that ROI, allowing to determine the material preferential orientation. In addition, using a bone tissue phenomenological law, the pixel information of the selected ROI was used to obtain the homogenized material properties of the microscale patch. This homogenization technique allows to define the homogenized anisotropic material proprieties of the trabecular bone, a highly heterogeneous material. The algorithm describing the proposed homogenization technique is presented in Figure 1 and its features are presented in the following subsections.

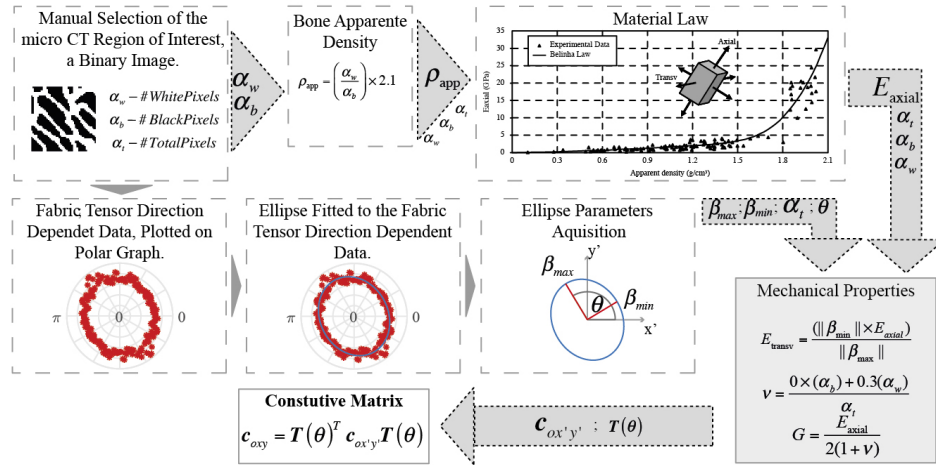


Figure 1 - Microscale homogenization technique

2.3. Fabric tensor morphologic based method

In order to apply the fabric tensor methodology, it is necessary to transform the ROI's gray-scale image into a binary image (black and white image), which in this work is identified as I_S . An example of an I_S is shown in the left-upper box of Figure 1.

The methodology developed by Whitehouse [19] was used to define the fabric tensor. Thus, the number of interceptions between a parallel family line set, with direction τ , with the interface between both phases of the material is counted, $Int(\tau)$. Furthermore, the length of the parallel lines family, h for the τ direction is also obtained. Possessing h and τ , it is possible to defined the an orientation distribution function (ODF), which in this case is called mean interception length (MIL), equation (3).

$$MIL(\tau) = \frac{h}{Int(\tau)} \quad (3)$$

In the literature, it is possible to find several works showing the robustness and accuracy of this technique in the prediction of the material properties of trabecular bone [8,19,22]. The work of Moreno et al. [15] shows that when the ODF data is disposed on a polar plot and fitted in an ellipse, the corresponding ellipse parameters can be correlated with the material orientation (its anisotropy). The dimensional information of I_s is used to define the size of an image containing the family of parallel lines with $\tau = 0^\circ$. Counting the interceptions of those parallel lines with the boundaries of the binary image square patch, it is possible to obtain the orientation-dependent feature. The ODF of the I_s can be obtained by rotating the family of parallel line image with τ between 0° and 180° , and then counting the interception of the family of parallel lines with the square patch binary image I_s . The created data for τ between $]180^\circ, 360^\circ[$ is a $[0^\circ, 180^\circ]$ data repetition, because the orientation-dependent feature is not influenced by the direction (it only depends on the orientation).

In order to obtain the material orientation, the ODF data is plotted using polar coordinates. This data is then fitted into an ellipse. Observing now both central boxes of Figure 1, it is perceptible that it is possible to obtain the material orientation of the trabecular micropatch from the ellipse orientation. In addition, from the fitted ellipse, it is possible to obtain the ellipse minor axis length, β_{\min} , and major axis length, β_{\max} , and θ , the angle of ellipse major axis with the polar plot horizontal axis.

2.4. Phenomenological material law method

In this work, the homogenized anisotropic mechanical properties of I_s are defined using the information from the fitted ellipse and the average apparent density of the binary

image I_S . As equation (4) shows, the average apparent density, ρ_{app} , of the binary image I_S can be obtained using the number of white pixels, α_w , and black pixels, α_b , of I_S :

$$\rho_{app} = \left(\frac{\alpha_w}{\alpha_b} \right) \rho_{app}^{cortical} \quad (4)$$

in which the cortical bone apparent density is considered as $\rho_{app}^{cortical} = 2.1 \text{ g/cm}^3$. Assuming the phenomenological material law proposed by Belinha and co-workers [3], it is possible to defined the axial Young's modulus E_{axial} using the homogenized ρ_{app} from equation (4). In order to adjust more closely to the experimental results, Belinha's phenomenological law is divided in two equations [3]. Thus, if $\rho_{app} \leq 1.3$ it should be applied equation (5), otherwise it should be used equation (6). The coefficients a_j and b_j can be found in Table 1.

$$E_{axial} = \sum_{j=0}^3 a_j \rho_{app} \text{ if } \rho_{app} \leq 1.3 \quad (5)$$

$$E_{axial} = \sum_{j=0}^3 b_j \rho_{app} \text{ if } \rho_{app} > 1.3 \quad (6)$$

	$j = 0$	$j = 1$	$j = 2$	$j = 3$
a_j	0.0E+00	7.216E+02	8.059E+02	0.0E+00
b_j	-1.770E+05	3.861E+05	-2.798E+05	6.836E+04

Table 1 - Coefficients from Belinha's material law [3].

The transverse elastic modulus E_{transv} is defined using the relation between the ellipse minor axis length, β_{min} , and major axis length, β_{max} , as shown in equation (7),

$$E_{transv} = \frac{(\|\beta_{min}\| E_{axial})}{\|\beta_{max}\|} \quad (7)$$

Considering the well-known mixture theory, it is possible to define the Poisson's coefficient, ν , using the relation between white and black pixels. Notice that white pixels represent solid bone (for which it was assumed $\nu = 0.3$) and black pixels represent void space (for which it was assumed $\nu = 0.0$).

$$\nu = \frac{0.0(\alpha_b) + 0.3(\alpha_w)}{\alpha_t} \quad (8)$$

In equation(8), α_t represents the total number of pixels of the binary image I_s . The shear modulus, G , was expeditiously calculated using equation (9).

$$G = \frac{E_{axial}}{2(1+\nu)} \quad (9)$$

After defining all the required homogenized material properties (E_{axial} , E_{transv} , ν and G), it is possible to build the constitutive matrix: $\mathbf{c}_{ox'y'}$, for the $ox'y'$ local coordinate system (oriented with the material principal axis, following the principal directions 'axial' and 'transverse'). In fact, first it is defined the orthotropic compliance matrix for the material axis $ox'y'$. Only after, $\mathbf{c}_{ox'y'}$ is defined with $\mathbf{c} = \mathbf{s}^{-1}$. For this it is necessary to rotate the $\mathbf{c}_{ox'y'}$ to the global axis using the angle θ obtained from the ellipse fitting, using the transformation rotation matrix \mathbf{T} , equation (10),

$$\mathbf{T}(\theta) = \begin{bmatrix} \cos(\theta) & -\sin(\theta) & 0 \\ \sin(\theta) & \cos(\theta) & 0 \\ 0 & 0 & 1 \end{bmatrix} \quad (10)$$

and then, finally, it is possible to write the material constitutive matrix in the global axis with equation (11),

$$\mathbf{c}_{oxy} = \mathbf{T}(\theta)^T \mathbf{c}_{ox'y'} \mathbf{T}(\theta) = \begin{bmatrix} c_{11} & c_{12} & c_{13} \\ c_{21} & c_{22} & c_{23} \\ c_{31} & c_{32} & c_{33} \end{bmatrix} \quad (11)$$

3. Results

Aiming to validate the proposed homogenization methodology, some numerical tests were performed. The tests involved size and rotation analyses of predefined I_s binary images and static analysis using the homogenized material properties.

First, it is presented a study in which the RVE size is varied, allowing to understand the influence of this scale parameter in the accuracy of the proposed methodology. Second, in order to access the robustness of the proposed technique, it was analyzed a predefined binary image showing a clear preferential material orientation. Afterwards, the input image was rotated, and it was verified if the ellipse fitted from the fabric tensor based methodology had β_{\max} aligned with the material orientation of the image. In this validation example, it was assumed angle increments of 20° for the family of parallel lines rotation.

In the end, in order to show the efficiency and accuracy of the proposed homogenization technique, it was performed a numerical structural analysis using two distinct geometrical models (a homogeneous model and a heterogeneous model). To show the versatility of the proposed methodology, the technique was combined with two distinct numerical methods, the FEM and the RPIM. For the FEM formulation, in this study, it was used the standard plane strain triangular element. Concerning the RPIM formulation used in this work, it was assumed influence-domain with 16 nodes inside; one integration point per each integration triangular cell (matching the triangular elements of the FEM analysis for comparison proposes); the MQ-RBF shape parameters suggested in the literature ($c = 0.0001$ and $p = 0.9999$); and a constant polynomial basis.

3.1. Validation of MIL methodology

3.1.1. RVE size

In this section, two distinct RVE models were constructed, Figure 2a and Figure 2d. The RVE model shown in Figure 2a is a benchmark fabricated unitary binary image possessing a well-defined material orientation (90°). In order to understand the influence of size of the RVE in the proposed methodology, this fabricated model was repeated $r_n \times r_n$, being r_n the number of repetitions of the RVE. For illustration purposes, Figure 2b shows its 2×2 repetition and in Figure 2c it is shown its 10×10 repetition. Regarding the model of Figure 2d, it represents a realistic trabecular square patch unitary binary image obtained from a micro-CT image. Likewise, this realistic RVE was repeated $r_n \times r_n$. In Figure 2e and Figure 2f are shown examples for the 2×2 repetition and 10×10 repetition, respectively.

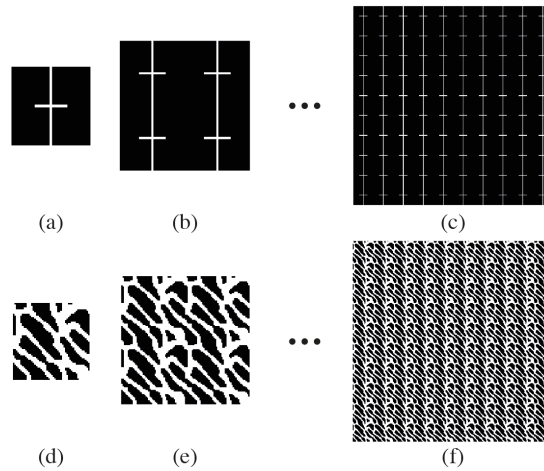


Figure 2 - Binary images used to verify the MIL dependence on the RVE size. Benchmark fabricated unitary image, (a). Realistic binary image from a micro-CT, (d); To analyze the effect of using different RVE sizes, the binary images were repeated from a 2×2 repetition, (b) and (e) to a 10×10 repetitions, (c) and (f) respectively

The homogenization methodology proposed was applied to all models: fabricated image and realistic image, and corresponding RVE repetitions ($r_n = 1, 2, 3, \dots, 10$). Thus, all the components of the constitutive tensor c_{oxy} , equation (11), were obtained for each one of the analyzed RVEs. Thus, Figure 3a and Figure 3b show the components of the constitutive matrix that are obtained using the proposed homogenization methodology for the fabricated benchmark RVE and the realistic trabecular RVE, respectively.

As equation (11) and Figure 1 indicates, angle θ represents the approximated orientation of the material. Thus, using the developed methodology, the angle θ for each RVE model (and corresponding repetitions) is obtained and the results are presented in Table 2. For the fabricated benchmark RVE, it was obtained an average value of 90° with a standard deviation of 0° . For realistic trabecular RVE, it was obtained an average value of 127° with a standard deviation of 0° .

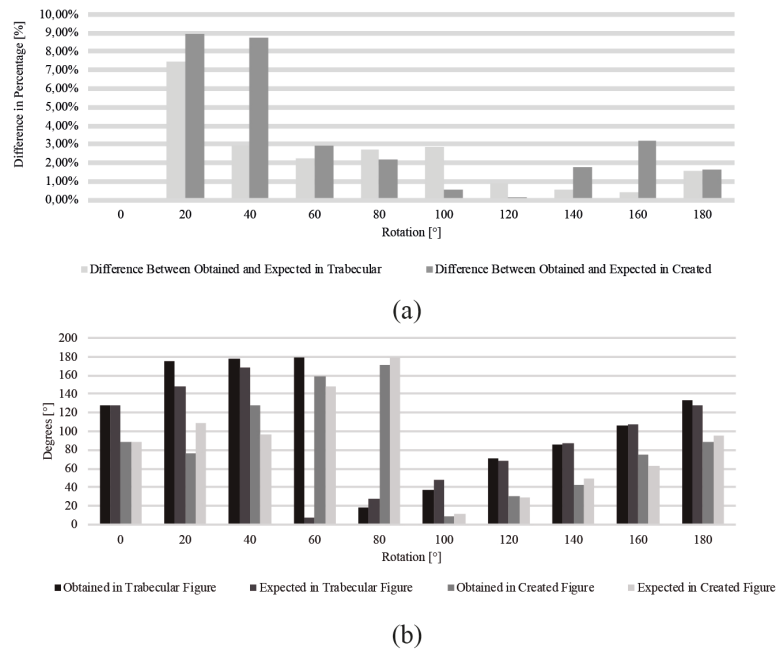


Figure 3- Constitutive matrix values obtained using a image up to $10 \times$ repetitions. Figure 3a: Results for realistic. Figure 3b: Results for the benchmark image

Repetition	1	2	3	4	5	6	7	8	9	10	Average	SD
θ Created	90	90	90	90	90	90	90	90	90	90	90	0
θ Trabecular	124	127	126	127	127	127	127	127	127	127	127	0

Table 2 - Relation between the image repetition and θ

3.1.2. RVE Rotation

In order to verify if the developed methodology is capable to deliver accurate material orientations, an RVE rotation study was performed. The two created models, the benchmark fabricated RVE, Figure 2a, and the realistic trabecular RVE, Figure 2d, were rotated in relation to their initial position following increment angles of 20° , between the interval $[0^\circ, 180^\circ]$. As Figure 4 and Figure 5 show, it is possible to visualize the orientation/size of the produced ellipse and the corresponding approximated material angle.

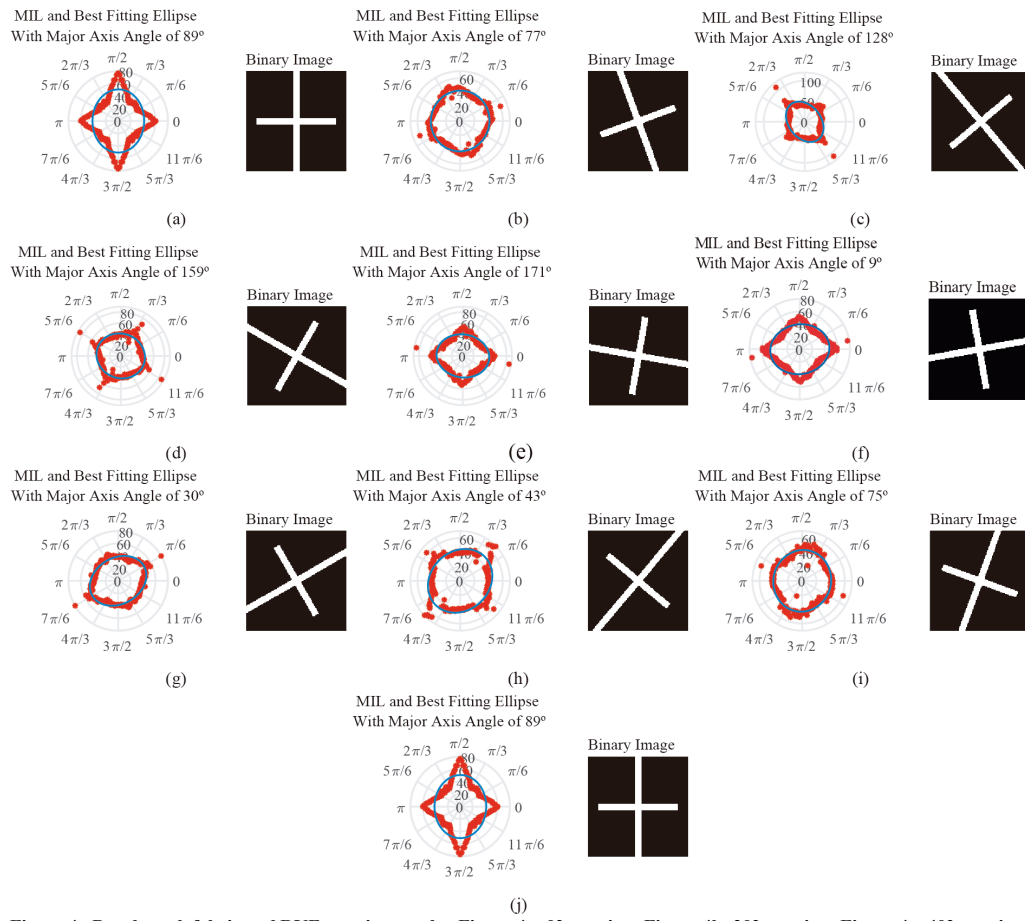


Figure 4 - Benchmark fabricated RVE rotation results. Figure 4a: 0° rotation; Figure 4b: 20° rotation; Figure 4c: 40° rotation; Figure 4d: 60° rotation; Figure 4e: 80° rotation; Figure 4f: 100° rotation; Figure 4g: 120° rotation; Figure 4h: 140° rotation; Figure 4i: 160° rotation; Figure 4j: 180° rotation.

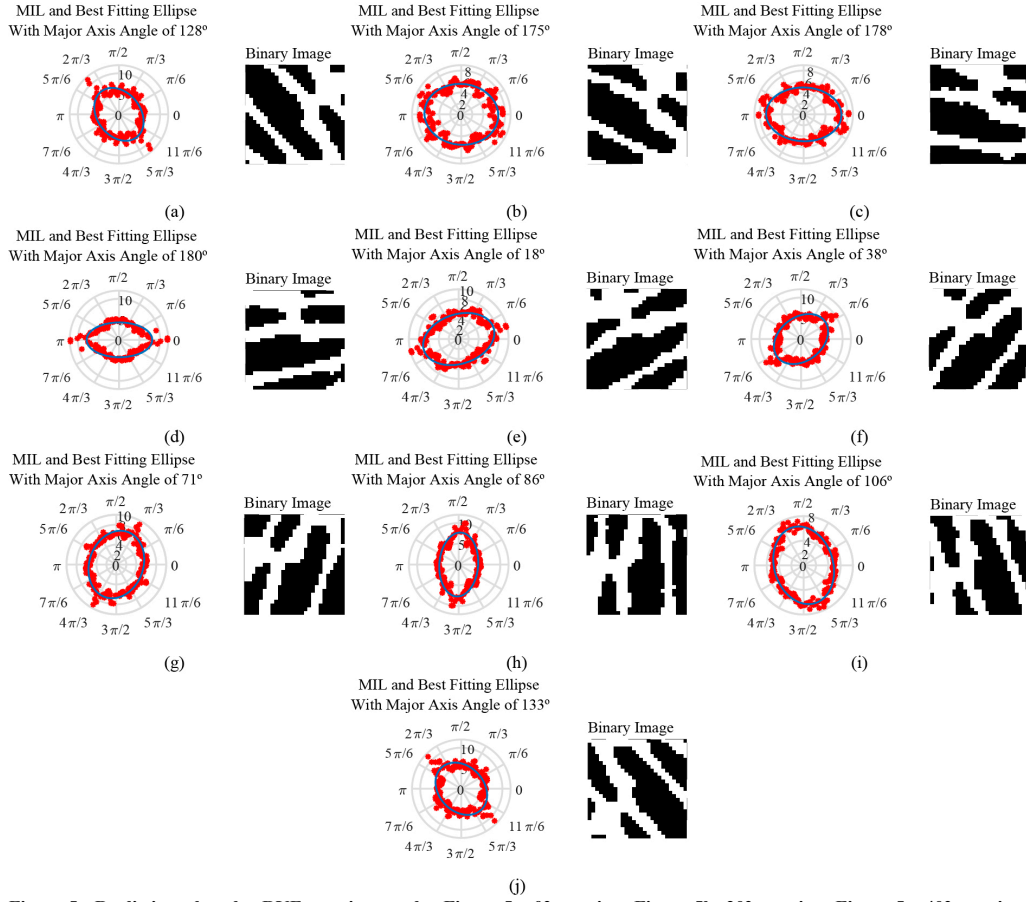


Figure 5 - Realistic trabecular RVE rotation results. Figure 5a: 0° rotation; Figure 5b: 20° rotation; Figure 5c: 40° rotation; Figure 5d: 60° rotation; Figure 5e: 80° rotation; Figure 5f: 100° rotation; Figure 5g: 120° rotation; Figure 5h: 140° rotation; Figure 5i: 160° rotation; Figure 5j: 180° rotation.

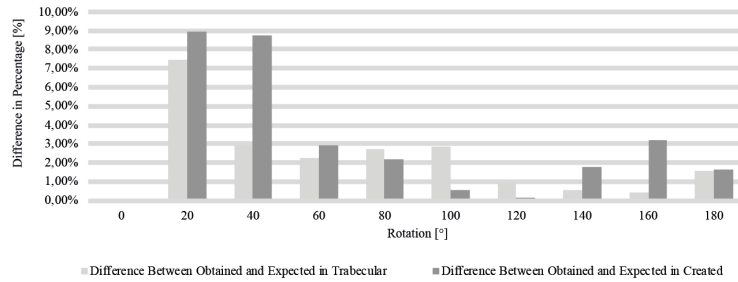


Figure 6 - Figure 6a: Obtained material orientation angles θ of the fitted ellipse versus the expected ones for the benchmark fabricated RVE (Figure 2a) and the realistic trabecular RVE (Figure 2b). Figure 6b: Difference between the obtained θ results and the expected ones, in percentage.

3.2. Stress Analysis

In this section distinct RVEs are structurally analyzed using two distinct discretization techniques, the FEM and the RPIM. This study aims to verify if a homogeneous RVE is capable to produce a homogenized von Mises effective stress similar to the one obtained

with a heterogeneous RVE. The homogenized orthotropic mechanical properties are obtained with proposed methodology.

Therefore, the realistic trabecular RVE previously presented, Figure 2d, and its $r_n \times r_n$ repetitions are structurally analyzed using the elasto-static formulation. The obtained results are compared with the ones obtained with a homogeneous RVE using much lower discretization levels.

All the analyzed RVEs are squares micro patches with dimensions $L \times L$ and were submitted to the same essential boundary conditions, Figure 7. Thus, it was imposed a displacement of $0.1 \times L$ at the nodes of the top layer, $y = L$. The nodes at $x = 0$ and $x = L$ where constrained along Ox direction, $\bar{u} = 0$, and the nodes at $y = 0$ and $y = L$ where constrained along Oy direction, $\bar{v} = 0$.

As Figure 8a shows, the homogeneous RVE is typically discretized by a set of $n \times n$ nodes uniformly distributed within the RVE domain and every integration point within its domain possess the same homogenized material properties. Conversely, heterogeneous RVEs (realistic trabecular RVE) are formed by trabecular bone and void space. Naturally, as Figure 8b shows, the discretization of such complex domain is more demanding. Concerning the element type used in the finite element analyses, in the case of the heterogeneous model, it were used plane strain/plane stress 2D triangular elements with 3 nodes. Alternatively, for the homogeneous model, the authors have considered 2D Lagrangian quadrilateral elements with four nodes (full integration scheme).

Using the RVE represented in Figure 2a, and applying the proposed homogenization technique, allow to obtain the orthotropic material properties presented in Table 3, column "Homogeneous RVE". Notice that, as already mentioned, every integration point of the homogeneous RVEs will assume these materials properties.

Due to their binary nature, all realistic trabecular RVEs possess or solid bone tissue or void space. Thus, it is necessary to define the material properties of these two domains. Hence, in Table 3 are indicated the mechanical properties for the two domains (trabecular bone and void space). Following the literature, the mechanical properties of the trabecular bone (solid material) was defined as isotropic, [17].

Concerning the void domain, the geometrical information coming from the micro-CT forces the existence of a void space between trabeculae. Thus, it was necessary to define the void domain as solid. In order to ensure that the void material does not (significantly)

interfere with the global structural response of the RVE, to the 'void space' was attributed a Young's modulus with a much lower magnitude when compared with the trabecular bone.

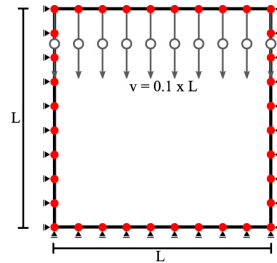


Figure 7- Boundary conditions applied to all RVEs.

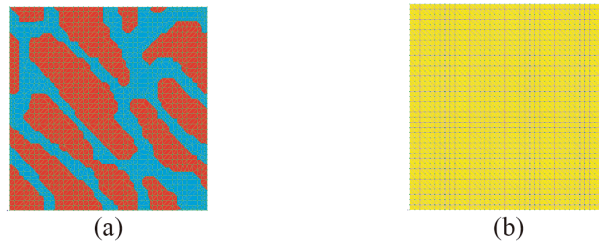


Figure 8 - Figure 8a Discretized homogeneous RVE (41×41 nodes uniformly distributed). Figure 8b: Example of a discretized heterogeneous RVE created using micro-CT image information

Mechanical Proprieties								
	Homogenized RVE			Trabecular bone			Void Space	
E_{axial}	4488,548		[MPa]	E	11600	[MPa]	E	100 [MPa]
E_{transv}	2520,426		[MPa]					
G	10066,1		[MPa]					
θ	56		[degrees]					
ν	0.3			ν	0,36		ν	0,459

Table 3-Mechanical properties used in the structural analysis.

The results from the homogeneous RVEs, regardless the level of the discretization or the used numerical method (FEM or RPIM), were very similar, as can be seen in Figure 9a and Figure 9b. In these figures it is also perceptible the preferential orientation of the material, that was obtained using the developed methodology applied to Figure 2a. Concerning the heterogeneous RVEs, Figure 9, the results obtained using FEM are slightly different from the one obtained with the RPIM, as can be seen in Figure 9e and Figure 9g and in Figure 9f and Figure 9h. The von Mises effective stress maps obtained with both FEM and RPIM techniques are presented in Figure 9a and Figure 9c for the FEM and in Figure 9b and Figure 9d for the RPIM.

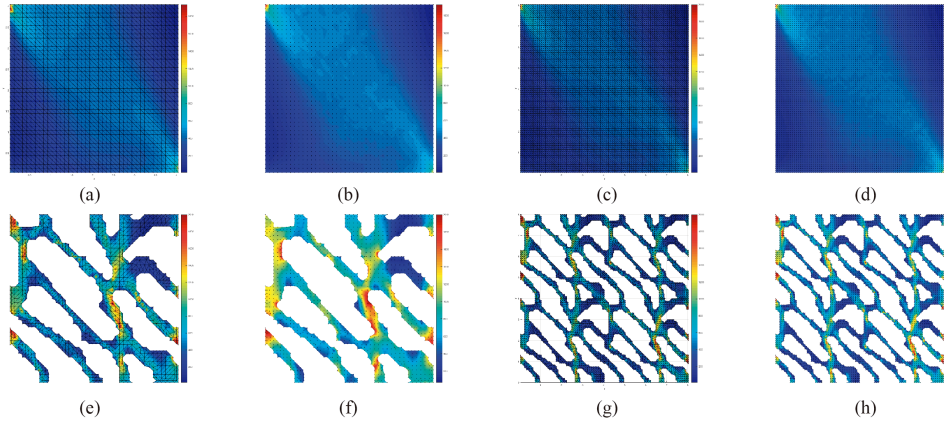


Figure 9 - Effective stress σ_{eff}^h for homogeneous model: Figure 9a: FEM 1X1; Figure 9b: RPIM 1X1; Figure 9c: FEM 2X2; Figure 9d: RPIM 2X2; and for heterogeneous models: Figure 9e: FEM 1X1; Figure 9f: RPIM 1X1; Figure 9g: FEM 2X2; Figure 9h: RPIM 2X2

It was used the homogenized stress concept to compare the stress fields obtained with the homogeneous RVE and with the heterogeneous RVE. The RVE's von Mises effective stress field (or any other RVE's stress/strain field) can be summarized in one scalar value - the homogenized von Mises effective stress - which can be defined with equation (12).

$$\sigma_{eff}^h = \frac{1}{n_Q} \sum_{i=1}^{n_Q} \sigma(\mathbf{x}_i)_{eff} \quad (12)$$

The number of integration points discretizing the problem domain not belonging to the boundary of the domain boundary is represented by n_Q . FEM integration mesh is constructed differently from the RPIM. Thus, the integration points of both techniques possess different spatial positions. To minimize this effect in order to avoid the (inaccurate) stress concentrations that appear at the domain boundaries, as Figure 9 shows, part of the domain was excluded: 2% of the domain boundary integration points that form the complete integration mesh from equation (12).

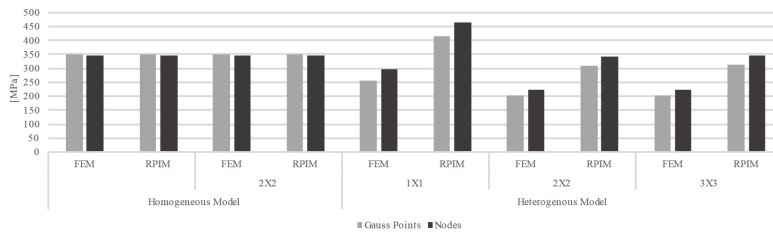


Figure 10 Homogenized von Mises effective stress σ_{eff}^h obtained with the FEM and the RPIM.

One of the main objectives of this work was to achieve a low-cost and efficient homogenization technique. Thus, in order to understand the computational cost of each analysis, the time-lapse of each structural analysis was recorded. Hence, in Figure 11 are shown the time-lapse of each structural analysis for the heterogeneous RVEs (with $r_n \times r_n$, $r_n = 1, 2, 3$) and for the homogeneous model (with $r_1 \times r_1$). In this comparison study, only the computational cost of the 1×1 homogeneous model is presented, since, as seen in Figure 10, it provides a similar result when compared with the 2×2 , and it also provides a close result when compared with the 3×3 heterogeneous model.

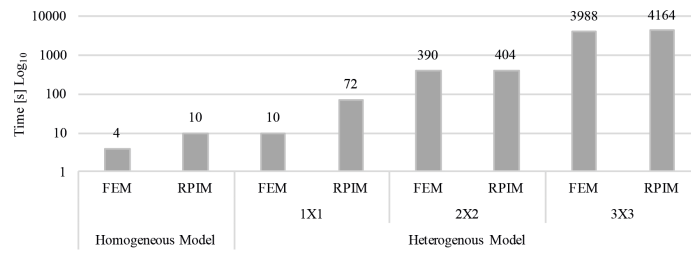


Figure 11 - Computational cost (in seconds) of each analysis.

4. Discussion

Regarding the RVE size analysis, it is possible to visualize in both figures the evolution of c_{ij} with respect to the number of repetitions of the corresponding basic unit RVE. Notice that for both RVEs types (benchmark and realistic), the value of each component of the constitutive matrix, c_{ij} , does not vary significantly with the number of repetitions, r_n . The results also indicate that for the fabricated benchmark RVE, as expected, θ does not suffers any significant variation (the average value is 90° with a standard deviation of 0°). For the realistic trabecular RVE the number of repetitions do not relevantly change the material orientation angle of the basic unit RVE, being the obtained average value: 127° with a standard deviation of 0° . Regarding the RVE rotation some of the differences obtained between the expected orientation and the obtained approximated material orientation θ are related with the modification of the source image due to the rotation process. In Figure 12 it is perceptible that due to the rotation the initial image is modified. The red circle marks the same region in distinct rotated images, and it is visible the modification of that region with the image rotation. This effect is caused by the low number of pixels of the figure. Increasing the number of pixels will lead to lower differences. However, it will lead also to a higher computational cost. The methodology here proposed is based in pixel information. Changing of the number of white pixels of

the image (a parameter highly related with the calculus of the MIL, as equation (3) indicates) result in the modification of the MIL value. This effect can be also observed in Figure 6, in which are represented the material orientation angles θ of the fitted ellipse and the expected ones.



Figure 12 - Image rotation process and inherent morphologic change, (a): Original Image; (b): 20° rotation; (c): 40° rotation; (d): 60° rotation; (e): 80° rotation.

Regarding the results obtained in Stress Analysis section, the homogenized von Mises effective stresses, σ_{eff}^h , obtained for each analyzed RVE (using both FEM and RPIM methodologies), are shown in Figure 10. From this figure it is perceptible that for the considered heterogeneous RVEs, as the model detail increases, σ_{eff}^h decreases. Notice that the model detail is governed by the number of repetitions (the 1×1 RVE has a lower detail than the 3×3 RVE). The analyses of the homogeneous models, regardless the discretization technique (FEM or RPIM) or the repetition pattern (1×1 and 2×2), present very similar results. Furthermore, these results are also very similar with the ones obtained with the RPIM using the 2×2 and 3×3 repetition heterogeneous models. Such similarity indicates that the proposed homogenization technique is capable to approximate the homogenized orthotropic material properties of a trabecular patch. Comparing the FEM with the RPIM, it is visible that the results obtained with the homogeneous RVEs are equivalent. However, the FEM and RPIM results obtained with the heterogeneous RVEs are not so close. This difference could be explained by locking effects in the FEM (plane strain triangular elements are being used).

Concerning the computational cost presented in Figure 10 it was shown that the 3×3 heterogeneous RVE produces results very close with the 1×1 homogeneous RVE. However, Figure 11 shows that the 3×3 heterogeneous RVE takes 4164s to analyze and the homogeneous RVE only requires 4-10s. Commonly, multiscale techniques use highly discretized RVEs, leading to high computational costs. However, as this study demonstrates, the proposed homogenization methodology is capable to reduce significantly the cost of a multiscale analysis, enabling more demanding and complex simulations.

5. Conclusions

In this work, a new multiscale methodology is proposed. The methodology uses a homogenization technique that, without any a-priory knowledge, allows to estimate the material properties of bone tissue using standard imaging techniques. The results obtained show that the methodologies used to create the fabric tensor and to obtain the mechanical properties are stable. Regarding the RVE size studies, it was demonstrated that the methodology is capable to consistently approximate the bone tissue material mechanical properties. It is expected that the proposed technique will be capable to reduce the cost of the multiscale analyses, allowing to simulate more complex problems.

Acknowledgement

The authors truly acknowledge the funding provided by Ministério da Ciência, Tecnologia e Ensino Superior - Fundação para a Ciência e a Tecnologia (Portugal), under Grants SFRH/BD/110047/2015 and by project funding MIT-EXPL/ISF/0084/2017. Additionally, the authors gratefully acknowledge the funding of Project NORTE-01-0145-FEDER-000022 - SciTech - Science and Technology for Competitive and Sustainable Industries, cofinanced by Programa Operacional Regional do Norte (NORTE2020), through Fundo Europeu de Desenvolvimento Regional (FEDER).

References

- [1] Abdelwahed B, Abdessalem C, Tarek M, Ridha H, Ali M. Multiscale approach including microfibril scale to assess elastic constants of cortical bone based on neural network computation and homogenization method. *International Journal for Numerical Methods in Biomedical Engineering*. 30(3):318–338. doi:10.1002/cnm.2604
- [2] Belinha J. *Meshless Methods in Biomechanics: Bone Tissue Remodelling Analysis*. Brimkov VE, Barneva RP, editors. Dordrecht: Springer Netherlands; 2014. (Lecture Notes in Computational Vision and Biomechanics). doi:10.1007/978-94-007-4174-4
- [3] Belinha J, Jorge RMN, Dinis LMJS. A meshless microscale bone tissue trabecular remodelling analysis considering a new anisotropic bone tissue material law. *Computer Methods in Biomechanics and Biomedical Engineering*. 2012;5842(August 2012):1–15. doi:10.1080/10255842.2012.654783
- [4] Belytschko T, Lu YY, Gu L. Element-free Galerkin methods. *International Journal for Numerical Methods in Engineering*. 1994 [accessed 2016 May 9];37(2):229–256. <http://onlinelibrary.wiley.com/doi/10.1002/nme.1620370205/abstract>. doi:10.1002/nme.1620370205
- [5] Carter DR, Fyhrie DP, Whalen RT. Trabecular bone density and loading history: Regulation of connective tissue biology by mechanical energy. *Journal of Biomechanics*. 1987;20(8):785–794. doi:10.1016/0021-9290(87)90058-3
- [6] Carter DR, Van Der Meulen MC, Beaupré GS. Mechanical factors in bone growth and development. *Bone*. 1996;18(1 Suppl):5S--10S. doi:10.1016/8756-3282(95)00373-8
- [7] Cowin SC. The relationship between the elasticity tensor and the fabric tensor.

- Mechanics of Materials. 1985;4(2):137–147. doi:10.1016/0167-6636(85)90012-2
- [8] Cowin SC, Doty SB. Tissue Mechanics. Springer Science; 2007.
- [9] Dinis LMJS, Jorge RMN, Belinha J. A 3D shell-like approach using a natural neighbour meshless method: Isotropic and orthotropic thin structures. Composite Structures. 2010;92(5):1132–1142. doi:10.1016/j.compstruct.2009.10.014
- [10] Dorozhkin S V. Nanosized and nanocrystalline calcium orthophosphates. Acta Biomaterialia. 2010;6(3):715–734. doi:10.1016/j.actbio.2009.10.031
- [11] Hart RT, Davy DT, Heiple KG. A Computational Method for Stress Analysis of Adaptive Elastic Materials With a View Toward Applications in Strain-Induced Bone Remodeling. Journal of Biomechanical Engineering. 1984;106(4):342. doi:10.1115/1.3138503
- [12] Huiskes R, Chao EYS. A survey of finite element analysis in orthopedic biomechanics: The first decade. Journal of Biomechanics. 1983;16(6):385–409. doi:10.1016/0021-9290(83)90072-6
- [13] Landis WJ. The strength of a calcified tissue depends in part on the molecular structure and organization of its constituent mineral crystals in their organic matrix. Bone. 1995;16(5):533–544. doi:10.1016/8756-3282(95)00076-P
- [14] Liu WK, Jun S, Zhang YF. Reproducing kernel particle methods. International Journal for Numerical Methods in Fluids. 1995;20(8–9):1081–1106. doi:10.1002/flid.1650200824
- [15] Moreno R, Borga M, Smedby O. Techniques for Computing Fabric Tensors - A Review. In: Mathematics and Visualization. Vol. 5. 2014. p. pp 271-292. doi:10.1007/978-3-642-54301-2_12
- [16] Moreno R, Smedby Ö, Pahr DH. Prediction of apparent trabecular bone stiffness through fourth-order fabric tensors. Biomechanics and Modeling in Mechanobiology. 2016 [accessed 2016 Nov 14];15(4):831–844. <http://link.springer.com/10.1007/s10237-015-0726-5>. doi:10.1007/s10237-015-0726-5
- [17] Natali AN, Carniel EL, Pavan PG. Constitutive modelling of inelastic behaviour of cortical bone. Medical Engineering & Physics. 2008;30(7):905–912. doi:10.1016/j.medengphy.2007.12.001
- [18] Wang JG, Liu GR. A point interpolation meshless method based on radial basis functions. International Journal for Numerical Methods in Engineering. 2002 [accessed 2016 May 9];54(11):1623–1648. <http://doi.wiley.com/10.1002/nme.489>. doi:10.1002/nme.489
- [19] Whitehouse WJ. The quantitative morphology of anisotropic trabecular bone. Journal of Microscopy. 1974;101(2):153–168. doi:10.1111/j.1365-2818.1974.tb03878.x
- [20] Wnek GE, Bowlin GL. Encyclopedia of Biomaterials and Biomedical Engineering. 2nd Editio. Wnek GE, Gary LB, editors. New York: CRC Press; 2008.
- [21] Wolff J. The Law of Bone Remodelling. Journal of Anatomy. 1886;155:217. doi:10.1097/00006534-198810000-00036
- [22] Zysset PK. A review of morphology–elasticity relationships in human trabecular bone: theories and experiments. Journal of Biomechanics. 2003 [accessed 2018 Apr 16];36(10):1469–1485. <https://www.sciencedirect.com/science/article/pii/S0021929003001283>. doi:10.1016/S0021-9290(03)00128-3

3.7 Contribution V: A multiscale homogenisation procedure combining the fabric tensor with a natural neighbour meshless method.

3.7.1 Highlights of Contribution: 3.7

This contribution focused on the bone mechanical properties definition using a homogenisation technique, defined by the fabric tensor concept, combined with the NNRPIM meshless method.

Therefore, the main contents of this publication include:

- I. Literature review on multiscale homogenisation techniques;
- II. Literature review on the usage of discrete numerical methods in biomechanics;
- III. Literature review on meshless methods applied in biomechanics;
- IV. Review of the NNRPIM formulation;
- V. Application and description of a homogenisation technique, where it is used the fabric tensor concept and a bone tissue phenomenological law, applied in cuboid bone micro-CT images that describe locally the bone morphology at its microscale;
- VI. Validation of the homogenisation methodology defined by a morphologically based fabric tensor methodology;
 - (a) Rotation Validation: by observing figure 3.8, were are present the differences between the expected principal direction angle and the obtained principal direction angle was possible to verify that the methodology it was able to identify the material principal direction, with a maximum error of 3,5%;
 - (b) Scale Validation: by observing the results in figure 3.9a and 3.9b it was possible to verify that the results were consistent despite the changes in the RVE size/scale. It was possible to verify that in the case of a truly periodic RVE, figure 3.9b, results are exactly the same despite the size/scale;
- VII. A structural application using FEM and NNRPIM was used to verify and to compare the heterogenous and equivalent homogeneous domains.
- VIII. The NNRPIM meshless method results were similar to the FEM methods, reinforcing the applicability of meshless methods in biomechanical applications.
- IX. Conclusions: Contribution V describes a methodology that allows to define the mechanical

properties of a micro-CT trabecular bone square patch without any a-priory knowledge. This contribution used the MIL methodology where it was proved that it was possible to acquire data to define the material orientation using medical images and so, define a homogenous methodology that allows to define homogeneous domains, with a less discretised mesh, by mechanical properties that are equivalent to a highly discretised heterogeneous domain. Thus, as demonstrated in figure 3.11, this methodology provides models defined with the homogeneous domains and mechanical properties that have a lower computational cost, when compared to the equivalent heterogeneous models.

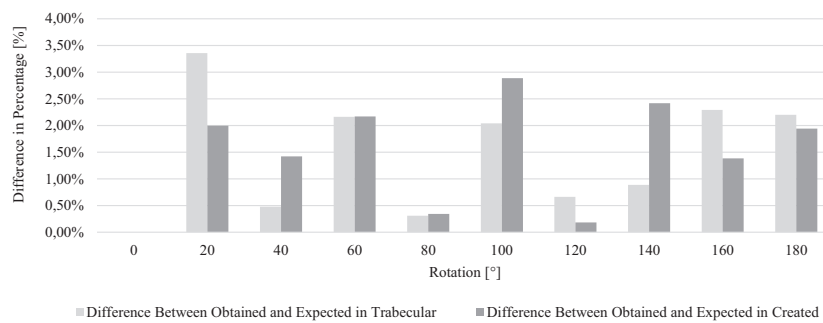
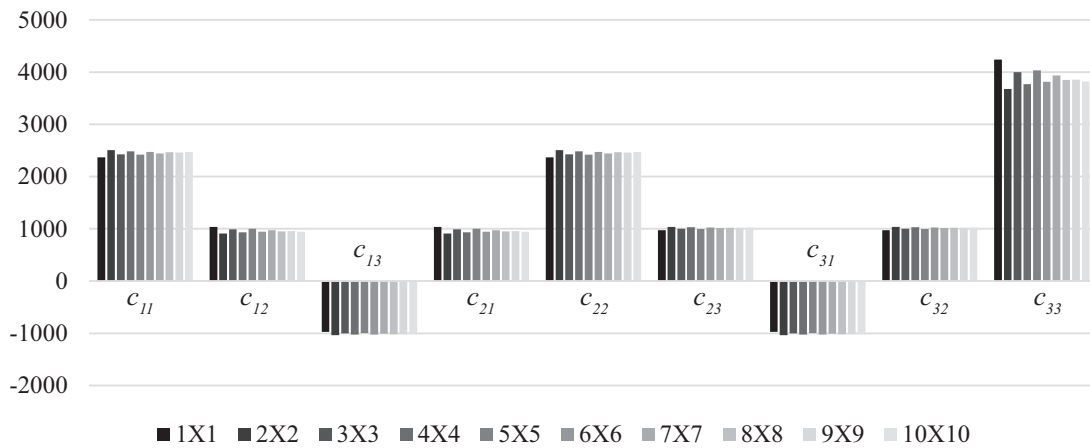
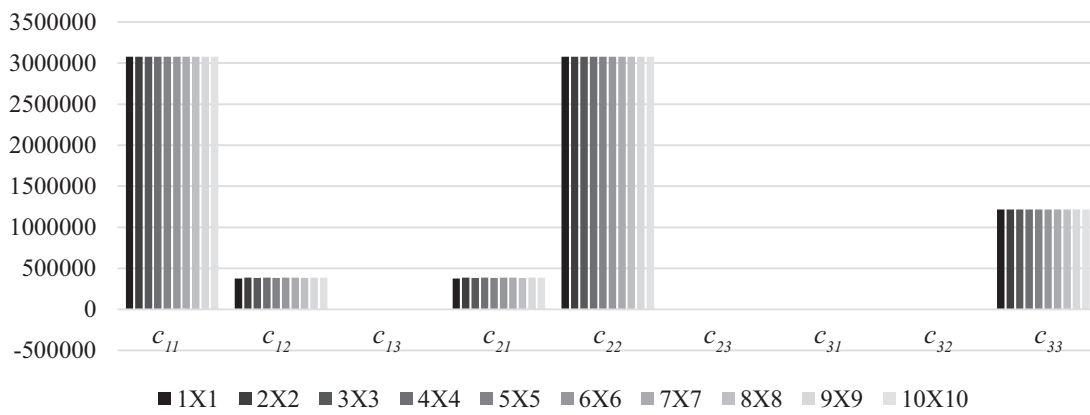


Figure 3.8: Contribution V: Rotation validation data.



(a)



(b)

Figure 3.9: Contribution V: Scale validation data: [3.9a](#) - data from a trabecular bone RVE; and [3.9b](#) - data from a created periodic benchmark.

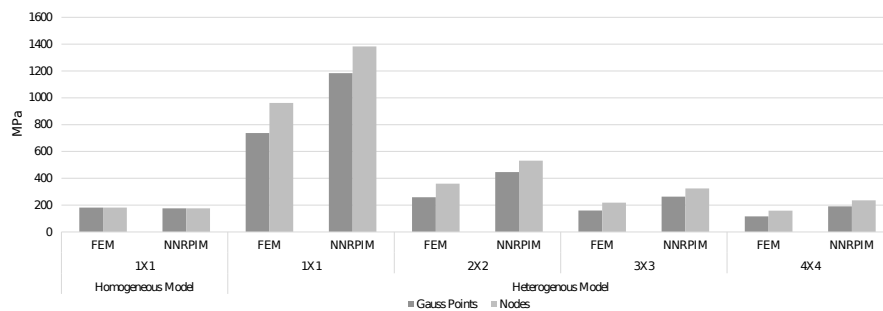


Figure 3.10: Contribution V: FEM vs NNRPIM methodology and homogenous and heterogeneous models convergence.

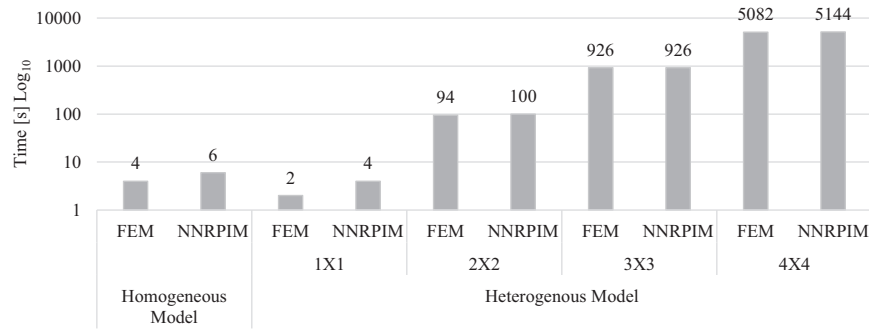


Figure 3.11: Contribution V: Computational cost.

The complete document can be found in the next pages.

A multiscale homogenization procedure combining the fabric tensor with a natural neighbour meshless method

M. Marques^a, J. Belinha^{a,b}, A.F. Oliveira^c, M.C. Manzanares Céspedes^d, R.M. Natal Jorge^{a,b}

^aINEGI- Institute of Science and Innovation in Mechanical and Industrial Engineering,
Porto, Portugal

^bFEUP - Faculty of Engineering of University of Porto, Porto, Portugal

^cICBAS - Institute of Biomedical Sciences Abel Salazar, Porto, Portugal

^dMuscular and Skeletal Pathology Research, Human Anatomy and Embryology Unit,
Universitat de Barcelona, Barcelona, Spain

Abstract

Bone is a material that can be classified as a hierarchical structure, where the different structural levels can be identified from the microscale to macroscale. Multiscale models enable to model the material using homogenization techniques. In this work an innovative homogenization technique for trabecular bone tissue is proposed, which uses the fabric tensor concept and a bone phenomenological material law, linking the apparent density with the trabecular bone mechanical proprieties. The proposed methodology efficiently homogenize the trabecular bone highly heterogeneous medium, allowing to define its homogenized microscale mechanical properties and to reduce the analysis computational cost (when compared with classical homogenization techniques). The homogenization technique is combined with the natural neighbour radial point interpolation method (NNRPIM). The NNRPIM uses the natural neighbour mathematical concept to enforce the nodal connectivity and build the background integration mesh, required to numerically integrate the integro-differential elasticity equations. Furthermore, the NNRPIM uses the radial point interpolators technique to construct its interpolating shape functions. In order to verify the efficiency of the technique several examples are solved using a confined square patch of trabecular bone under compression. In the end, the results obtained with a classic homogenization technique and the proposed methodology are compared.

Keywords: Meshless Methods, Natural Neighbour Radial Point Interpolation Method, Fabric Tensor, homogenization, multiscale

1. Introduction

Bone biomechanics is based on the idea that load bearing bone tissues are structurally optimized for their mechanical function [1, 2]. Being one of the main biomechanics field, bone biomechanics includes bone tissue engineering, mechanical characterization, bone remodelling and bone regeneration. Bone is a structure defined by bone matrix and by bone cells. Bone cells are responsible for producing bone matrix, where they became entrapped. These cells are the same that reabsorb bone to allow the replacement of old bone matrix by a newer one [3]. Bone can be classified as a hierarchical structure, where the different structural levels can be identified from the macroscale to microscale [4]. The macroscale (the entire bone) and the microscale (the trabecular architecture level) can be defined by different physical properties due to its different functional requirements, such as bone density and corresponding mechanical properties. At the microscale it is possible to recognize a non-homogeneous trabecular structure, which after being homogenized allows to define local anisotropic homogeneous mechanical properties, such as apparent density and directional Young moduli. Being bone a living tissue, it renews itself in the course of life by a biological process called bone remodelling [5]. In general, other biological process (such as growth, reinforcement, and resorption) are collectively termed as remodelling. This remodelling is progressive and is induced to adapt the bone morphology to any new external load. The concept that strain/stress induces bone remodelling was firstly reported by Wolff in 1886 [6]. Thus, Wolff reported that the orientation of trabecular bone coincides with the direction of the stress trajectories, proposing that bone loading is for some reason sensed by the bone. This principle of functional adaptation is known as Wolff's law. In 1939 Wolff's law was firstly described in vitro by Glucksmann in 1939 [7] and was described mathematically in 1965 by Pauwels et al. [8]. This formulation assumed that

exist and optimal mechanical stimulus that balanced the bone tissue resorption and deposition [9].

To study the remodelling process of the bone some authors developed models that considered bone as an isotropic material, a simplistic approach on the behaviour of trabecular bone, disregarding the importance of orientation in the remodelling process [10, 11, 12, 13]. To overcome this simplification, other models were created linking material density and orientation with its anisotropic mechanical properties. These remodelling models not only avoid any a priori assumption on material but also take into account the trabecular architecture features [14, 15, 16, 17]. Afterwards, considering both biological and mechanical factors based on bone cell activity, mechanobiological models were proposed, allowing to simulate the evolution of bone tissue considering both mechanical and biological stimuli [18, 19, 20, 21].

Recent works are starting to characterize bone mechanical properties with a concept called fabric tensor [22, 23]. The fabric tensor is a symmetric second rank tensor that characterizes the arrangement of a multiphase material, encoding the orientation and anisotropy of the material. Back in 1985, Cowin [24] developed a relation between the fourth rank elasticity tensor \mathbf{C}_{ijkl} and a fabric tensor \mathbf{A} , proving that an ellipsoid may be associated with the varieties of material symmetries observed in many natural materials. The fabric tensor can be obtained using mechanical based techniques or morphologic-based methods. Recall that morphologic-based methods use the interface between phases of the material to estimate the fabric tensor. The bone morphology is usually obtained using a micro-CT (at the microscale) or a CT (at the macroscale). Most of the available techniques, using morphologic-based methods, obtain the fabric tensor applying an orientation distribution function (ODF), which is estimated from an orientation-dependent feature of interest.

In mechanics, and in biomechanics, the accurate determination/characterization

of the material's mechanical properties is a key parameter, which will allow to describe and predict numerically the behaviour of such materials for different scenarios. Naturally, there is a never-ending interest from the scientific community concerning the material characterization, by developing/enhancing: constitutive laws, experimental procedures and computational tools/methodologies.

Discrete numerical methods allow to study and analyze in silico the behaviour of materials and structures. Today, the finite element method (FEM) is one of the most popular discrete numerical method [25]. Nevertheless, in the last few years a new class of discrete numerical method have appeared - the meshless methods [26]. The first developed meshless method dates from 1977, when Gingold et al. 1977 proposed the smoothed-particle hydrodynamics (SPH) method, that has a kernel approximation for a single function $u(x)$ in a domain Ω . This method was used for modeling astrophysical phenomena without boundaries, such as exploding stars and dust clouds [27]. From 1997 to now, many different methods were developed using different approaches: generalized finite difference method (Liszka et al., 1980) [28], diffuse element method (DEM) [29], element free Galerkin (EFG) method [30], meshless local Petrov-Galerkin (MLPG) method [31]. All these first developed meshless methods use approximation functions to construct the shape functions. Although this approach allows to obtain smooth variable fields, the shape functions obtained with it do not possess the delta Kronecker property, which hinders the imposition of the natural and essential boundary conditions. Thus, in order to overcome this difficulty and increase the efficiency of meshless methods, researchers start to focus on new approaches capable to produce interpolating shape functions. As a consequence, several efficient interpolating meshless methods were developed, such as the point interpolation method (PIM) [32, 33, 34] and the radial point interpolation method (RPIM) [35, 36] and its more recent variants, the Natural Neighbor Radial Point Interpolation Method (NNRPIM) [37] (based on the combination of the natural neighbour concept with the radial point interpolators), the Natural Radial Element Method (NREM) [38] (that combines the

simplicity of low-order finite elements connectivity with the geometric flexibility of meshless methods), the Meshless Local Radial Point Interpolation (MLRPI) method [39, 40, 41, 42] and the Spectral Meshless Radial Point Interpolation (SMRPI) method [43, 44, 45, 46, 47, 48, 49].

The main objective of this work is to combine a new developed multiscale homogenization technique with a truly meshless methods (the NNRPIM), aiming to achieve a low-cost and efficient multiscale technique. This manuscript is divided in the next following sections. In section 2 it is presented a brief description of the NNRPIM formulation - nodal connectivity, integration mesh, shape functions and elasto-static linear equations. Then, in section 3 the proposed homogenization technique is fully presented. The fabric tensor is introduced as well as all the required steps to determine consistently the material constitutive matrix. Afterwards, comes section 4, in which several micro-patches are analyzed in order to validate and calibrate the proposed methodology. Additionally, in the same section 4, a realistic bone patch is analyzed and the efficiency of the proposed homogenization technique is demonstrated. The manuscripts ends with a description of the main conclusions and final remarks in section 5.

2. Natural Neighbour Meshless Formulation

In meshless methods it is not necessary to discretize the problem domain using elements or any other lattice possessing a pre-established nodal/element connectivity. With meshless methods the problem domain can be discretized using an unstructured nodal set, whose nodes can be regularly or irregularly distributed [26]. In biomechanics this discretization flexibility is advantageous, since it permits to discretize the problem domains using directly medical images. This nodal set discretizing the problem domain does not represents a mesh because, besides the spatial coordinates of the nodes and possibly its individually material properties, no previous or additionally information is required. The

nodal connectivity (how each node interacts with its neighbours) is obtained after applying geometrical and mathematical constructions, allowing to define the influence-domain concept. Since the fundamental equations ruling the linear elastic problem studied in this work are integro-differential equations, it is necessary to construct a background integration mesh, which can be nodal dependent or nodal independent. Nodal independent constructions rely on the Gauss-Legendre quadrature scheme. A regular lattice is defined (covering the complete problem domain) and then each lattice cell is filled with integration points following Gauss-Legendre quadrature scheme [26]. Afterwards, integration points outside the problem domain are removed from the background mesh. Alternatively, nodal dependent constructions are much more appealing because they allow to directly define the spatial position and the integration weight of all integration points only using the spatial positions of the nodes. Meshless methods using this last approach are called truly meshless methods [26]. Regarding the shape functions, there are several approximation functions available in the literature for the construction of suitable meshless shape functions [26]. Preferentially, the produced shape functions should possess the delta Kronecker property, since it will ease the imposition of the essential and natural boundary conditions.

In this work it is used a truly interpolating meshless method - the NNRPIM. Thus, in this section, the main features of the NNRPIM are described with detail.

2.1. Nodal connectivity

The NNRPIM combines the Natural Neighbour concept [50] with the Radial Point Interpolators (RPI) [36]. First, the problem domain is discretized with a nodal cloud with N nodes: $\mathbf{X} = \{\mathbf{x}_1, \mathbf{x}_2, \dots, \mathbf{x}_N\} \in \Omega$. Then, applying the Natural Neighbour concept to the nodal distribution it is possible to construct the Voronoï Diagram discretizing the problem domain [51].

Recall that the Voronoï diagram of $\mathbf{N} = \{n_1, n_2, \dots, n_N\}$ is the partition of

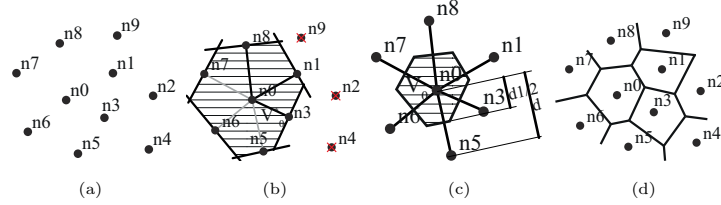


Figure 1: 1a: Neighbour nodes; 1b: Provisional Voronoi cell ; 1c: Voronoi cell ; 1d: Voronoi diagram

the function space discretized by \mathbf{X} in closed and convex sub-regions, V_i . Each V_i sub-region is associated to the node n_i in a way that no other point in the interior of V_i is closer to n_i than any other node $n_j \in \mathbf{N} \wedge j \neq i$. The set of Voronoi cells defines the Voronoi diagram, $\mathbf{V} = \{V_1, V_2, \dots, V_N\}$. The Voronoi cell is defined by, $V_i = \{\mathbf{x}_I \in \Omega \subset \mathbb{R}^d : \|\mathbf{x}_i - \mathbf{x}_I\| < \|\mathbf{x}_j - \mathbf{x}_I\|, \forall i \neq j\}$, being \mathbf{x}_I an interest point of the domain, d the domain's space dimensional order and $\|\cdot\|$ the Euclidean metric norm. Thus, the Voronoi cell V_I is the geometric place where all points are closer to \mathbf{x}_I than to any other node $\mathbf{x}_i \in \mathbf{X}$.

Since it is easy to represent, a 2D process to obtain the Voronoi cell of an hypothetical node n_0 is described in figure 1. Thus, starting from an initial set of nodes in the surroundings of a given central node n_0 , figure 1a, the closest nodes to the interest node n_0 are found using orthogonal planes and Boolean conditions, as shown in figure 1b. Then, the Voronoi cell of node n_0 is defined, figure 1c. Afterwards, the procedure can be applied to all the remaining nodes of the problem and the Voronoi diagram is constructed, figure 1d. The literature provides detailed description of this methodology [26].

Using the Voronoi diagram it is now possible to define the nodal connectivity. Consider a node $\mathbf{x}_i \in \mathbf{X}$, represented in figure 2, as the central node (inside the light-gray Voronoi cell). Notice that, as figure 2 shows, it is possible to define the levels of connectivity without using the influence-domain concept. Thus, the natural neighbours of the central node (the nodes inside the medium-gray Voronoi cells) are the first degree natural neighbours of the central node.

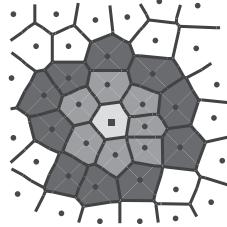


Figure 2: First and second degree natural neighbors in NNRPIM

This set (nodes inside the light-gray and medium-grey cells) is considered the first-degree influence cell of the central node. As figure 2 depicts, first-degree influence cells have a very low nodal connectivity, therefore other higher degree influence-cells can be defined, such as the second-degree influence cell. Thus, the second-degree influence cell is defined by adding to the first degree influence-cell all the nodes that are natural neighbours of the first natural neighbours of the central node (all the nodes inside the gray cells belong to the second-degree influence cell of the central node).

2.2. Numerical Integration

Additionally, using the Voronoï diagram it is possible to construct the background integration mesh. This feature allows to define a background integration mesh completely dependent on the nodal distributions, which is an advantage because it allows to obtain directly from the nodal cloud all the required mathematical entities for the meshless formulation (influence-domains, integration mesh and shape functions). Thus, as figure 3 shows, using the Delaunay triangulation [52], the geometrical dual of the Voronoï diagram, the integration cells and the integration points are fully defined [26]. This is done by taking the previously obtained Voronoï diagram and dividing each of its Voronoï cells into smaller sub-areas, using the Delaunay tessellation. The nodes of Voronoï cells sharing common boundaries are connected, figure 3a, and the overlap of both the Delaunay tessellation and the influence-cell boundaries lead to a smaller

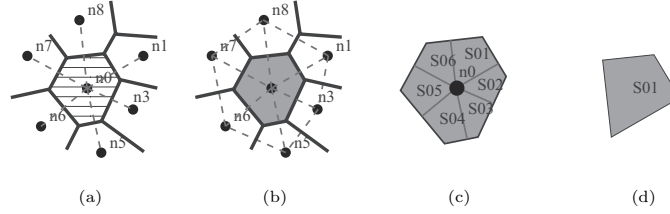


Figure 3: 3a: Voronoi cell; 3b: Delaunay triangulation, ; 3c: Sub-cells forming the initial Voronoi cell, ; 3d: Selected sub-cell

sub-cells, figure 3b [26]. As demonstrated in figure 3c, it is possible to divide each Voronoi cell, V_I into n sub-cells S_{Ii} , being n the total number of natural neighbors of a particular Voronoi cell, V_I . Having the sub-cells for all Voronoi cells, being each sub-area isoparameterized and filled with integration points using the Gauss-Legendre integration scheme, the integration mesh of the sub-cell is obtained, figure 3d. Repeating this process for all sub-cell, it is possible to obtain the complete background integration mesh of the problem domain.

2.3. Radial Point Interpolators

In order to construct the shape functions, the NNRPIM uses the Radial Point Interpolators (RPI) technique, which requires a radial basis function (RBF) and a complete polynomial basis [26]. Still, previous works on the NNRPIM showed that if the shape parameters of the RBF are chosen carefully, the polynomial basis can be removed from the formulation and substituted by a constant unity basis [37, 53]. Consider the function $u(\mathbf{x})$ defined in the domain $\Omega \subset \mathbb{R}^d$ and an interest point \mathbf{x}_I , possessing an influence-cell containing n nodes: $\mathbf{X}_I = \{\mathbf{x}_1, \mathbf{x}_2, \dots, \mathbf{x}_n\} \in \Omega \wedge \mathbf{x}_i \in \mathbb{R}^d$. It is assumed that only the nodes within the influence-cell of the interest point \mathbf{x}_I will be considered to interpolate $u(\mathbf{x}_I)$. Thus, the value of function $u(\mathbf{x}_I)$ can be defined with equation (1).

$$u(\mathbf{x}_I) = \sum_{i=1}^n [R_i(\mathbf{x}_I) \cdot a_i(\mathbf{x}_i)] + C_u \cdot b(\mathbf{x}_I) = \mathbf{R}(\mathbf{x}_I) \cdot \mathbf{a}(\mathbf{x}_I) + C_u \cdot b(\mathbf{x}_I) \quad (1)$$

In equation (1), $R_i(\mathbf{x}_I)$ is the RBF and $a_i(\mathbf{x}_i)$ are non-constant coefficients of $R_i(\mathbf{x}_I)$. The parameter C_u is the unity basis, being $C_u = 1$ and $b(\mathbf{x}_i)$ is a non-constant coefficient of C_u .

In this work it is used the multiquadric (MQ) RBF function, $R_i(\mathbf{x}_I) = R(r_{Ii}) = (r_{Ii}^2 + c^2)^p$, in which r_{Ii} is the distance between the interest point \mathbf{x}_I and a neighbour node \mathbf{x}_i , $r_{Ii} = |\mathbf{x}_i - \mathbf{x}_I|$, and c and p are two shape parameters of the MQ-RBF [54].

Notice that each integration weight possesses its own parameter. Thus, for integration point \mathbf{x}_I , the shape parameter c is obtained with: $c_I = \gamma\omega_I$, being ω_I the integration weight of integration point \mathbf{x}_I . In the literature it is possible to find research works showing the spatial dependence of the RBF's shape parameter [26] [55]. Previous works found that γ should be close to zero, $\gamma \cong 0$, and p should be close to one, $p \cong 1$, [37]. The work of Belinha and co-workers [37] [26] shows that these values cannot be $\gamma = 0$ and $p = 1$ because the use a null γ leads to singular moment matrix and the use of a positive integer value for p leads to a singular moment matrix. The same previous research works showed that values of p very close to the unit allow to obtain the most accurate solutions (regardless the analyzed problem). Thus, in this work, it was assumed $p = 0.9999$. Additionally, it was reported and demonstrated in [37] [26] that γ should be very close to zero, since when its magnitude grows, the RPI shape function loses its interpolation properties. Therefore, in order to "maximize" the interpolation property of the RPI shape functions, the authors have selected $\gamma = 0.0001$. In fact, optimizing the RBF's shape parameters is a never-ending research topic. Since the early works of Hardy [54] and Franke [56] up to today, several researchers have focus their efforts to this topic [57] [58] [59] [60].

Applying equation (1) to the node inside the influence-cell domain, considering each node as the interest point, and including an extra equation,

$$\sum_{i=1}^n a_i(\mathbf{x}_I) = 0 \quad (2)$$

to guarantee the unique solution [61], it is possible to obtain the following equation system (3),

$$\begin{bmatrix} u_1 \\ u_2 \\ u_3 \\ \vdots \\ 0 \end{bmatrix} = \begin{bmatrix} R(r_{11}) & R(r_{12}) & \dots & R(r_{1n}) & 1 \\ R(r_{21}) & R(r_{22}) & \dots & R(r_{2n}) & 1 \\ \vdots & \vdots & \ddots & \vdots & \vdots \\ R(r_{n1}) & R(r_{n2}) & \dots & R(r_{nn}) & 1 \\ 1 & 1 & \dots & 1 & 0 \end{bmatrix} \begin{bmatrix} a_1(\mathbf{x}_I) \\ a_2(\mathbf{x}_I) \\ \vdots \\ a_n(\mathbf{x}_I) \\ b(\mathbf{x}_I) \end{bmatrix} \Leftrightarrow \quad (3)$$

$$\begin{bmatrix} \mathbf{u}_s \\ 0 \end{bmatrix} = \begin{bmatrix} \mathbf{R} & \mathbf{C}_u \\ \mathbf{C}_u & 0 \end{bmatrix} \begin{bmatrix} \mathbf{a} \\ b \end{bmatrix}$$

where $\mathbf{u}_s = \{u_1, u_2, \dots, u_n\}^T$ is the vector of the nodal function values for the nodes in the influence-cell. Therefore, reorganizing equation (3) it is possible to obtain the non-constant coefficients,

$$\begin{bmatrix} \mathbf{a} \\ b \end{bmatrix} = \begin{bmatrix} \mathbf{R} & \mathbf{C}_u \\ \mathbf{C}_u & 0 \end{bmatrix}^{-1} \begin{bmatrix} \mathbf{u}_s \\ 0 \end{bmatrix} \Rightarrow \begin{bmatrix} \mathbf{a} \\ b \end{bmatrix} = [\mathbf{M}]^{-1} \begin{bmatrix} \mathbf{u}_s \\ 0 \end{bmatrix} \quad (4)$$

Substituting in equation (1), the result from equation (4), allows to obtain the interpolation function (5) for an interest point \mathbf{x}_I .

$$\Phi(\mathbf{x}_I) = \{\varphi_1(\mathbf{x}_I), \varphi_2(\mathbf{x}_I), \dots, \varphi_n(\mathbf{x}_I), \Psi_c\} \quad (5)$$

$$u(\mathbf{x}_I) = \{R_1(\mathbf{x}_I), R_2(\mathbf{x}_I), \dots, R_n(\mathbf{x}_I), C_u\} M^{-1} \begin{Bmatrix} \mathbf{u}_s \\ 0 \end{Bmatrix} = \Phi(\mathbf{x}_I) \begin{Bmatrix} \mathbf{u}_s \\ 0 \end{Bmatrix} \quad (6)$$

The last term of the interpolation function, Ψ_c , comes from the constant term C_u and it does not possess useful physical meaning. Thus, only the n first components of $\Phi(\mathbf{x}_I)$ are relevant and form the interpolation function [38]. The

partial derivative of $\Phi(\mathbf{x}_I)$ with respect to a variable ξ is defined by equation (7),

$$\Phi_\xi(\mathbf{x}_I) = \{R_1(\mathbf{x}_I), R_2(\mathbf{x}_I), \dots, R_n(\mathbf{x}_I), C_u\}_\xi M^{-1} \quad (7)$$

Notice that since C_u is a constant scalar, then $C_{u,\xi} = 0$. The partial derivatives of the MQ-RBF with respect to a variable ξ are obtained with equation (8),

$$R_\xi(r_{ij}) = 2p(r_{ij}^2 + c^2)^{p-1}(\xi_j - \xi_i) \quad (8)$$

The NNRPIM shape functions possess several important numerical properties, such as the unit partition property and the delta Kronecker property, which permits to impose the essential and natural boundary conditions using direct imposition methods. In the literature it is possible to find complete studies regarding its numerical properties [26], [51].

2.4. Discrete System of Equations

Consider the body described by the domain $\Omega \subset \mathbb{R}^2$ and bounded by Γ , where $\Gamma \in \Omega : \Gamma_u \cup \Gamma_t = \Gamma \wedge \Gamma_u \cap \Gamma_t = \emptyset$, being Γ_u the essential boundary and Γ_t the natural boundary. The equilibrium equations governing the linear elastostatic problem are defined as $\nabla \mathbf{\Lambda} + \mathbf{b} = 0$ in Ω . Being ∇ the gradient operator; $\mathbf{\Lambda}$ the Cauchy stress tensor for a kinematic admissible displacement field \mathbf{u} and \mathbf{b} the body force per unit volume. The boundary conditions are given by, $\mathbf{\Lambda} \mathbf{n} = \bar{\mathbf{t}}$ on Γ_t and $\mathbf{u} = \bar{\mathbf{u}}$ on Γ_u , where $\bar{\mathbf{u}}$ is the prescribed displacement on the essential boundary Γ_u , $\bar{\mathbf{t}}$ is the traction on the natural boundary Γ_t and \mathbf{n} is the unit outward normal to the boundary of domain Ω . Using the Voigt notation and assuming the Galerkin procedure for linear elasticity, the weak form for the discrete problem can be written as equation (9),

$$\delta L = \int_{\Omega} \delta \boldsymbol{\varepsilon}^T \boldsymbol{\sigma} d\Omega - \int_{\Omega} \delta \mathbf{u}^T \mathbf{b} d\Omega - \int_{\Gamma_t} \delta \mathbf{u}^T \bar{\mathbf{t}} d\Gamma_t = 0 \quad (9)$$

Where $\boldsymbol{\varepsilon}$ is the strain vector defined as $\boldsymbol{\varepsilon} = \mathbf{L}\mathbf{u}$, being \mathbf{L} a differential operator,

$$\mathbf{L}_{2D} = \begin{bmatrix} \frac{\partial}{\partial x} & 0 & \frac{\partial}{\partial y} \\ 0 & \frac{\partial}{\partial y} & \frac{\partial}{\partial x} \end{bmatrix}^T \quad (10)$$

It is possible to directly correlate the stress field with the strain field using the Hooke Law: $\boldsymbol{\sigma} = \mathbf{c}\boldsymbol{\varepsilon} = \mathbf{c}\mathbf{L}\mathbf{u}$. Being \mathbf{c} the material constitutive matrix, which can be obtained inverting the compliance elasticity matrix, $\mathbf{c} = \mathbf{s}^{-1}$. The compliance elasticity matrix \mathbf{s} for the general isotropic material case is defined by equation (11) for the 2D plane strain formulation.

$$S_{2D} = \begin{bmatrix} \frac{1-\nu_{xx}\nu_{xx}}{E_{xx}} & \frac{-\nu_{yz}-\nu_{zx}\nu_{yz}}{E_{yy}} & 0 \\ \frac{-\nu_{xy}-\nu_{zy}\nu_{xz}}{E_{xx}} & \frac{1-\nu_{yy}\nu_{yz}}{E_{yy}} & 0 \\ 0 & 0 & \frac{1}{G_{xy}} \end{bmatrix} \quad (11)$$

E_{ii} is the Young modulus in direction i , ν_{ij} is the Poisson ratio which characterizes the deformation rate in direction j when a force is applied in direction i , G_{ij} is the shear modulus which characterizes the variation angle between directions i and j . Each node \mathbf{x}_i discretizing the problem domain possesses two degrees of freedom: $\mathbf{u}_i = \{u_i, v_i\}$. Thus, in order to interpolate the virtual displacement at the interest point \mathbf{x}_i equation (6) can be written as,

$$\delta \mathbf{u}(\mathbf{x}_I) = \delta \mathbf{u}_I = \mathbf{I} \begin{Bmatrix} \Phi_I \\ \Phi_I \end{Bmatrix} \delta \mathbf{u}_s = \begin{bmatrix} \varphi_1(\mathbf{x}_I) & 0 & \dots & \varphi_n(\mathbf{x}_I) & 0 \\ 0 & \varphi_1(\mathbf{x}_I) & \dots & 0 & \varphi_n(\mathbf{x}_I) \end{bmatrix} \begin{Bmatrix} \delta u_1 \\ \delta v_1 \\ \vdots \\ \delta u_n \\ \delta v_n \end{Bmatrix} = \mathbf{H}_i \delta \mathbf{u}_s \quad (12)$$

Being \mathbf{I} a 2×2 identity matrix. Substituting $\boldsymbol{\varepsilon} = \mathbf{L}\mathbf{u}$ in the first term of

equation (9) and considering equation (12) it is possible to write,

$$\begin{aligned} \int_{\Omega} \delta \boldsymbol{\varepsilon}^T \boldsymbol{\sigma} d\Omega &= \int_{\Omega} (\mathbf{L} \delta \mathbf{u})^T \mathbf{c}(\mathbf{L} \mathbf{u}) d\Omega = \int_{\Omega} (\mathbf{L} \mathbf{H}_I \delta \mathbf{u}_s)^T \mathbf{c}(\mathbf{L} \mathbf{H}_I \mathbf{u}_s) d\Omega = \\ &= \int_{\Omega} \delta \mathbf{u}_s^T \mathbf{B}_I^T \mathbf{c} \mathbf{B}_I \mathbf{u}_s d\Omega = \delta \mathbf{u}_s^T \int_{\Omega} \mathbf{B}_I^T \mathbf{c} \mathbf{B}_I d\Omega \mathbf{u} \end{aligned} \quad (13)$$

Being \mathbf{B}_I the local deformation matrix defined for the n nodes constituting the influence-cell of interest point \mathbf{x}_I ,

$$\begin{bmatrix} \frac{\partial \varphi_1(\mathbf{x}_I)}{\partial x} & 0 & \frac{\partial \varphi_2(\mathbf{x}_I)}{\partial x} & 0 & \dots & \frac{\partial \varphi_n(\mathbf{x}_I)}{\partial x} & 0 \\ 0 & \frac{\partial \varphi_1(\mathbf{x}_I)}{\partial y} & 0 & \frac{\partial \varphi_2(\mathbf{x}_I)}{\partial y} & \dots & 0 & \frac{\partial \varphi_n(\mathbf{x}_I)}{\partial y} \\ \frac{\partial \varphi_1(\mathbf{x}_I)}{\partial y} & \frac{\partial \varphi_1(\mathbf{x}_I)}{\partial x} & \frac{\partial \varphi_2(\mathbf{x}_I)}{\partial y} & \frac{\partial \varphi_2(\mathbf{x}_I)}{\partial x} & \dots & \frac{\partial \varphi_n(\mathbf{x}_I)}{\partial y} & \frac{\partial \varphi_n(\mathbf{x}_I)}{\partial x} \end{bmatrix} \quad (14)$$

Using an analogous procedure for the second and third terms of equation (9), the following force vectors are obtained,

$$\mathbf{f}_b = \int_{\Omega} \delta \mathbf{u}_s^T \mathbf{b} d\Omega = \int_{\Omega} (\mathbf{H}_I \delta \mathbf{u}_s)^T \mathbf{b} d\Omega = \delta \mathbf{u}_s^T \int_{\Omega} \mathbf{H}_I^T \mathbf{b} d\Omega \quad (15)$$

$$\mathbf{f}_t = \int_{\Gamma_t} \delta \mathbf{u}_s^T \bar{\mathbf{t}} d\Gamma_t = \int_{\Gamma_t} (\mathbf{H}_I \delta \mathbf{u}_s)^T \bar{\mathbf{t}} d\Gamma_t = \delta \mathbf{u}_s^T \int_{\Gamma_t} \mathbf{H}_I^T \bar{\mathbf{t}} d\Gamma_t \quad (16)$$

Thus, equation (9) can be re-written as,

$$\delta L = \delta \mathbf{u}^T \int_{\Omega} \mathbf{B}_I^T \mathbf{c} \mathbf{B}_I d\Omega \mathbf{u} - \delta \mathbf{u}_s^T \int_{\Omega} \mathbf{H}_I^T \mathbf{b} d\Omega - \delta \mathbf{u}_s^T \int_{\Gamma_t} \mathbf{H}_I^T \bar{\mathbf{t}} d\Gamma_t = 0 \quad (17)$$

The equation system can be presented in the matrix form: $\mathbf{K} \mathbf{u} = \mathbf{f}$. Being \mathbf{K} the stiffness matrix, \mathbf{u} the displacement field vector and $\mathbf{f} = \mathbf{f}_b + \mathbf{f}_t$ the vector of applied forces. Since the RPI shape function possesses the delta Kronecker property, the essential boundary conditions can be directly applied in the stiffness matrix [37].

After the determination of the displacement field solving the linear equation system $\mathbf{K}^{-1}\mathbf{f} = \mathbf{u}$, the strain in an interest point $\mathbf{x}_I \in \Omega$ can be obtained using $\boldsymbol{\varepsilon}(\mathbf{x}_I) = \mathbf{L}\mathbf{u}(\mathbf{x}_I)$, and then, considering the Hooke Law, $\boldsymbol{\sigma}(\mathbf{x}_I) = \mathbf{c}(\mathbf{x}_I)\boldsymbol{\varepsilon}(\mathbf{x}_I)$, it is possible to determine the stress field at \mathbf{x}_I . It is possible to obtain the three principal stresses $\boldsymbol{\sigma}(\mathbf{x}_I)_i$ for each interest point, \mathbf{x}_I , $\det(\Lambda(\mathbf{x}_I) - \sigma(\mathbf{x}_I)_i \mathbf{I}) = 0$ and the three principal directions: $\mathbf{n}(\mathbf{x}_I)_i : (\Lambda(\mathbf{x}_I) - \sigma(\mathbf{x}_I)_i \mathbf{I})\mathbf{n}(\mathbf{x}_I)_i = 0$, being $\Lambda(\mathbf{x}_I)$ the Cauchy stress tensor obtained for the interest point and \mathbf{I} a identity 2×2 matrix. In the general 3D case, using the three principal stresses $\boldsymbol{\sigma}(\mathbf{x}_I)_i$ and equation (18), the von Mises effective stress of interest point \mathbf{x}_I is obtained.

$$\sigma(\mathbf{x}_I)_{eff} = \sqrt{\frac{1}{2} \left((\sigma(\mathbf{x}_I)_1 - \sigma(\mathbf{x}_I)_2)^2 + (\sigma(\mathbf{x}_I)_2 - \sigma(\mathbf{x}_I)_3)^2 + (\sigma(\mathbf{x}_I)_3 - \sigma(\mathbf{x}_I)_1)^2 \right)} \quad (18)$$

Comparing NNRPIM with other meshless methods, the NNRPIM shows a higher re-meshing flexibility and a higher accuracy on the solution variable field [62, 63]. Another benefit of the NNRPIM compared to others meshless methods it is the lower computational cost during the processing phase of the numerical analysis (after the construction of the nodal connectivity, integration mesh and shape functions), that can be relevant in demanding non-linear analysis, such as material non-linearity, large deformations, transient dynamic analysis [37, 64, 53, 65, 66, 67]. Being the nodal connectivity and integration mesh constructed only based on the nodal discretization, this becomes an advantage in the biomechanical analysis, since it is possible to analyze extremely irregular meshes and convex boundaries [68].

3. Homogenization Technique

In this section, the homogenization technique is fully described. First, from cuboid bone micro-CT images it were selected 2D images (thin slices) describing locally the bone morphology at its microscale. Then, the fabric tensor concept

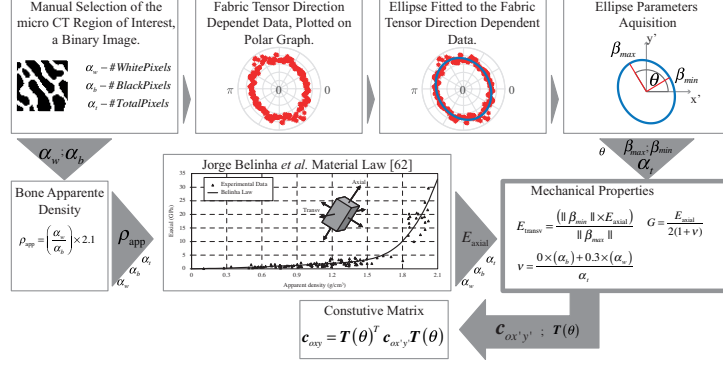


Figure 4: Microscale homogenization technique

was applied to these selected square microscale images in order to determine its material orientation. Additionally, a bone tissue phenomenological law was used to obtain the homogenized material properties of the microscale patch. This homogenization technique allows to define the anisotropic mechanical proprieties of the trabecular bone. The algorithm describing the proposed homogenization technique is presented in figure 4 and its features are presented in the following subsections.

3.1. Fabric tensor morphologic based method

The 2D square patch used to define the morphologic based fabric tensor can be selected from the set of micro-CT by defining a relevant micro-CT slice image and then identifying a square region of interest with relevant information (the binary image represented in the left-upper image of figure 4). This square patch, a gray scale image, is then binarized, resulting in a binary image I_s that contains the characteristic morphology of the (local) trabecular bone.

To define the fabric tensor it was used a methodology developed by Whitehouse [69]. In this methodology the number of interceptions between a parallel family line set, with direction ι , with the interface between both phases of the material is counted, $Int(\iota)$. The length of the parallel lines family, h for the ι direction is also obtained. With h and ι it is possible to defined the an orienta-

tion distribution function (ODF), which in this case is called mean interception length (MIL), equation (19).

$$MIL(\iota) = \frac{h}{Int(\iota)} \quad (19)$$

This methodology is considered a golden standard since exists a large amount of works that sustain its appropriateness to predict mechanical properties of trabecular bone [69, 70, 71, 72, 73]. The literature shows that for many types of materials, in particularly bone trabeculae, when the ODF data is disposed on a polar plot and fitted in an ellipse, the corresponding ellipse parameters can be correlated with the material orientation (its anisotropy) [74].

The dimensional information of I_s is used to define the size of an image containing the family of parallel lines with $\iota = 0^\circ$. Counting the interceptions of those parallel lines with the boundaries of the binary image square patch, it is possible to obtain the orientation-dependent feature.

Rotating the family of parallel line image with ι between 0° and 180° , and then counting the interception of the family of parallel lines with the square patch binary image I_s , is possible to obtain the ODF of the I_s . The created data for ι between $]180^\circ, 360^\circ[$ is a $[0^\circ, 180^\circ]$ data repetition, since the orientation-dependent feature depends only on the orientation and it is not influenced by the direction. Afterwards, the ODF data is plotted using polar coordinates. This data is then fitted into an ellipse, from which it is possible to obtain the material orientation of the trabecular micropatch (see both central boxes of figure 4). From the fitted ellipse it is possible to obtain the ellipse minor axis length, β_{min} , and major axis length, β_{max} and θ , the angle of ellipse major axis with the polar plot horizontal axis.

3.2. Phenomenological material law method

Using the information from the fitted ellipse and the average apparent density of the binary image I_s it will be possible to define the homogenized anisotropic mechanical properties of I_s . Notice that the average apparent density, ρ_{app} , of

Table 1: Coefficients from Belinha's material law [75].

	$j = 0$	$j = 1$	$j = 2$	$j = 3$
a_j	0.0E + 00	7.216E + 02	8.059E + 02	0.0E + 00
b_j	-1.770E + 05	3.861E + 05	-2.798E + 05	6.836E + 04

the binary image I_s can be obtained using the number of white pixels, α_w , and black pixels, α_b , of I_s as equation (20) shows.

$$\rho_{\text{app}} = \left(\frac{\alpha_w}{\alpha_b} \right) \rho_{\text{app}}^{\text{cortical}} \quad (20)$$

being the cortical bone apparent density assumed as $\rho_{\text{app}}^{\text{cortical}} = 2.1 \text{g/cm}^3$. Using the ρ_{app} and the phenomenological material law defined by Belinha and co-workers [75], the axial Young's modulus E_{axial} can be defined. As recommended in [75], if $\rho_{\text{app}} \leq 1.3$ it should be applied equation (21), otherwise it should be used equation (22). The coefficients a_j and b_j can be found in table 1.

$$E_{\text{axial}} = \sum_{j=0}^3 a_j \rho_{\text{app}} \text{ if } \rho_{\text{app}} \leq 1.3 \quad (21)$$

$$E_{\text{axial}} = \sum_{j=0}^3 b_j \rho_{\text{app}} \text{ if } \rho_{\text{app}} > 1.3 \quad (22)$$

To define the transverse elastic modulus E_{transv} it is used the relation between the ellipse minor axis length, β_{min} , and major axis length, β_{max} , and the axial elastic modulus E_{axial} as equation (23) shows.

$$E_{\text{transv}} = \frac{(\|\beta_{\text{min}}\| E_{\text{axial}})}{\|\beta_{\text{max}}\|} \quad (23)$$

The Poisson's coefficient, ν , was calculated according the mixture theory using the relation between white and black pixels, as represented in equation

(24).

$$\nu = \frac{0.0 (\alpha_b) + 0.3 (\alpha_w)}{\alpha_t} \quad (24)$$

being α_t the total number of pixels of the binary image I_s . The shear modulus, G , was expeditiously calculated using equation (25).

$$G = \frac{E_{\text{axial}}}{2(1 + \nu)} \quad (25)$$

As figure 4 shows, using the homogenized material properties (E_{axial} , E_{transv} , ν and G) the constitutive matrix is defined $\mathbf{c}_{ox'y'}$, for the $ox'y'$ local coordinate system (oriented with the material principal axis, following the principal directions 'axial' and 'transverse'). Using the angle θ obtained from the ellipse fitting, it is defined the transformation rotation matrix \mathbf{T} , equation (26).

$$\mathbf{T}(\theta) = \begin{bmatrix} \cos(\theta) & -\sin(\theta) & 0 \\ \sin(\theta) & \cos(\theta) & 0 \\ 0 & 0 & 1 \end{bmatrix} \quad (26)$$

Afterwards, it is possible to define the material constitutive matrix in the global axis with,

$$\mathbf{c}_{oxy} = \mathbf{T}(\theta)^T \mathbf{c}_{ox'y'} \mathbf{T}(\theta) = \begin{bmatrix} c_{11} & c_{12} & c_{13} \\ c_{21} & c_{22} & c_{23} \\ c_{31} & c_{32} & c_{33} \end{bmatrix} \quad (27)$$

being $\mathbf{c}_{ox'y'}$ defined with $\mathbf{c} = \mathbf{s}^{-1}$, in which the anisotropic compliance matrix \mathbf{s} is obtained for the material axis $ox'y'$ with equation (11).

4. Numerical Examples

First, in order to validate the homogenization methodology, some numerical tests were performed, involving size and rotation analyses of predefined I_s binary images.

Thus, to verify the robustness of the proposed technique, a predefined binary image (with a known preferential material orientation) was analyzed. Then, the input image was rotated and it was verified if the ellipse fitted from the fabric tensor based methodology had β_{max} aligned with the material orientation of the image. In this case it was considered an angle increment of 20° for the family of parallel lines rotation.

Furthermore, in order to verify the behaviour of the proposed homogenization technique, it was performed a numerical structural analysis using two distinct geometrical models (a homogeneous model and a heterogeneous model). The numerical analysis was performed with 2 distinct numerical methods, the FEM and the NNRPIM. Concerning the NNRPIM formulation used in this work, it was assumed: only first degree influence cells; one integration point per each integration sub-cell; the MQ-RBF shape parameters suggested in the literature ($c = 0.0001$ and $p = 0.9999$); and a constant polynomial basis.

4.1. Validation of MIL methodology

The validation of the MIL methodology will be assessed with two distinct studies. The first study will verify the influence of the size of the representative volume element (RVE) in the determination of the anisotropic constitutive matrix. In the second study, the consistency of the methodology will be tested, by imposing known material orientations to the model.

4.1.1. RVE size

In order to understand the influence of the size of the RVE in the proposed methodology, two distinct models were constructed, figure 5a and figure 5d. The model presented in figure 5a is a benchmark fabricated unitary binary image showing a well-defined material orientation (90°). This model was repeated $r_n \times r_n$, being r_n the number of repetitions of the RVE. For illustration purposes, figure 5b shows its 2×2 repetition and 5c its 10×10 repetition. Alternatively, the model shown in figure 5d represents a realistic trabecular square patch unitary binary image obtained from a micro-CT image. Similarly, this realistic RVE

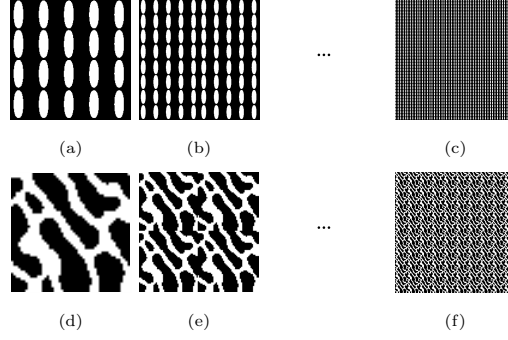


Figure 5: Binary images used to verify the *MIL* dependence on the RVE size. Benchmark fabricated unitary image, 5a. Realistic binary image from a micro-CT, 5d; To analyze the effect of using different RVE sizes, the binary images were repeated from a 2×2 repetition, 5b and 5e to a 10×10 repetitions, 5c and 5f, respectively

was repeated $r_n \times r_n$ and examples for the 2×2 repetition and 10×10 repetition are shown respectively in figure 5e and figure 5f.

The propose homogenization methodology was applied to each one of the RVEs (fabricated benchmark and realistic square patch) and their several corresponding repetitions $r_n \times r_n$, being $r_n = 1, 2, 3, \dots, 10$.

Following the methodology described in section 3 it was possible to obtain all the components of the constitutive tensor \mathbf{c}_{oxy} , equation (27). Figures 6a and 6b show the components of the constitutive matrix that are obtained using the proposed homogenization methodology for the fabricated benchmark RVE and the realistic trabecular RVE, respectively. In both figures it is possible to visualize the evolution of c_{ij} with respect the number of repetitions of the corresponding basic unit RVE. For both RVEs types (benchmark and realistic), it is perceptible that the value of each component of the constitutive matrix, c_{ij} , does not vary significantly with the number of repetitions, r_n .

Concerning the angle θ , which indicates the orientation of the material, see equation (27) and figure 4, the obtained values for θ for the distinct RVE's repetitions are presented in table 2. Notice that for the fabricated benchmark

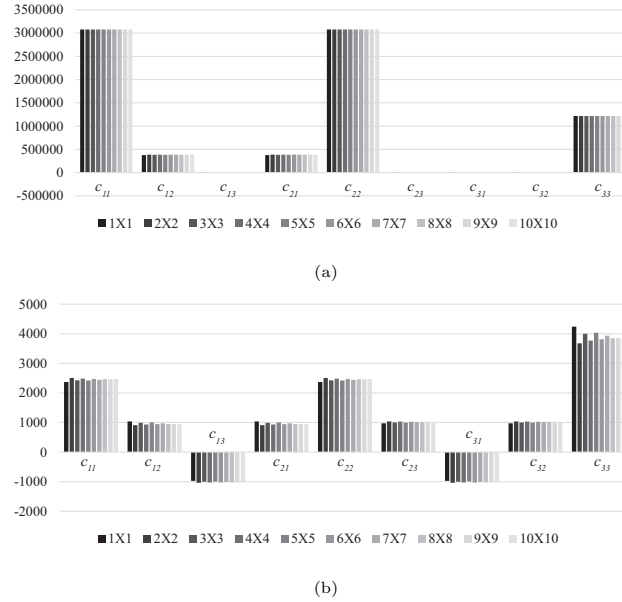


Figure 6: Constitutive matrix values obtained using a unitary image and up to $10\times$ repetitions. 6a: Results for the trabecular square patch obtained using the micro-CT image. 6b: Results for the created image.

RVE, as expected, θ does not suffers any significant variation (the average value is 90° with a standard deviation of 0°). Similar, for the realistic trabecular RVE the number of repetitions do not relevantly change the material orientation angle of the basic unit RVE (118°), being the obtained average value: 115.7° with a standard deviation of 1° .

4.1.2. RVE rotation

The aim of this study is to verify if the developed methodology is capable to deliver accurate material orientations. Thus, both RVEs already presented - the benchmark fabricated RVE, figure 5a, and the realistic trabecular RVE, figure 5d - were rotated in relation the their initial position following increment angles of 20° , between the interval $[0^\circ, 180^\circ]$. In figure 7 and figure 8 are shown the results

Table 2: Relation between the image repetition and the corresponding obtained θ

	Repetition	1	2	3	4	5	6	7	8	9	10	Average	SD
θ	Created	90	90	90	90	90	90	90	90	90	90	90	0
	Trabecular	118	114	116	115	117	115	116	115	115	115	116	1

of the several analysis performed. It is possible to visualize the orientation/size of the produced ellipse and the corresponding angle of the material. The originals images with respective *MIL* data and fitted ellipse are represented in figure 7a and figure 8a.

In figure 9a are represented the material orientation angles θ of the fitted ellipse and the expected ones. For instances, for the 20° rotation of the realistic trabecular RVE, it was obtained a 152.22° θ orientation, however it was expected 140.143° , resulting in a difference of 12.08° . For the cases presented in this work the average difference between the obtained material orientation and the expected angle is 5.83° .

The difference between the expected orientation and the obtained material orientation θ (coming from the proposed MIL algorithm) can be explained by the change of the source image upon the rotation process, performed using a MATLAB 2016b function. This leads to the change of the number of white pixels of the image, a parameter highly related with the calculus of the *MIL*, as equation (19) shows. To better illustrate this feature, figure 10 demonstrates the image modification due to its rotation, where the red circle marks the same region in different rotated images.

4.2. Structural application

The objective of this section is to verify if a homogenized RVE (whose homogenized anisotropic mechanical properties were obtained with proposed methodology) is capable to produce a homogenized von Mises effective stress field similar with the one obtained with a heterogeneous RVE.

Thus, in order to assess the efficiency of the proposed homogenization technique, it is performed a structural analysis of the realistic trabecular RVE pre-

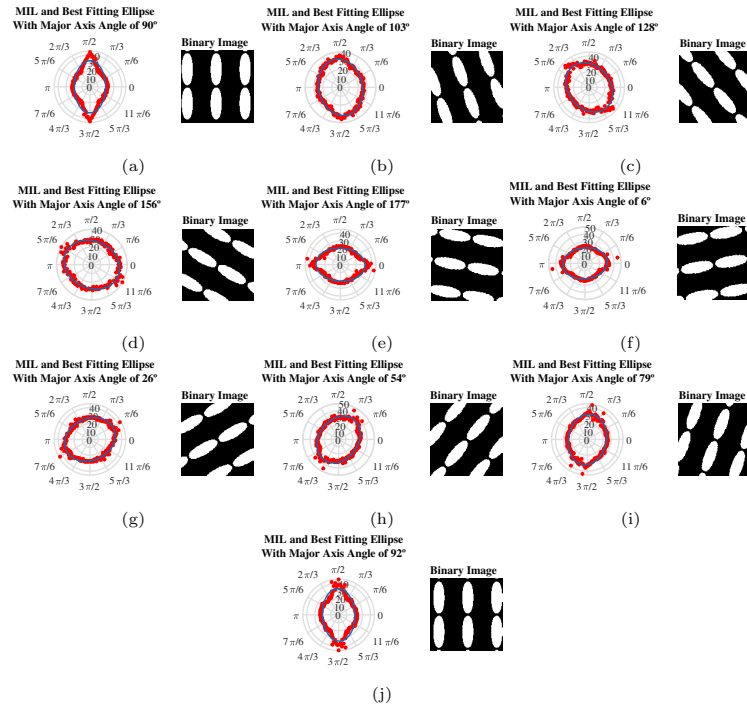


Figure 7: Benchmark fabricated RVE rotation results. 7a: 0° rotation; 7b: 20° rotation; 7c: 40° rotation; 7d: 60° rotation; 7e: 80° rotation; 7f: 100° rotation; 7g: 120° rotation; 7h: 140° rotation; 7i: 160° rotation; 7j: 180° rotation.

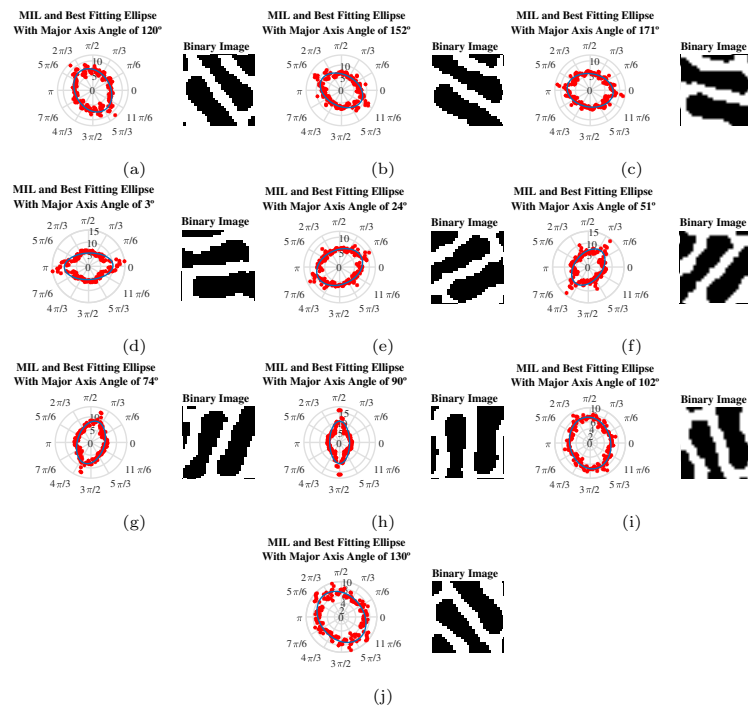


Figure 8: Realistic trabecular RVE rotation results. 8a: 0° rotation; 8b: 20° rotation; 8c: 40° rotation; 8d: 60° rotation; 8e: 80° rotation; 8f: 100° rotation; 8g: 120° rotation; 8h: 140° rotation; 8i: 160° rotation; 8j: 180° rotation.

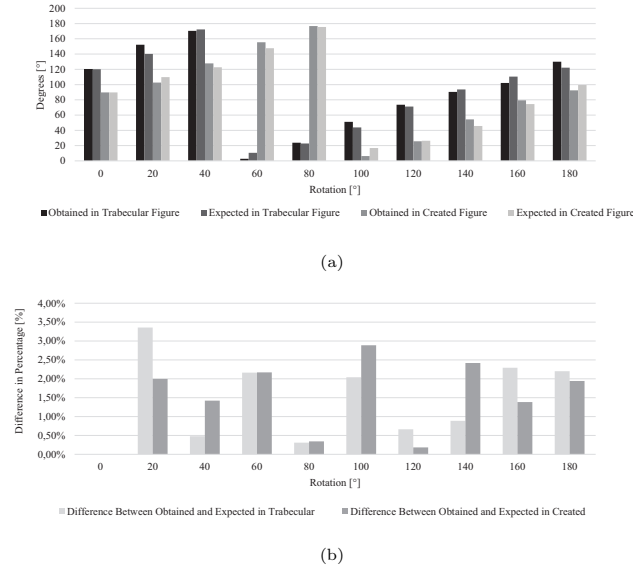


Figure 9: 9a: Obtained material orientation angles θ of the fitted ellipse versus the expected ones for the benchmark fabricated RVE (5a) and the realistic trabecular RVE (5d). 9b: Difference between the obtained θ results and the expected ones, in percentage %.

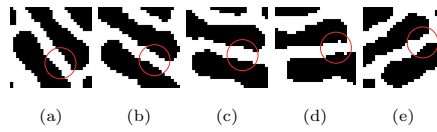


Figure 10: Image rotation process and inherent morphologic change, 10a: Original Image; 10b: 20° rotation; 10c: 40° rotation; 10d: 60° rotation; 10e: 80° rotation.

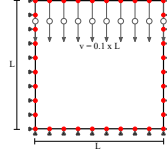
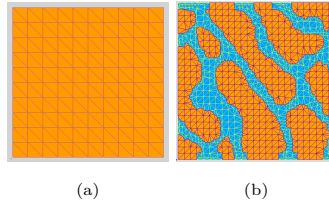


Figure 11: Boundary conditions applied to all RVEs.

Figure 12: 12a Discretized homogeneous RVE (11×11 nodes uniformly distributed). 12a Example of a discretized heterogeneous RVE created using micro-CT image information.

viously presented, figure 5d, and its $r_n \times r_n$ repetitions, and the results are compared with the ones obtained with a homogeneous RVE.

All the RVEs were submitted to the same essential and natural boundary conditions. Being all the RVEs squares micro patches with dimensions $L \times L$, it was imposed a displacement of $0.1 \times L$ at the nodes of the top layer, $y = L$. The nodes at $x = 0$ and $x = L$ where constrained on Ox direction, $\bar{u} = 0$, and the nodes at $y = 0$ and $y = L$ where constrained on Oy direction, $\bar{v} = 0$. This constrains are exemplified in figure 11.

The homogeneous RVE is typically discretized by a set of $n \times n$ nodes uniformly distributed within the RVE domain, figure 12a. All the integration points of the homogeneous RVEs models possess the same homogenized material properties. The heterogeneous RVEs (the realistic trabecular RVE) is formed by trabecular bone and void space, the discretization of such complex domain is exemplified in figure 12b.

Applying the proposed homogenization technique to the RVE represented in figure 5d, it is possible to obtain the anisotropic material properties presented in table 3, column "Homogeneous RVE". Thus, every integration point of the

Table 3: Mechanical properties used in the structural analysis

Mechanical Proprieties								
Homogenized RVE			Trabecular bone			Void Space		
E_{axial}	2366.0898	[MPa]	E	11600	[MPa]	E	100	[MPa]
E_{transv}	1035.8652	[MPa]						
G	4239.8785	[MPa]						
θ	62	[degrees]						
ν	0.1231		ν	0.36		ν	0.459	

homogeneous RVEs will assume these materials properties. Since the realistic trabecular RVEs are binary images, containing bone or void space, it is necessary to assume mechanical properties for these two materials. Thus, in table 3 are indicated the mechanical properties for the two domains (trabecular bone and void space). The mechanical properties of the trabecular bone were defined as isotropic according to the literature, [76]. Notice that since the geometrical information coming from the micro-CT forces the existence of the void space in between the trabeculae, it was necessary to define this 'material' as solid. Thus, the solution was to define it as a soft material that would not (significantly) interfere with the global structural response of the RVE. Thus, to the 'void space' was attributed a Young's modulus with a much lower magnitude when compared with the trabecular bone.

Two homogeneous RVEs were analyzed, one with 11×11 nodes and another with 21×21 nodes. The von Mises effective stress maps obtained with both FEM and NNRPIM techniques are presented in figure 13a and figure 13c for the FEM and in figure 13b and figure 13d for the NNRPIM.

The results for homogeneous RVEs, whose mechanical properties were obtained using the proposed homogenization technique, are very similar, regardless the level of the discretization or the used numerical method (FEM or NNRPIM). As can be seen in figure 13a and 13b the colour maps are similar, and demon-

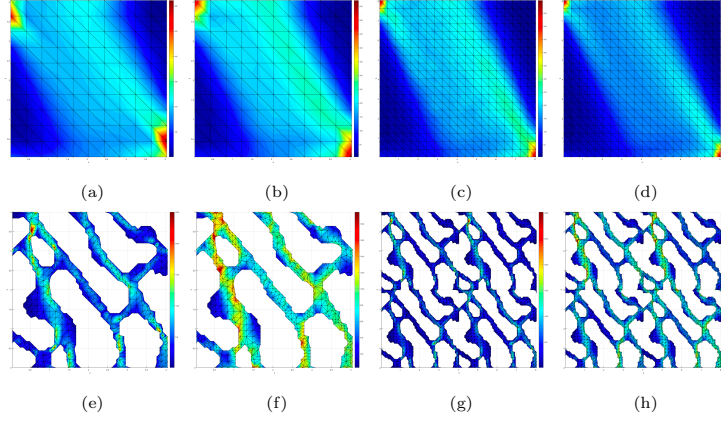


Figure 13: Effective stress S_{eff} for homogeneous model: 13a: FEM 1X1; 13b: NNRPIM 1X1; 13c:FEM 2X;13d: NNRPIM 2X2; and for heterogeneous models: 13e: FEM 1X1; 13f: NNRPIM 1X1; 13g: FEM 2X2; 13h: NNRPIM 2X2

strate the preferential orientation of the original realistic trabecular micro patch (from which the material properties were obtained, figure 5d).

Regarding the heterogeneous RVEs, in figure 13 only the von Mises effective stress distribution in the trabecular domain is shown. As figure 13e and figure 13g show, the results obtained for the FEM are slightly different from the one obtained with the NNRPIM, figure 13f and figure 13h.

In order to compare the stress field obtained with the homogeneous RVE with the heterogeneous RVE, the concept of homogenized stress is used.

The RVE's von Mises effective stress field (or any other RVE's stress/strain field) can be summarized in one scalar value - the homogenized von Mises effective stress - which can be defined with equation (28).

$$\sigma_{eff}^h = \frac{1}{n_Q} \sum_{i=1}^{n_Q} \sigma(\mathbf{x}_i)_{eff} \quad (28)$$

being n_Q the number of integration points discretizing the problem domain and not belonging to the vicinity of the domain boundary. Since, the integration mesh constructed within the FEM is fundamentally different from the

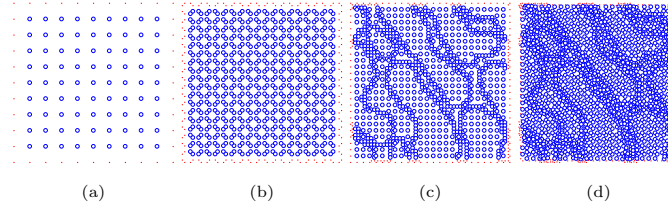


Figure 14: Integration points used to calculate the homogenized von Mises effective stress σ_{eff}^h . The blue points represent valid integration points, the red points represent excluded integration points. 14a: Integration mesh of the homogenized RVE for the FEM analysis; 14b: Integration mesh of the homogenized RVE for the NNRPIM analysis; 14c: Integration mesh of the heterogeneous RVE for the FEM analysis; 14d: Integration mesh of the heterogeneous RVE for the NNRPIM analysis.

integration mesh constructed with the NNRPIM formulation, the position of their integration points is very different. In figure 14 are presented the integration mesh of the homogenized RVE model for the FEM (14a) and for the NNRPIM (14b) and the integration mesh of the heterogeneous RVE model for the FEM (14c) and for the NNRPIM (14d). In blue are represented the integration points that will be included to calculate σ_{eff}^h and in red are shown the integration points that will be excluded from equation (28).

This homogenization excludes only 2% of the integration points forming the integration mesh. This exclusion is necessary to avoid the (inaccurate) stress concentrations that appear near the domain boundary, as can be seen in figure 13.

Thus, figure 15 shows the homogenized von Mises effective stress, σ_{eff}^h , obtained for each analyzed RVE, using both FEM and NNRPIM methodologies. Besides the homogenized von Mises effective stress determined in the integration points, in the figure are shown the σ_{eff}^h obtained in the nodes. This last variable is obtained using equation (28). However, instead of considering the stress at the integration points it is considered the stress extrapolated to the nodes.

Notice that four heterogeneous RVE were considered: a 1×1 heterogeneous

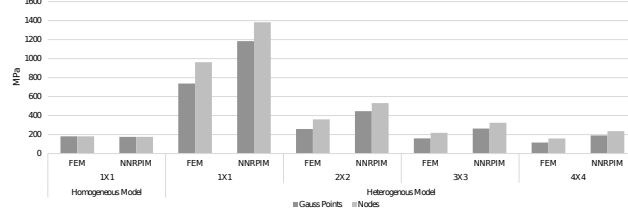


Figure 15: Homogenized von Mises effective stress σ_{eff}^h obtained with the FEM and the NNRPIM.

RVE (corresponding to the one represented in 5d), a 2×2 heterogeneous RVE (corresponding to the one represented in 5e), and then a 3×3 and 4×4 heterogeneous RVEs following the same repetition rule.

It is perceptible in figure 15 that increasing the level of detail and the size of the heterogeneous RVE, which are governed by the number of repetitions (the 1×1 RVE has a lower detail than the 4×4 RVE), the value of the homogenized stress decreases. Thus, when the analysis uses a heterogeneous model following a 4×4 repetition, the obtained homogenized stress is very close with the homogenized stress obtained with the homogeneous RVE. This indicates that the homogenization technique proposed in this work is capable to accurately obtain the homogenized anisotropic material properties of a trabecular patch. Comparing the FEM with meshless method is notorious that for the homogeneous RVEs' results are equivalent. However, the FEM and NNRPIM results obtained with the heterogeneous RVEs are not so close. This difference can be explain by locking effects in the FEM.

Each one the analyses has its own computational cost. In figure 16 are shown the time-lapse of each structural analysis. Observing the computational cost of each analysis, it is possible to understand that the analysis of the homogenized RVE is much faster than heterogeneous RVEs (with $r_n \times r_n$, $r_n = 2, 3, 4$). In figure 15 it was shown that the 4×4 heterogeneous RVE produces results very close with the homogeneous RVE. However, the 4×4 heterogeneous RVE takes 5000s to analyze and the homogeneous RVE only requires 4–6s. Generally, the

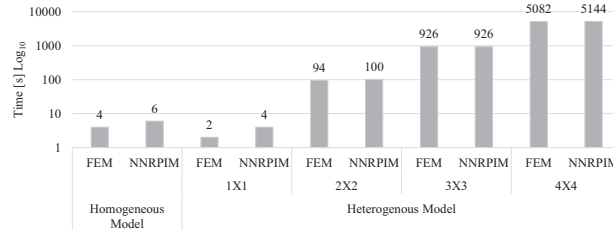


Figure 16: Computational cost (in seconds) of each analysis.

multiscale techniques use highly discretized RVEs, with a high computational cost associated. As this example shows, the proposed homogenization methodology is capable to reduce the cost of the multiscale analysis, enabling more demanding simulations.

5. Conclusions

The current work provided a methodology that allows to define the mechanical properties of a micro-CT trabecular bone square patch without any a-priory knowledge. Using the MIL methodology it is possible to acquire data to define the material orientation using a distribution function. Applying the methodology defined by Fitzgibbon et al. [77], the orientation distribution is approximated by an ellipse function. As described by Moreno et al. [74], bone trabeculae distribution/density can be defined by a tensor (a 2×2 matrix) representing the estimated ellipse. With this, it is possible to define the material mechanical properties, directly related with the trabeculae anisotropy encoded in the fabric tensor and with the material law developed by Belinha et al, 2012 [75].

The studies performed concerning the modification of the RVE scale and its rotation, demonstrated that the methodologies used to create the fabric tensor and to obtain the mechanical properties are stable and provide good results. Regarding the RVE rotation study, it were observed differences with an average of 1.62%. However, this magnitude is not relevant by itself or in the clinical use,

since in real scenarios the input images are not to be rotated.

It was verified that the homogeneous RVE, using the homogenized anisotropic material properties, is capable to produce the same results as the highly heterogeneous RVE (the 4×4 heterogeneous RVE). However, an elasto-static analysis with the homogeneous RVE only takes $4 - 6s$ to perform and the same analysis with the 4×4 heterogeneous RVE takes about $5000s$. Since usually multiscale techniques use highly discretized RVEs, it is expected that the homogenization technique here proposed combined with meshless methods will be capable to reduce the cost of the multiscale analyses, allowing to simulate more complex problems.

Additionally, the inclusion of the NNRPIM in multiscale analysis could be a true asset. In this manuscript it was shown that the NNRPIM is capable to produce accurate and smooth microscale variable fields (at the RVE scale), which will allow to obtain accurate final homogenized variable fields.

The results obtained with the NNRPIM are very close with the FEM results, showing that this technique is a valid alternative to the FEM. Furthermore, the NNRPIM does not shows the same locking behaviour demonstrated by the FEM.

Acknowledgement

The authors truly acknowledge the funding provided by Ministério da Ciência, Tecnologia e Ensino Superior - Fundação para a Ciência e a Tecnologia (Portugal), under Grants SFRH/BD/110047/2015 and SFRH/BPD/111020/2015, and by project funding MIT-EXPL/ISF/0084/2017 and UID/EMS/50022/2013. Additionally, the authors gratefully acknowledge the funding of Project NORTE-01-0145-FEDER-000022 - SciTech - Science and Technology for Competitive and Sustainable Industries, cofinanced by Programa Operacional Regional do Norte (NORTE2020), through Fundo Europeu de Desenvolvimento Regional (FEDER).

References

- [1] D. R. Carter, M. C. Van Der Meulen, G. S. Beaupré, Mechanical factors in bone growth and development, *Bone* 18 (1 Suppl) (1996) 5S–10S. doi: 10.1016/8756-3282(95)00373-8.
- [2] V. C. Mow, A. Ratcliffe, A. R. Poole, Cartilage and diarthrodial joints as paradigms for hierarchical materials and structures., *Biomaterials* 13 (2) (1992) 67–97.
URL <http://www.ncbi.nlm.nih.gov/pubmed/1550898>
- [3] X. Feng, J. M. McDonald, Disorders of bone remodeling., *Annual review of pathology* 6 (2011) 121–45. doi:10.1146/annurev-pathol-011110-130203.
- [4] E. Lucchinetti, Composite Models of Bone Properties, in: *Bone Mechanics Handbook*, Second Edition, CRC Press, 2001. doi:10.1201/b14263-16.
URL <http://www.crcnetbase.com/doi/10.1201/b14263-16>
- [5] G. E. Wnek, G. L. Bowlin, *Encyclopedia of Biomaterials and Biomedical Engineering*, no. April, Informa Healthcare USA, New York, 2008.
- [6] J. Wolff, *The Law of Bone Remodelling* (1886). arXiv:arXiv:1011.1669v3, doi:10.1097/00006534-198810000-00036.
- [7] A. Glucksmann, Studies on Bone mechanics in vitro, *Anat Rec* 73 (1939) 39–55. doi:10.1002/ar.1090730105.
- [8] F. Pauwels, *Gesammelte Abhandlungen zur funktionellen Anatomie des — Friedrich Pauwels —* Springer, Springer (1965) 543.
URL <http://www.springer.com/us/book/9783642868429>
- [9] H. E. Pettermann, T. J. Reiter, F. G. Rammerstorfer, Computational simulation of internal bone remodeling, *Archives of Computational Methods in Engineering* 4 (4) (1997) 295–323. doi:10.1007/BF02737117.

- [10] R. T. Hart, D. T. Davy, K. G. Heiple, A Computational Method for Stress Analysis of Adaptive Elastic Materials With a View Toward Applications in Strain-Induced Bone Remodeling, *Journal of Biomechanical Engineering* 106 (4) (1984) 342. doi:10.1115/1.3138503.
- [11] R. Huiskes, H. Weinans, H. J. Grootenboer, M. Dalstra, B. Fudala, T. J. Slooff, Adaptive bone-remodeling theory applied to prosthetic-design analysis, *Journal of Biomechanics* 20 (11-12) (1987) 1135–1150. doi:10.1016/S0021-9290(87)90030-3.
- [12] D. R. Carter, D. P. Fyhrie, R. T. Whalen, Trabecular bone density and loading history: Regulation of connective tissue biology by mechanical energy, *Journal of Biomechanics* 20 (8) (1987) 785–794. doi:10.1016/S0021-9290(87)90058-3.
- [13] G. S. Beaupré, T. E. Orr, D. R. Carter, An approach for time-dependent bone modeling and remodeling-theoretical development, *Journal of Orthopaedic Research* 8 (5) (1990) 651–661. doi:10.1002/jor.1100080506. URL <http://doi.wiley.com/10.1002/jor.1100080506>
- [14] C. R. Jacobs, J. C. Simo, G. S. Beaupre, D. R. Carter, Adaptive bone remodeling incorporating simultaneous density and anisotropy considerations, *Journal of Biomechanics* 30 (6) (1997) 603–613. doi:10.1016/S0021-9290(96)00189-3.
- [15] P. Fernandes, J. Guedes, H. Rodrigues, Topology optimization of three-dimensional linear elastic structures with a constraint on “perimeter”, *Computers & Structures* 73 (6) (1999) 583–594. doi:10.1016/S0045-7949(98)00312-5.
- [16] M. Doblaré, J. García, Application of an anisotropic bone-remodelling model based on a damage-repair theory to the analysis of the proximal femur before and after total hip replacement, *Journal of Biomechanics* 34 (9) (2001) 1157–1170. doi:10.1016/S0021-9290(01)00069-0.

- [17] M. Doblaré, G. J.M., Anisotropic bone remodelling model based on a continuum damage-repair theory, *Journal of Biomechanics* 35 (1) (2002) 1–17. doi:10.1016/S0021-9290(01)00178-6.
- [18] J. M. García-Aznar, T. Rueberg, M. Doblare, A bone remodelling model coupling microdamage growth and repair by 3D BMU-activity, *Biomechanics and Modeling in Mechanobiology* 4 (2-3) (2005) 147–167. doi:10.1007/s10237-005-0067-x.
- [19] S. J. Hazelwood, R. Bruce Martin, M. M. Rashid, J. J. Rodrigo, A mechanistic model for internal bone remodeling exhibits different dynamic responses in disuse and overload, *Journal of Biomechanics* 34 (3) (2001) 299–308. doi:10.1016/S0021-9290(00)00221-9.
- [20] D. Taylor, T. C. Lee, Microdamage and mechanical behaviour: predicting failure and remodelling in compact bone, *Journal of Anatomy* 203 (2) (2003) 203–211. doi:10.1046/j.1469-7580.2003.00194.x.
- [21] C. J. Hernandez, G. S. Beaupré, D. R. Carter, A model of mechanobiologic and metabolic influences on bone adaptation., *Journal of rehabilitation research and development* 37 (2) (2000) 235–244.
- [22] J. Hazrati Marangalou, K. Ito, B. van Rietbergen, A novel approach to estimate trabecular bone anisotropy from stress tensors, *Biomechanics and Modeling in Mechanobiology* 14 (1) (2015) 39–48. doi:10.1007/s10237-014-0584-6.
URL <http://link.springer.com/10.1007/s10237-014-0584-6>
- [23] R. Moreno, Ö. Smedby, D. H. Pahr, Prediction of apparent trabecular bone stiffness through fourth-order fabric tensors, *Biomechanics and Modeling in Mechanobiology* 15 (4) (2016) 831–844. doi:10.1007/s10237-015-0726-5.
- [24] S. C. Cowin, The relationship between the elasticity tensor and the fab-

- ric tensor, *Mechanics of Materials* 4 (2) (1985) 137–147. doi:10.1016/0167-6636(85)90012-2.
- [25] O. C. Zienkiewicz, R. L. Taylor, *The Finite Element Method*, 4th Edition, McGraw-Hill, London, 1994.
- [26] J. Belinha, *Meshless Methods in Biomechanics: Bone Tissue Remodelling Analysis*, Vol. 2 of *Lecture Notes in Computational Vision and Biomechanics*, Springer Netherlands, Dordrecht, 2014. doi:10.1007/978-94-007-4174-4.
- [27] R. A. Gingold, J. J. Monaghan, Smooth particle hydrodynamics: theory and application to non-spherical stars, *Monthly Notices of the Royal Astronomical Society* 181 (1977) 375–389.
- [28] T. Liszka, J. Orkisz, The finite difference method at arbitrary irregular grids and its application in applied mechanics, *Computers and Structures* 11 (1-2) (1980) 83–95. doi:10.1016/0045-7949(80)90149-2.
- [29] B. Nayroles, G. Touzot, P. Villon, Generalizing the finite element method: Diffuse approximation and diffuse elements, *Computational Mechanics* 10 (5) (1992) 307–318. doi:10.1007/BF00364252.
- [30] T. Belytschko, Y. Y. Lu, L. Gu, Element-free Galerkin methods, *International Journal* 37 (April 1993) (1994) 229–256. doi:10.1002/nme.1620370205.
- [31] S. N. Atluri, T. Zhu, A new Meshless Local Petrov-Galerkin (MLPG) approach in computational mechanics, *Computational Mechanics* 22 (2) (1998) 117–127. doi:10.1007/s004660050346.
- [32] G. R. Liu, Y. T. Gu, Local point interpolation method for stress analysis of two-dimensional solids, *Structural Engineering and Mechanics* 11 (2) (2001) 221–236. doi:10.12989/sem.2001.11.2.221.

- [33] G. R. Liu, Y. GU, A Local Radial Point Interpolation Method (LRPIM) for Free Vibration Analyses of 2-D Solids, *Journal of Sound and Vibration* 246 (1) (2001) 29–46. doi:10.1006/jsvi.2000.3626.
- [34] G. R. Liu, Y. T. Gu, A point interpolation method for two-dimensional solids, *International Journal for Numerical Methods in Engineering* 50 (4) (2001) 937–951. doi:10.1002/1097-0207(20010210)50:4<937::AID-NME62>3.0.CO;2-X.
- [35] J. G. Wang, G. R. Liu, A point interpolation meshless method based on radial basis functions, *International Journal for Numerical Methods in Engineering* 54 (11) (2002) 1623–1648. doi:10.1002/nme.489.
- [36] J. G. Wang, G. R. Liu, On the optimal shape parameters of radial basis functions used for 2-d meshless methods, *Computer Methods in Applied Mechanics and Engineering* 191 (23-24) (2002) 2611–2630. doi:10.1016/S0045-7825(01)00419-4.
- [37] L. M. J. S. Dinis, R. M. Natal Jorge, J. Belinha, Analysis of 3D solids using the natural neighbour radial point interpolation method, *Computer Methods in Applied Mechanics and Engineering* 196 (13-16) (2007) 2009–2028. doi:10.1016/j.cma.2006.11.002.
- [38] J. Belinha, L. M. J. S. Dinis, R. M. N. Jorge, The natural radial element method, *Int. J. Numer. Methods Eng* 93 (12) (2013) 1286–1313. doi:10.1002/nme.4427.
- [39] E. Shivanian, H. Reza Khodabandehlo, Meshless local radial point interpolation (MLRPI) on the telegraph equation with purely integral conditions, *The European Physical Journal Plus* 129 (11) (2014) 241. doi:10.1140/epjp/i2014-14241-9.
- [40] E. Shivanian, A. Rahimi, M. Hosseini, Meshless local radial point interpolation to three-dimensional wave equation with Neumann’s boundary

- conditions, *International Journal of Computer Mathematics* 93 (12) (2016) 2124–2140. doi:[10.1080/00207160.2015.1085032](https://doi.org/10.1080/00207160.2015.1085032).
- [41] H. R. K. Elyas Shivanian, Application of meshless local radial point interpolation (MLRPI) on a one-dimensional inverse heat conduction problem, *Ain Shams Engineering Journal* 7 (3) (2016) 993–1000. doi:<https://doi.org/10.1016/j.asej.2015.07.009>.
- [42] A. K. Elyas Shivanian, Meshless local radial point interpolation (MLRPI) for generalized telegraph and heat diffusion equation with non-local boundary conditions, *Journal of Theoretical and Applied Mechanics* 55 (2) (2017) 571–582. doi:[10.15632/jtam-p1.55.2.571](https://doi.org/10.15632/jtam-p1.55.2.571).
- [43] E. Shivanian, Spectral meshless radial point interpolation (SMRPI) method to two-dimensional fractional telegraph equation, *Mathematical Methods in the Applied Sciences* 39 (7) (2015) 1820–1835. doi:[10.1002/mma.3604](https://doi.org/10.1002/mma.3604).
- [44] H. Fatahi, J. Saberi-Nadjafi, E. Shivanian, A new spectral meshless radial point interpolation (SMRPI) method for the two-dimensional Fredholm integral equations on general domains with error analysis, *Journal of Computational and Applied Mathematics* 294 (1) (2016) 196–209. doi:<https://doi.org/10.1016/j.cam.2015.08.018>.
- [45] A. J. Elyas Shivanian, More accurate results for nonlinear generalized Benjamin-Bona-Mahony-Burgers (GBBMB) problem through spectral meshless radial point interpolation (SMRPI), *Engineering Analysis with Boundary Elements* 72 (1) (2016) 42–54. doi:<https://doi.org/10.1016/j.enganabound.2016.08.006>.
- [46] A. J. Elyas Shivanian, Inverse Cauchy problem of annulus domains in the framework of spectral meshless radial point interpolation, *Engineering with Computers* 2017 (3) (33) 431–442. doi:<https://doi.org/10.1007/s00366-016-0482-x>.

- [47] N. S. Elyas Shivanian, Majid Ghadiri, Influence of size effect on flapwise vibration behavior of rotary microbeam and its analysis through spectral meshless radial point interpolation, *Applied Physics A* 123 (1) (2017) 329. doi:<https://doi.org/10.1007/s00339-017-0955-9>.
- [48] A. J. Elyas Shivanian, An improved spectral meshless radial point interpolation for a class of time-dependent fractional integral equations: 2D fractional evolution equation, *Journal of Computational and Applied Mathematics* 325 (1) (2017) 18–33. doi:<https://doi.org/10.1016/j.cam.2017.04.032>.
- [49] A. J. Elyas Shivanian, Rayleigh–Stokes problem for a heated generalized second grade fluid with fractional derivatives: a stable scheme based on spectral meshless radial point interpolation, *Engineering with Computers* 34 (1) (2018) 77–90. doi:<https://doi.org/10.1007/s00366-017-0522-1>.
- [50] R. Sibson, "A Brief Description of Natural Neighbor Interpolation", in: V. Barnett (Ed.), *Interpolating Multivariate Data*, Wiley, Chichester, 1981, pp. 21–36.
- [51] G. Voronoi, Nouvelles applications des paramètres continus à la théorie des formes quadratiques. Deuxième mémoire. Recherches sur les paralléloèdres primitifs., *Journal fur die Reine und Angewandte Mathematik* 1908 (134) (1908) 198–287. doi:[10.1515/crll.1908.134.198](https://doi.org/10.1515/crll.1908.134.198).
- [52] B. Delaunay, Sur la sphère vide. A la memoire de Georges Voronoï. *Izv. Akad. Nauk SSSR, Otdelenie Matematicheskikh i Estestvennyh Nauk* 7 (1934) 793–800.
- [53] L. M. J. S. Dinis, R. M. Natal Jorge, J. Belinha, Analysis of plates and laminates using the natural neighbour radial point interpolation method, *Engineering Analysis with Boundary Elements* 32 (3) (2008) 267–279. doi:[10.1016/j.enganabound.2007.08.006](https://doi.org/10.1016/j.enganabound.2007.08.006).

- [54] R. L. Hardy, Theory and applications of the multiquadric-biharmonic method 20 years of discovery 1968-1988, *Computers and Mathematics with Applications* 19 (8-9) (1990) 163–208. [arXiv:arXiv:1011.1669v3](#), [doi:10.1016/0898-1221\(90\)90272-L](#).
- [55] J. Bengt Fornberg, The runge phenomenon and spatially variable shape parameters in rbf interpolation, *Computers & Mathematics with Applications* 54 (3) (2007) 379–398. [doi:https://doi.org/10.1016/j.camwa.2007.01.028](#).
- [56] R. Franke, Scattered Data Interpolation: Tests of Some Method, *Mathematics of Computation* 38 (157) (1982) 181–200. [doi:10.2307/2007474](#).
- [57] E. K. G. Z. Alexander Cheng, MA Golberg, Exponential convergence and H-C multiquadric collocation method for partial differential equations, *Numerical Methods for Partial Differential Equations* 19 (5) (2003) 571–594. [doi:DOI10.1002/num.10062](#).
- [58] A.-D. C.-S.Huang, C.-F.Lee, Error estimate, optimal shape factor, and high precision computation of multiquadric collocation method, *Engineering Analysis with Boundary Elements* 31 (7) (2007) 614–623. [doi:https://doi.org/10.1016/j.enganabound.2006.11.011](#).
- [59] G. P. Luca Vincenzo Ballestra, Computing the survival probability density function in jump-diffusion models: A new approach based on radial basis functions, *Engineering Analysis with Boundary Elements* 35 (9) (2011) 1075–1084. [doi:https://doi.org/10.1016/j.enganabound.2011.02.008](#).
- [60] G. P. Luca Vincenzo Ballestra, A radial basis function approach to compute the first-passage probability density function in two-dimensional jump-diffusion models for financial and other applications, *Engineering Analysis with Boundary Elements* 36 (11) (2012) 1546–1554. [doi:https://doi.org/10.1016/j.enganabound.2012.04.011](#).

- [61] M. Golberg, C. Chen, H. Bowman, Some recent results and proposals for the use of radial basis functions in the BEM, *Engineering Analysis with Boundary Elements* 23 (4) (1999) 285–296. doi:10.1016/S0955-7997(98)00087-3.
- [62] L. M. J. S. Dinis, R. M. N. Jorge, J. Belinha, A 3D shell-like approach using a natural neighbour meshless method: Isotropic and orthotropic thin structures, *Composite Structures* 92 (5) (2010) 1132–1142. doi:10.1016/j.compstruct.2009.10.014.
- [63] L. Dinis, R. M. Natal Jorge, J. Belinha, Composite Laminated Plates: A 3D Natural Neighbor Radial Point Interpolation Method Approach, *Journal of Sandwich Structures and Materials* 12 (2) (2009) 119–138. doi:10.1177/1099636209104735.
- [64] L. Dinis, R. M. Natal Jorge, J. Belinha, A natural neighbour meshless method with a 3D shell-like approach in the dynamic analysis of thin 3D structures, *Thin-Walled Structures* 49 (1) (2011) 185–196. doi:10.1016/j.tws.2010.09.023.
- [65] L. Dinis, R. M. Jorge, J. Belinha, The Radial Natural Neighbours Interpolators Extended to Elastoplasticity, *Progress on Meshless Methods - Computational Methods in Applied Sciences* (2009) 175–198doi:10.1007/978-1-4020-8821-6_11.
- [66] L. M. J. S. Dinis, R. M. Natal Jorge, J. Belinha, Large deformation applications with the radial natural neighbours interpolators, *CMES - Computer Modeling in Engineering and Sciences* 44 (1) (2009) 1–34. doi:10.3970/cmes.2009.044.001.
- [67] J. Belinha, L. Dinis, R. M. N. Jorge, The natural neighbour radial point interpolation method: dynamic applications, *Engineering Computations* 26 (8) (2009) 911–949. doi:10.1108/02644400910996835.

- [68] J. Belinha, L. M. J. S. Dinis, R. M. N. Jorge, The Mandible Remodeling Induced by Dental Implants: A Meshless Approach, *Journal of Mechanics in Medicine and Biology* 15 (4) (2015) 1550059. doi:10.1142/S0219519415500591.
URL <http://www.worldscientific.com/doi/10.1142/S0219519415500591>
- [69] W. J. Whitehouse, The quantitative morphology of anisotropic trabecular bone, *Journal of Microscopy* 101 (2) (1974) 153–168. doi:10.1111/j.1365-2818.1974.tb03878.x.
- [70] S. C. Cowin, S. B. Doty, *Tissue Mechanics*, Springer Science, 2007.
- [71] K. Mizuno, M. Matsukawa, T. Otani, M. Takada, I. Mano, T. Tsujimoto, Effects of structural anisotropy of cancellous bone on speed of ultrasonic fast waves in the bovine femur, *IEEE Transactions on Ultrasonics, Ferroelectrics, and Frequency Control* 55 (7) (2008) 1480–1487. doi:10.1109/TUFFC.2008.823.
- [72] A. Odgaard, Three-dimensional methods for quantification of cancellous bone architecture, *Bone* 20 (4) (1997) 315–328. doi:10.1016/S8756-3282(97)00007-0.
- [73] P. K. Zysset, A review of morphology–elasticity relationships in human trabecular bone: theories and experiments, *Journal of Biomechanics* 36 (10) (2003) 1469–1485. doi:10.1016/S0021-9290(03)00128-3.
- [74] R. Moreno, M. Borga, O. Smedby, Techniques for Computing Fabric Tensors - A Review, in: *Mathematics and Visualization*, Vol. 5, 2014, pp. pp 271–292. doi:10.1007/978-3-642-54301-2_12.
- [75] J. Belinha, R. M. N. Jorge, L. M. Dinis, A meshless microscale bone tissue trabecular remodelling analysis considering a new anisotropic bone tissue material law, *Computer Methods in Biomechanics and Biomedical Engi-*

neering 5842 (August 2012) (2012) 1–15. doi:10.1080/10255842.2012.654783.

- [76] A. N. Natali, E. L. Carniel, P. G. Pavan, Constitutive modelling of inelastic behaviour of cortical bone, *Medical Engineering & Physics* 30 (7) (2008) 905–912. doi:10.1016/j.medengphy.2007.12.001.
- [77] W. Andrew, F. Maurizio, P. Robert, F. Hill, E. Eh, A. W. Fitzgibbon, M. Pilu, R. B. Fisher, Direct Least Squares Fitting of Ellipses (1996) 253–257doi:10.1109/ICPR.1996.546029.

3.8 Contribution VI: A 3D trabecular bone homogenization technique. (Submitted)

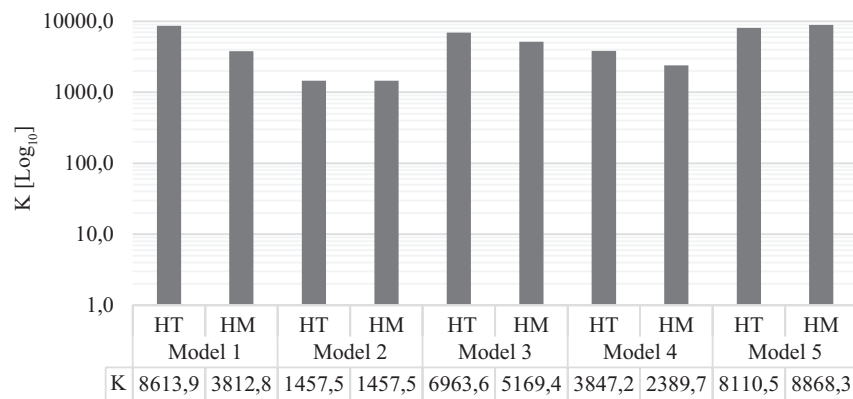
3.8.1 Highlights of Contribution: 3.8

This contribution focused on the bone mechanical properties definition using a 3D homogenisation technique defined by the fabric tensor concept and a set of phenomenological laws, combined with the FEM.

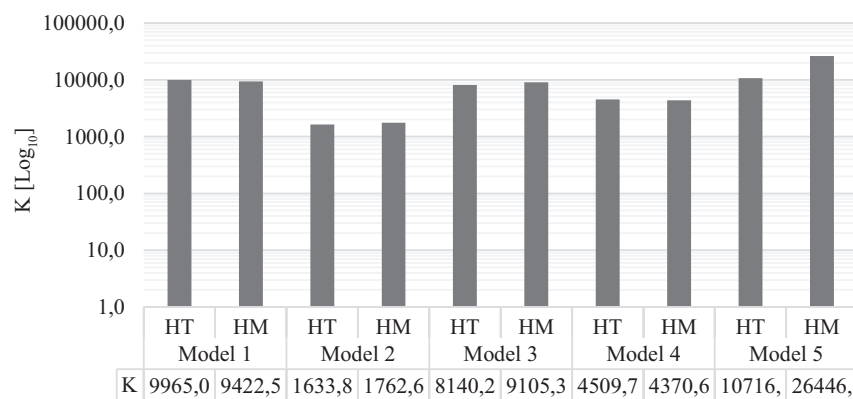
Therefore, the main contents of this publication include:

- I. Literature review on bone remodelling;
- II. Literature review on homogenisation techniques;
- III. Literature review on fabric tensor concept;
- IV. Application and description of a 3D homogenisation technique, where it is used the fabric tensor concept and a set of bone tissue phenomenological laws.
- V. Description of the 3D methodology to acquire the fabric tensor using the MIL methodology upon the 3D spatial dimension.
- VI. Material laws capable of defining bone mechanical proprieties using the fabric tensor data and using the medical images used to define the bone geometry.
- VII. Validation and evaluation of the robustness of the homogenisation methodology defined by a morphologically based fabric tensor methodology;
 - (a) Evaluation of effect of the change of the vectors number inside the search sphere, upon the obtained θ , ω , r_1 , r_2 and r_3 parameters;
 - (b) Evaluation of the obtained mechanical parameters (θ , ω , E_1 , E_2 , E_3 , G_1 , G_2 , G_3 , ν_1 , ν_2 , ν_3 and ρ_{app}) using different RVE with well defined characteristics;
- VIII. A structural application using FEM and two sets of applied boundary conditions, was used to verify and to compare the heterogenous and equivalent homogeneous domains. It was used the concept of homogenised stiffness K to compare the homogenous and heterogeneous models.
- IX. Conclusions: Contribution VI describes a methodology that allows to define the mechanical properties of a micro-CT trabecular bone RVE without any a-priori knowledge. This

contribution used a 3D MIL methodology that demonstrated to be robust and capable to encode the material orientation and morphology. Using the 3D fabric tensor and the phenomenological laws it was possible to define mechanically a homogenous domain that, as shown by the results obtained in the mechanical simulation, have a equivalent mechanical behaviour when compared to a highly discretised heterogeneous domain, 3.12. Also, one of the main objectives of using a homogenisation methodology is to reduce the computational cost, which in this case was achieved, as can be seen in figure 3.13.



(a)



(b)

Figure 3.12: 3.12a - Homogenised stiffness K for the mechanical simulation results performed using the first set of boundary conditions; 3.12b - Homogenised stiffness K value for the mechanical simulation results performed using the second set of boundary conditions.

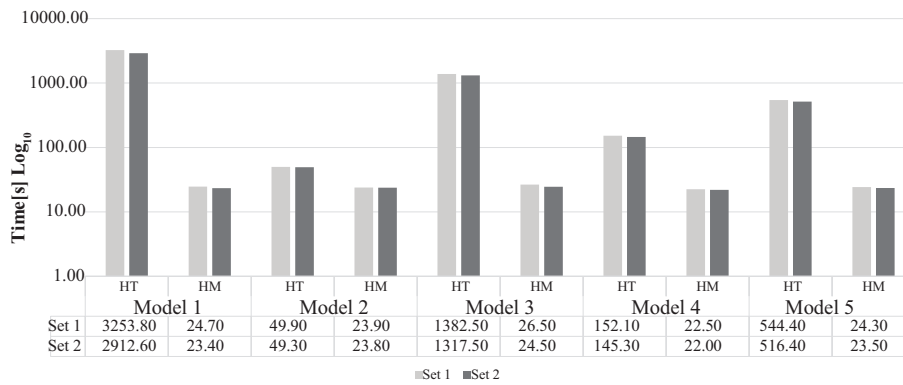


Figure 3.13: Computational cost of the models defined with the homogenised methodology versus the computational cost of the heterogeneous models.

The complete document can be found in the next pages.

Title: A 3D Trabecular Bone Homogenization Technique

Abstract:

Purpose: Bone is a hierarchical material that can be characterized from the microscale to macroscale. Multiscale models allow to study bone remodeling, inducing bone adaptation by using information of bone multiple scales. This work proposes a computationally efficient homogenization methodology useful for multiscale analysis. This technique is capable to define the homogenized microscale mechanical properties of the trabecular bone highly heterogeneous medium.

Methods: In this work, it was used a morphologic based fabric tensor and a set of anisotropic phenomenological laws for bone tissue, in order to define the bone micro-scale mechanical properties. To validate the developed methodology, several examples were performed in order to analyze its numerical behavior. Thus, trabecular bone and fabricated benchmarks patches (representing special cases of trabecular bone morphologies) were analyzed under compression.

Results: The results show that the developed technique is robust and capable to provide a consistent material homogenization, indicating that the homogeneous models were capable to accurately reproduce the micro-scale patch mechanical behavior.

Conclusions: The developed methodology has shown to be robust, computationally less demanding and allows to obtain close results when comparing the heterogeneous models with equivalent homogenized models. Therefore, it is capable to accurately predict the micro-scale patch mechanical behavior in a fraction of the time required by classic homogenization techniques.

Keywords: Fabric Tensor, Homogenization Technique, Multiscale; Bone

1. Introduction

Bone is a complex mineralized biological structure defined by bone matrix and by bone cells. It can be classified as a hierarchical material possessing distinct scales from the nanoscale to the macroscale [1]. To comprehend bone physiology it is necessary to understand bone at its different scales. Therefore, bone is studied at its macroscale level, [2], microscale level [3], and also crossing scale levels (multiscale analyses) [4]. Bone remodeling is one of the most trend research topics in computational biomechanics. In this process, bone cells are responsible to renew the bone matrix, by creating or

reabsorbing it, [5] This process is progressive and it is triggered to allow bone adaptation to any new external loads. Being bone a hierarchical structure, bone morphology adaptation leads to changes of its macro-scale mechanical properties, needed to fulfill and optimize the bone specific physiological function of structural support. [6] Bone remodeling can be studied using a multi-scale approach, where information from two or more scales can be used to define bone different functional requirements at different scales, reflecting bone's different behavior at different scales. [7] Wolff reported that the directions of the external applied loads directly influence the direction of the trabecular bone. [8] As a consequence, changes in bone's trabecular structure (at a microscale level), influence the macroscale mechanical behavior of bone, which in turn impacts the remodeling process.

Today, it is common to use computational biomechanics to study this type of biological problems [10]. The numerical methods and discretization techniques used in computational biomechanics allow to define, approximate and mimic biological processes using mathematical descriptions of the problem. Bio-mathematical formulations combined with distinct discretization approaches, such as finite element methods (FEM) [9] and meshless methods [10], allow to describe the mechanical behavior of bone at certain scale levels by using multiscale approaches [11] and homogenization techniques [12]. As in many other subjects, the use of the numerical approaches to study bone remodeling began with simplistic models. At first, it was considered that bone was only sensitive to mechanical stimuli [13]. In these early studies, bone tissues started to be considered as an isotropic-elastic material, a consideration that disregard the importance of material orientation and structure in the remodeling process. In the last few years, the complexity of bone models gradually increased, and models started to be combined with multiscale methodologies [11], in which are required homogenization techniques [14]. Trabecular bone is characterized by having a highly heterogeneous morphology, possessing a high surface-area-to-volume. Thus, trabecular bone is the major responsible for bone's metabolic activity, including the remodeling process. Thus, considering that many of bone remodeling studies are performed using discretization methodologies, the highly heterogeneous trabecular bone domain can have a negative impact in the perform of these methodologies. With this, some authors started to use homogenization techniques, which allow do define the trabecular bone highly heterogeneous domain as a homogeneous domain, but considering its orientation and anisotropy [15]. This homogenization techniques allow to determine equivalent

mechanical properties of a heterogeneous material by substituting the volume of the heterogeneous material with an equivalent volume of homogeneous material, and so, predict the behavior of the macro-scale using the mechanical properties coming from the micro-scale. The fabric tensor concept, \mathbf{A} , a symmetric second rank tensor, allows to characterize the arrangement of a multiphase material. Back in 1985, Cowin [16] described the relation between the fabric tensor and the fourth rank elasticity tensor \mathbf{C}_{ijkl} . The fabric tensor also provides information that allows to define an ellipsoid that can be related with the several material symmetries observed in many natural materials, such as bone tissue. The fabric tensor can be defined using two different methodologies, a mechanical based methodology and the morphologic-based methodology. The Mean Intercept Length (MIL) tensor [17], a morphologic-based method that uses the interface between phases of the material to estimate the tensor, is the most used technique to compute a fabric tensor [18]. When considering the bone structure, it is possible to obtain information regarding the material phase-change using computed tomography scan images, leading, naturally, to the use of morphologic-based techniques to define the fabric tensor. The morphologic-based methods use an orientation distribution function (ODF), which is estimated from an orientation-dependent feature of interest. ODF disposes the data in a polar plot and, then, fits the data with an ellipse. As Cowin initially suggested [16], it was afterwards demonstrated in the literature that the ODF fitted ellipse (specifically, the ellipse parameters) can be correlated with the material orientation, i.e., the material anisotropy [17]. This fabric tensor concept allows to numerically define bone mechanical proprieties, which is of high importance when studying the structural behavior of bone tissue or its biological processes, such as bone remodeling. Defining these mechanical properties allows to feed constitute laws, in order to better simulate the structural behavior of bone tissue. With this, the main objective of this work is to combine a new developed 3D homogenization technique, applying the fabric tensor concept combined with a previously developed bone tissue material law and with FEM, aiming to achieve a low-cost and efficient multiscale technique.

2. Material and Methods

The objective of this work is to develop a homogenization technique based in the fabric tensor concept. Thus, it was used a 3D MIL methodology to define an ellipsoid encoding the material anisotropy and orientation. This 3D MIL methodology uses as input a micro-

CT bone image Representative Volume Elements (RVE), which enables to represent the bone structure. The methodology was evaluate using a set of RVE benchmarks. Having the ellipsoid parameters and using a phenomenological material law from Belinha et al. [19] and from Agic et al. [20], it was possible to define an homogenized domain representative of a highly heterogeneous trabecular domain. Then, a set of mechanical simulations were performed, in which heterogeneous models were used. The geometry of these heterogeneous models was defined by micro-CT images representative of the trabecular bone. Additionally, homogenous geometrical models with regular shape (cubes) were constructed, with their mechanical proprieties defined using the developed homogenization technique.

2.1. 3D MIL

To define the fabric tensor encoding bone anisotropy, the methodology requires as input a medical image. These images are usually a set of grey-scale images, thus, the first operation of this methodology is to segment the medical images using the Otsu method. This allows to define in the RVE which voxels are bone material or void. The second step of the methodology is defined by an iterative process, where a random search using a sphere centered within the RVE boundaries is selected. This search sphere contains a set of vectors with random directions that are set constant in all the iterations. In each iteration, the search sphere centroid changes, and the intersection between the vectors from the vector list and the bone voxels are counted. These intersections are only counted if the bone voxel centroid has a maximum distance from the vector of at least the voxel size. Being the vector list constant within the iterative process, it is possible to sum for each vector the number of bone voxels that are intercepted in all the iterations. In this work, depending on the benchmark, the iterative process has a minimum and a maximum of 1000 and 5000 iterations, respectively, and has a variance stop criteria of 0.08. Using equation (1), it is possible to transform the intersection count into Cartesian coordinates. For each direction, ι , represented by a unique vector, it is multiplied the number iterations, $iter$, with the original vector size, h . Dividing this value with the number of interceptions of the vector with direction $Int(\iota)$ for all the iterations, it is obtained the $MIL(\iota)$. The original vector size, h , was defined by the search sphere size, that contained the vector list. Having the MIL value, the ODF data, it is possible to fit it into an ellipsoid using Fitzgibbon methodology. [21] After defining the ellipsoid, relevant parameters for

the methodology are extracted. Specifically, the parameters extracted are the radius that define the ellipsoid, r_1 , r_2 and r_3 being $r_1 > r_2 > r_3$, and the angles theta, θ , and azimuth ω , defined from r_1 , that defined the ellipsoid 3D orientation. r_1 , r_2 and r_3 are normalized by the r_1 size, being $r_1 = 1$ always.

$$MIL(\iota) = \frac{h \times iter}{Int(\iota)} \quad (1)$$

2.2. Material Law

Using the parameters obtained from the 3D MIL methodology, the RVE image information, and the phenomenological material laws from Belinha et al. [19] and Agic et al. [20], it is possible to create and define a material law.

The segmented image information was used to define the bone apparent density, ρ_{app} . This was obtained using a relation between the number of white voxels (bone voxels), w_v , and the black voxels (void voxels), b_v , as described in equation (2). In this equation, $\rho_o = 2.1 \text{ g / cm}^3$ represents the bone typical maximum apparent density.

$$\rho_{app} = \frac{w_v}{(b_v + w_v)} \times \rho_o [\text{g / cm}^3] \quad (2)$$

Also, using the image information, through the universal mixture laws, was possible to define ν_1 , equation (3), being $\nu = 0.3$ the typical poisson ratio for cortical bone (bone voxels, at the microscale).

$$\nu_1 = \frac{(0 \times b_v) + (0.3 \times w_v)}{(b_v + w_v)} \quad (3)$$

Regarding ν_2 and ν_3 in this work the values from Agic et al. [20] are assumed, Figure 1, where it is shown a relation between ν_2 and ν_3 and the bone apparent density, ρ_{app} . Fitting Agic et al. data it was possible to define two fourth order polynomial equations, equation (4) and (5), allowing to describe analytically the behavior of ν_2 and ν_3 , considering ρ_{app} .

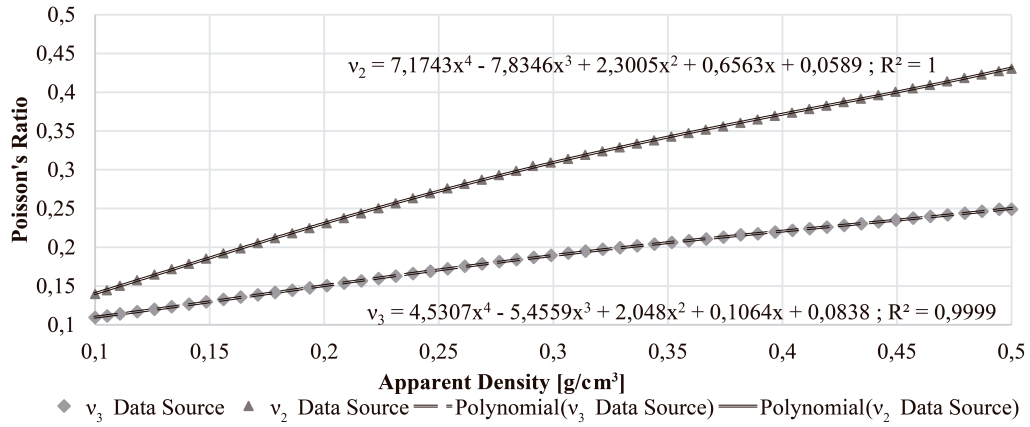


Figure 1 - Data from Agic et al.[20] fitted to polynomial functions.

$$v_2 = \begin{cases} 7.1743\rho_{app}^4 - 7.8346\rho_{app}^3 + 2.3005\rho_{app}^2 + 0.6563\rho_{app} + 0.0589 \rightarrow \text{if } \rho_{app} < 0.5 \text{ g/cm}^3 & (4) \\ 0.43 \rightarrow \text{if } \rho_{app} \geq 0.5 \text{ g/cm}^3 \end{cases}$$

$$v_3 = \begin{cases} 4.5307\rho_{app}^4 - 5.4559\rho_{app}^3 + 2.048\rho_{app}^2 + 0.1064\rho_{app} + 0.0838 \rightarrow \text{if } \rho_{app} < 0.5 \text{ g/cm}^3 & (5) \\ 0.245 \rightarrow \text{if } \rho_{app} \geq 0.5 \text{ g/cm}^3 \end{cases}$$

Considering Belinha's material law [22] and using equation (6) and coefficients from Table 1, it is possible to define E_1 . Concerning E_2 and E_3 , it is defined a relation between E_1 and the radius r_1 , r_2 and r_3 . Thus, E_2 is defined using a relation between r_1 , r_2 and E_1 equation (7), and E_3 , is defined using r_1 , r_3 and E_1 , equation (8).

Table 1 - Coefficients from Belinha's material law [22].

	$j = 0$	$j = 1$	$j = 2$	$j = 3$
a_j	0.0E+00	7.216E+02	8.059E+02	0.0E+00
b_j	-1.770E+05	3.861E+05	-2.798E+05	6.836E+04

$$E_1 = \begin{cases} \sum_{j=3}^0 a_j \rho_{app}^j & \text{if } \rho_{app} \leq 1.3 \text{ g/cm}^3 \\ \sum_{j=3}^0 b_j \rho_{app}^j & \text{if } \rho_{app} > 1.3 \text{ g/cm}^3 \end{cases} \quad (6)$$

$$E_2 = \frac{r_2 \times E_1}{r_1} \quad (7)$$

$$E_3 = \frac{r_3 \times E_1}{r_1} \quad (8)$$

The shear modulus, G_1 , G_2 and G_3 , are approximated using equation (9), (10) and (11), respectively:

$$G_1 = \frac{E_1}{2 \times (1 + \nu_1)} \quad (9)$$

$$G_2 = \frac{E_2}{2 \times (1 + \nu_2)} \quad (10)$$

$$G_3 = \frac{E_3}{2 \times (1 + \nu_3)} \quad (11)$$

Using the proposed methodology it is possible to define a set of mechanical properties capable of defining a homogenized RVE (E_1 , E_2 , E_3 , ν_1 , ν_2 , ν_3 , G_1 , G_2 , G_3 and θ and ω). This allowed do construct a constitutive matrix $\mathbf{c}_{ox'y'z'}$, equation (12) for the $ox'y'z'$ local coordinate system (oriented with the material principal axis, following the principal 'axial' and 'transverse' directions). Using θ and ω obtained from the ellipsoid fitting, the transformation rotation matrices \mathbf{T} , are defined, equation, (13) and (14).

$$\mathbf{c}_{ox'y'z'} = \begin{bmatrix} \frac{1}{E_1} & \frac{-\nu_1}{E_2} & \frac{-\nu_3}{E_3} & 0 & 0 & 0 \\ \frac{-\nu_1}{E_2} & \frac{1}{E_2} & \frac{-\nu_2}{E_3} & 0 & 0 & 0 \\ \frac{-\nu_3}{E_3} & \frac{-\nu_2}{E_3} & \frac{1}{E_3} & 0 & 0 & 0 \\ 0 & 0 & 0 & \frac{1}{G_1} & 0 & 0 \\ 0 & 0 & 0 & 0 & \frac{1}{G_2} & 0 \\ 0 & 0 & 0 & 0 & 0 & \frac{1}{G_3} \end{bmatrix} \quad (12)$$

$$\mathbf{T}_{oy}(\beta) = \begin{bmatrix} \cos^2 \beta & 0 & \sin^2 \beta & 0 & 0 & \sin 2\beta \\ 0 & 1 & 0 & 0 & 0 & 0 \\ \sin^2 \beta & 0 & \cos^2 \beta & 0 & 0 & -\sin 2\beta \\ 0 & 0 & 0 & \cos \beta & -\sin \beta & 0 \\ 0 & 0 & 0 & \sin \beta & \cos \beta & 0 \\ -\sin \beta \cos \beta & 0 & \sin \beta \cos \beta & 0 & 0 & \cos^2 \beta - \sin^2 \beta \end{bmatrix} \quad (13)$$

$$\mathbf{T}_{oz}(\beta) = \begin{bmatrix} \cos^2 \beta & \sin^2 \beta & 0 & -\sin 2\beta & 0 & 0 \\ \sin^2 \beta & \cos^2 \beta & 0 & \sin 2\beta & 0 & 0 \\ 0 & 0 & 1 & 0 & 0 & 0 \\ \sin^2 \beta & -\sin^2 \beta & 0 & \cos^2 \beta - \sin^2 \beta & 0 & 0 \\ 0 & 0 & 0 & 0 & \cos \beta & -\sin \beta \\ 0 & 0 & 0 & 0 & \sin \beta & \cos \beta \end{bmatrix} \quad (14)$$

Afterwards, it is possible to define the material constitutive matrix in the global axis with equation (15),

$$\mathbf{c}_{xyz} = [\mathbf{T}_{oz}]_{\theta}^T \left[[\mathbf{T}_{oy}]_{\omega}^T \mathbf{c}_{ox'y'z'} [\mathbf{T}_{oy}]_{\omega} \right] [\mathbf{T}_{oz}]_{\theta} \quad (15)$$

2.3. Algorithm Robustness

In order to evaluate the robustness of the 3D MIL methodology, benchmark examples were analyzed. One of the factors that could influence the methodology was the number of vectors in the vector list present inside the search sphere. Thus, it was evaluated the behavior of the methodology assuming distinct vector list sizes with: 50, 100, 250, 1000 and 1500 vectors. These sets are represented in Figure 2. Furthermore, 6 benchmarks RVEs were fabricated with well-defined geometric characteristics, containing bone-voxels and void-voxels, being bone voxels represented in blue (as Figure 3 shows). Benchmark 1, Figure 3(a), has a well-defined vertical material principal direction. Benchmark 2, Figure 3(b), has exactly the same number of bone and void voxels from Benchmark 1, but it was obtained applying a rotation to benchmark 1 in order to have a horizontal material principal direction. Benchmark 3, Figure 3(c), and benchmark 4, Figure 3(d) have an oblique material principal direction. The difference between benchmark 3 and 4, is the number of voxels that define the thickness of the bone region. Benchmark 5, Figure 3(e), and benchmark 6, Figure 3(f), have the same material principal direction, but have a different number of bone voxels defining the bone voxels central column. The corresponding ellipsoids and material directions are shown in Figure 3(g) to (l). It was expected that the material first principal direction was collinear with the material distribution. With Figure 3(g) to (l), it is possible to observe that using the proposed technique, the obtained material directions are in accordance with the expected material directions of each benchmark. The study of these benchmarks aimed to evaluate the obtained mechanical proprieties, prior to the transformation with equation (15), and verify if the obtained parameters translate correctly the benchmarks morphology, which was confirmed.

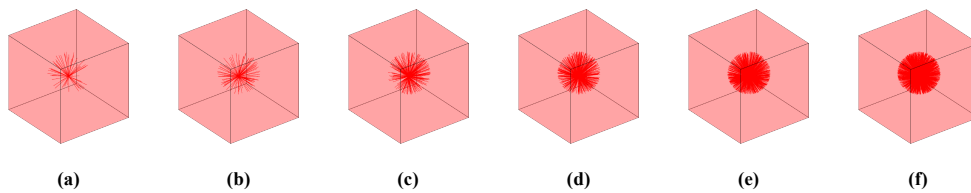
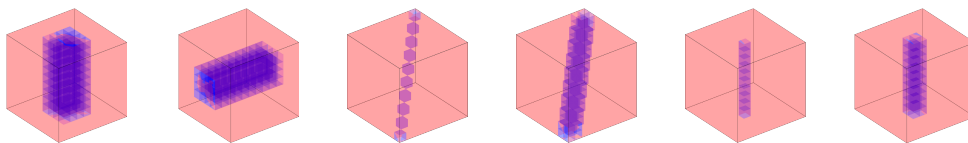


Figure 2 - Set of image is representing different numbers of vectors inside the search sphere (a): 50 vectors; (b): 100 vectors; (c): 250 vectors; (d): 500 vectors; (e): 1000 vectors; (f): 1500 vectors;



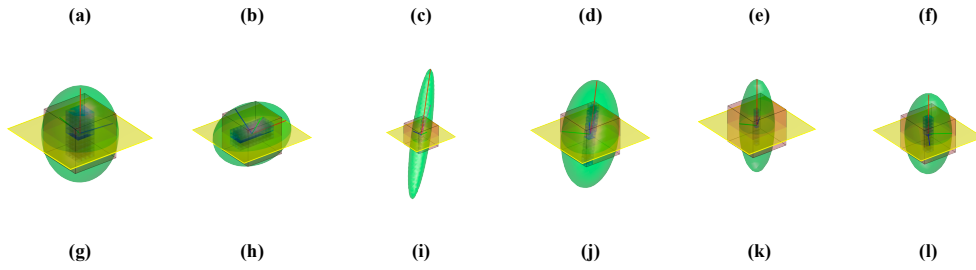


Figure 3 - Images (a) to (f) represent the constructed benchmarks, and images (g) to (l) represent the respective ellipsoid fitting.

2.4. Mechanical Simulation

Using the developed homogenization technique, it was possible to define the mechanical properties of homogeneous RVEs from the heterogeneous RVE (characterizing real trabecular bone morphology). With this, and using structural mechanical simulations, it was created a set of models that allow to analyze if the mechanical behavior of the homogenized RVEs is equivalent to the heterogeneous RVEs. Thus, 5 different geometrical models were constructed considering the trabecular bone morphology, Figure 4(b), Figure 4(c), Figure 4(d), Figure 4(e) and Figure 4(f), and 5 equivalent homogenized RVEs, represented in Figure 4(g) as an example (all homogenized RVEs are simple cubes discretized regularly as the one in Figure 4(g)). These mechanical simulations were performed using ABAQUS Unified FEA - SIMULIA™ 6.14 by Dassault Systèmes®.

The heterogeneous models were constructed using the same models on which the developed homogenization technique was applied to. The images used to create these models were obtained using micro-computerized tomography (micro-CT) from a foot cuboid bone. Since these images were obtained using micro-CT, they possess a sufficiently high resolution to represent the trabecular structure, but also possess information about the pixel and voxels dimensions, allowing to define, for each voxel a mesh element. Using the same threshold methodology and parameters used in the homogenization technique, each voxel corresponds to a hexahedric element, which could be defined as bone material or void space. The mechanical properties applied to the elements defined as bone and void in the heterogeneous models are represented in Table 2. Notice that the geometrical information from the micro-CT imposed the existence of void space in between the trabeculae, making necessary to define it has a solid 'material'. Thus, the solution was to define it as a soft material that would not (significantly) interfere with the global structural response of the RVE. Thus, for the “void space” it was attributed a Young's modulus with a much lower magnitude when compared with the Young's

modulus of the trabecular bone. Concerning the boundary condition, two sets of boundary conditions were considered, resulting in two simulation sets. Figure 4(a) represents a generalization of the geometrical models used in all simulations. For the first set of boundary conditions, at the top layer nodes ($z = L$) it was imposed a displacement of ($\bar{w} = 0.1 \times L$) and a displacement restriction $\bar{u} = 0 \wedge \bar{v} = 0$. It was also applied at the bottom layer nodes ($z = 0$) a displacement restriction $\bar{w} = 0$. For the second set of boundary conditions, at the top layer nodes ($z = L$) it was also imposed a displacement of ($\bar{w} = 0.1 \times L$) and a displacement restriction $\bar{u} = 0 \wedge \bar{v} = 0$. However, at the bottom layer nodes ($z = 0$) it was imposed a complete displacement restriction, $\bar{u} = 0 \wedge \bar{v} = 0 \wedge \bar{w} = 0$, being $\{u, w, w\}$ the displacement components along the $\{Ox, Oy, Oz\}$ axis, respectively.

Table 2 - Mechanical properties used to define the bone by Hong et al.[23] and void space in the heterogeneous models.

Mechanical Properties		
	Cortical Bone	Void Space
Young Modulus [GPa]	3.470	1.0×10^{-7}
Poisson's Ratio	0.36	0.1

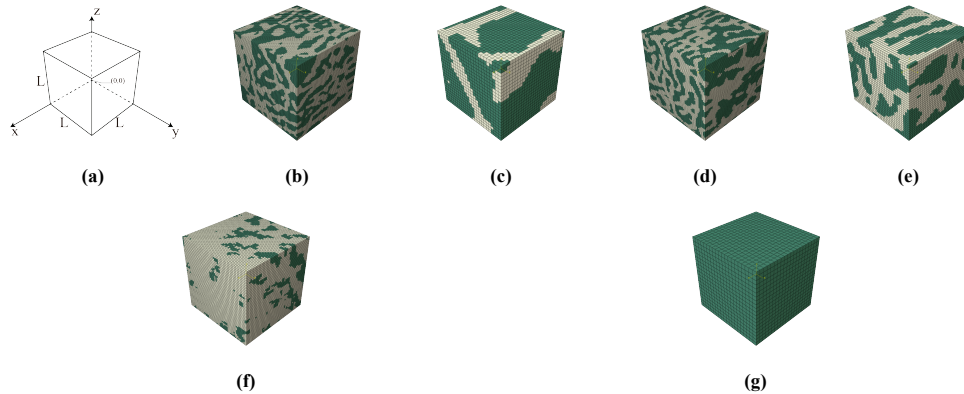


Figure 4 - Figure 4(a) - Geometrical models schematics; Figure 4(b) - Heterogeneous model 1; Figure 4(c) - Heterogeneous model 2; Figure 4(d) - Heterogeneous model 3; Figure 4(e) - Heterogeneous model 4; Figure 4(f) - Heterogeneous model 5; Figure 4(g) - Generic homogeneous model.

3. Results

This section presents the results obtained from the computational analyses performed to evaluate the behavior of the 3D MIL and also the results obtained from the mechanical simulations, where the mechanical properties of the homogeneous models were defined using the developed homogenization methodology.

3.1. Validation of MIL methodology

Using the created benchmarks, it was analyzed the number of vectors (in the vector list inside the search sphere) that provided stable results with the developed methodology. It was analyzed the behavior of theta, θ , and azimuth, ω , Figure 6(a), and the length of the radius that defines the fitted ellipsoid, Figure 6(b). The results in Figure 6(a) and Figure 6(b) were obtained from applying the proposed methodology to the benchmarks present in Figure 5. In Table 3, are shown the several parameters obtained using the proposed methodology for all benchmarks of Figure 3.

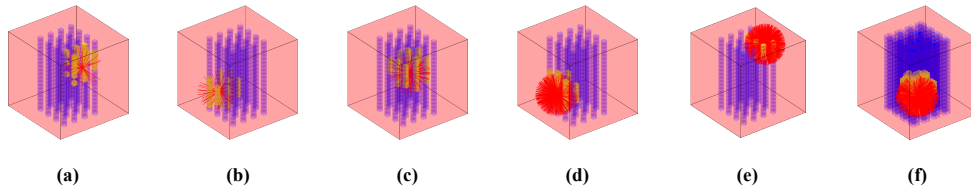
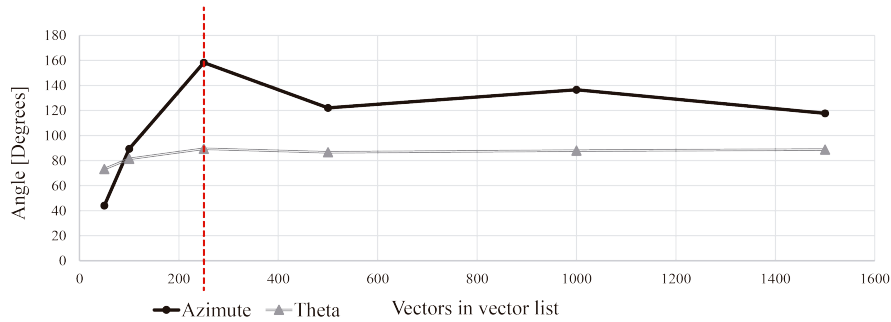
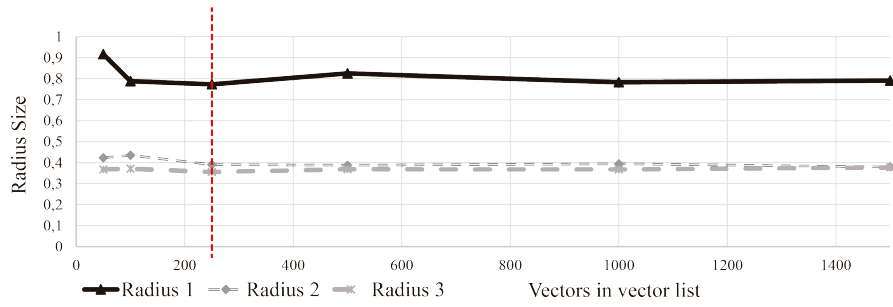


Figure 5 - Different number of vectors inside the search sphere (a): 50 vectors; (b): 100 vectors; (c): 250 vectors; (d): 500 vectors; (e): 1000 vectors and (f): 1500 vectors.



(a)



(b)

Figure 6 – (a): Evolution of the obtained ω and θ with the increase of the number of vectors in the vector list inside the search sphere; (b): Evolution of the obtained r_1 , r_2 and r_3 with the increase of the number of vectors in the vector list inside the search sphere.

Table 3 - Parameters obtained using the developed methodology, defining the local mechanical properties of the constructed benchmarks.

Benchmark						
	1	2	3	4	5	6
ω	11.985	0.219	43.701	44.373	28.517	26.107
θ	89.546	0.089	34.733	35.731	89.654	89.138
E_1	333.440	333.440	15.509	111.540	15.509	66.301
E_2	253.905	249.008	2.133	55.018	5.280	34.569
E_3	247.595	246.993	2.085	54.725	5.176	34.354
G_1	159.084	159.084	7.731	54.720	7.731	32.757
G_2	95.211	93.374	0.993	23.472	2.459	15.350
G_3	103.035	102.784	0.958	24.360	2.379	15.554
ν_1	0.048	0.048	0.003	0.019	0.003	0.012
ν_2	0.333	0.333	0.074	0.172	0.074	0.126
ν_3	0.202	0.202	0.088	0.123	0.088	0.104
ρ_{app}	0.336	0.336	0.021	0.134	0.021	0.084

3.2. Mechanical Simulation

The performed mechanical simulations aimed to evaluate if the developed homogenization technique was able to define the mechanical properties of the heterogeneous domains, allowing to define homogeneous models (mechanically equivalent to the trabecular heterogeneous models defined by the heterogeneous geometrical models). For the constructed models, both the von Mises stress field and the displacement field were obtained, Figure 7 and Figure 8, respectively. Figure 7 regards to the first set of boundary conditions applied to the models. In each sub-image of this figure it is presented the result for the heterogeneous model and its homogeneous equivalent. In Figure 8 concerns to the second set of boundary conditions. Also, in this figure, each sub-image shows the result for the heterogeneous model and its homogeneous equivalent.

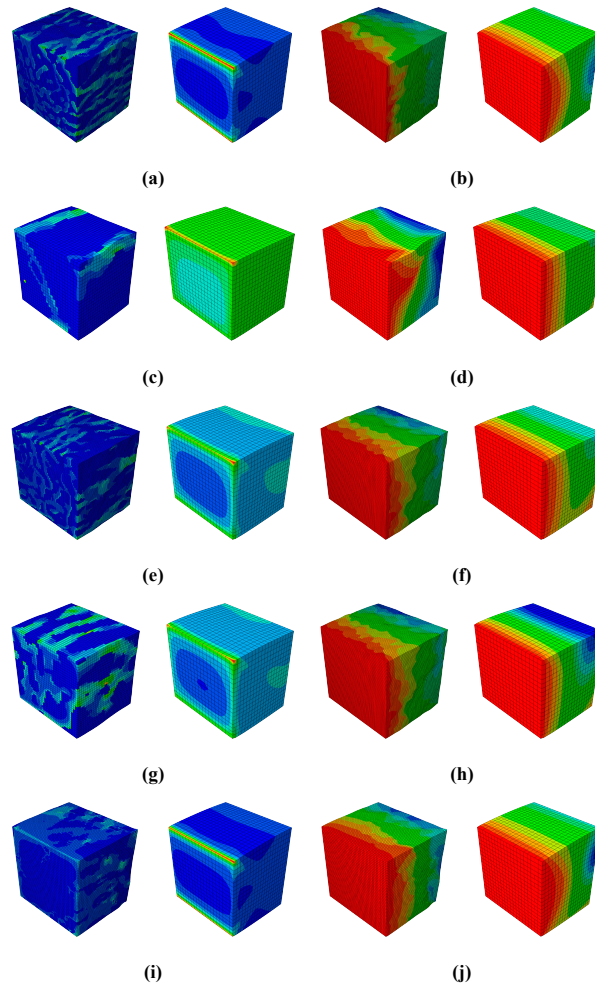


Figure 7 - Von Mises Stress and displacement for the mechanical simulations using the first set of boundary conditions. (a),(c),(e),(f),(i): Model 1 to 5, heterogeneous and equivalent homogeneous model von Mises stress; Figure 7(b),(d),(f),(h)(j): Model 1 to 5, heterogeneous and equivalent homogeneous model von Mises stress.

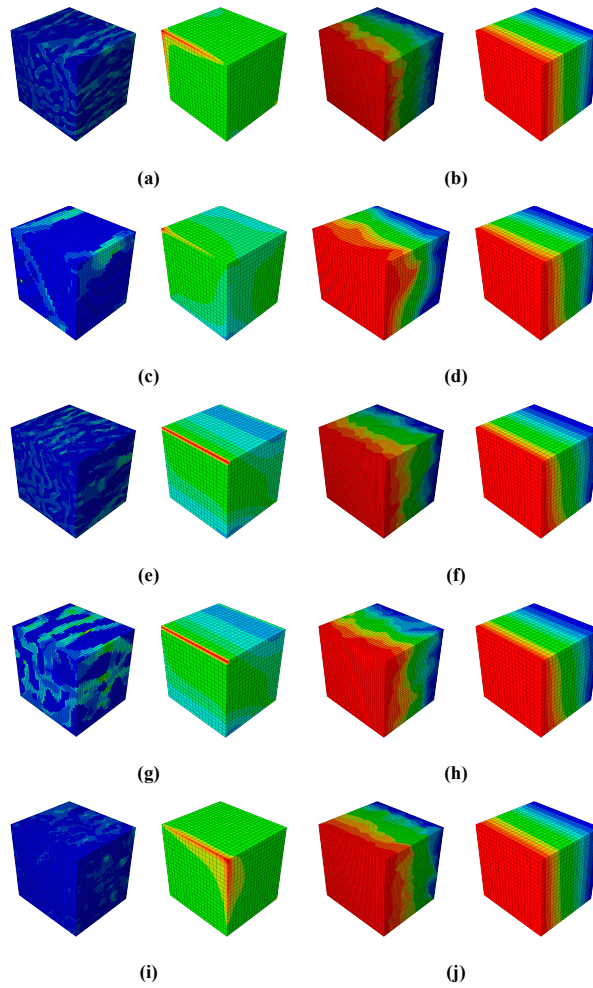


Figure 8 - Von Mises Stress and displacement for the mechanical simulations using the second set of boundary conditions. (a),(c),(e),(f),(i): Model 1 to 5, heterogeneous and equivalent homogeneous model von Mises stress. (b),(d),(f),(h),(j): Model 1 to 5, heterogeneous and equivalent homogeneous model von Mises stress.

4. Discussion

In this section, the discussion regarding the results obtained from the tests performed to evaluate the behavior of the 3D MIL are presented. More, also the results obtained from the mechanical simulations, where the mechanical properties of the homogeneous models were defined using the developed homogenization methodology, are also analyzed and discussed.

From the results obtained using the benchmarks, concerning the behavior of theta, θ , and azimuth, ω , Figure 6(a), and the length of the radius that defines the fitted ellipsoid, Figure 6(b), it is possible to visualize that starting from 250 vectors, highlighted with

vertical dotted line, the results stabilize, which means that the convergence is achieved and using a higher number of vectors does not increase significantly the accuracy of the solution. Thus, using 250 vectors allows to obtain results very close with the ones obtained considering 1500 vectors. The advantage is the computational time, an analysis with 250 vectors is much faster than an analysis with 1500 vectors. Concerning the values from Table 3, when comparing the results of benchmark 1 and 2, Figure 3(a) and Figure 3(b) respectively, and considering the benchmarks characteristic, it is possible to conclude that these results are as expected. Benchmark 1 and 2 have the same number of bone voxels, reflecting the high similarity between E_1 , E_2 , E_3 , G_1 , G_2 , G_3 , v_1 , v_2 , v_3 and ρ_{app} , however, when considering θ and ω these two parameters reflect the different benchmark principal direction.

Concerning benchmark 3 and 4, Figure 3(c) and Figure 3(d), that as previously described have an oblique principal direction, θ and ω parameters reflect this oblique topology. The remain parameters, E_1 , E_2 , E_3 , G_1 , G_2 , G_3 , v_1 , v_2 , v_3 and ρ_{app} , reflect the different number of voxels that define the thickness of the bone region. Comparing the results obtained with benchmark 5 and benchmark 6, Figure 3(e) and Figure 3(f), the values in Table 3 allow to understand that θ and ω parameters are highly similar. The remain parameters, E_1 , E_2 , E_3 , G_1 , G_2 , G_3 , v_1 , v_2 , v_3 and ρ_{app} are not comparable. These results were the expected ones, because as previously described, these benchmarks have the same material principal direction but a different number of bone voxels. Although insignificant, the difference between values (that should be exactly the same, as for example E_3) for benchmark 1 and 2, occurs because of the random selection of the centroid of the search sphere. In Figure 3(g) to Figure 3(l), are presented the fitted ellipsoids. In these images it is visible that the fitted ellipsoid, by visual inspection, have the same material principal direction as the fabricated benchmarks, re-enforcing that the developed methodology can define and encode trabecular bone orientation and anisotropy.

Concerning the mechanical simulation results, it was observed for all the heterogeneous models results that bone zones, which define the trabeculae, present higher values of the stress. For the case of the displacement values, as expected, higher values are observed in the region close to $z = L$, which is the location where the imposed displacement was applied. As expected, it is also observed a gradual apparent linear decrease of the

displacement from $z = L$ to $z = 0$. Concerning the homogeneous models, they present, when compared with the heterogeneous models, a smoother von Mises stress spatial distributions, reflecting the homogeneous nature of the model. Analyzing the displacement values, the images show that similarly to the heterogeneous models, the higher displacement values appear in the nodes where it was applied the enforced displacement, the region close to $z = L$, and that occurs a gradual decrease of the displacement values down to $z = 0$. Being the geometrical nature of the models so different, it is difficult to compare these models using a local perspective of the models. Thus, to evaluate if the homogeneous models have an equivalent behavior to the heterogeneous model, it was defined a relation between the sum of the z components of the reaction forces, at $z = 0$, $\sum R_z^{z=0}$, and the displacement applied at $z = L$, $u_3^{z=L}$, equation (16), leading to a homogenized value of stiffness K .

$$K = \frac{\sum R_z^{z=0}}{u_3^{z=L}} \quad (16)$$

The results obtained using equation (16) are represented in Figure 9 and in Figure 10. Concerning the results of Figure 9, concerning the first boundary conditions set, the difference between the homogeneous and the heterogeneous model is of 56% for the model 1, 0% for model 2, 26% for model 3, 38% for model 4 and 9% for the model 5, representing an overall average difference of 21%. For the case of mechanical simulations performed using the second set of boundary conditions, the difference between the homogeneous and the heterogeneous model is of 6% for the model 1, 7% for model 2, 11% for model 3, 3% for model 4 and 59% for the model 5, representing an overall average difference of 14%.

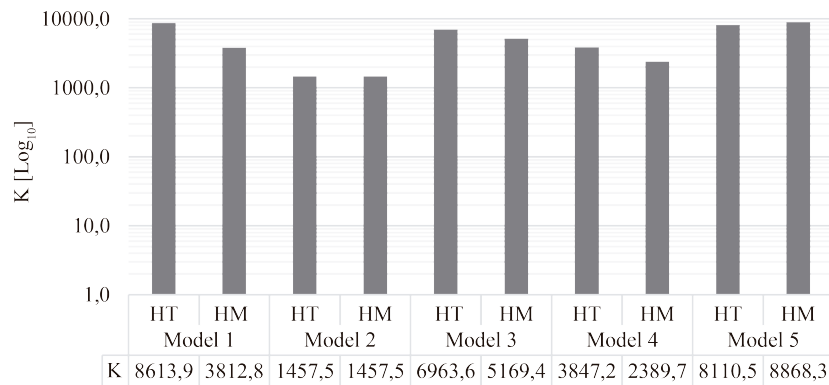


Figure 9 - Homogenized stiffness K for the mechanical simulation results performed using the first set of boundary conditions, for the homogeneous (HM) and heterogeneous (HT) models.

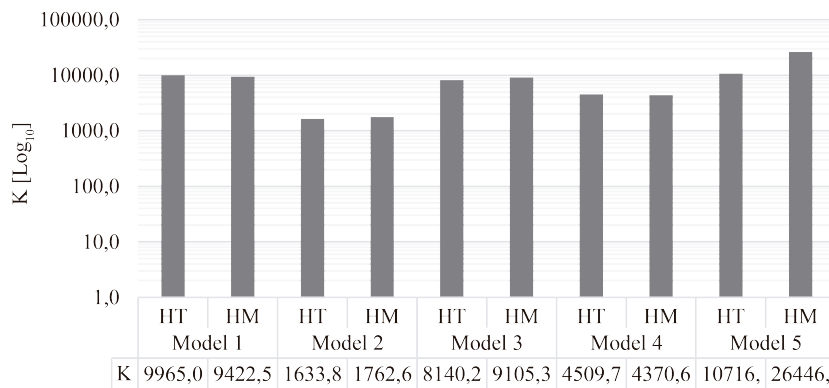


Figure 10 - Homogenized stiffness K for the mechanical simulation results performed using the second set of boundary conditions, for the homogeneous (HM) and heterogeneous (HT) models.

One factor possessing a significant impact in multiscale simulation is the computational cost. Thus, it was analyzed the computation cost of the developed methodology. In Figure 11 it is presented the computational cost of the performed mechanical simulation for each model, and for both boundary condition sets (set 1 and set 2). The developed methodology lead to a maximum decrease of 99.2% of the computation time, in the case of the model 1, a minimum of 51.7% for model 4 and a 90.3% average decrease of the computational time of all the models.

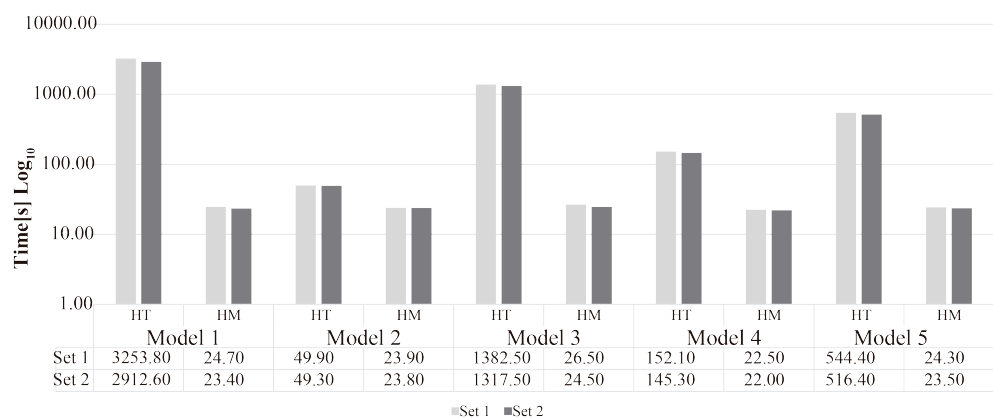


Figure 11 - Computational cost of the mechanical simulations performed using the 6 heterogeneous models (HT), and its 6 equivalent homogeneous models (HM), for the two sets of boundary conditions, set 1 and set 2.

5. Conclusions

In this work, it was proposed a methodology to define the homogeneous equivalent mechanical properties of the highly heterogeneous trabecular bone tissue. The methodology uses the fabric tensor concept and two material laws [8], [19], [20]. Concerning the fabric tensor, the results show that the fabric tensor actually encodes the trabecular bone orientation and anisotropy. Also, using the set of fabricated benchmarks, it was evaluated the robustness of the methodology, which allowed to conclude that it provides reliable information about the principal directions and anisotropy. The considered material laws (Belinha's law and Agic's law) complemented the fabric tensor information, by providing the Young's modulus of the homogenized material in the material's principal direction and the Poisson's coefficient (by using the average apparent density of the complete domain). The mechanical simulations analyzed heterogeneous and homogeneous models with equivalent mechanical properties obtained using the developed methodology. The simulations shown that the developed methodology define properly the equivalent mechanical proprieties of the homogeneous models. Since the analyzed geometric models have a distinct discretization (the nodes of two distinct models do not spatially coincide), it was not possible to compare the results using a local nodal comparison, in which are analyzed the displacements and stresses at the same nodal coordinates in both models. Thus, the concept of homogenized stiffness K was considered, proving to be an efficient tool to compare the homogeneous and heterogeneous models. Considering the differences in the homogenized stiffness K between the heterogeneous and the equivalent homogeneous models and the differences between the computation cost, it is possible to conclude that the proposed homogenization technique is capable to deliver accurate homogenized mechanical properties to be apply to very coarse homogenized discrete models in a fraction of time. Thus, the proposed homogenization methodology possesses the potential to decrease significantly the computational cost of demanding multiscale analyses without compromising its accuracy.

Acknowledgement

The authors truly acknowledge the funding provided by Ministério da Ciência, Tecnologia e Ensino Superior - Fundação para a Ciência e a Tecnologia (Portugal), under Grants SFRH/BD/110047/2015, and by project funding MIT-EXPL/ISF/0084/2017 and UIDB/50022/2020.

References

- [1] J.-Y. Rho, L. Kuhn-Spearing, and P. Zioupos, “Mechanical properties and the hierarchical structure of bone,” *Med. Eng. Phys.*, vol. 20, no. 2, pp. 92–102, Mar. 1998, doi: 10.1016/S1350-4533(98)00007-1.
- [2] M. Marco, E. Giner, J. R. Caeiro-Rey, M. H. Miguélez, and R. Larraínzar-Garijo, “Numerical modelling of hip fracture patterns in human femur,” *Comput. Methods Programs Biomed.*, vol. 173, pp. 67–75, May 2019, doi: 10.1016/J.CMPB.2019.03.010.
- [3] M. M. A. Peyroteo, J. Belinha, S. Vinga, L. M. J. S. Dinis, and R. M. Natal Jorge, “Mechanical bone remodelling: Comparative study of distinct numerical approaches,” *Eng. Anal. Bound. Elem.*, vol. 100, pp. 125–139, Mar. 2019, doi: 10.1016/j.enganabound.2018.01.011.
- [4] F. A. Sabet, A. Raeisi Najafi, E. Hamed, and I. Jasiuk, “Modelling of bone fracture and strength at different length scales: a review,” *Interface Focus*, vol. 6, no. 1, p. 20150055, 2016, doi: 10.1098/rsfs.2015.0055.
- [5] G. E. Wnek and G. L. Bowlin, *Encyclopedia of Biomaterials and Biomedical Engineering*, 2nd Editio., no. April. New York: CRC Press, 2008.
- [6] D. R. Carter, M. C. Van Der Meulen, and G. S. Beaupré, “Mechanical factors in bone growth and development,” *Bone*, vol. 18, no. 1 Suppl, pp. 5S–10S, Jan. 1996, doi: 10.1016/8756-3282(95)00373-8.
- [7] W. J. Landis, “The strength of a calcified tissue depends in part on the molecular structure and organization of its constituent mineral crystals in their organic matrix,” *Bone*, vol. 16, no. 5, pp. 533–544, May 1995, doi: 10.1016/8756-3282(95)00076-P.
- [8] J. Wolff, *The Law of Bone Remodelling*, vol. 82, no. 4. Berlin, Heidelberg: Springer Berlin Heidelberg, 1986.
- [9] O. Zienkiewicz, R. Taylor, and J. Z. Zhu, *The Finite Element Method: Its Basis and Fundamentals*, 7th ed. Butterworth-Heinemann, 2013.
- [10] J. Belinha, *Meshless Methods in Biomechanics*, vol. 16. Dordrecht: Springer International Publishing, 2014.
- [11] J. Martínez-Reina, J. Domínguez, and J. M. García-Aznar, “Effect of porosity and mineral content on the elastic constants of cortical bone: a multiscale approach,” *Biomech. Model. Mechanobiol.*, vol. 10, no. 3, pp. 309–322, Jun. 2011, doi: 10.1007/s10237-010-0236-4.
- [12] E. Perrin, B. Bou-Saïd, and F. Massi, “Numerical modeling of bone as a multiscale poroelastic material by the homogenization technique,” *J. Mech. Behav. Biomed. Mater.*, vol. 91, no. June 2018, pp. 373–382, Mar. 2019, doi: 10.1016/j.jmbbm.2018.12.015.
- [13] D. R. Carter, D. P. Fyhrie, and R. T. Whalen, “Trabecular bone density and loading history: Regulation of connective tissue biology by mechanical energy,” *J. Biomech.*, vol. 20, no. 8, pp. 785–794, Jan. 1987, doi: 10.1016/0021-9290(87)90058-3.
- [14] J. A. A. Sanz-Herrera, J. M. M. García-Aznar, and M. Doblaré, “On scaffold designing for bone regeneration: A computational multiscale approach,” *Acta Biomater.*, vol. 5, no. 1, pp. 219–229, Jan. 2009, doi: 10.1016/J.ACTBIO.2008.06.021.
- [15] R. Moreno, Ö. Smedby, and D. H. Pahr, “Prediction of apparent trabecular bone

- stiffness through fourth-order fabric tensors,” *Biomech. Model. Mechanobiol.*, vol. 15, no. 4, pp. 831–844, Aug. 2016, doi: 10.1007/s10237-015-0726-5.
- [16] S. C. Cowin, “The relationship between the elasticity tensor and the fabric tensor,” *Mech. Mater.*, vol. 4, no. 2, pp. 137–147, Jul. 1985, doi: 10.1016/0167-6636(85)90012-2.
- [17] W. J. Whitehouse, “The quantitative morphology of anisotropic trabecular bone,” *J. Microsc.*, vol. 101, no. 2, pp. 153–168, Jul. 1974, doi: 10.1111/j.1365-2818.1974.tb03878.x.
- [18] R. Moreno, M. Borga, and O. Smedby, “Techniques for Computing Fabric Tensors - A Review,” in *Mathematics and Visualization*, vol. 5, no. 12, 2014, p. pp 271-292.
- [19] J. Belinha, R. M. N. Jorge, and L. M. J. S. Dinis, “A meshless microscale bone tissue trabecular remodelling analysis considering a new anisotropic bone tissue material law,” *Comput. Methods Biomech. Biomed. Engin.*, vol. 16, no. 11, pp. 1170–84, Nov. 2013, doi: 10.1080/10255842.2012.654783.
- [20] A. Agić, V. Nikolić, and B. Mijović, “The cancellous bone multiscale morphology-elasticity relationship,” *Coll. Antropol.*, vol. 30, no. 2, pp. 409–14, Jun. 2006, Accessed: 13-Dec-2018. [Online]. Available: <http://www.ncbi.nlm.nih.gov/pubmed/16848160>.
- [21] A. W. Fitzgibbon, M. Pilu, and R. B. Fisher, “Direct least squares fitting of ellipses,” in *Proceedings of 13th International Conference on Pattern Recognition*, 1996, pp. 253–257 vol.1, doi: 10.1109/ICPR.1996.546029.
- [22] J. Belinha, L. M. J. S. M. J. S. Dinis, and R. M. M. Natal Jorge, “The analysis of the bone remodelling around femoral stems: A meshless approach,” *Math. Comput. Simul.*, vol. 121, pp. 64–94, Mar. 2016, doi: 10.1016/j.matcom.2015.09.002.
- [23] J. Hong, H. Cha, Y. Park, S. Lee, G. Khang, and Y. Kim, “Elastic Moduli and Poisson’s Ratios of Microscopic Human Femoral Trabeculae,” in *11th Mediterranean Conference on Medical and Biomedical Engineering and Computing 2007*, Berlin, Heidelberg: Springer Berlin Heidelberg, 2007, pp. 274–277.

3.9 Contribution VII. Application of an enhanced homogenization technique to the structural multiscale analysis of a femur bone. (Submitted)

3.9.1 Highlights of Contribution: 3.9

This contribution focused on the application of the developed homogenisation technique to a bone model. In this work, three meshes were developed and all three were used with the FEM to evaluated and compare the behaviour of the developed homogenisation technique.

Therefore, the main contents of this publication include:

- I. Literature review on homogenisation techniques;
- II. Application of a 3D homogenisation technique, where it is used the fabric tensor concept and a set of bone tissue phenomenological laws.
- III. Creation of a heterogenous geometrical model and of a homogenous geometrical model using medical images, giving origin to three meshes:
 - (a) Creation of a heterogeneous mesh (M1), with a real representation of the bone interior and exterior heterogeneous anatomy, with its mechanical properties defined using literature information.
 - (b) Creation of a homogeneous model (M2), representing bone as a single solid shell, with the mechanical properties defined using the developed homogenisation technique.
 - (c) Creation of a homogeneous model (M3), representing bone as a single solid shell, with two mechanical properties, defined according to the distribution of the DICOM image grey values.
- IV. Description of the methodology applied to use the homogenisation technique in the case of a mesh defined using medical images, where the methodology is applied to each element constituent of the homogenous mesh;
- V. A structural application using FEM was used to verify and to compare the mechanical behaviour of the three created meshes. In this structural analysis, two patches and three ROIS were used in each mesh, to allow a localised evaluation of the mechanical behaviour;

VI. Conclusions: The application of a bone homogenisation technique allows to develop 3D homogeneous models with equivalent mechanical behaviour to its 3D heterogeneous equivalent model, 3.14. The applied methodology is capable to accurately predict bone mechanical behaviour with less computational effort, and also, to decrease the computational effort associated with the mesh construction, that traditionally can present discretisation problems, reducing the ill-condition cases related with mesh distortion.

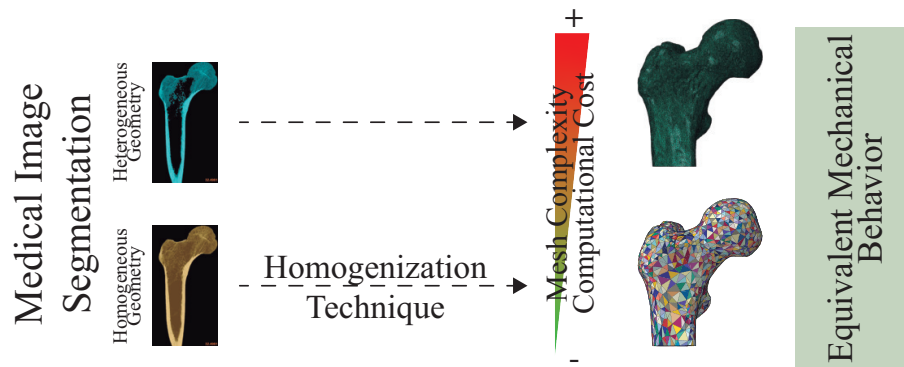


Figure 3.14: Computational cost of the models defined with the homogenised methodology versus the computational cost of the heterogenous models.

The complete document can be found in the next pages.

ARTICLE TEMPLATE

Application of an enhanced homogenization technique to the structural multiscale analysis of a femur bone

ARTICLE HISTORY

Compiled April 8, 2020

ABSTRACT

Bone is a complex hierarchical material that can be characterized from the microscale to macroscale. This work demonstrates the application of an enhanced homogenization methodology to the multiscale structural analysis of a femoral bone. The use of this homogenization technique allows to remove subjectivity and reduce the computational cost associated with the iterative process of creating a heterogeneous mesh. Thus, it allows to create simpler homogenized meshes with its mechanical properties defined using information directly from the mesh source: the medical images. Therefore, this methodology is capable to accurately predict bone mechanical behavior in a fraction of the time required by classical approaches. The results show that using the homogenization technique, despite the differences between the used homogeneous and heterogeneous meshes, its mechanical behavior is similar. The proposed homogenization technique is useful for a multiscale modelling and it is computationally efficient.

KEYWORDS

Fabric Tensor; Homogenization Technique; Multiscale; Bone; MIL

1. Introduction

Bone is a complex biological structure, which can be divided in distinct spatial scales, from the nanoscale to the macroscale Dorozhkin (2010); Barkaoui et al. (2014). To understand bone physiology, it is necessary to understand bone at its different scales and therefore understand the relation between different scales. Some previous research works focus on the study of bone's tissue using distinct approaches, such as the macroscale approach Marco et al. (2019), the microscale approach Belinha et al. (2016, 2013); Peyroteo et al. (2019), and the multiscale approach Sabet et al. (2016); Ghosh et al. (1995); Coelho et al. (2009). Bone remodeling process, the process responsible to renew bone matrix by creating or reabsorbing it Wnek and Bowlin (2004), is one of the subjects where multiscale approaches are advantageous. Using bone information from two or more scales it is possible to describe the distinct behavior of bone tissue at different scales Landis (1995). With multiscale models it is possible to describe the mechanical behavior of bone using homogenization techniques Moreno et al. (2016); Perrin et al. (2019). To define and approximate biological processes using mathematical descriptions, it is usual to apply analytical and numerical methodologies combined with distinct discretization approaches, such as finite element methods (FEM) and meshless methods Belinha (2014). The numerical approaches to study bone remodeling began with a simplistic approach where bone tissue was considered an homogeneous isotropic-elastic material, a consideration that disregarded the im-

portance of material orientation and structure - its anisotropy. In fact, bone's tissue anisotropic nature was a main material characteristic that Wolff reported as having a directly influence on the bone mechanical behavior impacting the remodeling process Wolff (1986). Having in consideration that many of bone remodeling studies are performed using discretization methodologies, where the highly heterogeneous trabecular bone domain can influence the performance of such methodologies, and that, bone remodeling leads to a morphological evolution (changing the physical domain where the discretization methodologies are being applied to), some authors started to use homogenization techniques. Such strategy allowed to define bone highly heterogeneous domain (observed at the microscale) as a homogeneous domain (at the macroscale), but still considering its local homogenized orientation and anisotropy Moreno et al. (2016). The homogenization methodology used in this work uses the fabric tensor concept and a set of phenomenological laws, allowing to determine properties of a heterogeneous material by substituting this material with an equivalent homogeneous material, and so, allowing to predict the behavior of the macro-scale using the micro-scale, and vice-versa Cowin (1985); Whitehouse (1974); Marques et al. (2019c,a,b, 2018). The homogenization techniques used to define bone mechanical properties (among many other methodologies, such as digital image correlation or mechanical experiments) are of high importance since they allow to define the material's mechanical properties, feeding constitutive matrices and laws for advanced discretization techniques and other analytical methodologies. Thus, the main objective of this work is to understand if the homogenized anisotropic material properties (obtained with the proposed homogenization technique combined with FEM) applied to the structural analysis of a femur bone, allow to achieve similar results with the structural analysis of a corresponding highly discretized heterogeneous multiscale femur bone. This work also has the goal to expand the previously developed 2D homogenization methodology, Marques et al. (2019c,a,b, 2018), to 3D, which results on a completely different approach. This work presents for the first time a new homogenization technique combining several computational mathematical/mechanical concepts. It combines the fabric tensor concept with medical image data to obtain the material principal axis. Furthermore, it uses the gray-tone information of the medical image to acquire the local mechanical properties of each material point by means of well-established phenomenological laws correlating the apparent bone density with the axial Young's modulus. Although being a preliminary study, this work extends the technique to a large scale problem showing its robustness and efficiency. Thus, this new methodology is capable to homogenize the mechanical properties of a heterogeneous medium at the microscale in a fraction of the time of traditional homogenization techniques, allowing to perform faster large scale multiscale analyses. Furthermore, it is aimed to report the difference between the computational cost and efficiency of a full heterogeneous analysis and a simplified multiscale homogeneous analysis.

2. Methodology

This work is divided in two parts. The first part intends to evaluate the robustness of the developed homogenization methodology algorithm. In the second part it is performed a structural analysis, where it is applied and analyzed the developed homogenization methodology on a femur bone mesh. In the first part of this work four benchmark with well-defined geometric characteristics were defined, containing bone voxels (represented in blue in figure 1) and non-bone voxels (not represented in figure

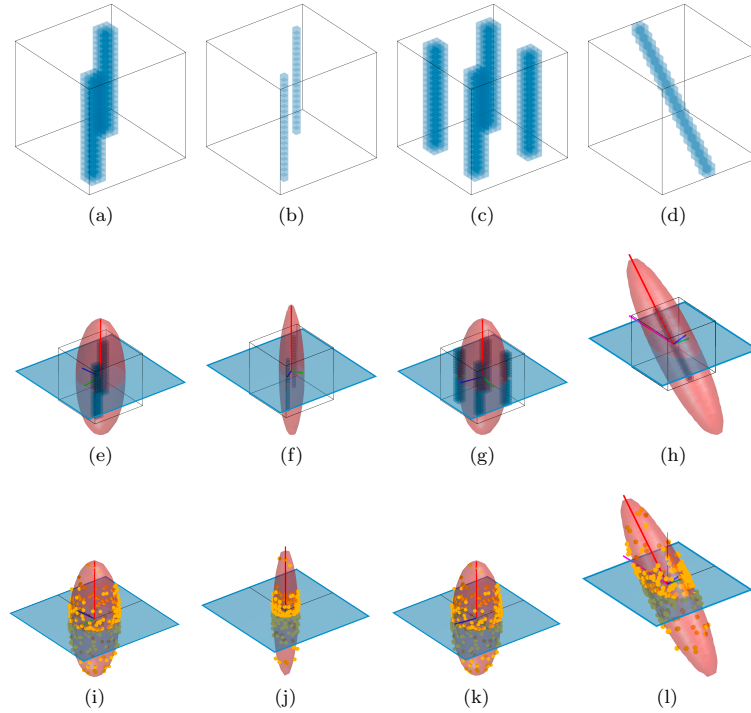


Figure 1.: Images 1a to 1d represent the fabricated benchmarks, images 1e to 1h represent the respective ellipsoid fitting, and images 1e to 1l represent the *MIL* Cartesian coordinates data scatter with the fitted ellipsoid.

1). Benchmark 1, figure 1a, has a well-defined vertical material principal direction, being defined by two groups of bone voxels. Benchmark 2, figure 1b, is a thinner version of Benchmark 1, also showing well-defined vertical material principal direction. Benchmark 3, figure 1c, represent a benchmark with a well-defined vertical material principal direction, but with the trabeculae showing a larger transversal section, when compared to benchmark 1 and 2. Benchmark 4, figure 1d has a diagonal material principal direction. The main difference between benchmark 1 and 2, is the number of voxels that define the thickness of the bone region. The analysis of these benchmarks aims to evaluate the obtained algorithm mechanical properties and verify if they translated the benchmarks morphology.

The created benchmarks were defined by binary information, bone or non-bone voxel. This information was used by the developed homogenization methodology to count the interceptions between the bone voxel and the vectors from a vector list contained inside a search sphere. The vectors inside the search sphere have random directions, ι , kept constant along all the iterations. In this methodology each iteration represents a change in the sphere position within the boundaries of the physical domain under study, in this case: the cubic domain of the benchmark. Within this domain boundary, the interceptions $Int(\iota)$ are counted between each vector with the specific vector direction, ι , and the bone voxels. Multiplying the number of iterations of the process with the characteristic size of the vectors, h , defined by the search sphere size, $h \times iter$ and dividing this value by the number of interceptions of a vector with

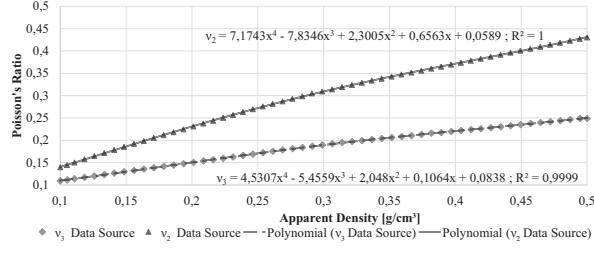


Figure 2.: Data from Agić et al. (2006) fitted to polynomial functions.

direction $Int(\iota)$, it was obtained the Mean Intercept Length MIL for the direction ι , equation (1). This equation allows to transform the intersection count into Cartesian coordinates, as represented in figure 1(i) to 1(l) by the scatter orange dots.

Having the MIL , the orientation distribution function (ODF) data, it was possible to fit this data into an ellipsoid using Fitzgibbon methodology, Fitzgibbon et al. (1996). Using the ellipsoid it is possible to extract its radius, r_1 , r_2 and r_3 being $r_1 > r_2 > r_3$, the angles theta, θ , and the azimuth ω , defined from r_1 , that defines the ellipsoid 3D orientation. r_1 , r_2 and r_3 are normalized by the r_1 size, being always $r_1 = 1$.

$$MIL(\iota) = \frac{h \times iter}{Int(\iota)} \quad (1)$$

Using these ellipsoid parameters, and applying Belinha et al. (2013) and from Agić et al. (2006) phenomenological material laws it was possible to create and define a material law for the domain in study. Using the domain binary information it was possible to define bone apparent density, ρ_{app} . The ρ_{app} was acquired using a relation between the number of bone voxels, w_v , and the non-bone voxels, b_v , equation 2. In this equation, $\rho_0 = 2.1g/cm^3$ represents the bone typical maximum apparent density. Also, using domain binary information and the universal mixture laws it was possible to define ν_1 , equation (3), where $\nu = 0.3$ is the typical Poisson's ratio for cortical bone (bone voxels, at the microscale). Using Agić et al. (2006) phenomenological material, figure 2, it was possible to obtain ν_2 and ν_3 , considering a relation with the bone apparent density, ρ_{app} , equation (4) and (5).

$$\rho_{app} = \frac{w_v}{(b_v + w_v)} \times \rho_0 \quad [g/cm^3] \quad (2)$$

$$\nu_1 = \frac{(0 \times b_v) + (0.3 \times w_v)}{(b_v + w_v)} \quad (3)$$

$$\nu_2 = \begin{cases} 7.1743\rho_{app}^4 - 7.8346\rho_{app}^3 + 2.3005\rho_{app}^2 + 0.6563\rho_{app} + 0.0589 & \rightarrow \text{if } \rho_{app} < 0.5 \\ 0.43 & \rightarrow \text{if } \rho_{app} \geq 0.5 \end{cases} \quad (4)$$

$$\nu_3 = \begin{cases} 4.5307\rho_{app}^4 - 5.4559\rho_{app}^3 + 2.048\rho_{app}^2 + 0.1064\rho_{app} + 0.0838 & \rightarrow \text{if } \rho_{app} < 0.5 \\ 0.245 & \rightarrow \text{if } \rho_{app} \geq 0.5 \end{cases} \quad (5)$$

In order to define E_1 it was used Belinha's material law Belinha et al. (2016). Concerning E_2 and E_3 , it was defined a relation between E_1 and the ellipsoid radius parameters r_1 , r_2 and r_3 . Thus, E_2 was defined using a relation between r_1 , r_2 and E_1 , equation (6), and E_3 , was defined using r_1 , r_3 and E_1 , equation (7).

$$E_2 = \frac{r_2 \times E_1}{r_1} \quad (6)$$

$$E_3 = \frac{r_3 \times E_1}{r_1} \quad (7)$$

The shear modulus, G_1 , G_2 and G_3 , were approximated using equation (8), (9) and (10), respectively:

$$G_1 = \frac{E_1}{2 \times (1 + \nu_1)} \quad (8)$$

$$G_2 = \frac{E_2}{2 \times (1 + \nu_2)} \quad (9)$$

$$G_3 = \frac{E_3}{2 \times (1 + \nu_3)} \quad (10)$$

Using the homogenization methodology it was possible to mechanically define each benchmark's domain, acquiring E_1 , E_2 , E_3 , ν_1 , ν_2 , ν_3 , G_1 , G_2 , G_3 and θ and ω . This parameters allow to evaluate if the obtained mechanical properties translate well the different morphologies and characteristics of each benchmark.

The second part of the work was to mechanically analyze, using the finite element analysis (FEA), the behavior of a mesh with its mechanical properties obtained using the developed homogenization technique. For this, three meshes were created, describing the femur geometry from the femur head to a few centimeters distal from the less trochanter. The information used to create these meshes was acquired using medical images with a resolution of 512×512 pixels over 706 slices and a voxel dimension of $0.27539 \times 0.27539 \times 0.625$ mm (x, y, z). Using MIMICS Innovation Suit from Materialize (2017), it was possible to segment the femur and create the meshes. To analyze and compare the behavior of an homogenous mesh defined using the developed homogenization two other meshes were created. Thus, in this work, it was defined an heterogeneous mesh M_{ht} , a simplified mesh M_s , and the homogenous mesh M_{hm} . The developed homogenization technique was applied only to the homogenous mesh, M_{hm} . The heterogeneous mesh, M_{ht} , figure 4a and 4b, defined using a MIMICS image mask that only represents the spacial information of bone voxels, represented in figure 3a. This mesh is highly heterogeneous, figure 3c, possessing void zones in its inner space, a characteristic of trabecular bone morphology. Using the segmentation

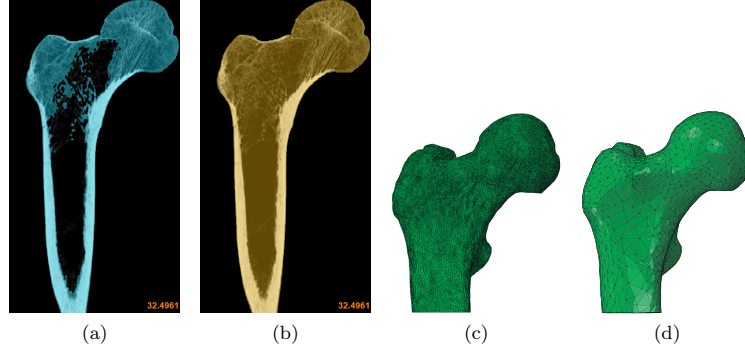


Figure 3.: Segmentation masks, Figure 3b and 3a, were created using MIMICS Materialise (2017) and gave origin to two geometrical models. Figure 3c represents the obtained heterogeneous geometrical model obtained using mask from Figure 3a; Figure 3d represents the homogeneous geometrical model obtained using the mask from Figure 3b.

information created to define the heterogeneous mesh, and using image processing tools, it was possible to define a new mask, figure 3b. This mask allowed to create a geometrical model that just represents the bone boundaries, ignoring the inner bone structure, figure 3d. Using this mask, it was possible to define a homogeneous geometrical model. This homogeneous geometrical model was used to define the simplified, M_s , and the homogenous, M_{hm} , meshes. For the homogenized mesh M_{hm} , figure 4c and 4d, the mechanical properties of each element are defined using the developed homogenization technique, which uses Belinha's and Agic's phenomenological laws Belinha et al. (2013); Agić et al. (2006) to correlate the bone apparent density with the Young's modulus and the Poisson's coefficient, respectively. The procedure to apply this homogenization technique into the created mesh, M_{hm} , is explained further. For the simplified mesh M_s , figure 4e and 4f, the mechanical properties were spatially distributed using BONEMAT software Taddei et al. (2007). Using the medical images and this software, it was possible to define for each mesh element which one correspond to cortical or trabecular bone. This was possible because the voxels intensity is related with the bone density. Thus, this allows the software to create two different element sets associated with the image voxels intensity values. Then, it is possible to define for each set distinct mechanical properties.

In order to use the developed homogenization technique to define the mechanical properties of the homogenized mesh, M_{hm} , each element of the mesh has to be mechanically defined. Thus, the homogenization technique, was applied to each mesh element, $e^i, i \in [1, 2, \dots, n]$, being n the total number of mesh elements. The first step of this procedure was to overlap M_{hm} mesh into the medical image, I , used to define the segmentation mask that gave origin to the geometrical model. For each tetrahedral element of the mesh, defined by 4 nodes $N_j^e, j \in [1, 2, 3, 4]$, it was possible to define the largest distance between all the nodes of each element, $e_{\Delta d}^i$. Then, using $e_{\Delta d}^i$ it was defined a cube C_e^i , with $e_{\Delta d}^i \times e_{\Delta d}^i \times e_{\Delta d}^i$ dimension. Defining the centroid for each element, e_C^i , the image I , and C_e^i , it was defined for each element, a sub-image, I_{e^i} that has its center in C_e^i , and the same C_e^i dimensions. To apply the homogenization methodology it was applied to each sub-image I_{e^i} , a binary segmentation process

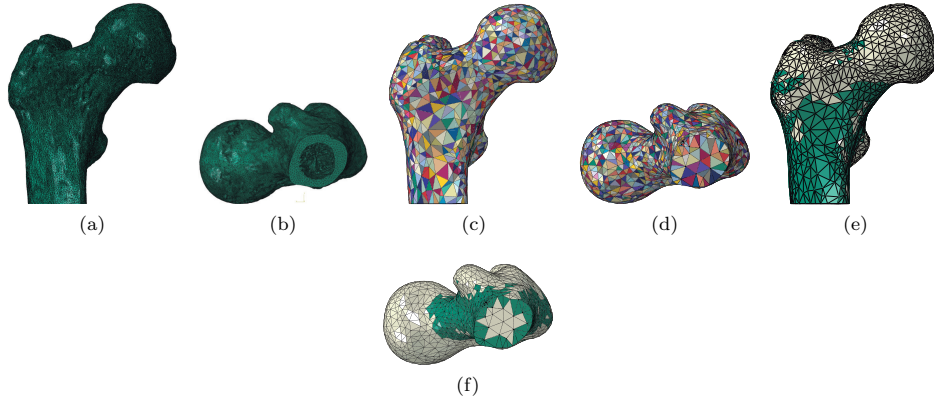


Figure 4.: Created meshes: 4a: - M_{ht} mesh frontal view; 4b: - M_{ht} mesh down view; 4c: - M_{hm} mesh frontal view ; 4d: - M_{hm} down view. In this image the different colors elements represent elements with different mechanical properties; 4e: - M_s mesh frontal view; 4f: - M_s mesh down view. In this image the two different colors represent two different mechanical properties distributed in the mesh.

using the Otsu method Otsu (1979), allowing to define which DICOM voxels represent bone or non-bone space. After defining the binary information to each sub-image I_{e^i} , it was applied the homogenization methodology that mechanically define each I_{e^i} correspondent element. In figure 5 , three random M_{hm} elements are represented, to which the methodology was applied to, being the red pale rectangle I , the green zone M_{hm} nodes, and the red scatter inside the green zone the I_{e^i} sub-image.

In this case, since each element has its own local axis, the acquired informations needed to be transformed to the mesh global axis. Thus, defining a constitutive matrix $\mathbf{c}_{ox'y'z'}$, equation (11) for the elements $ox'y'z'$ local coordinate system (oriented with the material principal axis), and using θ and ω , it was possible to define the transformation rotation matrices \mathbf{T} , equation (12) and (13), allowing to define the material constitutive matrix in the global axis with equation (14), for each element.

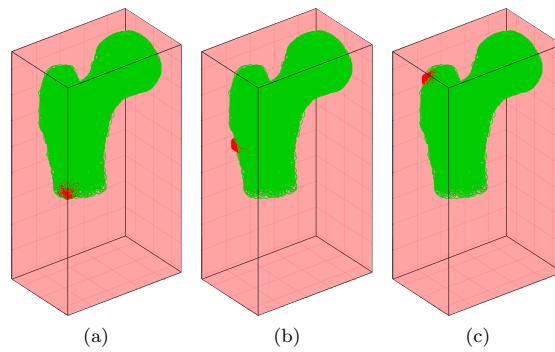


Figure 5.: 5a, 5b and 5c represent different iteration examples of the used methodology to define the mechanical properties of a specific element $e^i, i \in [1, 2, \dots, n]$.

Table 1.: M_{ht} , M_{hm} and M_s Mesh Properties.

Mesh Properties			
	M_{ht}	M_{hm}	M_s
# Nodes	210725	1939	1939
# Elements	799331	7248	7248
# Materials	1	7248	2

$$\mathbf{c}_{ox'y'z'} = \begin{bmatrix} \frac{1}{E_1} & \frac{-\nu_1}{E_2} & \frac{-\nu_3}{E_3} & 0 & 0 & 0 \\ \frac{-\nu_1}{E_1} & \frac{1}{E_2} & \frac{-\nu_2}{E_3} & 0 & 0 & 0 \\ \frac{-\nu_3}{E_1} & \frac{-\nu_2}{E_2} & \frac{1}{E_3} & 0 & 0 & 0 \\ 0 & 0 & 0 & \frac{1}{G_1} & 0 & 0 \\ 0 & 0 & 0 & 0 & \frac{1}{G_2} & 0 \\ 0 & 0 & 0 & 0 & 0 & \frac{1}{G_3} \end{bmatrix} \quad (11)$$

$$\mathbf{T}_{oy}(\beta) = \begin{bmatrix} \cos^2 \beta & 0 & \sin^2 \beta & 0 & 0 & \sin 2\beta \\ 0 & 1 & 0 & 0 & 0 & 0 \\ \sin^2 \beta & 0 & \cos^2 \beta & 0 & 0 & -\sin 2\beta \\ 0 & 0 & 0 & \cos \beta & -\sin \beta & 0 \\ 0 & 0 & 0 & \sin \beta & \cos \beta & 0 \\ -\sin \beta \cos \beta & 0 & \sin \beta \cos \beta & 0 & 0 & \cos^2 \beta - \sin^2 \beta \end{bmatrix} \quad (12)$$

$$\mathbf{T}_{oz}(\beta) = \begin{bmatrix} \cos^2 \beta & \sin^2 \beta & 0 & -\sin 2\beta & 0 & 0 \\ \sin^2 \beta & \cos^2 \beta & 0 & \sin 2\beta & 0 & 0 \\ 0 & 0 & 1 & 0 & 0 & 0 \\ \sin^2 \beta & -\sin^2 \beta & 0 & \cos^2 \beta - \sin^2 \beta & 0 & 0 \\ 0 & 0 & 0 & 0 & \cos \beta & -\sin \beta \\ 0 & 0 & 0 & 0 & \sin \beta & \cos \beta \end{bmatrix} \quad (13)$$

$$\mathbf{c}_{xyz} = [\mathbf{T}_{oz}]_{\theta}^T \left[[\mathbf{T}_{oy}]_{\omega}^T \mathbf{c}_{ox'y'z'} [\mathbf{T}_{oy}]_{\omega} \right] [\mathbf{T}_{oz}]_{\theta} \quad (14)$$

2.1. Structural Application

Using the created meshes, it was performed a structural analysis that allowed to compare the behavior of the meshes defined with different mechanical properties. The number of nodes, elements and the number of mechanical properties used in each mesh are described in Table 1. The three meshes were defined by four-nodes constant strain 3D solid tetrahedral elements (C3D4). M_{ht} and M_s mechanical properties are described in Table 2. For M_{hm} mesh it is inconvenient to represent the used mechanical properties, once its number is equal to the number of elements.

Table 2.: Mechanical properties used to define bone mechanical properties Hong et al. (2007); Kelly and McGarry (2012).

Mechanical Properties		
	Cortical Bone	Trabecular Bone
Young's Modulus [GPa]	3.470	0.3055
Poisson's Ratio	0.36	0.16

2.1.1. Boundary Conditions

The three meshes were defined with the same boundary conditions. The nodes at $z = 0$, in the lower bone zone, were fully constrained. Two forces were applied in two different zones. F_a it was applied to the femur head zone, presented in figure 6c as the red zone in the femur head, S1. F_b was applied in the femur greater trochanter, represented in figure 6c by the left red zone in the bone, S2. The magnitude of the applied loads was obtained from the literature, being $F_a = [-942.409, 0, -2116.68]$ N and $F_b = [330.039, 0, 620.712]$ N Belinha et al. (2012). The F_a load case considers a simple vertical load applied to the head of the femur. This load case corresponds to a vertical load of 725N induced by the weight of a 74Kg human being minus the weight of one leg. The one-legged stance considered here cannot be maintained without the action of the hip abductor muscles that prevent the rotation movement of the body around the hip joint rotation axis. This force has an estimated value of 1592N. The addition of this force gives a total combined load at the head of the femur of 2317N, increasing the compression the femoral neck. The load F_b represents the force on the trochanter, representing the abductor muscle actuation upon the one-legged stance position. To compare the three meshes, two linear paths were defined in each mesh. The first path, P1 was defined from the femur neck to the subtrochanteric zone, as represented in figure 6a. This path starts in point O_{P1} and finishes in point L_{P1} , being L the path total length. The second path was defined in the mesh base, P2, crossing it from one side to other starting in point O_{P2} and finishing in point L_{P2} , being L the path total length, as represented in figure 6b. With the same comparison purpose, four regions of interest (ROI) were defined: ROI_1 , ROI_2 , ROI_3 and ROI_4 . For each ROI, possessing a 7.5mm radius, the average von Mises stress was obtained. The created ROIs are represented as the blue zones, in figure 6.

3. Results and Discussion

In this section, the results obtained are described and discussed, allowing to understand the robustness and stability of the developed algorithm and its structural viability.

3.1. Fabric Tensor Algorithm Robustness

In Table 3, the parameters obtained with the developed methodology for each benchmark, figure 1, are shown. Comparing the results of benchmark 1 and 2, figure 1a and

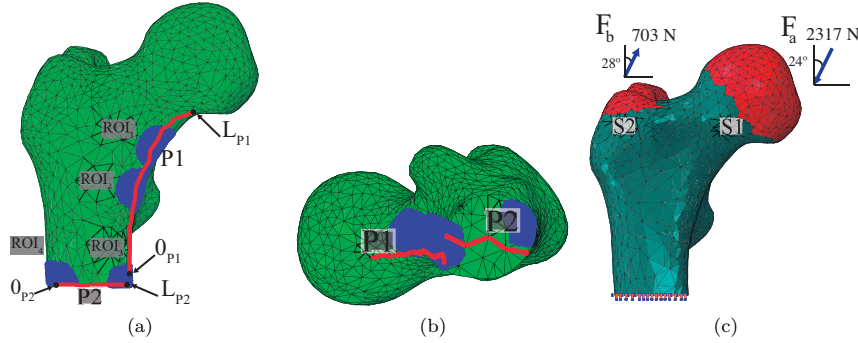


Figure 6.: Red Lines: path 1 (P1) and path 2 (P2); Blue zones: ROIs. 6a - Frontal View; 6b - Down View; 6c - S1 and S2 and respective F_a and F_B loads; Mesh constraints, in the bone lower zone.

figure 1b, and considering the benchmarks characteristic, it can be conclude that these results are as expected. Benchmark 1 and 2 have the same principal direction, reflected in θ and ω and in E_1 and G_1 , that are higher when compared to E_2 , E_3 and to G_2 , G_3 . Having benchmark 1 a thicker morphology, when compared to benchmark 2, ρ_{app} reflect this aspect by being higher in benchmark 1. Concerning benchmark 3, figure 1c, it also has a vertical principal direction, reflected in $\theta = 89.71$, and also reflected by the higher E_1 and G_1 , compared to E_2, E_3 and G_2, G_3 . Comparing benchmark 3 with benchmark 1 and 2, it is noticeable the higher E_2 , E_3 , G_2 and G_3 , that reflects the higher transversal cross section and so, a higher stiffness in direction 2 and 3. The ρ_{app} from benchmark 3, has the higher value when comparing to all of the other benchmarks, reflecting the higher number of bone voxels in the benchmark. Benchmark 4, figure 1h, as previously described, has a diagonal principal direction, reflected in θ and ω parameters from Table 3. The remain parameters, E_1 , E_2 , E_3 , G_1 , G_2 , G_3 , ν_1 , ν_2 , ν_3 and ρ_{app} , reflect the different number of voxels that define the thickness of the bone region. The obtained fitted ellipsoids and the fitted ellipsoids with *MIL* data are presented in figure 1e to 1l. In these images it is visible that the fitted ellipsoid and the *MIL* data have the same material principal direction, re-enforcing the fact that the developed methodology is able to define and encode trabecular bone orientation and anisotropy.

3.2. Structural Analysis

It is important to recall that mesh M_{ht} possesses much more nodes than meshes M_{hm} and M_s . Such discretization difference is important to understand the relevance of the obtained results. The M_{hm} and M_s meshes have $108.6\times$ less nodes and $110.28\times$ less elements when compared to the M_{ht} mesh. The three meshes show that the maximum displacement u_{max} occurs on the femoral head: $u_{max}^{M_{ht}} = 2,611$ mm, $u_{max}^{M_{hm}} = 6,337$ mm and $u_{max}^{M_s} = 4,642$ mm. The distribution of the equivalent von Mises stress in the meshes is similar, as represented in figure 7. It was observed that a stress concentration occurs in the lower part of the femur neck down to the subtrochanteric zone. Also in the neck upper zone, the three meshes have a visible stress concentration. This two concentration zones are expected due to the applied loads, as described by Belinha et al. Belinha et al. (2012). Observing the stress distribution for the three meshes, it is

Table 3.: Parameters obtained using the developed methodology, defining the mechanical properties of the created benchmarks, before the transformation using equation (14), used to evaluate the algorithm robustness.

	Benchmark			
	1	2	3	4
ω	83,7	90,11	138,55	90,51
θ	89,94	89,79	89,71	44,54
E_1	75,39	7,67	165,17	22,72
E_2	28,82	1,34	62,9	5,27
E_3	28,78	1,34	62,45	4,96
G_1	37,19	3,83	80,41	11,31
G_2	12,69	0,63	25,75	2,44
G_3	12,99	0,61	27,25	2,28
ν_1	0,014	0,002	0,03	0,01
ν_2	0,14	0,07	0,22	0,08
ν_3	0,11	0,09	0,15	0,09
ρ_{app}	0,09	0,01	0,19	0,03

possible to understand that the stress concentrations are similar in the three meshes, re-enforcing that the three meshes have a similar mechanical behavior. Concerning M_{ht} , the higher equivalent stress value is 741 MPa, a value much more higher than the average stress value of the mesh, but also from the other two meshes. This can occur because of the high heterogeneous nature of the meshes that can lead to stress concentrations and numerical inaccuracies. Comparing M_{hm} and M_s stress distribution it is visualized that the stress distribution of M_{hm} is smoother, and that it is possible to observe the absence of the abrupt transitions of stress resultant from the material properties spatial distribution. Afterwards, new numerical approaches to compare the results had to be developed, since the use of different meshes (in discretization size) hinder a direct comparison of M_{ht} , M_{hm} and M_s results using the traditional node to node and element to element comparison. Thus, the results obtained of the paths (P1 and P2) and for the ROI (ROI_1, \dots, ROI_4) were compared. The results regarding the von Mises equivalent stress for each path, figure 6a and 6b, are represented in figure 8. For P2, the three meshes have a VM average stress value of $\sigma_{eq}^{M_{ht}} = 28,59$ MPa, $\sigma_{eq}^{M_{hm}} = 33,88$ MPa and $\sigma_{eq}^{M_s} = 31,74$ MPa. These results show that it exists a larger difference in the results when comparing mesh M_{ht} with M_{hm} , and a lower difference when comparing M_{hm} with M_s . Concerning P1, comparing M_{hm} and M_s meshes, it can be said that they possess a similar behavior, having lower VM equivalent stress values in the path zone corresponding to the interior part of the bone, characteristic of having trabecular bone. Comparing M_{ht} with M_{hm} and M_s , this mesh has higher VM stress values, and have null values in the path zone correspondent to the mesh zone where there is no bone tissue, as can be seen in figure 4b. The higher values of M_{ht} can be explained by the highly heterogeneous mesh, that can lead to unexpected results in the structural analysis. The P1 path VM average stress are $\sigma_{eq}^{M_{ht}} = 6.53$ MPa, $\sigma_{eq}^{M_{hm}} = 5.69$ MPa and $\sigma_{eq}^{M_s} = 5.32$ MPa. Concerning the average VM values of the created ROIs, Table 4, it is possible to observe that the M_{ht} mesh has lower

Table 4.: M_{ht} , M_{hm} and M_s , ROIs average VM stress.

Average VM Stress in ROI [MPa]			
Mesh	M_{ht}	M_{hm}	M_s
ROI_1	25.87	34.74	36.45
ROI_2	18.87	37.98	31.33
ROI_3	16.82	31.44	19.91
ROI_4	15.96	17.27	16.01

values when compared to both M_{hm} and M_s . As expected, the higher values for the three meshes occur in ROI_1 and ROI_2 , since they are located in the femoral neck zone. This observation is reinforced with the information provided with the stress filed color maps from figure 7, where ROI_1 and ROI_2 are located in the zones with colors matching higher VM values. Concerning the computational cost of the structural analysis of the three meshes, the M_{ht} mesh finished the analysis in 2012 s, the M_{hm} mesh finished the analysis in 5 s and the M_s meshes finished the analysis in 1 s, being notorious that the M_{ht} mesh was the meshes with higher computational cost, $402,5\times$ and $2012\times$ more when compared with M_{hm} and M_s meshes, respectively. One factor that has high impact in this process, is the creation of the M_{ht} mesh. The creation of the mask and subsequent manipulation to create a functional mesh, is iterative, often leading to invalid or unusable meshes. Also its construction and the procedure to achieve the final mesh is highly subjective and strongly depends on the user ability. This comes from the fact that many of the processes used to define the geometry from the mask are not fully automatic (depend on the user decision and ability/efficiency with the software), leading to the creation of different meshes from the same mask. This process can be time consuming, and can lead to the definition of meshes that are not representative of the created segmentation masks. On the other hand, using the masks from figure 3b all the subjective processes from the mesh creation are reduced, since it is easier to create meshes that are confined to a single shell, where its inner elements can be homogeneously distributed, leading to a lower time consuming process to create the mesh. This study uses a methodology well-established in medical image processing, in particularly in the use of automatic image segmentation. The use of a unique segmentation threshold value for all the study sub-images, I_{e^i} normalizes the image set image processing. However, considering a unique value can translate into a poor-quality outcome if the image set possesses a high intensity variability. In the future, the authors expect to apply this methodology to study bone remodeling, where bone mechanical properties are constantly changing with the remodeling. Thus, with this methodology, it will possible to define the transient bone mechanical properties, considering the morphological changes resultant from bone remodeling.

4. Conclusion

In this work, it was demonstrated a methodology that enables to define the homogeneous equivalent mechanical properties of the highly heterogeneous bone tissue. The

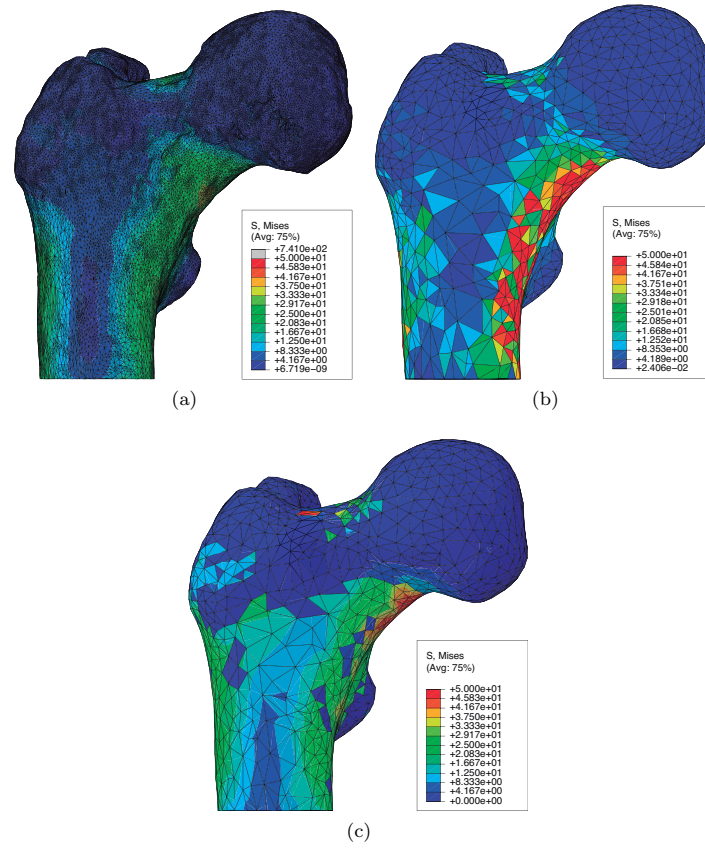


Figure 7.: 7a - Heterogenous mesh, M_{ht} , Von Misses stress field maps; 7b - Homogeneous mesh, M_{hm} , Von Misses stress field maps; 7c - Simplified mesh, M_s , Von Misses stress field maps.

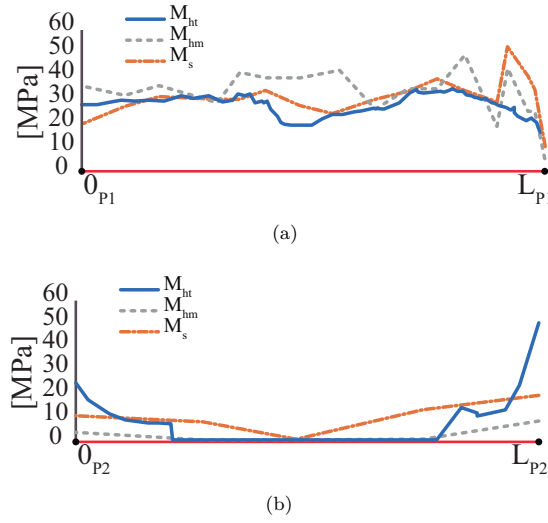


Figure 8.: Von Misses Stress Distribution 8a - Path P1; 8b - Path P2.

methodology uses the fabric tensor concept and two phenomenological laws Belinha et al. (2013); Agić et al. (2006). The fabric tensor robustness analysis showed that the methodology is capable to mechanically define a structure by considering the CT images and the bone domain anisotropy. The performed structural analysis shown that the homogenization methodology properly defines the equivalent mechanical properties of the homogeneous meshes. Having the M_{ht} and M_{hm}/M_s different meshes, $108.6 \times$ less nodes, for comparison purposes, two approaches were defined, the paths and ROIs, that allowed to locally compare the results. This approaches revealed to be capable to demonstrate that the observed stress levels are equivalents. Plus, VM stress average values and local displacement values between meshes are similar. Considering the differences between the M_{ht} , M_{hm} and M_s and the differences between the computation cost, it is possible to conclude that the homogenization technique is capable to define the mechanical properties of bone tissue using medical images information, reducing the overall computational cost of the analysis. In addition, the proposed technique removes some of the subjectivity associated with the creation of the heterogeneous meshes. This allows to conclude that this methodology is efficient and possesses the potential to be used in demanding multiscale analyses without compromising its accuracy and increasing the computational efficiency, by reducing the analyses computational cost.

Acknowledgements

The authors truly acknowledge the funding provided by Ministério da Ciência, Tecnologia e Ensino Superior - Fundação para a Ciência e a Tecnologia (Portugal), under Grants SFRH/BD/110047/2015, and by project funding MIT-EXPL/ISF/0084/2017 and UIDB/50022/2020.

References

- Agić A, Nikolić V, Mijović B. 2006. The cancellous bone multiscale morphology-elasticity relationship. *Collegium antropologicum*. 30(2):409–14. Available from: <http://www.ncbi.nlm.nih.gov/pubmed/16848160>.
- Barkaoui A, Chamekh A, Merzouki T, Hambli R, Mkaddem A. 2014. Multiscale approach including microfibril scale to assess elastic constants of cortical bone based on neural network computation and homogenization method. *International Journal for Numerical Methods in Biomedical Engineering*. 30(3):318–338. Available from: <https://onlinelibrary.wiley.com/doi/abs/10.1002/cnm.2604>.
- Belinha J. 2014. Meshless Methods in Biomechanics. (Lecture Notes in Computational Vision and Biomechanics; vol. 16). Dordrecht: Springer International Publishing. Available from: <http://link.springer.com/10.1007/978-3-319-06400-0>.
- Belinha J, Dinis L, Natal Jorge RM. 2016. The analysis of the bone remodelling around femoral stems: A meshless approach. *Mathematics and Computers in Simulation*. 121:64–94. Available from: <http://www.sciencedirect.com/science/article/pii/S0378475415001895>.
- Belinha J, Jorge RMN, Dinis LMJS. 2013. A meshless microscale bone tissue trabecular remodelling analysis considering a new anisotropic bone tissue material law. *Computer methods in biomechanics and biomedical engineering*. 16(11):1170–84. Available from: <http://www.tandfonline.com/doi/abs/10.1080/10255842.2012.654783><http://www.ncbi.nlm.nih.gov/pubmed/22309146>.
- Belinha J, Natal Jorge RM, Dinis LMJS. 2012. Bone tissue remodelling analysis considering a radial point interpolator meshless method. *Engineering Analysis with Boundary Elements*. 36(11):1660–1670. Available from: <http://dx.doi.org/10.1016/j.enganabound.2012.05.009>.
- Coelho PG, Fernandes PR, Rodrigues HC, Cardoso JB, Guedes JM. 2009. Numerical modeling of bone tissue adaptation-A hierarchical approach for bone apparent density and trabecular structure. *Journal of Biomechanics*. 42(7):830–837. Available from: <http://www.ncbi.nlm.nih.gov/pubmed/19269639>.
- Cowin SC. 1985. The relationship between the elasticity tensor and the fabric tensor. *Mechanics of Materials*. 4(2):137–147. Available from: <https://linkinghub.elsevier.com/retrieve/pii/0167663685900122>.
- Dorozhkin SV. 2010. Nanosized and nanocrystalline calcium orthophosphates. *Acta Biomaterialia*. 6(3):715–734. Available from: <http://linkinghub.elsevier.com/retrieve/pii/S1742706109004668>.
- Fitzgibbon A, Pilu M, Fisher R. 1996. Direct least squares fitting of ellipses. In: *Proceedings of 13th International Conference on Pattern Recognition*. IEEE. p. 253–257 vol.1. Available from: www.dai.ed.ac.uk/group/ssmvuellipse-demo.html<http://ieeexplore.ieee.org/document/546029/>.
- Ghosh S, Lee K, Moorthy S. 1995. Multiple scale analysis of heterogeneous elastic structures using homogenization theory and voronoi cell finite element method. *International Journal of Solids and Structures*. 32(1):27–62. Available from: <https://www.sciencedirect.com/science/article/pii/002076839400097G>.
- Hong J, Cha H, Park Y, Lee S, Khang G, Kim Y. 2007. Elastic Moduli and Poisson's Ratios of Microscopic Human Femoral Trabeculae. In: *11th mediterranean conference on medical and biomedical engineering and computing 2007*. Berlin, Heidelberg: Springer Berlin Heidelberg; p. 274–277.
- Kelly N, McGarry JP. 2012. Experimental and numerical characterisation of the elastoplastic properties of bovine trabecular bone and a trabecular bone analogue. *Journal of the Mechanical Behavior of Biomedical Materials*. 9:184–197. Available from: <https://linkinghub.elsevier.com/retrieve/pii/S1751616111003018>.
- Landis W. 1995. The strength of a calcified tissue depends in part on the molecular structure and organization of its constituent mineral crystals in their organic matrix. *Bone*. 16(5):533–544. Available from: <https://linkinghub.elsevier.com/retrieve/pii/>

- 875632829500076P.
- Marco M, Giner E, Caeiro-Rey JR, Miguélez MH, Larraínzar-Garijo R. 2019. Numerical modelling of hip fracture patterns in human femur. *Computer Methods and Programs in Biomedicine*. 173:67–75. Available from: <https://www.sciencedirect.com/science/article/pii/S0169260719302275>.
- Marques M, Belinha J, AFonseca Oliveira, Manzanares Céspedes MC, Jorge RMN. 2019a. Combining radial point interpolation meshless method with a new homogenization technique for trabecular bone multiscale structural analyses. *Acta of Bioengineering and Biomechanics*. 21(2).
- Marques M, Belinha J, Oliveira AF, Manzanares Céspedes MC, Jorge RN. 2018. A multiscale homogenization procedure using the fabric tensor concept. *Science and Technology of Materials*. 30(1):27–34. Available from: <https://doi.org/10.1016/j.stmat.2018.01.002>.
- Marques M, Belinha J, Oliveira AF, Manzanares Céspedes MC, Natal Jorge RM. 2019b. A multiscale homogenization procedure combining the fabric tensor with a natural neighbour meshless method. *Engineering Analysis with Boundary Elements*. 100(August 2017):211–224. Available from: <https://linkinghub.elsevier.com/retrieve/pii/S0955799717304538>.
- Marques M, Belinha J, Oliveira AF, Natal Jorge RM. 2019c. Determination of the Anisotropic Mechanical Properties of Bone Tissue Using a Homogenization Technique Combined With Meshless Methods. In: *Advances in biomechanics and tissue regeneration*. Elsevier; p. 201–213. Available from: <https://linkinghub.elsevier.com/retrieve/pii/S0955799717304538>.
- Materialise. 2017. Mimics® Medical Image Segmentation for Engineering on Anatomy™. Available from: <http://biomedical.materialise.com/mimics>.
- Moreno R, Smedby Ö, Pahr DH. 2016. Prediction of apparent trabecular bone stiffness through fourth-order fabric tensors. *Biomechanics and Modeling in Mechanobiology*. 15(4):831–844.
- Otsu N. 1979. A Threshold Selection Method from Gray-Level Histograms. *IEEE Transactions on Systems, Man, and Cybernetics*. 9(1):62–66. Available from: <http://ieeexplore.ieee.org/document/4310076/>.
- Perrin E, Bou-Saïd B, Massi F. 2019. Numerical modeling of bone as a multiscale poroelastic material by the homogenization technique. *Journal of the Mechanical Behavior of Biomedical Materials*. 91(June 2018):373–382. Available from: <https://doi.org/10.1016/j.jmbbm.2018.12.015><https://linkinghub.elsevier.com/retrieve/pii/S1751616118309020>.
- Peyroteo M, Belinha J, Vinga S, Dinis L, Natal Jorge R. 2019. Mechanical bone remodelling: Comparative study of distinct numerical approaches. *Engineering Analysis with Boundary Elements*. 100:125–139. Available from: <http://www.sciencedirect.com/science/article/pii/S0955799717304022>.
- Sabet FA, Raeisi Najafi A, Hamed E, Jasiuk I. 2016. Modelling of bone fracture and strength at different length scales: a review. *Interface focus*. 6(1):20150055. Available from: <http://www.ncbi.nlm.nih.gov/pubmed/26855749>.
- Taddei F, Schileo E, Helgason B, Cristofolini L, Viceconti M. 2007. The material mapping strategy influences the accuracy of ct-based finite element models of bones: An evaluation against experimental measurements. *Medical Engineering & Physics*. 29(9):973 – 979. Available from: <http://www.sciencedirect.com/science/article/pii/S1350453306002293>.
- Whitehouse WJ. 1974. The quantitative morphology of anisotropic trabecular bone. *Journal of Microscopy*. 101(2):153–168. Available from: <http://doi.wiley.com/10.1111/j.1365-2818.1974.tb03878.x>.
- Wnek GE, Bowlin GL. 2004. *Encyclopedia of biomaterials and biomedical engineering*. 2nd ed.; vol. 42. Boca Raton: CRC Press. Available from: <https://www.crcpress.com/Encyclopedia-of-Biomaterials-and-Biomedical-Engineering/Wnek-Bowlin/p/book/9781420078022>.
- Wolff J. 1986. *The Law of Bone Remodelling*. vol. 82. Berlin, Heidelberg: Springer Berlin Heidelberg. Available from: <https://insights.ovid.com/crossref?an=00006534-198810000-00036><http://link.springer.com/10.1007/978-3-642-71031-5>.

3.10 Book Chapters

In this section, two published book chapters are presented. In the first publication, section 3.10.1, it is introduced the bone remodelling and bone regeneration topic, associated with numerical methods, with focus in the meshless methods. This book chapter has a review character, dealing with models that use numerical methods to engage bone remodelling and regeneration processes. The second book chapter, section 3.10.2, intends to expand the explanation of the development of the 2D methodology used to anisotropically define bone tissue, combined with the meshless methods.

3.10.1 Contribution VIII: "Meshless, Bone Remodelling and Bone Regeneration Modelling."

This contribution focused on the review of the bone remodelling and regeneration process, and its modulation. Both processes were reviewed under a biological point of view. It was also performed a review about the existent models that define these processes, considering mechanical, biological and mechanobiological stimuli. In addition, some of the existent numerical method that are used in the topic were enumerated, focusing in the FEM and meshless methods.

The complete document can be found in the next pages.

Meshless, Bone Remodelling and Bone Regeneration Modelling

M. Marques ¹, J. Belinha ², R. Natal Jorge ³ and A.F. Oliveira ⁴

Abstract In this chapter it is presented an extensive bibliographic survey about meshless methods, bone remodelling and bone regeneration modelling. Here, the regeneration and remodelling processes are shown with detail and, in addition, it is presented a description of the mathematical models approaching both regeneration and remodelling processes. Three different classification of models are presented, the mechanoregulated models, the bioregulated models and the mechanobioregulated models. The literature shows that the combination of remodelling models with meshless techniques allows to numerically achieve more realistic trabecular distributions. Thus, in this chapter, an introduction to meshless methods is presented, with a special focus on radial point interpolation meshless methods, such as the Radial Point Interpolation Method (RPIM) and the Natural Neighbour RPIM (NNRPIM).

¹ M. Marques
Institute of Mechanical Engineering and Industrial Management (INEGI)- Portugal,
Rua Dr. Roberto Frias, s/n, 4600-465, Porto Portugal, email: mcmarques@inegi.up.pt

² J. Belinha (corresponding author)
School of Engineering, Polytechnic of Porto (ISEP), Mechanical Engineering Department
Rua Dr. António Bernardino de Almeida, 431, 4200-072, Porto, Portugal, email: job@isep.ipp.pt

³ R. Natal Jorge
Faculty of Engineering of the University of Porto (FEUP), Mechanical Engineering Department
Rua Dr. Roberto Frias, s/n, 4600-465, Porto, Portugal, email: rnatal@fe.up.pt

⁴ A.F. Oliveira
Instituto de Ciencias Biomédicas Abel Salazar (ICBAS), Medical Teaching Department - CHP/HSA
Rua de Jorge Viterbo Ferreira, 228, 4050-313 Porto, Portugal, Porto, email: afoiveira@netc.pt

1. Introduction

Bone is a structure mainly defined by bone matrix and by bone cells, being these bone cells responsible to produce the bone matrix, in which they became entrapped. The bone cells that create the bone matrix are the same that reabsorb it to allow the replacement of old bone matrix by a newer one. These bone cells also act in the bone regeneration and remodelling processes. All the bones in the human body form the skeletal system, which possesses several vital functions, such as: support, protection, movement, storage and blood cell production [13, 54, 111, 124].

Bone possesses the intrinsic capacity for regeneration and remodelling, being bone remodelling the biological process whereby living bone tissue renews itself in the course of life. Regeneration, besides being the repair process in response to injury, is as well a process that starts with the skeletal development in early life and continues in the form of bone remodelling throughout adult life [128].

One of the most significant activities performed by engineers and scientists is to model natural phenomena in order study and simulate them. Much of the physical phenomena studied, particularly those related to transient continuum mechanics theory (involving both time and space changes), can be formulated in terms of algebraic, ordinary or partial differential and/or integral equations. These conceptual and mathematical models simulate physical events, whether they are biological, chemical, geological, or mechanical, they are based on scientific laws of physics. Thus, it is possible to formulate constitutive equations and laws ruling distinct phenomena, such as heat transfer, stress/strain relations, solid deformations, fluid flow, etc. [113].

Depending on the importance of the constitutive equations in the studied phenomenon they may or not be considered, and their combination results in the differential equations that govern the phenomenon. There are many phenomena associated with different fields, that can be obtained using the same mathematical model and consequently the same differential equations [113]. Most real engineering problems cases are characterized by very complex equations modelled on geometrically complex regions and defined by equations with nonlinear nature, making it virtually impossible to achieve an analytical exact solution. For these cases, in order to obtain the solutions, numerical approximation methods are preferable. The development of computers in recent decades allowed to use these methods more efficiently and so, to obtain the solution of many problems heretofore unsolvable. Additionally, computer progress as allowed the development of new formulations and new algorithms for solving many other complex problems [113]. With massive use of computers, it has been an increase in the development and use of numerical methods and simulate in-silico several biomechanical scenarios. The finite difference method, the finite element method, meshless methods, and their variants, are the most

used numerical methods in the analysis of practical engineering problems. These methods are created on the idea that the complete system is could be analysed as the integrated sum of its different parts.

1.1 Bone Regeneration

Bone regeneration is a well-arranged series of biological events where the damaged bone, with deficiencies or discontinuities, is regenerated to a newly formed bone, rescuing its original biomechanical properties. This process is affected by a gathering of genetic, environmental, mechanical, cellular, and endocrine factors, which in the end allows to obtain a newly formed bone properties possessing almost indistinguishable properties from the properties of the adjacent old bone. This process results in a bone geometry, in the healing site, that usually is the same to its initial shape and with the peculiarity of the non-formation of a scar tissue [41, 51]. The most common case of bone regeneration is the fracture healing that is divided in three main stages, the inflammatory phase, bone repair and bone remodelling, that are represented in Fig. 1. During these three stages two types of ossification occur, intramembranous and the endochondral ossification [64, 118].

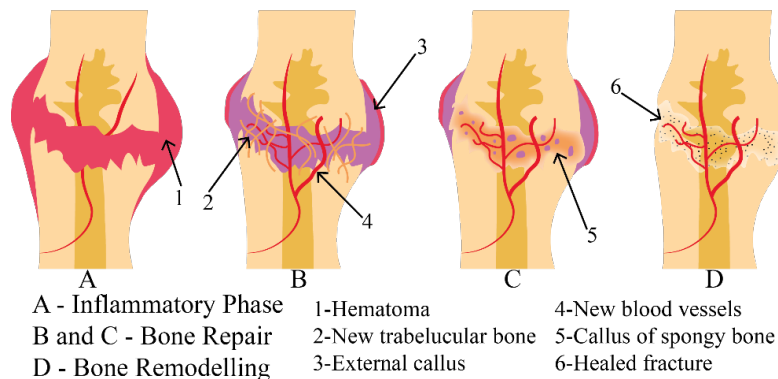


Fig. 1 Bone regeneration three main stages

The inflammatory phase, the first stage, starts immediately after the injury, that is characterized by the hemorrhage, occurring from the damaged blood vessels and leading to the supply suspension of nutrient and oxygen to the bone cells. This first inflammatory reaction leads to the fracture immobilization in a direct and indirect way. Indirectly, since the pain caused leads the individual to protect the injury, and directly by swelling hydrostatically in the fracture zone, that keeps it from moving. Just after the start of the hemorrhage the blood began to clot and the platelets

(trapped in the clot) become activated and start to release growth factors, which regulate the processes of bone healing. The supply interruption of nutrients and oxygen to the bone cells leads to its death. Thus, it occurs a necrotic process that starts an inflammatory response, which is characterized by the migration of macrophages, phagocytes, leukocytes to the wound site aiming to remove the necrotic tissue.

The reparative phase, the second stage, occurs before the inflammatory phase subsides, and lasts for several weeks. In this phase, it is developed the reparative callus in the fracture site, which in the last phase - the remodelling phase - will be replaced by bone. The composition of repair tissue and rate of repair may differ depending on where the fracture occurs in the bone, the extent of soft tissue damage, and mechanical stability of the fracture site [89].

In this phase, the fibroblasts, mesenchymal stem cells (MSC's) and endothelial cells, from the periosteum and from the soft tissues surrounding the bone, migrate into the healing site. This migration is regulated by growth factors released by the activated platelets and by the abovementioned cells. Under the effect of different stimuli, MSC's differentiate into different cells, as well as osteoblasts, chondrocytes and fibroblasts.

In the case that the MSC's differentiate into osteoblast, they start to synthesize bone directly on a pre-existing surface without the mediation of the cartilage phase, occurring the intramembranous ossification [118]. With this apposition of new bone matrix on a solid surface, it is observed the creation of a bone-forming surface that is often referred to as the hard callus [1, 28, 40].

In the case that the MSC's differentiate to chondrocytes, it occurs the endochondral ossification, that usually occurs in the middle of the fracture area. With the proliferation of chondrocytes, it follows the growth of cartilage tissue, that with the maturation of chondrocytes is followed by the calcification of cartilage. Chondrocytes are also responsible by the apoptosis and blood vessels grow into the cavities that were initially occupied by the chondrocytes. The mineralized extracellular matrix of the cartilage tissue acts as a scaffold where osteoblasts create woven bone [10].

The remodelling phase, the final phase, is characterized by the replacement of the woven bone by lamellar bone and by the resorption of excess callus. The woven bone is replaced by the osteoclastic resorption and by the osteoblastic deposition. This remodelling is a gradual modification of the fracture site that adapts itself to the new configuration to get the optimal stability under the new mechanical load scenario.

1.2 Bone Remodelling

Bone remodelling is a term usually used for the phase of general growth, reinforcement and resorption processes. This remodelling is progressive and it is induced in order to adapt the bone morphology to any new external

load. Bone remodelling is a complex process performed by the coordinated activities of osteoclasts (that resorb bone), osteoblasts (that replace bone), osteocytes (within the bone matrix), bone lining cells (covering the bone surface) and the capillary blood supply. Together, osteoclasts and the osteoblasts cells form temporary anatomical structures, called basic multicellular unite (BMU's), which execute bone remodelling. The interactions between osteoblasts and osteoclasts assuring a proper balance between bone gain and loss, is known as coupling [115].

All the millions BMU present in the skeleton are in different stages, being the life span of individual cells that create a BMU much shorter than that BMU itself [72, 83, 119].

These BMUs are constantly remodelling bone tissue during life, adult and senescent skeleton, preventing its premature deterioration and maintaining its overall strength. If there is an interruption of this bone remodelling process due to a biochemical or cellular link cut, such as osteoporosis or hyperparathyroidism, BMUs' activity might disrupted a metabolic bone disease.

Normal bone remodelling occurs in discrete bone locations, taking 2 to 5 years for a discrete location to complete one bone remodelling cycle [112]. Bone remodelling can be classified as targeted remodelling, or by random remodelling. For instances, if a specific region of the bone is induced to remodel due to a structural micro damage, it is said to occur a targeted remodelling [30, 104]. In this case remodelling permits the restore the micro damage caused by fatigue and/or by shock.

Bone remodelling a main biological process (possessing a relevant role in the mineral homeostasis) by providing calcium and phosphate. Thus, for example, if the calcium and phosphate are removed from random locations from the skeleton, it occurs a random remodelling [30, 104].

Bone balance is defined as the relation between the amount of bone removed and of new bone restored in the bone remodelling process. Bone balance can be easily modified by diseases, hormonal factors and even by external mechanical stimulus. Being bones a major reservoir of body calcium, bone are under the hormonal control of Parathyroid hormone (PTH), the most important hormone regulating calcium homeostasis and bone remodelling [81]. The modification of the bone remodelling behaviour, possessing a direct influence in the bone mass, is affected by the effect of PTH, in which a continuous increase of the PTH levels decreases bone mass and discontinuous PTH administration leads to a increases of bone mass [49, 78, 96, 116].

Also long-term physical activity on a regular basis plays a particularly important role in bone remodelling. The mechanical stimulus induced by physical exercise can maintain or increase bone strength by increasing bone mass or by changing bone structures at micro and macro levels. Two main types of exercise are beneficial to bone health: weight-bearing, exercise performed while a person is standing so that gravity is exerting a force, and resistance exercise, exercises involving lifting weights with arms or legs.

- Long-term physical activity on a regular basis plays a particularly important role in maintaining healthy bones. Exercise can maintain and increase bone strength by increasing bone mass or by changing bone structures at micro and macro levels [129]. More recently was reported that, as the presence of external loads leads to the bone remodelling, the absence of load occurring in conditions of disuse, such as during immobility, space flight, and long-term bed rest lead to the same processes, leads to the opposite result: bone loss and mineral changes [12, 111, 131].
- Bone remodelling can be divided in five distinct phases occurring in a coordinate and sequential way. This five phases are the activation, resorption, reversal, formation and the termination.
- The activation phase is characterized by a continuum process occurring in the boundaries of the BMU in which it is detected the presence of an inducing remodelling signal, that can be of mechanical or hormonal nature [112]. Bone cells are exposed to a dynamic environment of biophysical stimuli that includes strain, stress, shear, pressure, fluid flow, streaming potentials and acceleration, having these parameters the ability to regulate independently the cellular responses and influence the bone remodelling. The osteocytes located in the cortical bone possess the ability of sensing this biophysical stimulus and, using the canaliculi network, they are capable to activate the regulation of the proteins sclerostin and RANKL, which possess a major role in bone remodelling, [29, 129].
- The resorption phase is characterized by the formation and activity of osteoclasts that create a sealed section where the resorption process occurs. This formation and activity of osteoclasts is controlled by osteoblast cells that active the movement of mature osteoclasts into a bone remodelling site with the expression of CSF-1, RANKL, OPG and by PTH [13, 111, 112, 121, 123, 124].
- The reversal phase lasts around 9 days and occurs when the maximum eroded depth is achieved, between 60-40 μm . This phase is characterized by transition of the activity from osteoclast to osteoblast [83]. The osteoclasts start the process of apoptosis and at the same time the bone-lining cells enter the lacuna and clean bone matrix remains. This clean up allows the deposition of a proteins (collagenous) layer in the resorption pits that form a cement line (glycoprotein), which helps the attachment of preosteoblasts that begin to differentiate [52, 57, 98].
- The formation phase is the characterized by the formation of new bone. Once osteoclasts resorbed a cavity of bone, they are replaced by cells of the osteoblast lineage that initiate the bone formation, the preosteoblast. The preosteoblast are attracted by the growth factors liberated from the matrix that act as chemotactics and, in addition, stimulate its proliferation.
- The preosteoblasts synthesize a cementing substance upon which the new tissue is attached and express bone morphogenic proteins (BMP) responsible for differentiation.
- Bone resorption liberates TGF- β from the matrix, which is a key protein for recruiting mesenchymal stem cells to sites of bone resorption. This

recruitment of mesenchymal stem cells and the presence of the bone morphogenic proteins (BMP) lead to the differentiation of preosteoblasts to osteoblasts.

The already differentiated osteoblasts synthesize the osteoid matrix and also secrete collagen, whose accumulation contributes to the cessation of cell growth.

The osteoid, the non-mineralized organic portion of the bone matrix, has to be mineralized with hydroxyapatite to create a mature bone tissue [79, 129].

The termination phase is characterized by the terminal differentiation of the osteoblast. Some of the osteoblast transform to lining cells, covering the newly formed bone surface, while others osteoblast differentiate into osteocytes and remain in the matrix [29, 79, 129].

1.3 Meshless Methods

Nowadays, one of the most popular discrete numerical tool is the Finite Element Method (FEM), but in the last few years meshless methods, such as Smooth Particle Hydrodynamics (SPH) Method [66], Radial Point Interpolation Method (RPIM) [92–94], and as Natural Neighbour Radial Point Interpolation Method (NNRPIM) [45], came into focus of interest.

The first meshless method to be developed dates from 1977, when Gingold and co-workers proposed the smooth particle hydrodynamics (SPH) method [66]. The SPH possesses a kernel approximation for a single function $u(\mathbf{x})$ in a domain Ω . This method was used for modelling astrophysical phenomena without boundaries, such as exploding stars and dust clouds [66]. From 1997 to now many different methods were developed, using different approaches: generalized finite difference method [91], diffuse element method (DEM) [103], element free Galerkin method (EFGM) [27], meshless local Petrov–Galerkin (MLPG) method [8], point interpolation method (PIM) [92–94] and radial point interpolation method (RPIM) [125, 126].

The point interpolation method (PIM) was developed using the Galerkin weak form and shape functions that are constructed based only on a group of nodes arbitrarily distributed in a local support domain by means of polynomial interpolation [92–94].

The major advantage of PIM is that the shape functions created possess the Kronecker delta function property, which allows to enforcement essential boundary conditions using simple numerical techniques, as in the conventional finite element method. PIM can use two types of shape functions: polynomial basis functions and radial basis functions (RBFs), being termed RPIM when using the RBFs [125, 126].

More recently, new methods were developed, such as the Natural Neighbour Radial Point Interpolation Method (NNRPIM) [45], which is based on the combination of the natural neighbour finite element method with the radial point interpolation method, and Natural Radial Element Method (NREM) [22], combining the simplicity of low-order finite elements connectivity

with the geometric flexibility of meshless methods. The main advantage of the meshless methods is that they do not require elements to discretize the problem domain [13].

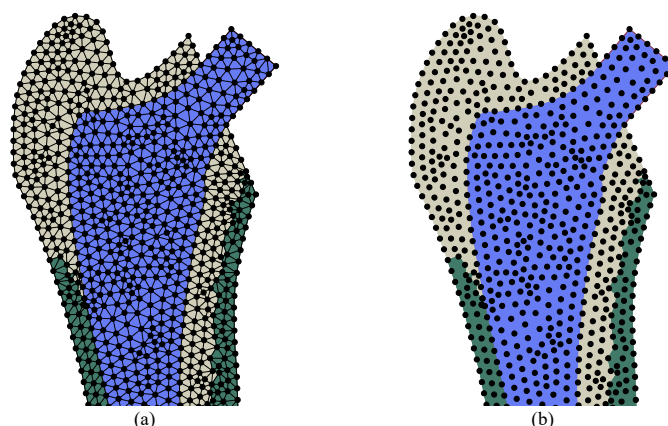


Fig. 2 a) Domain discretization in FEM using elements; b) Domains discretization in meshless using unstructured nodes.

In meshless methods, the problem domain is discretized using an unstructured nodal mesh, as can be seen in Fig. 2b), opposing with the domain discretization using elements used in FEM, represented in Fig. 2a). In biomechanics this discretization flexibility is advantageous, since it permits to discretize the problem domain using directly medical images.

Meshless methods can be divided in approximation meshless methods [44]–[46], [50] and interpolation meshless methods [41], [47], [49], [51]–[53]. The major advantage of using interpolator meshless methods is the possibility to impose directly the essential and natural boundary conditions, since the constructed test functions possess the delta Kronecker property.

They can also be separated in meshless methods that use the strong form solution, using directly the partial differential equations governing the studied physical phenomenon, and others that uses the weak form solution. The weak form stands for a formulation that uses the variational principle to minimize the residual weight of the differential equations ruling a phenomenon, where the residual is obtained replacing the exact solution by an approximated one, affected by a test function.

The meshless methods start with the problem domain being discretized by a regular or irregular node set. This nodal set is not considered a “mesh”, since the meshless method do not require any previous information about the nodes’ vicinity in order to create the approximation or interpolation functions to the unknown variable field function.

In meshless methods the nodal spatial distribution and nodal density discretization affects the performance of the method. Usually, having a denser nodal

distributions results in more accurate solutions, however the increase of the density of the dense distributions increases the computational costs. Furthermore, unbalanced nodal distribution leads to a lower accuracy, where location with predictable concentration of stress should have a higher nodal density when compared with locations with expected smoother stress distributions.

After discretising the problem domain with the nodal set, a background integration mesh is created, which can be nodal dependent or nodal independent. This background mesh allows to numerically integrate the weak form governing the problem. The most popular integration schemes use the Gauss-Legendre quadrature technique. However, the majority of the integration schemes is nodal dependent, which hinders the “meshless” concept. Thus, other techniques comprise integration schemes completely nodal independent, as the ones using the Voronoï diagram or the natural neighbour mathematical concept [45] [22].

After the domain discretization and the construction of the background integration mesh, the meshless method has to assure the nodal connectivity, which is not predefined by elements as in FEM. Thus, in meshless methods, for each point of interest, one must defined areas or volumes acting as influence-domains.

Meshless methods and the FEM are discrete numerical methods and so, both require the discretization of the problem domain. The FEM discretize the problem-domain using nodes and elements, where the finite element concept assures the nodal connectivity. In the meshless methods, the problem’s domain is discretized using only nodes, and consequently, there are no elements, as in the FEM assuring that the nodes belonging to the same element interact directly between each other and with the boundary nodes of neighbour finite elements. Herewith, in the meshless methods it is necessary to define the nodal interaction. Such interaction is enforced by means of “influence-domains”. A given node i , or interest point, searches for the closest nodes. The area or volume in which those closest nodes are contained is called the influence-domain of node i . In the literature it is possible to find several techniques to define influence-domains [13].

2. Bone Remodelling and Regeneration Modelling

The models used to simulate the behaviour of the bone regeneration and remodelling are based on various concepts and approaches. The models can be related to various forms of bone regeneration and remodelling, such as models for fracture healing, models for bone regeneration around endosseous implants and chemical models predicting the pharmacological effect on the remodelling process. As said before, the bone remodelling is the last phase of bone regeneration, even so there are models for both

processes. This occurs due to the distinct duration of both processes. Bone regeneration is a process that last for some months, but the regeneration (occurring as the last phase of the regeneration or as a natural process on a healthy bone) can last the entire bone life.

It is usually to separate the models into three different classes with respect to the essential mechanisms regulating the bone regeneration/regeneration process. The classification in mechanical, biological and mechanobiological model allows to characterise the model according to the nature of the fractures influencing the bone regeneration/remodelling process. Additionally, this classification permits to create a chronological perspective of the mathematical modelling of bone.

Mechanoregulatory models are governed by laws where the local mechanical environment is assumed as the only factor that influences the bone regeneration/remodelling. In bioregulatory models only biochemical factors are considered in the model, and in the mechanobioregulatory models both mechanical and biochemical factors are assumed. Despite mechanobioregulatory models are more realistic, when compared to mechanoregulatory and bioregulatory approaches, they also are more complex, due to the larger number of assumptions involved in their formulation.

The mechanoregulatory were the first to appear, in 1960 by Pauwels [105]. In 1999, Adam and co-workers [2, 7], created one of the firsts bioregulatory models to characterize the bone behaviour. Later the mechanobioregulatory models appeared as a combination of the mechanoregulatory with the bioregulatory. Curiously, the generalisation of the bioregulatory models did not stop the developments of the mechanoregulatory models and the development of the mechanobioregulatory models did not stop the developments of the bioregulatory models.

2.1 Mechanoregulatory Models

The first mathematical model related to mechanoregulation of bone remodelling describing 'Wolff's law' was developed in 1960 by Pauwels [105], and later applied in 1965 [106]. This law defines that a tissue differentiation depends on local stresses and strains. Pauwels assumed that deviatoric strains stimulate the formation of fibrous tissue and that hydrostatic pressure stimulate formation of cartilage.

In 1964 Frost developed the "Curvature Model" describing the remodelling process controlled by strain actions [55].

Later in 1976, Cowin and co-workers presented the Adaptive Elasticity model, defining bone internal remodelling as the sum of chemical reactions between bone matrix and the extracellular fluids, where the rates of these chemical reactions depend upon the strain values [37–39, 73]. In 1979, Perren presented a model for bone regeneration where was considered the influence of the local mechanical environment on the morphology of fracture healing, suggesting that a repair tissue can only be formed if the

tissue tolerates the local mechanical strain. This approach sustains that different bone repair patterns occur when different physical influences are present, including strain tolerance [107].

In 1986, Carter and co-workers, introduced the “self-optimization” concept, a remodelling model that assumed that mechanical stimulus is proportional to effective stress field. Thus, stress can be related with trabecular orientation and apparent density based on the idea that bone is a self-optimizing material [33, 35, 56, 127].

In 1987, Huiskes and co-workers, developed an adaptive remodelling model that used the Strain Energy Density (SED) as a feed-back control variable to determine shape or bone density adaptations [76].

Later in 1990 Reiter and co-workers modified Huiskes’ model, introducing the effects of overstrain necrosis [114]. Harrigan and Hamilton, in 1992, introduced the SED for stress induced remodelling as mechanical stimuli, using “Adaptive Elasticity” concept [69–71].

In 1997 Pettermann and co-workers (also using a modified Huiskes’ model), introduced the anisotropic material behaviour in a regeneration model [108]. Prendergast and co-workers considered the biological tissues based on a poroelastic (biphasic) material. In this model, the differentiation process assumes as feed-back controller the maximal distortional strain and relative fluid velocity [110].

In 2000, similar to the model developed by Prendergast and co-workers (1997) [110], Kuiper and co-workers created a regeneration model to study the fracture healing process as a function of applied movement. In this model, the shear strain and fluid shear stress regulate bone fracture healing, by adding or resorbing tissue and by modifying tissue properties. The model was able to control the callus development with the proliferation of granulation tissue [82]. Also in 2000 Ament and Hofer [3], developed a fuzzy logic formulation that using strain energy density as mechanical stimulus modified the behaviour of the tissue differentiation in the process of bone regeneration [3].

Later on 2002, Lacroix, Prendergast and co-workers extended Prendergast’s work (1997) to include mesenchymal cell migration in a regeneration model [84, 85]. McNamara and Prendergast developed in 2007 four mechanoregulated regeneration models where the mechanical stimulus was strain, damage, combined strain/damage, and either strain or damage with damage-adaptive remodelling prioritised when damage was above a critical level. Each model was implemented with both bone lining cell (surface) sensors and osteocyte cell (internal) sensors, and it also was applied to predict the BMU remodelling on the surface of a bone trabecula [99].

Also in 2002, Doblaré and García-Aznar proposed a remodelling model based on the principles of Damage Mechanics [48]. This model identifies bone voids with the cavities or micro cracks of other material damage models, but changes some of the standard assumptions in damage-mechanics theory to adapt it to the special requirements of living adaptive materials. A

remodelling tensor, defined in terms of the apparent density and analogous to the standard damage tensor, was proposed to characterize the state of the homogenised bone microstructure.

- In 2008, Liu and Niebur, developed and modified version of Lacroix's regeneration algorithm. This version enforces tissue differentiation pathway by transitioning from differentiation to bone adaptation [95]. In 2010, Mulvihill and Prendergast, using the concepts of the algorithms developed by McNamara and Prendergast, 2007, and the concept proposed by Frost (1987), developed a new regeneration algorithm where both strain and micro-damage work as stimuli for BMU activity and that ON/OFF thresholds operate to control osteoclast and osteoblast activation [102].
- Later in 2012, Belinha *et al.* [25, 26], developed a material law correlating the bone apparent density and the obtained level of stress. Using this new material law, it was developed a biomechanical remodelling model, an adaptation of Carter's models for predicting bone density distribution, based on the assumption that the bone structure is a gradually self-optimizing anisotropic biological material that maximizes its own structural stiffness [34, 35, 56, 127]. This model assumes that mechanical stimulus acts as the principal driving force in the bone tissue remodelling process [25, 26].

2.2 Bioregulatory Models

- In 1999, Adam and co-workers developed a regeneration model where the critical size defect in the fracture healing site was defined by a set of a partial differential equation (PDE) governing a growth factor concentration [2, 7].
- By 2001, Bailon-Plaza and Vander Meulen developed a more extended biological regeneration model that was defined by a system of PDE's [10]. In this approach the PDE's system was defined by seven variables: densities of MSC's, of osteoblasts, of chondrocytes, concentrations of chondrogenic and osteogenic growth factors, and densities of connective/cartilage extracellular matrix and bone extracellular matrix. This model allowed the authors to represent the processes of cell differentiation, proliferation, migration and death, synthesis and resorption of tissues. This model is rather popular due to its generality. This model can be modified, allowing the development of several other bioregulatory models [10].
- Later in 2003, Komarova *et al.*, [80] developed a remodelling model describing the population dynamics of bone cells accordingly with the number of osteoclasts and osteoblasts at a single BMU. The interactions occurring among osteoblasts and osteoclasts encouraged by autocrine and paracrine allowed the authors to calculate cell population dynamics and changes in bone mass at a discrete site of bone remodelling [80]. To condense the net effect of local factors on the rates of cell production, this model uses a power law approximation that was developed by Herries [74], as effective tools for analysis of highly nonlinear biochemical systems. In this model all factors leading to a cell response are taken together in a single exponential parameter [80].

- In 2004, Martin and Buckland-Wright developed a mathematical remodelling model to predict the depth of erosion and the duration of the resorption phases in healthy adult cancellous bone based wholly on biological information. This model uses Michaelis-Menten-like feedback mechanics to affect bone resorption [97].
- Also in 2004, Lemaire and co-workers developed the first mathematical remodelling model that includes the RANKL/RANK/OPG pathway, which affects the bone remodelling process. This model is based on the idea that the relative proportions of immature and mature osteoblasts control the degree of osteoclastic activity [87].
- In 2008, Geris and co-workers extended the work of Bailon-Plaza and Meulen [10], by creating a regeneration model that considers angiogenesis. This was achieved by separating fibrous tissue and cartilage densities, and by defining additional chemotactic and haptotaxis terms for cell migration in the governing equations [62, 63].
- Also in 2008, Pivonka and co-workers, using as base the Lemaire's model [87], suggested a new remodelling model where were added four new parameters, a rate equation (describing changes in bone volume with time), a rate equation (describing release of TGF- β from the bone matrix), the expression of OPG and RANKL on osteoblastic cell lines, and a modified activator/repressor functions [109].
- In 2009, Ryser co-workers using as base Komarova's work, developed a mathematical remodelling model of BMU describing changes in time and space of the concentrations of proresorptive cytokine RANKL and its inhibitor osteoprotegerin (OPG), in osteoclast and osteoblast numbers, and in bone mass [117].
- In 2011, Amor and co-workers adapted the Bailon-Plaza and Vander Meulen model [10] for peri-implant osseointegration [4, 5]. This regeneration model postulates that intermediate cartilaginous phase is not observed experimentally in bone healing occurring near implants, [1, 28, 31, 36] and so, the model disregard chondrogenic growth factors, chondrocytes and cartilage. The big difference from the original Bailon-Plaza and Vander Meulen model, is that the chemotaxis of MSC's is represented in equations and that the density of activated platelets was included.

2.3 *Mechanobioregulatory Models*

- In 2002, Lacroix and co-workers, using the models developed by Prendergast [110] and by Huiskes [75] developed a new regeneration model considering cellular processes together with mechanical factors by incorporating the random walk of MSC's [84, 85].
- Later in 2003, Bailon-Plaza and Meulen, extending their previous work [10], created a new regeneration model in which it was predicted the beneficial effects of moderate, early loading and adverse effects of delayed or excessive loading on bone healing. The mechanical factors were modelled

- by stimulating and inhibiting the effects of dilatational and deviatoric strains [11].
- In 2005, Gómez-Benito and co-workers and García-Aznar and co-workers developed a mechanobioregulatory regeneration model as a system of PDE's model that had as main variables cell concentrations of the four basic skeletal cells: MSC's, osteoblasts, fibroblasts and cartilage cells, and the four types of skeletal tissues, namely granulation tissue, fibrous tissue, cartilage and bone [58, 60, 67]. In this model, it was assumed that the fracture site is invaded by proliferating and migrating MSCs in the first stage of the bone healing process and that these may differentiate into cartilage cells, bone cells or fibroblasts, depending on the value of a mechanical stimulus. It was also assumed that very high mechanical stimulus causes MSCs to die. In this model the process of bone healing was simulated as a process driven by a mechanical stimulus, the second invariant of the deviatoric strain tensor [67].
- In 2008, Andreykiv co-workers [6] and Isaksson co-workers [77] developed a regeneration model where the biological part allowed the simulation of cell migration, proliferation, differentiation, tissue deposition and replacement. The mechanical component of the model calculates the mechanical stimuli influencing the cellular processes. Cell differentiation, proliferation and tissue production in this model are regulated by tissue shear strain and interstitial fluid velocity, as proposed by Prendergast and co-workers [110].
- In 2014, Hambli [68] developed a remodelling model where the cellular behaviour was based on Komarova *et al.* [80] dynamic law. In this model the mechanical stimuli are related with the biological one using strain–damage stimulus function controlled by the level of autocrine and paracrine. In 2010, Geris and co-workers [65], extended their previous bioregulatory model [61] by defining dependencies for the model parameters based on mechanical stimuli, according to Prendergast and co-workers [110]. This model was applied to study impaired fracture healing. The authors checked predictions of the model for various mechanoregulatory relations. In this model, both angiogenesis and osteogenesis were assumed to be affected by the mechanical loading.
- Later in 2015, Yi and co-workers developed a microscale bone remodelling model using the equivalent strain as the mechanical stimuli. In this model, the mechanical stimuli affects the proliferation and differentiation of the osteoblast cells. The influence of the different physiological conditions, restricted by Denosumab (a used drug for treating osteoporosis), on the formation/resorption rate were also considered [130].
- In 2016, Lerebours and co-workers [88] developed a multiscale mechanobiological remodelling model describing the evolution of a human mid-shaft femur scan subjected in osteoporosis and mechanical disuse. In this model, hormonal regulation and biochemical coupling of bone cell populations are included. This models also includes a mechanical adaptation of the tissue and factors that influence the microstructure on bone turnover rate [88].

3. Meshless Methods Applications

3.1 *Meshless Methods and Mechanics*

Many studies were performed using meshless method in order to prove its efficiency in many different fields of mechanics. Belinha and Dinis, 2006 extended the usage of Element Free Galerkin Method (EFGM) in order to perform the elasto-plastic analysis of isotropic plates [16]. Later in 2007, Belinha and Dinis extended the EFGM to the analysis of anisotropic plates and laminates considering a Reissner–Mindlin laminate theory (FSDT) [17]. Also in 2007, Dinis and co-workers proposed a new meshless method, the natural neighbour radial point interpolation method (NNRPIM) based on the combination of the natural neighbour finite element method with the radial point interpolation method. In order to prove the high accuracy and convergence rate of the proposed method well-known 2D and 3D problems were solved and compared with other studies and methods [45]. Later in 2008, NNRPIM was extended for the analysis of thick plates and laminates [46], being later in 2009 NNRPIM extended to dynamic analysis (free vibrations and forced vibrations) of 2D, 3D and bending plate problems [18]. In 2010, NNRPIM was used in the numerical implementation of an Unconstrained Third-Order Plate Theory applied to functionally graded plates [42], being later in 2011, using also Unconstrained Third-Order Plate Theory applied to laminates [44]. Also in 2010, Dinis and co-workers developed a unique NNRPIM approach when 3D thin structures are considered. In order to demonstrate the effectiveness of the method, several isotropic and orthotropic thin plates and shells problems were solved [43]. Later in 2013, NNRPIM was extended to the analysis of composite laminated plates [19] and to the elastostatic analysis of thick plates [23]. In 2014, NNRPIM was extended to the analysis of laminated plates using Timoshenko theory [100]. In 2015, NNRPIM was extended to the field of fracture mechanics [9], and the radial point interpolation method (RPIM) to the elasto-static analysis of circular plates assuming the 2D axisymmetric deformation theory [53]. Later in 2016 was analysed and compared the performance of distinct meshless techniques assuming first-order shear deformation theory (FSDT) using FEM, and also an approximation meshless method (EFGM) and three interpolation meshless methods RPIM, NNRPIM and Natural Radial Element Method (NREM) [14]. Also in 2016, NNRPIM was used to simulate the crack growth phenomenon in brittle materials [15].

3.2 *Meshless Methods and Biomechanics*

Meshless methods are used in different fields, but are getting an increasing interest on the biomechanical field, since the discretization flexibility in meshless is advantageous, allowing to discretize the problem domains using directly medical images.

These biomechanical studies focus in the bone tissue. Belinha and co-workers extended the NNRPIM to bone remodelling analysis, developing a biomechanical model to predict the bone density distribution [20, 26]. Later, some studies using meshless approach were performed in order to evaluate the bone response after the insertion of implants. Most of these studies focus in dental implants, [21, 50, 122]. More recent studies analysed the bone remodelling behaviour after the insertion of a femoral stem [24].

3.3 Meshless Methods and Bone remodelling

In the last few years, meshless methods gradually become to enter into bone remodelling simulation field [47].

García and co-workers in 2000, developed one of the first works using bone structures and the meshless methods, studying the bone internal remodelling by means of α -shape-based Natural Element Method (α -NEM). The considered remodelling model is based on the principles of Continuum Damage Mechanics [59].

Liew and co-workers in 2002, explored stress distribution phenomena in the human proximal femur, having in consideration the detrimental effects of infarction as well as aging. Liew and co-workers in 2002 concluded that meshless methods were efficient numerical techniques suitable for biomechanics [90].

James and co-workers in 2007, developed a model to analyse osteoporosis process. In this model the CT imaging data was linked to the meshless method in order to analyse the mechanical properties of the porous, heterogeneous trabecular bone and the property–microstructure relationship [86].

Buti and co-workers in 2010 developed a uniform, particle-based, space and geometry oriented approach for bone remodelling. The developed methodology uses a multi scale approach, at tissue scale and at cell scale. This methodology uses a meshless method approach developed by Taddei and co-workers in 2008 [120], which is a numerical approach based on a direct discrete formulation of physical laws - the Cell Method [32].

Recently Belinha and co-workers started to use meshless methods applied to bone tissue analysis. Firstly, using a micro-scale analysis of the bone remodelling phenomenon [26], and later using a macro-scale analysis to study innumerable structures as the calcaneus, femur, mandible and the maxillary bone [21, 25, 101].

In 2016 Belinha and co-workers, using the developed bone remodelling algorithm, the developed material law and the developed meshless methods, analysed the bone tissue remodelling of the femur due to the insertion of a stem [24].

4. Conclusion

Bone remodelling and bone regeneration are natural processes that are controlled very efficiently by the human body, by a combination of mechanical and biological factors. Along the years, many mathematical models were

developed to simulate these two processes, evolving from simpler models (that considered only one type of factors) to the more recent models (that combine both mechanical and biological factors) - the mechanobiological models. These models in many cases are evolutions of previous models by adding more variables. The objective of these more complex models is to simulate the natural events in a more precise way. In the case of the biological models, it was found in the literature survey that they usually are well supported on laboratory experiments using bone tissue.

As said before, the last phase of the regeneration process is the remodelling phase. The models concerning the regeneration process consider the remodelling phase, although with a much smaller temporal windows when compared with the pure remodelling models. Thus, tell apart both model phases might not be immediately.

Being FEM a mature and widely used method, it is natural that the first remodelling and regeneration models where firstly combined with the FEM.

Meshless methods are discretization techniques similar to FEM. Thus, the same fields and studies that have been explored using the FEM, can now be explored using meshless methods (and also some topics where the FEM cannot be used).

For the particular case of bone regeneration, in the bibliographic survey the authors did not found any study in which meshless methods where applied, which creates a research opportunity for meshless methods.

Taking into account some of the vantages of the meshless methods, such as the fact that they do not require elements to discretize the problem domain, and that in biomechanics domains with high complexity are very common, it is very likely that meshless methods became a standard in biomechanical analysis.

In the particular case of bone remodelling, the literature shows some relevant recent studies combining meshless methods with bone remodelling models. This recent interest could be explained by the meshing flexibility of meshless methods and by the fact that meshless methods can discretise numerically the problem domain using directly the medical images. In addition, meshless methods allow to adapt and update the discretization along the simulation, for example, by adding or removing nodes (domain) at any time-step during the simulation.

Acknowledgements The authors truly acknowledge the funding provided by Ministério da Educação e Ciência, – Fundação para a Ciência e a Tecnologia (Portugal), under grants SFRH/BD/110047/2015, and by project funding MIT-EXPL/ISF/0084/2017. Additionally, the authors gratefully acknowledge the funding of Project NORTE-01-0145-FEDER-000022 – SciTech – Science and Technology for Competitive and Sustainable Industries, co-financed by Programa Operacional Regional do Norte (NORTE2020), through Fundo Europeu de Desenvolvimento Regional (FEDER).

5. References

1. Abrahamsson I, Berglundh T, Linder E, Lang NP, Lindhe J (2004) Early

- bone formation adjacent to rough and turned endosseous implant surfaces. An experimental study in the dog. *Clin Oral Implants Res* 15:381–392. doi: 10.1111/j.1600-0501.2004.01082.x
2. Adam JA (1999) A simplified model of wound healing (with particular reference to the critical size defect). *Math Comput Model* 30:23–32. doi: 10.1016/S0895-7177(99)00145-4
3. Ament C, Hofer EP (2000) A fuzzy logic model of fracture healing. *J Biomech* 33:961–968. doi: 10.1016/S0021-9290(00)00049-X
4. Amor N, Geris L, Sloten J Vander, Van Oosterwyck H (2009) Modelling the early phases of bone regeneration around an endosseous oral implant. *Comput Methods Biomech Biomed Engin* 12:459–468. doi: 10.1080/10255840802687392
5. Amor N, Geris L, Vander Sloten J, Van Oosterwyck H (2011) Computational modelling of biomaterial surface interactions with blood platelets and osteoblastic cells for the prediction of contact osteogenesis. *Acta Biomater* 7:779–790. doi: 10.1016/j.actbio.2010.09.025
6. Andreykiv A, Van Keulen F, Prendergast PJ (2008) Simulation of fracture healing incorporating mechanoregulation of tissue differentiation and dispersal/proliferation of cells. *Biomech Model Mechanobiol* 7:443–461. doi: 10.1007/s10237-007-0108-8
7. Arnold JS, Adam JA (1999) A simplified model of wound healing II: The critical size defect in two dimensions. *Math Comput Model* 30:47–60. doi: 10.1016/S0895-7177(99)00197-1
8. Atluri SN, Zhu T (1998) A new Meshless Local Petrov-Galerkin (MLPG) approach in computational mechanics. *Comput Mech* 22:117–127. doi: 10.1007/s004660050346
9. Azevedo JMC, Belinha J, Dinis LMJS, Natal Jorge RM (2015) Crack path prediction using the natural neighbour radial point interpolation method. *Eng Anal Bound Elem* 59:144–158. doi: 10.1016/j.enganabound.2015.06.001
10. Bailón-Plaza A, Van Der Meulen MCH (2001) A mathematical framework to study the effects of growth factor influences on fracture healing. *J Theor Biol* 212:191–209. doi: 10.1006/jtbi.2001.2372
11. Bailón-Plaza A, Van Der Meulen MCH (2003) Beneficial effects of moderate, early loading and adverse effects of delayed or excessive loading on bone healing. *J Biomech* 36:1069–1077. doi: 10.1016/S0021-9290(03)00117-9
12. Bauman WA, Spungen AM, Wang J, Pierson RN, Schwartz E (1999) Continuous loss of bone during chronic immobilization: A monozygotic twin study. *Osteoporos Int* 10:123–127. doi: 10.1007/s001980050206
13. Belinha J (2014) *Meshless Methods in Biomechanics: Lecture Notes in Computational Vision and Biomechanics*. Volume 16. Springer International Publishing, Switzerland, ISBN: 9783319063997
14. Belinha J, Araújo AL, Ferreira AJM, Dinis LMJS, Natal Jorge RM (2016) The analysis of laminated plates using distinct advanced discretization meshless techniques. *Compos Struct* 143:165–179. doi:

- 10.1016/j.compstruct.2016.02.021
15. Belinha J, Azevedo JMC, Dinis LMJS, Natal Jorge RM (2016) The Natural Neighbor Radial Point Interpolation Method Extended to the Crack Growth Simulation. *Int J Appl Mech* 08:1650006. doi: 10.1142/S175882511650006X
16. Belinha J, Dinis LMJS (2006) Elasto-plastic analysis of plates by the element free Galerkin method. *Eng Comput* 23:525–551. doi: 10.1108/02644400610671126
17. Belinha J, Dinis LMJS (2007) Nonlinear analysis of plates and laminates using the element free Galerkin method. *Compos Struct* 78:337–350. doi: 10.1016/j.compstruct.2005.10.007
18. Belinha J, Dinis LMJS, Jorge RMN (2009) The natural neighbour radial point interpolation method: dynamic applications. *Eng Comput* 26:911–949. doi: 10.1108/02644400910996835
19. Belinha J, Dinis LMJS, Jorge RMN (2013) Composite laminated plate analysis using the natural radial element method. *Compos Struct* 103:50–67. doi: 10.1016/j.compstruct.2013.03.018
20. Belinha J, Dinis LMJS, Jorge RMN (2015) The meshless methods in the bone tissue remodelling analysis. *Procedia Eng* 110:51–58. doi: 10.1016/j.proeng.2015.07.009
21. BELINHA J, DINIS LMJS, JORGE RMN (2015) the Mandible Remodeling Induced By Dental Implants: a Meshless Approach. *J Mech Med Biol* 15:1550059. doi: 10.1142/S0219519415500591
22. Belinha J, Dinis LMJS, Natal Jorge RM (2013) The natural radial element method. *Int J Numer Methods Eng* 93:1286–1313. doi: 10.1002/nme.4427
23. Belinha J, Dinis LMJS, Natal Jorge RM (2013) Analysis of thick plates by the natural radial element method. *Int J Mech Sci* 76:33–48. doi: 10.1016/j.ijmecsci.2013.08.011
24. Belinha J, Dinis LMJS, Natal Jorge RMM (2016) The analysis of the bone remodelling around femoral stems: A meshless approach. *Math Comput Simul* 121:64–94. doi: 10.1016/j.matcom.2015.09.002
25. Belinha J, Jorge RMN, Dinis LMJS (2012) A meshless microscale bone tissue trabecular remodelling analysis considering a new anisotropic bone tissue material law. *Comput Methods Biomech Biomed Engin* 5842:1–15. doi: 10.1080/10255842.2012.654783
26. Belinha J, Natal Jorge RMM, Dinis LMJS (2012) Bone tissue remodelling analysis considering a radial point interpolator meshless method. *Eng Anal Bound Elem* 36:1660–1670. doi: 10.1016/j.enganabound.2012.05.009
27. Belytschko T, Lu YY, Gu L (1994) Element-free Galerkin methods. *Int J Numer Methods Eng* 37:229–256. doi: 10.1002/nme.1620370205
28. Berglundh T, Abrahamsson I, Lang NP, Lindhe J (2003) De novo alveolar bone formation adjacent to endosseous implants. A model study in the dog. *Clin Oral Implants Res* 14:251–262. doi: 10.1034/j.1600-0501.2003.00972.x

29. Bonewald LF (2011) The amazing osteocyte. *J Bone Miner Res* 26:229–238. doi: 10.1002/jbmr.320
30. Burr DB, Robling AG, Turner CH (2002) Effects of biomechanical stress on bones in animals. *Bone* 30:781–786. doi: 10.1016/S8756-3282(02)00707-X
31. Buser D, Broggini N, Wieland M, Schenk RK, Denzer AJ, Cochran DL, Hoffmann B, Lussi A, Steinemann SG (2004) Enhanced Bone Apposition to a Chemically Modified SLA Titanium Surface. *J Dent Res* 83:529–533. doi: 10.1177/154405910408300704
32. Buti F, Cacciagrano D, Corradini F, Merelli E, Tesei L, Pani M (2010) Bone Remodelling in BioShape. *Electron Notes Theor Comput Sci* 268:17–29. doi: 10.1016/j.entcs.2010.12.003
33. Carter DR (1987) Mechanical loading history and skeletal biology. *J Biomech* 20:1095–1109. doi: 10.1016/0021-9290(87)90027-3
34. Carter DR, Fyhrie DP, Whalen RT (1987) Trabecular bone density and loading history: Regulation of connective tissue biology by mechanical energy. *J Biomech* 20:785–794. doi: 10.1016/0021-9290(87)90058-3
35. Carter DR, Orr TE, Fyhrie DP (1989) Relationships between loading history and femoral cancellous bone architecture. *J Biomech* 22:231–244. doi: 10.1016/0021-9290(89)90091-2
36. Colnot C, Romero DM, Huang S, Rahman J, Currey JA, Nanci A, Brunski JB, Helms JA (2007) Molecular Analysis of Healing at a Bone-Implant Interface. *J Dent Res* 86:862–867. doi: 10.1177/154405910708600911
37. Cowin SC, Hegedus DH (1976) Bone remodeling I: theory of adaptive elasticity. *J Elast* 6:313–326. doi: 10.1007/BF00041724
38. Cowin SC, Nachlinger RR (1978) Bone remodeling III: uniqueness and stability in adaptive elasticity theory. *J Elast* 8:285–295. doi: 10.1007/BF00130467
39. Cowin SC, Sadeh AM, Luo GM (1992) An Evolutionary Wolff's Law for Trabecular Architecture. *J Biomech Eng* 114:129. doi: 10.1115/1.2895436
40. Davies J (2003) Understanding peri-implant endosseous healing. *J Dent Educ* 67:932–949
41. Dimitriou R, Jones E, McGonagle D, Giannoudis P V (2011) Bone regeneration: current concepts and future directions. *BMC Med* 9:66. doi: 10.1186/1741-7015-9-66
42. Dinis LMJS, Jorge RMN, Belinha J (2010) An Unconstrained Third-Order Plate Theory Applied to Functionally Graded Plates Using a Meshless Method. *Mech Adv Mater Struct* 17:108–133. doi: 10.1080/15376490903249925
43. Dinis LMJS, Jorge RMN, Belinha J (2010) A 3D shell-like approach using a natural neighbour meshless method: Isotropic and orthotropic thin structures. *Compos Struct* 92:1132–1142. doi: 10.1016/j.compstruct.2009.10.014
44. Dinis LMJS, Jorge RMN, Belinha J (2011) Static and dynamic analysis

- of laminated plates based on an unconstrained third order theory and using a radial point interpolator meshless method. *Comput Struct* 89:1771–1784. doi: 10.1016/j.compstruc.2010.10.015
45. Dinis LMJS, Natal Jorge RM, Belinha J (2007) Analysis of 3D solids using the natural neighbour radial point interpolation method. *Comput Methods Appl Mech Eng* 196:2009–2028. doi: 10.1016/j.cma.2006.11.002
 46. Dinis LMJS, Natal Jorge RM, Belinha J (2008) Analysis of plates and laminates using the natural neighbour radial point interpolation method. *Eng Anal Bound Elem* 32:267–279. doi: 10.1016/j.enganabound.2007.08.006
 47. Doblaré M, Cueto E, Calvo B, Martínez MA, Garcia JM, Cegoñino J (2005) On the employ of meshless methods in biomechanics. *Comput Methods Appl Mech Eng* 194:801–821. doi: 10.1016/j.cma.2004.06.031
 48. Doblaré M, García JM (2002) Anisotropic bone remodelling model based on a continuum damage-repair theory. *J Biomech* 35:1–17. doi: 10.1016/S0021-9290(01)00178-6
 49. Dobnig H, Turner RT (1997) The Effects of Programmed Administration of Human Parathyroid Hormone Fragment (1 – 34) on Bone Histomorphometry and Serum Chemistry in Rats. *Endocrinology* 138:4607–4612. doi: 10.1210/endo.138.11.5505
 50. Duarte HMS, Andrade JR, Dinis LMJS, Jorge RMN, Belinha J (2016) Numerical analysis of dental implants using a new advanced discretization technique. *Mech Adv Mater Struct* 23:467–479. doi: 10.1080/15376494.2014.987410
 51. Epari DR, Duda GN, Thompson MS (2010) Mechanobiology of bone healing and regeneration: In vivo models. *Proc Inst Mech Eng Part H J Eng Med* 224:1543–1553. doi: 10.1243/09544119JEIM808
 52. Everts V, Delaissié JM, Korper W, Jansen DC, Tigchelaar-Gutter W, Saftig P, Beertsen W (2002) The bone lining cell: Its role in cleaning Howship's lacunae and initiating bone formation. *J Bone Miner Res* 17:77–90. doi: 10.1359/jbmr.2002.17.1.77
 53. Farahani B V., Berardo JM V., Drgas R, Sá JC de, Ferreira A, Belinha J (2015) The Axisymmetric Analysis Of Circular Plates Using The Radial Point Interpolation Method. *J Comput Methods Eng Sci Mech* 16:336–353. doi: 10.1080/15502287.2015.1103819
 54. Feng X, McDonald JM (2011) Disorders of Bone Remodeling. *Annu Rev Pathol Mech Dis* 6:121–145. doi: 10.1146/annurev-pathol-011110-130203
 55. Frost HM (1964) *The laws of bone structure*, 1st ed. Springfield, Ill, Thomas., ISSN: 0002-9629
 56. Fyhrie DP, Carter DR (1986) A unifying principle relating stress to trabecular bone morphology. *J Orthop Res* 4:304–317. doi: 10.1002/jor.1100040307
 57. Gallagher JC, Sai AJ (2010) Molecular biology of bone remodeling: Implications for new therapeutic targets for osteoporosis. *Maturitas*

- 65:301–307. doi: 10.1016/j.maturitas.2010.01.002
58. García-Aznar JM, Kuiper JH, Gómez-Benito MJ, Doblaré M, Richardson JB (2007) Computational simulation of fracture healing: Influence of interfragmentary movement on the callus growth. *J Biomech* 40:1467–1476. doi: 10.1016/j.jbiomech.2006.06.013
59. García-Aznar JM, Rueberg T, Doblaré M (2005) A bone remodelling model coupling microdamage growth and repair by 3D BMU-activity. *Biomech Model Mechanobiol* 4:147–167. doi: 10.1007/s10237-005-0067-x
60. García JM, Doblaré M, Cueto E (2000) Simulation of bone internal remodeling by means of the α -shape-based natural element method. In: *European Congress on Computational Methods in Applied Sciences and Engineering*. Barcelona
61. Geris L, Gerisch A, Sloten J Vander, Weiner R, Oosterwyck H Van (2008) Angiogenesis in bone fracture healing: A bioregulatory model. *J Theor Biol* 251:137–158. doi: 10.1016/j.jtbi.2007.11.008
62. Geris L, Reed AAC, Vander Sloten J, Simpson AHRW, van Oosterwyck H (2010) Occurrence and treatment of bone atrophic non-unions investigated by an integrative approach. *PLoS Comput Biol* 6:e1000915. doi: 10.1371/journal.pcbi.1000915
63. Geris L, Sloten J Vander, Oosterwyck H Van (2008) Mathematical Modelling of Bone Regeneration including Angiogenesis : Design of Treatment Strategies for Atrophic Non-union. In: *54th Annual Meeting of the Orthopaedic Research Society*. p 2005
64. Geris L, Sloten J Vander, Van Oosterwyck H (2009) In silico biology of bone modelling and remodelling: Regeneration. *Philos Trans R Soc A Math Phys Eng Sci* 367:2031–2053. doi: 10.1098/rsta.2008.0293
65. Geris L, Sloten J Vander, Oosterwyck H Van (2010) Connecting biology and mechanics in fracture healing: An integrated mathematical modeling framework for the study of nonunions. *Biomech Model Mechanobiol* 9:713–724. doi: 10.1007/s10237-010-0208-8
66. Gingold RA, Monaghan JJ (1977) Smoothed particle hydrodynamics: theory and application to non-spherical stars. *Mon Not R Astron Soc* 181:375–389. doi: 10.1093/mnras/181.3.375
67. Gómez-Benito MJ, García-Aznar JM, Kuiper JH, Doblaré M (2005) Influence of fracture gap size on the pattern of long bone healing: a computational study. *J Theor Biol* 235:105–119. doi: 10.1016/j.jtbi.2004.12.023
68. Hambli R (2014) Connecting Mechanics and Bone Cell Activities in the Bone Remodeling Process: An Integrated Finite Element Modeling. *Front Bioeng Biotechnol* 2:6. doi: 10.3389/fbioe.2014.00006
69. Harrigan TP, Hamilton JJ (1992) An analytical and numerical study of the stability of bone remodelling theories: Dependence on microstructural stimulus. *J Biomech* 25:477–488. doi: 10.1016/0021-9290(92)90088-I
70. Harrigan TP, Hamilton JJ (1992) Optimality conditions for finite element simulation of adaptive bone remodeling. *Int J Solids Struct* 29:2897–

2906. doi: 10.1016/0020-7683(92)90147-L
71. Harrigan TP, Hamilton JJ (1993) Finite element simulation of adaptive bone remodelling: A stability criterion and a time stepping method. *Int J Numer Methods Eng* 36:837–854. doi: 10.1002/nme.1620360508
72. Hauge EM, Qvesel D, Eriksen EF, Mosekilde L, Melsen F (2001) Cancellous bone remodeling occurs in specialized compartments lined by cells expressing osteoblastic markers. *J Bone Miner Res* 16:1575–1582. doi: 10.1359/jbmr.2001.16.9.1575
73. Hegedus DH, Cowin SC (1976) Bone remodeling II: small strain adaptive elasticity. *J Elast* 6:337–352. doi: 10.1007/BF00040896
74. Herries DG (1977) Biochemical Systems Analysis. A Study of Function and Design in Molecular Biology. *Biochem Educ* 5:84. doi: 10.1016/0307-4412(77)90075-9
75. Huiskes R, Driel WD Van, Prendergast PJ, Søballe K (1997) A biomechanical regulatory model for periprosthetic fibrous-tissue differentiation. *J Mater Sci Mater Med* 8:785–788. doi: 10.1023/A:1018520914512
76. Huiskes R, Weinans H, Grootenboer HJ, Dalstra M, Fudala B, Slooff TJ (1987) Adaptive bone-remodeling theory applied to prosthetic-design analysis. *J Biomech* 20:1135–1150. doi: 10.1016/0021-9290(87)90030-3
77. Isaksson H, van Donkelaar CC, Huiskes R, Ito K (2008) A mechano-regulatory bone-healing model incorporating cell-phenotype specific activity. *J Theor Biol* 252:230–246. doi: 10.1016/j.jtbi.2008.01.030
78. Karaplis AC, Goltzman D (2000) PTH and PTHrP Effects on the Skeleton. *Rev Endocr Metab Disord* 1:331–341. doi: 10.1023/A:1026526703898
79. Kini U, Nandeesh BN (2012) Physiology of bone formation, remodeling, and metabolism. In: *Radionuclide and Hybrid Bone Imaging*. Springer Berlin Heidelberg, Berlin, Heidelberg, pp 29–57
80. Komarova S V., Smith RJ, Dixon SJ, Sims SM, Wahl LM (2003) Mathematical model predicts a critical role for osteoclast autocrine regulation in the control of bone remodeling. *Bone* 33:206–215. doi: 10.1016/S8756-3282(03)00157-1
81. Kroll M (2000) Parathyroid Hormone Temporal Effects on Bone Formation and Resorption. *Bull Math Biol* 62:163–188. doi: 10.1006/bulm.1999.0146
82. Kuiper JH, Richardson JB, Ashton BA (2000) Computer Simulation to Study the Effect of Fracture Site Movement on Tissue Formation and Fracture Stiffness Restoration. *Eur Congr Comput Methods Appl Sci Eng* 1–6
83. Kular J, Tickner J, Chim SM, Xu J (2012) An overview of the regulation of bone remodelling at the cellular level. *Clin Biochem* 45:863–873. doi: 10.1016/j.clinbiochem.2012.03.021
84. Lacroix D, Prendergast PJ, Li G, Marsh D (2002) Biomechanical model to simulate tissue differentiation and bone regeneration: Application to fracture healing. *Med Biol Eng Comput* 40:14–21. doi:

- 10.1007/BF02347690
85. Lacroix D, Prendergast PJJ (2002) A mechano-regulation model for tissue differentiation during fracture healing: analysis of gap size and loading. *J Biomech* 35:1163–1171. doi: 10.1016/S0021-9290(02)00086-6
86. Lee JD, Chen Y, Zeng X, Eskandarian A, Oskard M (2007) Modeling and simulation of osteoporosis and fracture of trabecular bone by meshless method. *Int J Eng Sci* 45:329–338. doi: 10.1016/j.ijengsci.2007.03.007
87. Lemaire V, Tobin FL, Greller LD, Cho CR, Suva LJ (2004) Modeling the interactions between osteoblast and osteoclast activities in bone remodeling. *J Theor Biol* 229:293–309. doi: 10.1016/j.jtbi.2004.03.023
88. Lerebours C, Buenzli PR, Scheiner S, Pivonka P (2016) A multiscale mechanobiological model of bone remodelling predicts site-specific bone loss in the femur during osteoporosis and mechanical disuse. *Biomech Model Mechanobiol* 15:43–67. doi: 10.1007/s10237-015-0705-x
89. Lieberman JR, Friedlaender GE (2005) *Bone Regeneration and Repair: in Biology and Clinical Applications*, 1st ed. Humana Press, Totowa, NJ, ISBN: 9780896038479
90. Liew KM, Wu HY, Ng TY (2002) Meshless method for modeling of human proximal femur: Treatment of nonconvex boundaries and stress analysis. *Comput Mech* 28:390–400. doi: 10.1007/s00466-002-0303-5
91. Liszka T, Orkisz J (1980) The finite difference method at arbitrary irregular grids and its application in applied mechanics. *Comput Struct* 11:83–95. doi: 10.1016/0045-7949(80)90149-2
92. Liu GR, Gu YT (2001) Local point interpolation method for stress analysis of two-dimensional solids. *Struct Eng Mech* 11:221–236. doi: 10.12989/sem.2001.11.2.221
93. Liu GR, Gu YT (2001) A local radial point interpolation method (LRPIM) for free vibration analyses of 2-D solids. *J Sound Vib* 246:29–46. doi: 10.1006/jsvi.2000.3626
94. Liu GR, Gu YT (2001) A point interpolation method for two-dimensional solids. *Int J Numer Methods Eng* 50:937–951. doi: 10.1002/1097-0207(20010210)50:4<937::AID-NME62>3.0.CO;2-X
95. Liu X, Niebur GL (2008) Bone ingrowth into a porous coated implant predicted by a mechano-regulatory tissue differentiation algorithm. *Biomech Model Mechanobiol* 7:335–344. doi: 10.1007/s10237-007-0100-3
96. Locklin RM, Khosla S, Turner RT, Riggs BL (2003) Mediators of the biphasic responses of bone to intermittent and continuously administered parathyroid hormone. *J Cell Biochem* 89:180–190. doi: 10.1002/jcb.10490
97. Martin MJ, Buckland-Wright JC (2004) Sensitivity analysis of a novel mathematical model identifies factors determining bone resorption rates. *Bone* 35:918–928. doi: 10.1016/j.bone.2004.06.010
98. Matsuo K, Irie N (2008) Osteoclast-osteoblast communication. *Arch Biochem Biophys* 473:201–209. doi: 10.1016/j.abb.2008.03.027

99. McNamara LM, Prendergast PJ (2007) Bone remodelling algorithms incorporating both strain and microdamage stimuli. *J Biomech* 40:1381–1391. doi: 10.1016/j.jbiomech.2006.05.007
100. Moreira S, Belinha J, Dinis LMJSJS, Jorge RMNN (2014) Análise de vigas laminadas utilizando o natural neighbour radial point interpolation method. *Rev Int Metod Numer para Calc y Disen en Ing* 30:108–120. doi: 10.1016/j.rimni.2013.02.002
101. Moreira SF., Belinha J. b, Dinis LMJS. b, Natal Jorge RM. b (2014) A global numerical analysis of the “central incisor/local maxillary bone” system using a meshless method. *MCB Mol Cell Biomech* 11:151–184. doi: 10.3970/mcb.2014.011.151
102. Mulvihill BM, Prendergast PJ (2010) Mechanobiological regulation of the remodelling cycle in trabecular bone and possible biomechanical pathways for osteoporosis. *Clin Biomech* 25:491–498. doi: 10.1016/j.clinbiomech.2010.01.006
103. Nayroles B, Touzot G, Villon P (1992) Generalizing the finite element method: Diffuse approximation and diffuse elements. *Comput Mech* 10:307–318. doi: 10.1007/BF00364252
104. Parfitt AM (2002) Targeted and nontargeted bone remodeling: Relationship to basic multicellular unit origination and progression. *Bone* 30:5–7. doi: 10.1016/S8756-3282(01)00642-1
105. Pauwels F (1960) Eine neue Theorie über den Einfluß mechanischer Reize auf die Differenzierung der Stützgewebe. *Brain Struct Funct* 121:478–515. doi: 10.1007/BF00523401
106. Pauwels F (1965) *Gesammelte Abhandlungen zur funktionellen Anatomie des Bewegungsapparates*. Springer Berlin Heidelberg, Berlin, Heidelberg, ISBN: 978-3-642-86842-9
107. Perren SM (1979) Physical and biological aspects of fracture healing with special reference to internal fixation. *Clin Orthop Relat Res* 175–96
108. Pettermann HE, Reiter TJ, Rammerstorfer FG (1997) Computational simulation of internal bone remodeling. *Arch Comput Methods Eng* 4:295–323. doi: 10.1007/BF02737117
109. Pivonka P, Zimak J, Smith DW, Gardiner BS, Dunstan CR, Sims NA, John Martin T, Mundy GR, Martin TJ, Mundy GR, John Martin T, Mundy GR (2008) Model structure and control of bone remodeling: A theoretical study. *Bone* 43:249–263. doi: 10.1016/j.bone.2008.03.025
110. Prendergast PJ, Huiskes R, Soballe K (1997) Biophysical stimuli on cells during tissue differentiation at implant interfaces. *J Biomech* 30:539–548. doi: 10.1016/S0021-9290(96)00140-6
111. Qin Q-H (2012) *Mechanics of Cellular Bone Remodeling: Coupled Thermal, Electrical, and Mechanical Field Effects.*, 1st ed. CRC Press, Boca Raton, ISBN: 9781466564176
112. Raggatt LJ, Partridge NC (2010) Cellular and molecular mechanisms of bone remodeling. *J Biol Chem* 285:25103–25108. doi: 10.1074/jbc.R109.041087
113. Reddy JN (2004) *An Introduction to Nonlinear Finite Element Analysis*,

- 1st ed. Oxford University Press, ISBN: 9780198525295
114. Reiter TJ, Rammerstorfer FG, Bohm HJ (1990) Numerical algorithm for the simulation of bone remodeling. *Am Soc Mech Eng Bioeng Div BED* 17:181–184
115. Rodan GA, Martin TJ (1981) Role of osteoblasts in hormonal control of bone resorption—A hypothesis. *Calcif Tissue Int* 33:349–351. doi: 10.1007/BF02409454
116. Rubin MR, Bilezikian JP (2003) New anabolic therapies in osteoporosis. *Endocrinol Metab Clin North Am* 32:285–307. doi: 10.1016/S0889-8529(02)00056-7
117. Ryser MD, Nigam N, Komarova S V (2009) Mathematical Modeling of Spatio-Temporal Dynamics of a Single Bone Multicellular Unit. *J Bone Miner Res* 24:860–870. doi: 10.1359/jbmr.081229
118. Shapiro F (2008) Bone development and its relation to fracture repair. The role of mesenchymal osteoblasts and surface osteoblasts. *Eur Cells Mater* 15:53–76. doi: vol015a05 [pii]
119. Smit TH, Burger EH (2010) Is BMU-Coupling a Strain-Regulated Phenomenon? A Finite Element Analysis. *J Bone Miner Res* 15:301–307. doi: 10.1359/jbmr.2000.15.2.301
120. Taddei F, Pani M, Zovatto L, Tonti E, Viceconti M (2008) A new meshless approach for subject-specific strain prediction in long bones: Evaluation of accuracy. *Clin Biomech* 23:1192–1199. doi: 10.1016/j.clinbiomech.2008.06.009
121. Tang Y, Wu X, Lei W, Pang L, Wan C, Shi Z, Zhao L, Nagy TR, Peng X, Hu J, Feng X, Van Hul W, Wan M, Cao X (2009) TGF- β 1-induced migration of bone mesenchymal stem cells couples bone resorption with formation. *Nat Med* 15:757–765. doi: 10.1038/nm.1979
122. Tavares CSS, Belinha J, Dinis LMJS, Jorge RMN (2015) The Elastoplastic Response of the Bone Tissue Due to the Insertion of Dental Implants. *Procedia Eng* 110:37–44. doi: 10.1016/j.proeng.2015.07.007
123. Teti A (2011) Bone Development: Overview of Bone Cells and Signaling. *Curr Osteoporos Rep* 9:264–273. doi: 10.1007/s11914-011-0078-8
124. VanPutte CL, Regan J, Russo A, Seeley RR, Stephens T, Tate P, Regan J, Russo A, Seeley RR, Stephens T, Tate P (2014) Seeley's anatomy & physiology., 10th Ed. McGraw-Hill, New York, ISBN: 9780073403632
125. Wang JG, Liu GR (2002) A point interpolation meshless method based on radial basis functions. *Int J Numer Methods Eng* 54:1623–1648. doi: 10.1002/nme.489
126. Wang JG, Liu GR (2002) On the optimal shape parameters of radial basis functions used for 2-D meshless methods. *Comput Methods Appl Mech Eng* 191:2611–2630. doi: 10.1016/S0045-7825(01)00419-4
127. Whalen RT, Carter DR, Steele CR (1988) Influence of physical activity on the regulation of bone density. *J Biomech* 21:825–837. doi: 10.1016/0021-9290(88)90015-2
128. Wnek GE, Bowlin GL (2008) Encyclopedia of Biomaterials and

- Biomedical Engineering, 2nd ed. CRC Press, Boca Raton, ISBN: 9781420078022
129. Y. A, Valds-Flores M, Orozco L, Velzquez-Cruz R (2013) Molecular Aspects of Bone Remodeling. In: Valds-Flores M (ed) Topics in Osteoporosis. InTech, pp 1–28
 130. Yi W, Wang C, Liu X (2015) A microscale bone remodeling simulation method considering the influence of medicine and the impact of strain on osteoblast cells. *Finite Elem Anal Des* 104:16–25. doi: 10.1016/j.finel.2015.04.007
 131. Zerwekh JE, Ruml LA, Gottschalk F, Pak CYC (2009) The Effects of Twelve Weeks of Bed Rest on Bone Histology, Biochemical Markers of Bone Turnover, and Calcium Homeostasis in Eleven Normal Subjects. *J Bone Miner Res* 13:1594–1601. doi: 10.1359/jbmr.1998.13.10.1594

3.10.2 Contribution IX: Advances in Biomechanics and Tissue Regeneration: 10. Determination of the Anisotropic Mechanical Properties of Bone Tissue.

The main goal of this contribution was to expand the explanation of the development of the 2D methodology used to anisotropically define the bone and its combination with the meshless methods. In this contribution, it was reviewed the fabric concept used in the development of the homogenisation technique, and it was explained how the image processing tools were able to define it. The material laws that able to anisotropically define the bone were explained and the methodology was validated using two tests: a scale and a rotation test. Two sets of domains that define the bone, one homogenised set and one heterogeneous, were structurally analysed in order to validate the methodology.

The complete document can be found in the next pages.

Determination of the anisotropic mechanical properties of bone tissue using a homogenization technique combined with meshless methods

M. Marques^{a,b}, Jorge Belinha^{a,c}, A.F. Oliveira^d, R.M. Natal Jorge^{a,b}

^aINEGI- Institute of Science and Innovation in Mechanical and Industrial Engineering,
Porto, Portugal

^bFEUP - Faculty of Engineering of University of Porto, Porto, Portugal

^cISEP - School of Engineering, Polytechnic of Porto, Porto, Portugal

^dICBAS - Abel Salazar Biomedical Sciences Institute

Abstract

Bone has different functional requirements at different scales, from macro-scale to micro-scale. Bone remodeling has as consequence the change of the bone morphology at its micro-scale, leading to the change of bone mechanical properties. The literature shows that it is possible to obtain the fourth rank elasticity tensor from the fabric tensor. Furthermore, previous studies have demonstrated that the fabric tensor can be directly correlated with a material image using a fabric tensor morphologic-based methodology - the mean intercept length tensor (MIL). In this work, the same methodology is applied in order to obtain the homogenized material elasticity tensor. Thus, the main objective of this work was to combine a new developed homogenization technique, applying the fabric tensor concept to medical CT/micro-CT images, with a previously developed bone tissue material law, allowing to expeditiously define the homogenized mechanical properties of trabecular bone at its micro-scale, and to reduce the analysis computational cost.

Keywords: Meshless Methods, Fabric Tensor, Homogenization, Multi-scale

10.1. Introduction

Bones is the main integrant of the skeletal system by witch the body support, protect and move itself as well as store and produce blood cells. Bone is

a complex structure that consist of two different tissue types, the cortical bone,
 5 a thin and stiff outer layer, and the trabecular bone, more flexible and a foam-
 like inner structure [1–3]. Bone biomechanics is based on the idea that bone
 provides a high load-carrying capacity and that bone tissue is structurally op-
 timized for this mechanical function [4, 5]. Considering this purpose, bone has
 a mechanism, bone remodeling, that allows its micro-structural integrity to be
 10 continuously maintained. This process can lead to bone removal via osteoclasts
 or bone regeneration via osteoblasts [6–11]. It also occurs in other biological pro-
 cess, such as growth, reinforcement, and resorption. Bone remodeling has been
 continuously studied, resulting in the development of semi-empirical mathemat-
 ical descriptions. These models simulate and predict experimental results using,
 15 for example, computer science methodologies such as Finite Element Methods
 (FEM). The efforts to understand bone remodeling phenomenon lead to a con-
 tinuous development of semi-empirical mathematical descriptions, but also lead
 to better comprehend bone structure. It was observed that bone has different
 functional requirements at different scales, the reason why some authors start
 20 to classify bone as a hierarchical multi-scale material, with different structural
 levels from macro-scale (whole bone) to sub-nanoscale (hydroxyapatite crystals,
 constituent of the inorganic phase of bone) [12–17]. Since the bone has different
 functional requirements at different scales, it was necessary to investigate the
 mechanical properties of its distinct components and the structural relationships
 25 across different scales [18, 19]. The evolution of the hierarchical bone classifi-
 cation also lead to the evolution of models that allow to study bone biological
 and mechanical processes by incorporating a multi-scale approach.

Mechanoregulatory models are defined by laws that only consider the influ-
 ence of mechanical factors in the bone remodeling. In bioregulatory models,
 30 only the biochemical factors are considered while in the mechanobioregulatory
 models, both mechanical and biochemical factors are considered. Despite be-
 ing more representative in comparison with mechanoregulatory and bioregula-
 tory models, mechanobioregulatory models are more complicated due to the
 higher number of assumptions and restrictions involved in their formulation.

35 The mechanoregulatory was the first to appear, in 1960 by Pauwels [20]. In
 1999, Adam and co-workers [21], created one of the firsts bioregulatory modes
 to characterize the bone behavior. Later, the mechanobioregulatory models ap-
 pear as a combination of the mechanoregulatory with the bioregulatory. The
 first mathematical model related to mechanoregulation of bone remodeling that
 40 described the ‘Wolff’s law’ was developed in 1960 by Pauwels [20], that was
 later applied in 1965 [22]. Wolff’s law, developed by Julius Wolff, anatomist
 and surgeon, states that bone adapts itself to applied loads. Wolff reported
 that the directions of the applied external loads directly influence the direction
 of the trabecular bone, by changing trabecular bone physical disposition and
 45 distribution. Today, it is generally accepted that bone remodeling is mainly
 caused by the transient nature of its strain/stress fields, induced by the exter-
 nal loads applied in its physical boundary. From 1960 up to now, many other
 models were created using novel ideas, or modifying/enhancing existent models
 [23–39]. In 2012, Belinha *et al.* [40] developed a material law that permits to
 50 correlate the bone apparent density with the bone level of stress. Using this new
 material law, a biomechanical remodeling model was developed, as an adapta-
 tion of Carter’s models for predicting bone density distribution that assumes
 that bone structure is a gradually self-optimizing anisotropic biological mate-
 rial that maximizes its own structural stiffness [27, 29, 30, 41]. Peyroteo *et*
 55 *al.* [42, 43], developed another model, considering Belinha *et al.* [40] material
 law as part of a mechanoregulation model. Among many bioregulatory models,
 [21, 44–48], one of the most known bioregulatory is the Komarova’s model [45].
 Komarova’s model describes the population dynamics of bone cells accordingly
 with the number of osteoclasts and osteoblasts at a single basic multicellular
 60 unit (BMU). The development of these mechanoregulatory and bioregulatory
 models lead to the development of mechanobioregulatory modes, being one of
 the first versions developed by Lacroix and co-workers in 2002. Using the models
 developed by Prendergast *et al.* [34] and by Huiskes *et al.* [49], this first model
 considered cellular processes together with mechanical factors by incorporating
 65 the random walk of mesenchymal stem cells [35, 36]. One other numerical model

was developed by Mousavi and Doweidar [50], that allow to study mesenchymal stem cells differentiation to osteoblast as well as osteoblast proliferation due to mechanical stimulations. The latest developed mechanobiological remodeling model was developed in 2016, where it was included the hormonal regulation and biochemical coupling of bone cell populations, the mechanical adaptation of the tissue and factors that influence the microstructure on bone turnover rate [51].

One key factor in all of these models is the characterization of the bone mechanical properties. The first models considered bone as an isotropic material, a simplistic approach on the behavior of trabecular bone, disregarding the importance of orientation in the remodeling process [31, 41, 52, 53]. Later, models start to considered material density and orientation with bone anisotropic mechanical properties, taking into account the trabecular architecture features [38, 54–56]. More recently, some works start to characterize bone mechanical properties using the fabric tensor concept [57–62]. The fabric tensor is a symmetric second rank tensor that characterizes the arrangement of a multiphase material, encoding the orientation and anisotropy of the material.

Numerical methods combined with computer science are widely used in a variety of areas, from civil engineering, mechanical engineer, chemistry up to biomechanics. These methodologies allow to study and analyze, *in silicio*, the behavior of materials and structures, being firstly used in the biomechanics area in 1972 by Huiskes and co-workers [63], in order to evaluate stresses in human bones. Today, FEM is one of the most popular discrete numerical method [64] while other methods like meshless methods start to appear. Meshless methods evolved, from the first developed meshless method dated from 1977, where Gingold *et al.* [65], proposed the smoothed-particle hydrodynamics (SPH), to more recent methods such as the Natural Neighbor Radial Point Interpolation Method (RPIM) [66] and the Natural Radial Element Method (NREM) [67].

The main difference between meshless methods and the finite element method is the methodology to discretizing the problem domain. Meshless methods, in opposition to the FEM, do not use elements to established nodal/element con-

nectivity, and so discretize the problem domain using an unstructured node set that can be distributed regularly or irregularly. Because of this, meshless methods can have advantages, such as the capability to discretize high complex
 100 problem domains using information gathered directly from medical images, a feature of high importance in the biomechanics field.

In meshless methods, the nodal discretization is constructed just by using the spatial coordinates of the nodes, allowing to define individually the material properties of each node. The concept of influence-domain, equivalent to
 105 elements in FEM, defines how each node interacts with its neighbor by using geometrical and mathematical constructions. Only meshless methods that use nodal dependent constructions of the integration mesh are called truly meshless methods because they allow to directly define the spatial position and the integration weight of all integration points only using the spatial positions of the
 110 nodes. The untruly meshless methods use a nodal independent background integration mesh to establish the system of equations from the integro-differential equations ruling the physical phenomenon under study [1]. Meshless methods are used in many different fields of mechanics, such as laminates [68–78], 2D and 3D linear elasticity [79], plate and shell bending problems [80], composites
 115 [81, 82], fracture [83–85], etc. Meshless are also widely used in biomechanics. They are used, for example, to study the behavior of bone response to the insertion of implants [86–89], to analyze the behavior of soft tissue under stress [90, 91], to evaluate the behavior of the inner ear [92, 93], and bone remodeling computational research [42, 43, 86, 87, 94–102].

120 Some of the models and methodologies presented in this chapter, analyze structures like bone, that has an underlying microstructure. The behavior of the structure at its micro scale significantly influences the behavior of the structure observed at the macro-scale. Finding the relation across scales, will allow to develop multi-scale models capable to predict the behavior of the macro-scale using
 125 the micro-scale, and vice-versa. Homogenization techniques allow homogenizing the mechanical properties of the heterogeneous material under study, thereby allowing to substitute this material with an equivalent homogeneous material.

This homogenization can be integrated into multi-scale methods allowing to define, for example, the mechanical properties of highly complex microstructure as trabecular bone, and replace this microstructure by a simple structure with equivalent mechanical proprieties. This simplification allows to relate the multi scales and simplify the problem complexity, solving it at the macro-scale [103].

The main objective of this chapter is to show how it is possible to combine a new homogenization technique (applied to the trabecular bone micro scale) with meshless methods, aiming to achieve a low-cost and efficient multi-scale technique.

10.2. Homogenization Technique

In this section, the homogenization technique that allows to expeditiously define the homogenized mechanical properties of trabecular bone at its micro-scale is fully described. This technique allows to define the mechanical properties of a trabecular bone representative volume element (RVE). In this technique images generated by micro-CT are used, allowing to acquire information of the trabecular bone morphology. In this homogenization technique, in order define the mechanical properties of the trabecular bone RVE, it was used the fabric tensor concept and a bone tissue phenomenological law. Fabric tensors can be obtained by two different methodologies, mechanical based or morphologic based. In the case of the morphologic based methodology, the information of the interface between phases of the material is used to obtain the orientation distribution function (ODF). Micro-CT images provide information about the changes of the phase of trabecular bone that is required to define the ODF data, and so define the fabric tensor. This process is further explained in this section. First, aiming to define a RVE from a 2D micro-CT, the images must be segmented. Thus, the obtained RVE describes the local trabecular bone micro scale morphology and the information regarding the changes of phase of the RVE are recorded. The image segmentation creates binarized information, ones and zeros, that can identify what is bone, ones, and what is void space, zeros. This

binarizations can be obtained using image processing methodologies, such as Ostu's method [104]. In Fig. 10.1c an example of the image type that is acquired using a micro-CT to be used in this methodology is presented. These binary
 160 images, I_s , are employed in the methodology developed by Whitehouse [105] to define the fabric tensor. This methodology is considered as golden standard in this kind of application, since there exists a large amount of works sustaining its appropriateness to predict mechanical properties of trabecular bone [60, 62, 105–107]. When the ODF data is acquired by this method, disposed on a polar
 165 plot, and fitted into an ellipse, it is possible to obtain parameters that can be correlated with the material orientation, allowing to further define the trabecular bone mechanical properties.

Fabric tensor morphologic based method

In this methodology, the number of interceptions between a parallel family
 170 line in direction ι , the interface between both phases of the material is counted, $\text{Int}(\iota)$. The length of the parallel lines family, h , is also considered. The parameters h and ι define the ODF, which in this case is called mean interception length (MIL), Eq. (10.1).

$$\text{MIL}(\iota) = \frac{h}{\text{Int}(\iota)} \quad (10.1)$$

The dimensional information of I_s is used to define the size of an image
 175 containing the family of parallel lines with $\iota = 0^\circ$. Fig. 10.2a represents an example of an image containing a family of parallel lines I_ι , in this case, with $\iota = 0^\circ$. Counting the interceptions of those parallel lines with changes of phase of RVE, represented by the boundaries of the I_s , it is possible to obtain the orientation-dependent feature.

180 Rotating the family of parallel line image with ι between 0° and 180° using a defined angle increment, and then counting the interception of the family of parallel lines with I_s , it is possible to obtain the ODF of the I_s . The generated data for ι between $]180^\circ, 360^\circ[$ is a $[0^\circ, 180^\circ]$ data repetition, since the orientation-dependent feature is not influenced by the direction. For example,

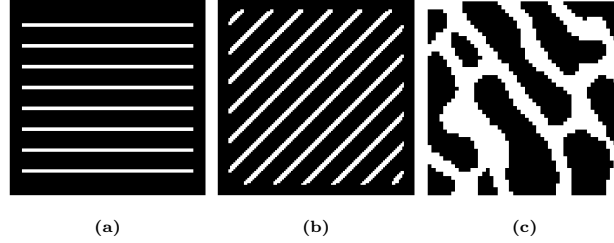


Figure 10.1: In this figure, the I_s used in this work are presented (a) - Benchmark Image 1; (b) - Benchmark Image 2; (c) Trabecular Bone

185 Fig. 10.2 represent the rotation of I_t between 0° and 180° with a ι increment of 45° .

To better understand how the ODF data is acquired using I_s and I_t , Figs. 10.5, 10.6 and 10.7 are presented. Each image makes reference to one of the images presented in Fig. 10.1, with ι between 0° and 180° , using an increment of
 190 45° . In each one of the images, five pixel colors: black, blue, cyan, red and pink are presented, as a result of the combination of multiple images information. The blue pixels represent the correspondent white pixels from the I_s image. The black pixels represent the background of the I_s image. This information is constant in each set of images with origin in the same I_s image. The only
 195 pixels that changes in these images are the pixels in red, cyan and pink. The red pixels represent the I_t . The creation of this I_t results in five different images, as can be observed in each set of images, Figs. 10.5, 10.6 and 10.7. The union of the pink pixels with the cyan pixels represent the intersection of I_s with each one of the I_t images. The methodology to acquire the ODF data only needs
 200 the information of the material phase change, and for this reason, only the cyan pixels are used to obtain the ODF data. Counting the number of cyan pixels that result from combining I_s with each I_t , and considering the length of the parallel family lines, Eq. (10.1), the resulting ODF data is plotted in Fig. 10.3.

Fitting an ellipse into this data, it is possible to obtain the material orienta-
 205 tion of the trabecular RVE. In Fig. 10.4 the fitted ellipses to the corresponding

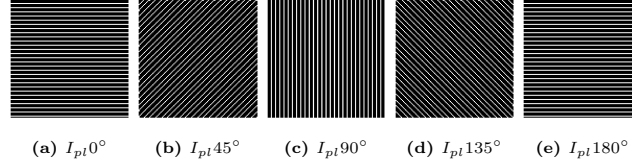


Figure 10.2: Images of parallel lines rotation I_L with an angle increment of 45° , within the interval of $\iota = [0, 180]$

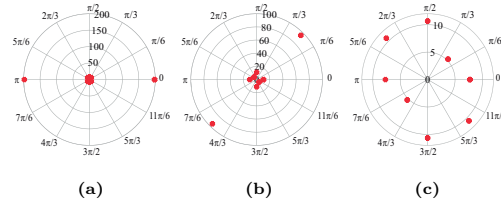


Figure 10.3: Polar plot of ODF data, the red points, from Figs. 10.1a, 10.1b, and 10.1c, respectively.

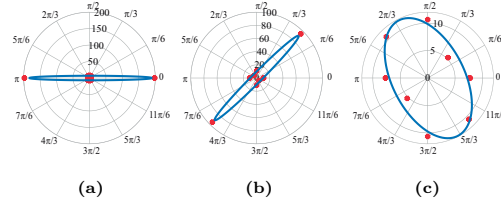


Figure 10.4: Polar plot of ODF data and correspondent fitted ellipse from Figs. 10.1a, 10.1b, and 10.1c, respectively. (a) - $\theta = 0^\circ$; (b) - $\theta = 45^\circ$; (c) - $\theta = 117^\circ$

ODF data present in Fig. 10.3. Considering Wolff's Law, it is understandable that this ellipse is aligned with the RVE preferential trabecular directions, it has the result of the functional requirements of the trabecular bone. From the fitted ellipse, it is possible to obtain the ellipse minor axis length, β_{min} , and major axis length, β_{max} and θ , the angle of ellipse major axis with the polar plot horizontal axis, that for the case of Fig. 10.1c represents the preferential trabecular direction.

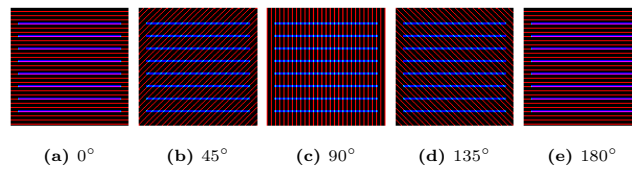


Figure 10.5: Grid Lines Rotation Interceptions of Fig. 10.1a

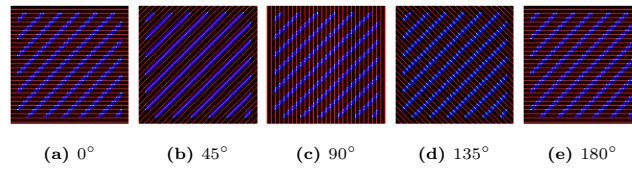


Figure 10.6: Grid Lines Rotation Interceptions of Fig. 10.1b

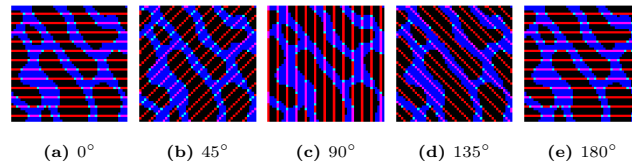


Figure 10.7: Grid Lines Rotation Interceptions of Fig. 10.1c

Phenomenological material law method

Merging the information obtained using the fabric tensor concept and the
 215 phenomenological material law, it is possible to define the homogenized or-
 thotropic mechanical properties of a RVE. To use the phenomenological mate-
 rial law defined by Belinha and co-workers [40], it was required to define the
 average apparent density, ρ_{app} . This was achieved by using the binary image
 I_s information as represented in Eq. (10.2), being the α_w the number of white
 220 pixels and α_b the number of black pixels.

$$\rho_{app} = \left(\frac{\alpha_w}{\alpha_b} \right) \rho_{app}^{cortical} \quad (10.2)$$

Using the ρ_{app} , it is possible to define the axial Young's modulus, E_{axial} . To
 define the transverse elastic modulus, E_{transv} , it can be used the relation between
 the ellipse minor axis length, β_{min} , and major axis length, β_{max} , and the axial
 elastic modulus E_{axial} , as Eq. (10.3) shows.

$$E_{transv} = \frac{(\|\beta_{min}\| E_{axial})}{\|\beta_{max}\|} \quad (10.3)$$

225 The Poisson's coefficient, ν , can be calculated according to the mixture the-
 ory using the relation between white and black pixels, as represented in Eq.
 (10.4).

$$\nu = \frac{0.0(\alpha_b) + 0.3(\alpha_w)}{\alpha_t} \quad (10.4)$$

being α_t the total number of pixels of the binary image I_s . The shear
 modulus, G , can be expeditiously calculated using Eq. (10.5).

$$G = \frac{E_{axial}}{2(1 + \nu)} \quad (10.5)$$

230 Using the homogenized material properties (E_{axial} , E_{transv} , ν , and G), it is
 possible to define the constitutive matrix $\mathbf{c}_{ox'y'}$, for the $ox'y'$ local coordinate
 system. Transforming $\mathbf{c}_{ox'y'}$ with the transformation rotation matrix \mathbf{T} , it is
 possible to define the material constitutive matrix in the global axis.

10.3. Validation

235 To validate this homogenization technique, some tests are performed, which
 allowed to understand the behavior of the methodology used to acquire the
 fabric tensor. Thus, three numerical studies were tested, one concerning the
 influence of the size of the RVE, another related to scale analysis, and a third
 one concerning the rotation effect of the RVE in the acquisition of the θ ellipse
 240 parameter.

10.3.1. Scale Study

In order to understand the influence of the size of the RVE, three distinct
 models were constructed based on Fig. 10.1a, 10.1b and 10.1c. The models
 presented in Fig. 10.8a and 10.8d are benchmark fabricated unitary binary
 245 image with a well-defined material orientation, 0° and 45° , respectively.

Alternatively, it was also used a realistic trabecular model RVE, represented in
 Fig. 10.8g, obtained from 10.1c, a micro-CT binary image. The three models
 were repeated $r_n \times r_n$, being $r_n = 1, 2, \dots, 10$. Applying the homogenization
 technique to all of the RVE and corresponding repetitions and comparing the
 250 results between each element of the constitute matrix, Fig. 10.9, it is perceptible
 that the scale of the RVE does not affect significantly the acquisition of the
 mechanical properties. The small changes visible in Fig. 10.9c occur since the
 unitary image, Fig. 10.8g is not periodic, which means that the repetition of
 the image result in the creation of new changes of phase.

255 10.3.2. Rotation Study

To understand the influence of the rotation in this methodology, the already
 presented RVEs were rotated with respect to their initial position using an
 increment of 20° , in the interval between $[0^\circ, 180^\circ]$. For the cases presented
 in this chapter, Fig. 10.1, the average difference between the obtained material
 260 orientation and the expected angle was of 5.83° . This difference can be explained
 by the changes occurring on the source image upon the rotation process, as it
 can be observed in Fig. 10.10, where the red circle marks the changes in the

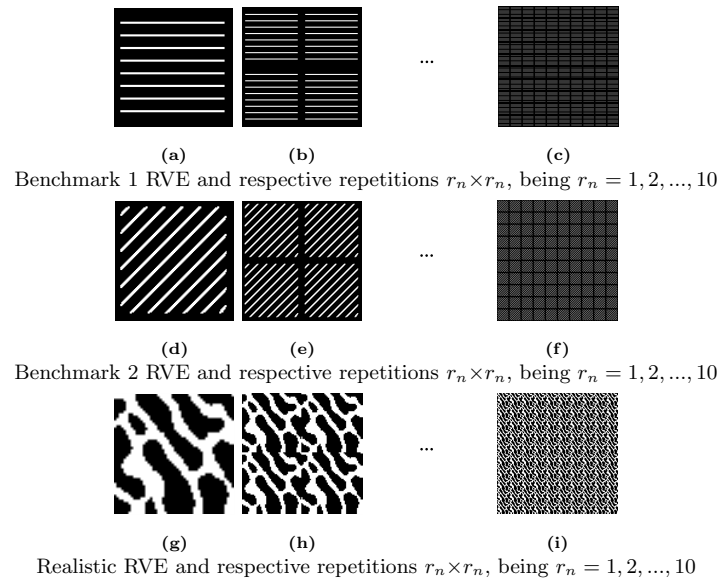


Figure 10.8: Model set used to validate the behavior of the methodology used to define de fabric tensor.

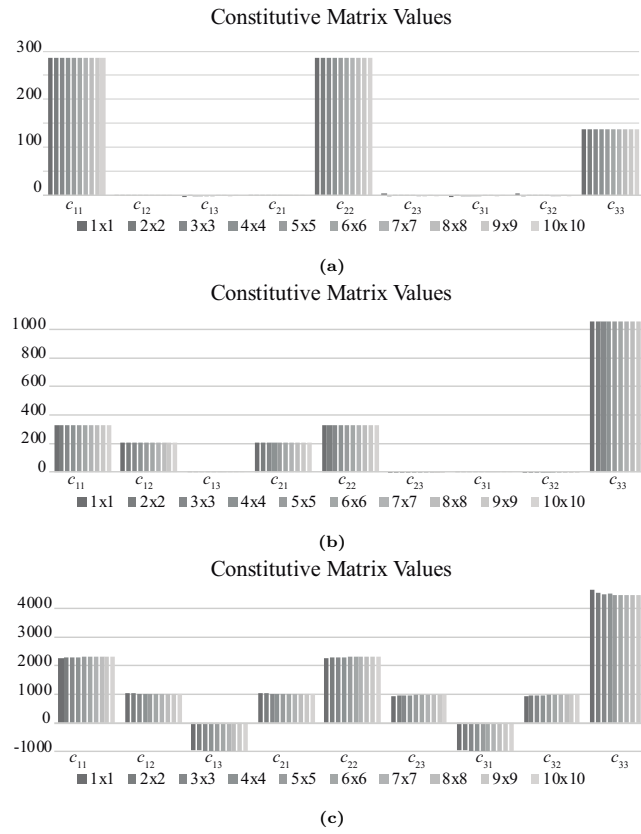


Figure 10.9: Constitutive matrix values obtained using a unitary RVE and up to 10×10 repetitions. **(a):** Results for the benchmark 1 RVE with principal direction of 0° . **(b):** Results for the benchmark 2 RVE with principal direction of 45° . **(c):** Results for the trabecular RVE.

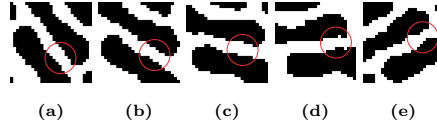


Figure 10.10: Image rotation process and inherent morphologic change, (a): Original Image; (b): 20° rotation; (c): 40° rotation; (d): 60° rotation; (e): 80° rotation.

same region in different rotated images. In Fig. 10.11, it is perceptible that applying a rotation to the image, the principal direction of the fitted ellipse, θ , reflects the applied rotation.

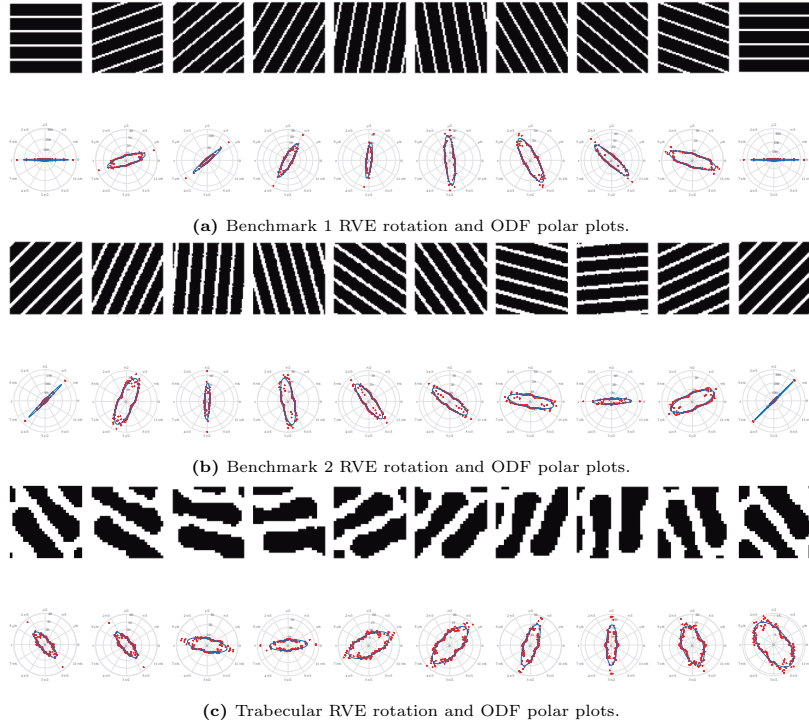


Figure 10.11: Set of images with respective ODF polar plot, and respective rotations with an increment angle of 20°, between the interval $[0^\circ, 180^\circ]$.

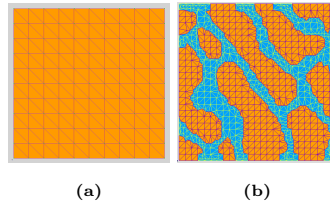


Figure 10.12: (a): Discretized homogeneous RVE (11×11 nodes uniformly distributed). (b): Example of a discretized heterogeneous RVE created using micro-CT image information.

10.3.3. Structural application

This homogenization methodology is intended to be used as an improvement of existent methodologies, usually used in highly heterogeneous problem domains. Thus, it was necessary to compare the structural response of a heterogeneous material domain with the structural response of the corresponding homogenized material domain, whose mechanical properties were obtained using the proposed methodology. I.e., to concede the different problem domains used in this study to be equivalent, the mechanical properties of the homogenous domain had to be defined using the information of the heterogeneous models problem domain. This allows defining equivalent models despite the different levels of heterogeneousness.

The heterogeneous RVE was defined using a heterogeneous domain, Fig. 10.1c. This problem domain, Fig. 10.12b, it is complex and it is formed by two different materials, the trabecular bone and void space. The homogeneous RVE, Fig. 10.12a, was defined by a homogeneous domain, discretized by a set of uniformly distributed nodes and integration points, with the same homogenized material properties acquired using the described methodology. The RVE's were constructed with a $L \times L$ dimension. To define the problem, it was imposed a displacement of $0.1 \times L$ at the nodes of the top layer, $y = L$. The nodes at $x = 0$ and $x = L$ were constrained on Ox direction, $\bar{u} = 0$, and the nodes at $y = 0$ and $y = L$ were constrained on Oy direction, $\bar{v} = 0$.

Two different numerical approaches, the FEM and the NNRPIM, were used

the compare the mechanical behavior of these RVEs. The integration mesh constructed within the FEM is fundamentally different from the integration mesh
 290 constructed with the NNRPIM formulation, resulting in very different positions of the integration points. Thus, in order to compare the stress field obtained with the two different RVEs, the concept of von Misses homogenized stress, σ_{eff}^h , is used. The σ_{eff}^h , defined by Eq. (10.6), allows to combine the stress field in one scalar value, facilitating the comparison of different models. In this Eq.,
 295 n_Q represent the number of integration points, which discretizing the problem domain, that do not belong to the vicinity of the domain boundary, typically 2%, avoiding the inaccurate stress concentrations that appear near the domain boundary.

$$\sigma_{eff}^h = \frac{1}{n_Q} \sum_{i=1}^{n_Q} \sigma(\mathbf{x}_i)_{eff} \quad (10.6)$$

The acquisition of the σ_{eff}^h , obtained for each analyzed RVE, using both FEM
 300 and NNRPIM methodologies, Fig. 10.13, provide the necessary data to validate the developed methodology. It is perceptible by this figure that increasing the level of detail and the size of the heterogeneous RVE, the value of the homogenized stress decreases. Thus, when the analysis uses a heterogeneous model following a 4×4 repetition, the obtained homogenized stress is very close with
 305 the homogenized stress obtained with the homogeneous RVE, indicating that the presented homogenization technique is capable to accurately obtain the homogenized orthotropic material properties of a trabecular patch. Comparing the FEM with NNRPIM meshless method, despite the equivalent results in the homogeneous RVE, the results of heterogeneous RVEs are not so close. This
 310 difference in the results can be explained by the locking effects that occur in the FEM.

Each analysis has its own computational cost. In Fig. 10.14, the time-lapse of each structural analysis is shown. Observing the computational cost of each analysis, it is possible to understand that the analysis of the homogenized RVE
 315 is much faster than heterogeneous RVEs. Generally, the multi-scale techniques use highly discretized RVEs, with a high computational cost associated. As this

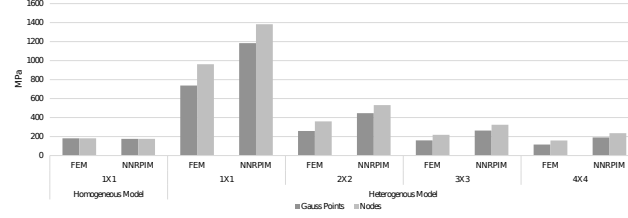


Figure 10.13: Homogenized von Mises effective stress σ_{eff}^h obtained with the FEM and the NNRPIM.

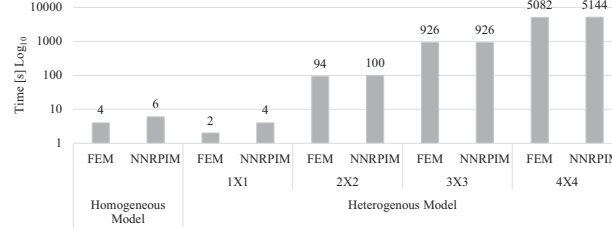


Figure 10.14: Computational cost (in seconds) of each analysis.

example shows, the proposed homogenization methodology is capable to reduce the cost of the multi-scale analysis, enabling more demanding simulations.

10.4. Conclusions

320 The presented methodology allows defining the mechanical properties of a
 micro-CT RVE patch without any a-priory knowledge. Using a morphologic
 methodology to acquire de ODF data from the micro-CT RVE, and combining
 this data with a phenomenological material law, it was defined a methodology
 that allows defining a homogeneous material that it is equivalent to a het-
 325 erogeneous material. The defined material mechanical properties are directly
 related with the trabecular anisotropy encoded in the fabric tensor and with
 the material law developed by Belinha *et al.*, 2012 [40]. It was demonstrated
 that the methodology is stable and provide good results, even when consider-
 ing different RVEs scales and different material principal directions. It was also

330 shown that the NNRPIM is capable to produce accurate and smooth micro-scale
variable fields (at the RVE scale), which allow obtaining accurate final homoge-
nized variable fields. Multi-scale techniques usually use highly discretized RVEs.
The homogenization technique here proposed showed that when combined with
335 meshless methods it is capable to reduce the cost of the analyzing highly het-
erogeneous domains. Thus, using this methodology in multi-scale analyses will
allow simulating more complex problems with lower cost. Also, as bone is a
hierarchal material, this methodology might be a powerful tool to understand
the remodeling process, using a multi-scale approach, where the mechanical
properties of trabecular bone can be defined at the micro-scale, considering the
340 trabeculae architecture.

Acknowledgment

The authors truly acknowledge the funding provided by Ministério da Ciência,
Tecnologia e Ensino Superior - Fundação para a Ciência e a Tecnologia (Por-
tugal), under Grants SFRH/BD/110047/2015, and by project funding MIT-
345 EXPL/ISF/0084/2017. Additionally, the authors gratefully acknowledge the
funding of Project NORTE-01-0145-FEDER-000022 - SciTech - Science and
Technology for Competitive and Sustainable Industries, co-financed by Pro-
grama Operacional Regional do Norte (NORTE2020), through Fundo Europeu
de Desenvolvimento Regional (FEDER).

350 References

References

- [1] J. Belinha, Meshless Methods in Biomechanics: Bone Tissue Remod-
elling Analysis, Vol. 2 of Lecture Notes in Computational Vision and
Biomechanics, Springer Netherlands, Dordrecht, 2014. doi:10.1007/
355 978-94-007-4174-4.

- [2] C. VanPutte, J. Regan, A. Russo, R. Seeley, T. Stephens, P. Tate, Seeley's Anatomy & Physiology, 10th Edition, Vol. 2, McGraw-Hill Companies, 2003.
- [3] Q.-H. Qin, Mechanics of cellular bone remodeling, CRC Press Taylor & Francis Group, 2012.
- [4] D. R. Carter, M. C. Van Der Meulen, G. S. Beaupré, Mechanical factors in bone growth and development, Bone 18 (1 Suppl) (1996) 5S–10S. doi:10.1016/8756-3282(95)00373-8.
URL <http://www.ncbi.nlm.nih.gov/pubmed/8717541>
- [5] V. C. Mow, A. Ratcliffe, A. R. Poole, Cartilage and diarthrodial joints as paradigms for hierarchical materials and structures., Biomaterials 13 (2) (1992) 67–97.
URL <http://www.ncbi.nlm.nih.gov/pubmed/1550898>
- [6] L. F. Bonewald, The amazing osteocyte, Journal of Bone and Mineral Research 26 (2) (2011) 229–238. doi:10.1002/jbmr.320.
- [7] J. A. Buckwalter, M. J. Glimcher, R. R. Cooper, R. Recker, Bone biology. II: Formation, form, modeling, remodeling, and regulation of cell function., Instructional course lectures 45 (1996) 387–99.
URL <http://www.ncbi.nlm.nih.gov/pubmed/8727758>
- [8] R. B. Martin, D. B. Burr, N. A. Sharkey, D. P. Fyhrie, Skeletal Tissue Mechanics, Springer New York, New York, NY, 2015. doi:10.1007/978-1-4939-3002-9.
URL <http://link.springer.com/10.1007/978-1-4939-3002-9>
- [9] E. Ozcivici, Y. K. Luu, B. Adler, Y.-X. Qin, J. Rubin, S. Judex, C. T. Rubin, Mechanical signals as anabolic agents in bone, Nature Reviews Rheumatology 6 (1) (2010) 50–59. doi:10.1038/nrrheum.2009.239.
URL <http://www.ncbi.nlm.nih.gov/pubmed/20046206>

- [10] A. G. Robling, P. J. Niziolek, L. A. Baldrige, K. W. Condon, M. R. Allen, I. Alam, S. M. Mantila, J. Gluhak-Heinrich, T. M. Bellido, S. E. Harris, C. H. Turner, Mechanical Stimulation of Bone in Vivo Reduces Osteocyte Expression of Sost/Sclerostin, *Journal of Biological Chemistry* 283 (9) (2008) 5866–5875. doi:10.1074/jbc.M705092200.
URL <http://www.ncbi.nlm.nih.gov/pubmed/18089564>
- [11] S. Theoleyre, Y. Wittrant, S. K. Tat, Y. Fortun, F. Redini, D. Heymann, The molecular triad OPG/RANK/RANKL: involvement in the orchestration of pathophysiological bone remodeling, *Cytokine & Growth Factor Reviews* 15 (6) (2004) 457–475. doi:10.1016/j.cytogfr.2004.06.004.
URL <http://www.ncbi.nlm.nih.gov/pubmed/15561602>
- [12] E. Lucchinetti, Composite Models of Bone Properties, in: *Bone Mechanics Handbook*, Second Edition, CRC Press, 2001, pp. 12–1–12–19. doi:10.1201/b14263-16.
URL <http://www.crcnetbase.com/doi/10.1201/b14263-16>
- [13] E. Hamed, I. Jasiuk, Elastic modeling of bone at nanostructural level, *Materials Science and Engineering R: Reports* 73 (3-4) (2012) 27–49. doi:10.1016/j.mser.2012.04.001.
URL <http://dx.doi.org/10.1016/j.mser.2012.04.001>
- [14] A. Barkaoui, B. Tlili, A. Vercher-Martínez, R. Hambli, A multiscale modelling of bone ultrastructure elastic proprieties using finite elements simulation and neural network method, *Computer Methods and Programs in Biomedicine* 134 (2016) 69–78. doi:10.1016/j.cmpb.2016.07.005.
URL <http://dx.doi.org/10.1016/j.cmpb.2016.07.005>
- [15] E. Hamed, Y. Lee, I. Jasiuk, Multiscale modeling of elastic properties of cortical bone, *Acta Mechanica* 213 (1-2) (2010) 131–154. doi:10.1007/s00707-010-0326-5.
URL <http://link.springer.com/10.1007/s00707-010-0326-5>

- [16] I. Jasiuk, Micromechanics of Bone Modeled as a Composite Material, in: *Micromechanics and Nanomechanics of Composite Solids*, Springer International Publishing, Cham, 2018, pp. 281–306. doi:10.1007/978-3-319-52794-9_10.
 415 URL http://link.springer.com/10.1007/978-3-319-52794-9_{_}10
- [17] R. O. Ritchie, M. J. Buehler, P. Hansma, Plasticity and toughness in bone, *Physics Today* 62 (6) (2009) 41–47. doi:10.1063/1.3156332.
 URL <http://physicstoday.scitation.org/doi/10.1063/1.3156332>
- [18] W. J. Landis, The strength of a calcified tissue depends in part on the
 420 molecular structure and organization of its constituent mineral crystals in their organic matrix, *Bone* 16 (5) (1995) 533–544. doi:10.1016/8756-3282(95)00076-P.
- [19] S. Weiner, W. Traub, Bone structure: From angstroms to microns, *FASEB Journal* 6 (3) (1992) 879–885, cited By 330.
 425 URL <https://www.scopus.com/inward/record.uri?eid=2-s2.0-0026529338&partnerID=40&md5=c4ec41504f12b3b6a1f237e1f88984ae>
- [20] F. Pauwels, Eine neue theorie über den einfluß mechanischer reize auf die differenzierung der stützgewebe, *Zeitschrift für Anatomie und Entwicklungsgeschichte* 121 (6) (1960) 478–515. doi:10.1007/BF00523401.
 430 URL <http://link.springer.com/10.1007/BF00523401>
- [21] J. Adam, A simplified model of wound healing (with particular reference to the critical size defect), *Mathematical and Computer Modelling* 30 (5–6) (1999) 23–32. doi:10.1016/S0895-7177(99)00145-4.
 435 URL <http://linkinghub.elsevier.com/retrieve/pii/S0895717799001454>
- [22] F. Pauwels, *Gesammelte Abhandlungen zur funktionellen Anatomie des — Friedrich Pauwels —* Springer, Springer (1965) 543.
 URL <http://www.springer.com/us/book/9783642868429>

- 440 [23] H. M. Frost, The laws of bone structure, 1964.
- [24] D. H. Hegedus, S. C. Cowin, Bone remodeling ii: small strain adaptive elasticity, *Journal of Elasticity* 6 (4) (1976) 337–352. doi:10.1007/BF00040896.
URL <http://link.springer.com/10.1007/BF00040896>
- 445 [25] S. C. Cowin, R. R. Nachlinger, Bone remodeling iii: uniqueness and stability in adaptive elasticity theory, *Journal of Elasticity* 8 (3) (1978) 285–295. doi:10.1007/BF00130467.
URL <http://link.springer.com/10.1007/BF00130467>
- [26] S. C. Cowin, A. M. Sadegh, G. M. Luo, An evolutionary wolff’s law for trabecular architecture, *Journal of Biomechanical Engineering* 114 (1) (1992) 129–136. doi:10.1115/1.2895436.
URL <http://link.aip.org/link/JBENDY/v114/i1/p129/s1&Agg=doi>
- [27] D. R. Carter, T. E. Orr, D. P. Fyhrie, Relationships between loading history and femoral cancellous bone architecture, *Journal of Biomechanics* 22 (3) (1989) 231–244. doi:10.1016/0021-9290(89)90091-2.
455 URL [http://linkinghub.elsevier.com/retrieve/pii/0021929089900912](http://linkinghub.elsevier.com/retrieve/pii/S0021929089900912)
- [28] D. R. Carter, Mechanical loading history and skeletal biology, *Journal of Biomechanics* 20 (11–12) (1987) 1095–1109. doi:10.1016/0021-9290(87)90027-3.
460 URL [http://linkinghub.elsevier.com/retrieve/pii/0021929087900273](http://linkinghub.elsevier.com/retrieve/pii/S0021929087900273)
- [29] D. P. Fyhrie, D. R. Carter, A unifying principle relating stress to trabecular bone morphology, *Journal of orthopaedic research: official publication of the Orthopaedic Research Society* 4 (3) (1986) 304–17. doi:10.1002/jor.1100040307.
465 URL <http://www.ncbi.nlm.nih.gov/pubmed/3734938>

- [30] R. T. Whalen, D. R. Carter, C. R. Steele, Influence of physical activity on the regulation of bone density, *Journal of Biomechanics* 21 (10) (1988) 825–837. doi:10.1016/0021-9290(88)90015-2.
 470 URL <http://linkinghub.elsevier.com/retrieve/pii/S0021929088900152>
- [31] R. Huiskes, H. Weinans, H. J. Grootenboer, M. Dalstra, B. Fudala, T. J. Slooff, Adaptive bone-remodeling theory applied to prosthetic-design analysis, *Journal of Biomechanics* 20 (11-12) (1987) 1135–1150.
 475 doi:10.1016/0021-9290(87)90030-3.
- [32] H. E. Pettermann, T. J. Reiter, F. G. Rammerstorfer, Computational simulation of internal bone remodeling, *Archives of Computational Methods in Engineering* 4 (4) (1997) 295–323. doi:10.1007/BF02737117.
 480 URL <http://link.springer.com/10.1007/BF02737117>
- [33] T. J. Reiter, F. G. Rammerstorfer, H. J. Bohm, Numerical algorithm for the simulation of bone remodeling, *American Society of Mechanical Engineers, Bioengineering Division (Publication) BED* 17 (1990) 181–184.
 485 URL <http://www.scopus.com/inward/record.url?eid=2-s2.0-0025555125&partnerID=tZ0tx3y1>
- [34] P. Prendergast, R. Huiskes, K. Søballe, Biophysical stimuli on cells during tissue differentiation at implant interfaces, *Journal of Biomechanics* 30 (6) (1997) 539–548. doi:10.1016/S0021-9290(96)00140-6.
 490 URL <http://linkinghub.elsevier.com/retrieve/pii/S0021929096001406>
- [35] D. Lacroix, P. J. Prendergast, G. Li, D. Marsh, Biomechanical model to simulate tissue differentiation and bone regeneration: Application to fracture healing, *Medical and Biological Engineering and Computing* 40 (1) (2002) 14–21. doi:10.1007/BF02347690.
 495 URL <https://doi.org/10.1007/BF02347690>

- [36] D. Lacroix, P. Prendergast, A mechano-regulation model for tissue differentiation during fracture healing: analysis of gap size and loading, *Journal of Biomechanics* 35 (9) (2002) 1163–1171. doi:10.1016/S0021-9290(02)00086-6.
- 500 [37] L. M. McNamara, P. J. Prendergast, Bone remodelling algorithms incorporating both strain and microdamage stimuli, *Journal of Biomechanics* 40 (6) (2007) 1381–1391. doi:10.1016/j.jbiomech.2006.05.007.
- [38] M. Doblaré, G. J.M., Anisotropic bone remodelling model based on a continuum damage-repair theory, *Journal of Biomechanics* 35 (1) (2002) 1–17. doi:10.1016/S0021-9290(01)00178-6.
- 505 [39] B. M. Mulvihill, P. J. Prendergast, Mechanobiological regulation of the remodelling cycle in trabecular bone and possible biomechanical pathways for osteoporosis, *Clinical Biomechanics* 25 (5) (2010) 491–498. doi:10.1016/j.clinbiomech.2010.01.006.
- 510 [40] J. Belinha, R. M. N. Jorge, L. M. Dinis, A meshless microscale bone tissue trabecular remodelling analysis considering a new anisotropic bone tissue material law, *Computer Methods in Biomechanics and Biomedical Engineering* 5842 (August 2012) (2012) 1–15. doi:10.1080/10255842.2012.654783.
- 515 [41] D. R. Carter, D. P. Fyhrie, R. T. Whalen, Trabecular bone density and loading history: Regulation of connective tissue biology by mechanical energy, *Journal of Biomechanics* 20 (8) (1987) 785–794. doi:10.1016/0021-9290(87)90058-3.
- 520 [42] M. Peyroteo, J. Belinha, L. Dinis, R. Natal Jorge, The mechanologic bone tissue remodeling analysis, *Numerical Methods and Advanced Simulation in Biomechanics and Biological Processes* (2018) 303–323doi:10.1016/b978-0-12-811718-7.00017-4.
URL <http://dx.doi.org/10.1016/B978-0-12-811718-7.00017-4>

- [43] M. Peyroteo, J. Belinha, S. Vinga, L. Dinis, R. N. Jorge, Mechanical bone remodelling: Comparative study of distinct numerical approaches, *Engineering Analysis with Boundary Elements* doi:10.1016/j.enganabound.2018.01.011.
URL <http://www.sciencedirect.com/science/article/pii/S0955799717304022>
- [44] A. Bailón-Plaza, M. C. Van Der Meulen, A Mathematical Framework to Study the Effects of Growth Factor Influences on Fracture Healing, *Journal of Theoretical Biology* 212 (2) (2001) 191–209. doi:10.1006/jtbi.2001.2372.
URL <http://linkinghub.elsevier.com/retrieve/pii/S0022519301923720>
- [45] S. V. Komarova, R. J. Smith, S. J. Dixon, S. M. Sims, L. M. Wahl, Mathematical model predicts a critical role for osteoclast autocrine regulation in the control of bone remodeling, *Bone* 33 (2) (2003) 206–215. doi:10.1016/S8756-3282(03)00157-1.
URL <http://www.ncbi.nlm.nih.gov/pubmed/14499354>
- [46] V. Lemaire, F. L. Tobin, L. D. Greller, C. R. Cho, L. J. Suva, Modeling the interactions between osteoblast and osteoclast activities in bone remodeling, *Journal of Theoretical Biology* 229 (3) (2004) 293–309. doi:10.1016/j.jtbi.2004.03.023.
URL <http://www.ncbi.nlm.nih.gov/pubmed/15234198>
- [47] P. Pivonka, J. Zimak, D. W. Smith, B. S. Gardiner, C. R. Dunstan, N. A. Sims, T. J. Martin, G. R. Mundy, T. John Martin, G. R. Mundy, Model structure and control of bone remodeling: A theoretical study, *Bone* 43 (2) (2008) 249–263. doi:10.1016/j.bone.2008.03.025.
URL <http://www.ncbi.nlm.nih.gov/pubmed/18514606>
- [48] M. D. Ryser, N. Nigam, S. V. Komarova, Mathematical modeling of spatio-temporal dynamics of a single bone multicellular unit, *Journal of*

- Bone and Mineral Research 24 (5) (2009) 860–870. doi:10.1359/jbmr.081229.
 555 URL <http://dx.doi.org/10.1359/jbmr.081229>
- [49] R. Huiskes, W. D. V. Driel, P. J. Prendergast, K. Søballe, A biomechanical regulatory model for periprosthetic fibrous-tissue differentiation, Journal of Materials Science Materials in Medicine 8 (12) (1997) 785–788. doi:10.1023/A:1018520914512.
 560 URL <http://link.springer.com/10.1023/A:1018520914512>
- [50] S. J. Mousavi, M. Hamdy Doweidar, Role of Mechanical Cues in Cell Differentiation and Proliferation: A 3D Numerical Model, PLOS ONE 10 (5) (2015) e0124529. doi:10.1371/journal.pone.0124529.
 URL <http://dx.plos.org/10.1371/journal.pone.0124529>
- 565 [51] C. Lerebours, P. R. Buenzli, S. Scheiner, P. Pivonka, A multiscale mechanobiological model of bone remodelling predicts site-specific bone loss in the femur during osteoporosis and mechanical disuse, Biomechanics and Modeling in Mechanobiology 15 (1) (2016) 43–67. doi:10.1007/s10237-015-0705-x.
 570 URL <http://dx.doi.org/10.1007/s10237-015-0705-x>
- [52] R. T. Hart, D. T. Davy, K. G. Heiple, A Computational Method for Stress Analysis of Adaptive Elastic Materials With a View Toward Applications in Strain-Induced Bone Remodeling, Journal of Biomechanical Engineering 106 (4) (1984) 342. doi:10.1115/1.3138503.
- 575 [53] G. S. Beaupré, T. E. Orr, D. R. Carter, An approach for time-dependent bone modeling and remodeling-theoretical development, Journal of Orthopaedic Research 8 (5) (1990) 651–661. doi:10.1002/jor.1100080506.
 URL <http://doi.wiley.com/10.1002/jor.1100080506>
- [54] C. R. Jacobs, J. C. Simo, G. S. Beaupre, D. R. Carter, Adaptive bone remodeling incorporating simultaneous density and anisotropy consider-
 580

ations, *Journal of Biomechanics* 30 (6) (1997) 603–613. doi:10.1016/S0021-9290(96)00189-3.

[55] P. Fernandes, J. Guedes, H. Rodrigues, Topology optimization of three-dimensional linear elastic structures with a constraint on "perimeter", *Computers & Structures* 73 (6) (1999) 583–594. doi:10.1016/S0045-7949(98)00312-5.

[56] M. Doblaré, J. M. García, Application of an anisotropic bone-remodelling model based on a damage-repair theory to the analysis of the proximal femur before and after total hip replacement, *Journal of Biomechanics* 34 (9) (2001) 1157–1170. doi:10.1016/S0021-9290(01)00069-0.

[57] J. Hazrati Marangalou, K. Ito, B. van Rietbergen, A novel approach to estimate trabecular bone anisotropy from stress tensors, *Biomechanics and Modeling in Mechanobiology* 14 (1) (2015) 39–48. doi:10.1007/s10237-014-0584-6.

[58] R. Moreno, Ö. Smedby, D. H. Pahr, Prediction of apparent trabecular bone stiffness through fourth-order fabric tensors, *Biomechanics and Modeling in Mechanobiology* 15 (4) (2016) 831–844. doi:10.1007/s10237-015-0726-5.

[59] J. Kabel, B. van Rietbergen, A. Odgaard, R. Huiskes, Constitutive relationships of fabric, density, and elastic properties in cancellous bone architecture, *Bone* 25 (4) (1999) 481–486. doi:10.1016/S8756-3282(99)00190-8.

URL <https://www.sciencedirect.com/science/article/pii/S8756328299001908>

[60] S. C. Cowin, S. B. Doty, *Tissue Mechanics*, Springer Science, 2007.

[61] J. Rice, S. Cowin, J. Bowman, On the dependence of the elasticity and strength of cancellous bone on apparent density, *Journal of Biomechanics* 21 (2) (1988) 155–168. doi:10.1016/0021-9290(88)90008-5.

- URL <https://www.sciencedirect.com/science/article/pii/S0021929088900085>
610
- [62] P. K. Zysset, A review of morphology–elasticity relationships in human trabecular bone: theories and experiments, *Journal of Biomechanics* 36 (10) (2003) 1469–1485. doi:10.1016/S0021-9290(03)00128-3.
URL <https://www.sciencedirect.com/science/article/pii/S0021929003001283>
615
- [63] R. Huiskes, E. Chao, A survey of finite element analysis in orthopedic biomechanics: The first decade, *Journal of Biomechanics* 16 (6) (1983) 385–409. doi:10.1016/0021-9290(83)90072-6.
URL <http://linkinghub.elsevier.com/retrieve/pii/S0021929083900726>
620
- [64] O. C. Zienkiewicz, R. L. Taylor, *The Finite Element Method*, 4th Edition, McGraw-Hill, London, 1994.
- [65] R. A. Gingold, J. J. Monaghan, Smooth particle hydrodynamics: theory and application to non-spherical stars, *Monthly Notices of the Royal Astronomical Society* 181 (1977) 375–389.
625
- [66] L. M. J. S. Dinis, R. M. Natal Jorge, J. Belinha, Analysis of 3D solids using the natural neighbour radial point interpolation method, *Computer Methods in Applied Mechanics and Engineering* 196 (13-16) (2007) 2009–2028. doi:10.1016/j.cma.2006.11.002.
- [67] J. Belinha, L. M. J. S. Dinis, R. M. N. Jorge, The natural radial element method, *Int. J. Numer. Methods Eng* 93 (12) (2013) 1286–1313. doi:10.1002/nme.4427.
630
- [68] J. Belinha, L. Dinis, Elasto-plastic analysis of plates by the element free galerkin method, *Engineering Computations* 23 (5) (2006) 525–551. doi:10.1108/02644400610671126.
635
- URL <http://www.emeraldinsight.com/10.1108/02644400610671126>

- [69] J. Belinha, L. M. J. S. Dinis, Nonlinear analysis of plates and laminates using the element free galerkin method, *Composite Structures* 78 (3) (2007) 337–350. doi:10.1016/j.compstruct.2005.10.007.
 640 URL <http://linkinghub.elsevier.com/retrieve/pii/S0045794906000915>
- [70] L. M. J. S. Dinis, R. M. Natal Jorge, J. Belinha, Analysis of plates and laminates using the natural neighbour radial point interpolation method, *Engineering Analysis with Boundary Elements* 32 (3) (2008) 267–279.
 645 doi:10.1016/j.enganabound.2007.08.006.
 URL <http://linkinghub.elsevier.com/retrieve/pii/S0955799707001415>
- [71] J. Belinha, L. Dinis, R. M. N. Jorge, The natural neighbour radial point interpolation method: dynamic applications, *Engineering Computations* 26 (8) (2009) 911–949. doi:10.1108/02644400910996835.
 650 URL <http://www.emeraldinsight.com/doi/abs/10.1108/02644400910996835>
- [72] L. M. J. S. Dinis, R. M. N. Jorge, J. Belinha, An unconstrained third-order plate theory applied to functionally graded plates using a meshless method, *Mechanics of Advanced Materials and Structures* 17 (2) (2010) 108–133. doi:10.1080/15376490903249925.
 655 URL <http://www.tandfonline.com/doi/abs/10.1080/15376490903249925#.VQQ1FXysWE4>
- [73] L. Dinis, R. N. Jorge, J. Belinha, Static and dynamic analysis of laminated plates based on an unconstrained third order theory and using a radial point interpolator meshless method, *Computers & Structures* (19) 1771 – 1784, civil-Comp. doi:10.1016/j.compstruc.2010.10.015.
 660
- [74] J. Belinha, L. M. J. S. Dinis, R. M. Natal Jorge, Analysis of thick plates by the natural radial element method, *International Journal of Mechanical*

- 665 Sciences 76 (2013) 33–48. doi:10.1016/j.ijmecsci.2013.08.011.
 URL <http://dx.doi.org/10.1016/j.ijmecsci.2013.08.011>
- [75] S. Moreira, J. Belinha, L. M. J. S. Dinis, R. M. N. Jorge, Análise de
 vigas laminadas utilizando o natural neighbour radial point interpola-
 tion method, Revista Internacional de Metodos Numericos para Calculo
 670 y Diseno en Ingenieria 30 (2) (2014) 108–120. doi:10.1016/j.rimni.
 2013.02.002.
 URL <http://dx.doi.org/10.1016/j.rimni.2013.02.002>
- [76] B. V. Farahani, J. M. Berardo, R. Drgas, J. M. César de Sá, A. J. Fer-
 reira, J. Belinha, The Axisymmetric Analysis of Circular Plates Using
 675 the Radial Point Interpolation Method, International Journal for Com-
 putational Methods in Engineering Science and Mechanics 16 (6) (2015)
 336–353. doi:10.1080/15502287.2015.1103819.
- [77] B. V. Farahani, J. Berardo, J. Belinha, A. Ferreira, P. J. Tavares,
 P. Moreira, On the optimal shape parameters of distinct ver-
 680 sions of rbf meshless methods for the bending analysis of plates,
 Engineering Analysis with Boundary Elements 84 (2017) 77 – 86.
 doi:10.1016/j.enganabound.2017.08.010.
 URL [http://www.sciencedirect.com/science/article/pii/
 S0955799717302680](http://www.sciencedirect.com/science/article/pii/S0955799717302680)
- [78] B. V. Farahani, J. Berardo, J. Belinha, A. Ferreira, P. J. Tavares,
 P. Moreira, An optimized rbf analysis of an isotropic mindlin plate in
 bending, Procedia Structural Integrity 5 (2017) 584 – 591, 2nd Interna-
 tional Conference on Structural Integrity, ICSI 2017, 4-7 September 2017,
 Funchal, Madeira, Portugal. doi:10.1016/j.prostr.2017.07.018.
 690 URL [http://www.sciencedirect.com/science/article/pii/
 S2452321617301038](http://www.sciencedirect.com/science/article/pii/S2452321617301038)
- [79] L. M. J. S. Dinis, R. M. Natal Jorge, J. Belinha, Analysis of 3d solids
 using the natural neighbour radial point interpolation method, Computer

- Methods in Applied Mechanics and Engineering 196 (13–16) (2007) 2009–2028. doi:10.1016/j.cma.2006.11.002.
 695 URL <http://www.sciencedirect.com/science/article/pii/S0045782506003446>
- [80] L. M. J. S. Dinis, R. M. N. Jorge, J. Belinha, A 3d shell-like approach using a natural neighbour meshless method: Isotropic and orthotropic thin structures, Composite Structures 92 (5) (2010) 1132–1142. doi:10.1016/j.compstruct.2009.10.014.
 700
- [81] J. Belinha, L. M. S. J. S. Dinis, R. M. N. Jorge, Composite laminated plate analysis using the natural radial element method, Composite Structures 103 (2013) 50–67. doi:10.1016/j.compstruct.2013.03.018.
- 705 [82] D. Rodrigues, J. Belinha, F. Pires, L. Dinis, R. N. Jorge, Homogenization technique for heterogeneous composite materials using meshless methods, Engineering Analysis with Boundary Elements doi:10.1016/j.enganabound.2017.12.012.
 URL <http://www.sciencedirect.com/science/article/pii/S0955799717304496>
 710
- [83] J. M. C. Azevedo, J. Belinha, L. M. J. S. Dinis, R. M. Natal Jorge, Crack path prediction using the natural neighbour radial point interpolation method, Engineering Analysis with Boundary Elements 59 (2015) 144–158. doi:10.1016/j.enganabound.2015.06.001.
 715 URL <http://linkinghub.elsevier.com/retrieve/pii/S0955799715001344>
- [84] J. Belinha, J. M. C. Azevedo, L. M. J. S. Dinis, R. M. Natal Jorge, The natural neighbor radial point interpolation method extended to the crack growth simulation, International Journal of Applied Mechanics 08 (01) (2016) 1650006. doi:10.1142/S175882511650006X.
 720 URL <http://www.worldscientific.com/doi/10.1142/S175882511650006X>

- [85] B. V. Farahani, R. Amaral, J. Belinha, P. J. Tavares, P. Moreira, A gtn failure analysis of an aa6061-t6 bi-failure specimen, *Procedia Structural Integrity* 5 (2017) 981 – 988, 2nd International Conference on Structural Integrity, ICSI 2017, 4-7 September 2017, Funchal, Madeira, Portugal. doi:10.1016/j.prostr.2017.07.147.
URL <http://www.sciencedirect.com/science/article/pii/S2452321617302597>
- [86] J. Belinha, L. Dinis, R. M. Natal Jorge, The analysis of the bone remodelling around femoral stems: A meshless approach, *Mathematics and Computers in Simulation* 121 (2016) 64–94. doi:10.1016/j.matcom.2015.09.002.
URL <http://www.sciencedirect.com/science/article/pii/S0378475415001895>
- [87] J. Belinha, L. M. J. S. Dinis, R. M. N. Jorge, The mandible remodeling induced by dental implants: A meshless approach, *Journal of Mechanics in Medicine and Biology* 15 (4) (2015) 1550059. doi:10.1142/S0219519415500591.
URL <http://www.worldscientific.com/doi/10.1142/S0219519415500591>
- [88] H. M. S. Duarte, J. R. Andrade, L. M. J. S. Dinis, R. M. N. Jorge, J. Belinha, Numerical analysis of dental implants using a new advanced discretization technique, *Mechanics of Advanced Materials and Structures* 23 (4) (2015) 467–479. doi:10.1080/15376494.2014.987410.
URL <http://www.tandfonline.com/doi/abs/10.1080/15376494.2014.987410>
- [89] C. S. S. Tavares, J. Belinha, L. M. J. S. Dinis, R. M. Natal Jorge, The elasto-plastic response of the bone tissue due to the insertion of dental implants, Vol. 110, 2015, pp. 37–44. doi:10.1016/j.proeng.2015.07.007.

URL <http://www.sciencedirect.com/science/article/pii/S1877705815012485>

- [90] M. Doweidar, B. Calvo, I. Alfaro, P. Groenenboom, M. Doblaré, A comparison of implicit and explicit natural element methods in large strains problems: Application to soft biological tissues modeling, Computer Methods in Applied Mechanics and Engineering 199 (25-28) (2010) 1691–1700. doi:10.1016/j.cma.2010.01.022.

URL <http://linkinghub.elsevier.com/retrieve/pii/S0045782510000575>

- [91] M. Marques, J. Belinha, L. M. J. Dinis, R. Natal Jorge, A brain impact stress analysis using advanced discretization meshless techniques, Proceedings of the Institution of Mechanical Engineers, Part H: Journal of Engineering in Medicine 232 (3) (2018) 257–270. doi:10.1177/0954411917751559.

URL <http://dx.doi.org/10.1177/0954411917751559>

- [92] C. F. Santos, J. Belinha, F. Gentil, M. Parente, B. Areias, R. N. Jorge, Biomechanical study of the vestibular system of the inner ear using a numerical method, Procedia IUTAM 24 (2017) 30 – 37, iUTAM Symposium on Advances in Biomechanics of Hearing. doi:10.1016/j.piutam.2017.08.040.

URL <http://www.sciencedirect.com/science/article/pii/S2210983817301529>

- [93] C. F. Santos, J. Belinha, F. Gentil, M. Parente, R. N. Jorge, The free vibrations analysis of the cupula in the inner ear using a natural neighbor meshless method, Engineering Analysis with Boundary Elements doi:10.1016/j.enganabound.2018.01.002.

URL <http://www.sciencedirect.com/science/article/pii/S0955799717304526>

- [94] M. Doblaré, E. Cueto, B. Calvo, M. A. Martínez, J. M. Garcia,

- 780 J. Cegoñino, On the employ of meshless methods in biomechanics,
Computer Methods in Applied Mechanics and Engineering 194 (6-8)
(2005) 801–821. doi:10.1016/j.cma.2004.06.031.
URL [http://www.sciencedirect.com/science/article/pii/
S0045782504003007](http://www.sciencedirect.com/science/article/pii/S0045782504003007)
- 785 [95] J. M. García, M. Doblaré, E. Cueto, Simulation of bone internal remod-
eling by means of the α -shape-based natural element method, European
Congress on Computational Methods in Applied Sciences and Engineering
(ECCOMAS 2000) (September) (2000) 11–14.
- [96] K. M. Liew, H. Y. Wu, T. Y. Ng, Meshless method for modeling of
790 human proximal femur: Treatment of nonconvex boundaries and stress
analysis, Computational Mechanics 28 (5) (2002) 390–400. doi:10.1007/
s00466-002-0303-5.
URL <http://link.springer.com/10.1007/s00466-002-0303-5>
- [97] J. D. Lee, Y. Chen, X. Zeng, A. Eskandarian, M. Oskard, Modeling and
795 simulation of osteoporosis and fracture of trabecular bone by meshless
method, International Journal of Engineering Science 45 (2–8) (2007)
329–338. doi:10.1016/j.ijengsci.2007.03.007.
URL [http://www.sciencedirect.com/science/article/pii/
S0020722507000134](http://www.sciencedirect.com/science/article/pii/S0020722507000134)
- 800 [98] F. Taddei, M. Pani, L. Zovatto, E. Tonti, M. Viceconti, A new meshless
approach for subject-specific strain prediction in long bones: Evaluation of
accuracy, Clinical Biomechanics 23 (9) (2008) 1192–1199. doi:10.1016/
j.clinbiomech.2008.06.009.
URL <http://www.ncbi.nlm.nih.gov/pubmed/18678436>
- 805 [99] F. Buti, D. Cacciagrano, F. Corradini, E. Merelli, L. Tesei, M. Pani,
Bone remodelling in bioshape, Electronic Notes in Theoretical Computer
Science 268 (C) (2010) 17–29. doi:10.1016/j.entcs.2010.12.003.

- [100] J. Belinha, R. M. Natal Jorge, L. M. J. S. Dinis, Bone tissue remodelling analysis considering a radial point interpolator meshless method, Engineering Analysis with Boundary Elements 36 (11) (2012) 1660–1670. doi:10.1016/j.enganabound.2012.05.009.
URL <http://dx.doi.org/10.1016/j.enganabound.2012.05.009>
- [101] J. Belinha, R. M. N. Jorge, L. M. J. S. Dinis, A meshless microscale bone tissue trabecular remodelling analysis considering a new anisotropic bone tissue material law, Computer Methods in Biomechanics and Biomedical Engineering 5842 (August 2012) (2012) 1–15. doi:10.1080/10255842.2012.654783.
URL <http://www.tandfonline.com/doi/abs/10.1080/10255842.2012.654783>
- [102] S. Moreira, J. Belinha, L. Dinis, R. Natal Jorge, A global numerical analysis of the "central incisor/local maxillary bone" system using a meshless method, MCB Molecular and Cellular Biomechanics 11 (3) (2014) 151–184. doi:10.3970/mcb.2014.011.151.
URL <https://www.scopus.com/inward/record.uri?eid=2-s2.0-84920059394&partnerID=40&md5=95ef7a6385bf86d571bdf23a2ac385c2>
- [103] V. P. NGUYEN, M. STROEVEN, L. J. SLUYS, Multiscale Continuous and Discontinuous Modeling of Heterogeneous Materials: a Review on Recent Developments, Journal of Multiscale Modelling 03 (04) (2011) 229–270. doi:10.1142/S1756973711000509.
URL <http://www.worldscientific.com/doi/abs/10.1142/S1756973711000509>
- [104] N. Otsu, A Threshold Selection Method from Gray-Level Histograms, IEEE Transactions on Systems, Man, and Cybernetics 9 (1) (1979) 62–66. arXiv:arXiv:1011.1669v3, doi:10.1109/TSMC.1979.4310076.
URL <http://ieeexplore.ieee.org/document/4310076/>

- [105] W. J. Whitehouse, The quantitative morphology of anisotropic trabecular bone, *Journal of Microscopy* 101 (2) (1974) 153–168. doi:10.1111/j.1365-2818.1974.tb03878.x.
- ⁸⁴⁰ [106] K. Mizuno, M. Matsukawa, T. Otani, M. Takada, I. Mano, T. Tsujimoto, Effects of structural anisotropy of cancellous bone on speed of ultrasonic fast waves in the bovine femur, *IEEE Transactions on Ultrasonics, Ferroelectrics, and Frequency Control* 55 (7) (2008) 1480–1487. doi:10.1109/TUFFC.2008.823.
- ⁸⁴⁵ URL <http://ieeexplore.ieee.org/document/4559645/>
- [107] A. Odgaard, Three-dimensional methods for quantification of cancellous bone architecture, *Bone* 20 (4) (1997) 315–328. doi:10.1016/S8756-3282(97)00007-0.

Chapter 4

Conclusion

4.1 General Discussion

The human body is a complex and well-regulated system. To understand this complexity of systems and, subsystems and processes, it often required to join and use knowledge from different fields. Bone remodelling is one of these processes that occur in the human body, that benefits from the multidisciplinary and heterogeneity that exist in the scientific community. Bone remodelling benefits the knowhow and perspective of biologists, mathematicians, chemistries, engineers, among others. This lead to exciting improvements of experimental techniques that allow researchers to obtain a considerable amount of data at several spatial scales that can mathematically validate the bone remodelling behaviour. To study and analyse these models, that define biological processes that occur in physical domains, are often used numerical methods, by being considered as a standard approach in this type of application. Several discrete numerical methods are available, such as meshless methods. In the first two contributions, Contribution I and II, it was analysed the behaviour of RPIM and NNRPIM, against the FEM, when applied to biological structures. The main conclusion of this two contributions was that is common to observe that FEM analysis available in the literature do not consider the importance of the discretisation level, and that in many cases the discretisation level in commercial software is automatic. Thus, the lack of awareness regarding the value of the discretisation level can lead to invalid analyses. It can be also concluded, re-enforcing work present in the literature, that the RPIM and NNRPIM results are similar to the results obtained in FEM. Thereby, it can be also concluded that meshless

methods are capable to produce faster converge rates than the FEM, allowing the usage of sparse meshes, still capable of providing valid results, and with smoother stress fields, when compared with the FEM. In this contributions is concluded that since biological structures are different between different subjects, one must be capable to develop a standardisation procedure to allow the comparison between the results from the same biological structures between different subjects. This standardisation, inspired in the Gruen zones, a standardised system widely used to evaluate stress upon the use of prothesis in the femoral bone, could allow a better understanding of different studies using different sources of the same biological structure. In general, contribution III, IV, V, VI and VII, allow to conclude that the developed homogenisation technique permits to define bone using a homogenous domain with its mechanical proprieties defined using information of medical images and using the fabric tensor concept, being this domain mechanical characterisation equivalent to a heterogeneous domain with its mechanical properties defines ignoring the domain anisotropy. In contribution III, IV and V the methodology was explored in the 2D space, where it was concluded, that homogenisation technique was capable to define bone mechanical properties using a methodology that uses medical images information, of a homogenised domain that is equivalent to a heterogeneous domain with its morphology equivalent to the trabecular bone. In these contributions, the use of the meshless methods has high importance since the problems that can occur with discrete numerical methods in highly heterogeneous are attenuated when using meshless methods that use advanced discretisation methodologies. In these contribution it was observed that the developed methodology was capable of characterising bone mechanical properties considering its morphological characteristics, one factor of main importance when taking into account that this material definition can be used in the bone remodelling studies, and that is not influenced by the scale of the region of interest, which is used to defined the material mechanical properties. The 3D homogenisation methodology, explored in contribution VI and VI, complemented the 2D methodology, by confirming that the homogenous domains mechanically defined using the homogenisation technique are mechanically similar to the equivalent heterogeneous models. The 3D methodology is likely to be the one applied in the future application, since it is the one that can consider bone domains representative of real bone structures. One of the mains advantages of using the proposed homogenisation technique is the possibility of reducing the subjectiveness when creating the geometrical models that define the bone structures. A geometrical

model defined using medical images, where it is considered the bone as being a simplistic shell, lead to fewer discretisation errors, medical images interpretation errors, less iterative processes, when compared to models that consider all the morphologic characteristic of bone, in specific of the trabecular bone. This simplification in the geometrical creation is balanced by the definition of the mechanical properties of the model elements, by considering the trabecular bone morphology and apparent density, as parameters that are acquired using the medical images information, and are used in the homogenisation methodology. One key factor of this homogenisation methodology is that it can be used in the existent remodelling simulation models. It is usual to this remodelling models to have an iterative nature, where at each iteration the bone morphology changes, resulting in the remodelling process. Considering the fact that bone mechanical properties change with bone morphology, its mechanical properties should change in each iteration. When it is not used a homogenisation technique applied to this morphologic change, a new domain that reflects this change, has to be created. Using this homogenisation technique, the domain discretisation could be kept between iterations, but the mechanical properties that reflect the morphological changes (resultant from the remodelling process, which changes the bone macroscale mechanical behaviour), would be considered. This also has the advantage the homogenisation technique only depends on the bone morphology and the phenomenological laws, allowing to use this method with no user interference. If it is considered this iterative simplification in the remodelling process and the fact that medical images can reflect the specific characteristics of a patient bone, that can be encoded in the homogenisation technique, this can lead to a better understanding of the mechanical behaviour, for example, of the insertion of a specific implant into a specific patient. This can lead to a faster development of patient specific implants where is not just considering bone pre-implantation morphology, but also consider the effect of that implant in the bone morphology, and thus, allowing to choose the best implant to a specific patient.

4.2 Conclusion and Future Work

The proposed aims and challenges were successfully achieved, leading to a knowledge improvement in the bone remodelling modelling, and the consequent production and publication of research outputs in international journals. The remodelling process it was not directly studied but

was improved and expanded the knowledge concerning homogenisation methodologies, that are often used in bone remodelling studies. These methodologies can acquire a main importance on the development of patient specific implants, by allowing the analysis of the behaviour of specific implants into a specific bone, with its mechanical properties well translated. Furthermore, with this methodology it will be possible to create the geometrical models used in the computational analyses with less human interaction, allowing the automatisisation of the process and reducing the subjectiveness that occurs upon the creation of geometrical models. Concerning the evolution of this methodology and taking into account the great amount of data created in its processing, could be of interest to use the latest AI methodologies to develop a tool that could (using the same assumptions) define bone mechanical properties using its multiscale structure.

Bibliography

- [1] C. VanPutte, J. Regan, A. Russo, R. Seeley, T. Stephens, and P. Tate, *Seeley's Anatomy & Physiology*, vol. 2. McGraw-Hill Companies, 10th ed ed., 2003.
- [2] J. Belinha, *Meshless Methods in Biomechanics: Bone Tissue Remodelling Analysis*, vol. 2 of *Lecture Notes in Computational Vision and Biomechanics*. Dordrecht: Springer Netherlands, 2014.
- [3] X. Feng and J. M. McDonald, "Disorders of bone remodeling," *Annual Review of Pathology: Mechanisms of Disease*, vol. 6, pp. 121–145, Feb 2011.
- [4] Q.-H. Qin, *Mechanics of cellular bone remodeling*. CRC Press Taylor & Francis Group, 2012.
- [5] J. E. Aubin and J. N. M. Heersche, "Osteoprogenitor cell differentiation to mature bone-forming osteoblasts," *Drug Development Research*, vol. 49, pp. 206–215, Mar 2000.
- [6] S. C. Cowin, L. Moss-Salentijn, and M. L. Moss, "Candidates for the mechanosensory system in bone.," *Journal of biomechanical engineering*, vol. 113, pp. 191–197, May 1991.
- [7] L. E. Lanyon, "Osteocytes, strain detection, bone modeling and remodeling.," *Calcified tissue international*, vol. 53 Suppl 1, pp. S102–S106; discussion S106–S107, Jan 1993.
- [8] G. E. Wnek and G. L. Bowlin, *Encyclopedia of Biomaterials and Biomedical Engineering*. No. April, New York: Informa Healthcare USA, 2008.
- [9] J. Wolff, *The Law of Bone Remodelling*, vol. 155. Berlin, Heidelberg: Springer Berlin Heidelberg, 1886.
- [10] A. Glucksmann, "Studies on Bone mechanics in vitro," *Anat Rec*, vol. 73, pp. 39–55, 1939.

- [11] F. Pauwels, “Gesammelte Abhandlungen zur funktionellen Anatomie des | Friedrich Pauwels | Springer,” *Springer*, p. 543, 1965.
- [12] H. E. Pettermann, T. J. Reiter, and F. G. Rammerstorfer, “Computational simulation of internal bone remodeling,” *Archives of Computational Methods in Engineering*, vol. 4, pp. 295–323, dec 1997.
- [13] G. A. Rodan and T. J. Martin, “Role of osteoblasts in hormonal control of bone resorption—a hypothesis,” *Calcified Tissue International*, vol. 33, pp. 349–351, Dec 1981.
- [14] E. M. Hauge, D. Qvesel, E. F. Eriksen, L. Mosekilde, and F. Melsen, “Cancellous bone remodeling occurs in specialized compartments lined by cells expressing osteoblastic markers,” *Journal of bone and mineral research: the official journal of the American Society for Bone and Mineral Research*, vol. 16, pp. 1575–1582, Sep 2001.
- [15] J. Kular, J. Tickner, S. M. Chim, and J. Xu, “An overview of the regulation of bone remodelling at the cellular level,” *Clinical Biochemistry*, vol. 45, pp. 863–873, Aug 2012.
- [16] T. H. Smit and E. H. Burger, “Is bmu-coupling a strain-regulated phenomenon? a finite element analysis,” *Journal of Bone and Mineral Research*, vol. 15, pp. 301–307, Feb 2010.
- [17] L. J. Raggatt and N. C. Partridge, “Cellular and molecular mechanisms of bone remodeling,” *Journal of Biological Chemistry*, vol. 285, pp. 25103–25108, Aug 2010.
- [18] D. Burr, A. Robling, and C. Turner, “Effects of biomechanical stress on bones in animals,” *Bone*, vol. 30, pp. 781–786, May 2002.
- [19] A. M. Parfitt, “Targeted and nontargeted bone remodeling: Relationship to basic multicellular unit origination and progression,” *Bone*, vol. 30, pp. 5–7, Jan 2002.
- [20] M. Kroll, “Parathyroid hormone temporal effects on bone formation and resorption,” *Bulletin of Mathematical Biology*, vol. 62, pp. 163–188, Jan 2000.
- [21] H. Dobnig and R. T. Turner, “The effects of programmed administration of human parathyroid hormone fragment (1 – 34) on bone histomorphometry and serum chemistry in rats,” *Endocrinology*, vol. 138, pp. 4607–4612, Nov 1997.

- [22] A. C. Karaplis and D. Goltzman, "Pth and pthrp effects on the skeleton," *Reviews in Endocrine & Metabolic Disorders*, vol. 1, no. 4, pp. 331–341, 2000.
- [23] R. M. Locklin, S. Khosla, R. T. Turner, and B. L. Riggs, "Mediators of the biphasic responses of bone to intermittent and continuously administered parathyroid hormone," *Journal of Cellular Biochemistry*, vol. 89, no. 1, pp. 180–190, 2003.
- [24] M. R. Rubin and J. P. Bilezikian, "New anabolic therapies in osteoporosis," *Endocrinology and Metabolism Clinics of North America*, vol. 32, pp. 285–307, Mar 2003.
- [25] A. Y., M. Valds-Flores, L. Orozco, and R. Velzquez-Cruz, *Molecular Aspects of Bone Remodeling*, pp. 1–28. InTech, May 2013.
- [26] W. A. Bauman, A. M. Spungen, J. Wang, R. N. Pierson, and E. Schwartz, "Continuous loss of bone during chronic immobilization: A monozygotic twin study," *Osteoporosis International*, vol. 10, no. 2, pp. 123–127, 1999.
- [27] J. E. Zerwekh, L. A. Ruml, F. Gottschalk, and C. Y. C. Pak, "The effects of twelve weeks of bed rest on bone histology, biochemical markers of bone turnover, and calcium homeostasis in eleven normal subjects," *Journal of Bone and Mineral Research*, vol. 13, pp. 1594–1601, Nov 2009.
- [28] L. F. Bonewald, "The amazing osteocyte," *Journal of Bone and Mineral Research*, vol. 26, pp. 229–238, feb 2011.
- [29] Y. Tang, X. Wu, W. Lei, L. Pang, C. Wan, Z. Shi, L. Zhao, T. R. Nagy, X. Peng, J. Hu, X. Feng, W. Van Hul, M. Wan, and X. Cao, "TGF- β 1-induced migration of bone mesenchymal stem cells couples bone resorption with formation," *Nature Medicine*, vol. 15, pp. 757–765, jul 2009.
- [30] A. Teti, "Bone development: Overview of bone cells and signaling," *Current Osteoporosis Reports*, vol. 9, pp. 264–273, Dec 2011.
- [31] J. C. Gallagher and A. Sai, "Molecular biology of bone remodeling: Implications for new therapeutic targets for osteoporosis," *Maturitas*, vol. 65, pp. 301–307, Apr 2010.

- [32] K. Matsuo and N. Irie, "Osteoclast-osteoblast communication," *Archives of Biochemistry and Biophysics*, vol. 473, pp. 201–209, May 2008.
- [33] U. Kini and B. N. Nandeesh, *Physiology of bone formation, remodeling, and metabolism*, vol. 9783642024, pp. 29–57. Springer Berlin Heidelberg, 2012.
- [34] H. M. Frost, *The laws of bone structure*. C. C. Thomas, 1964, 1964.
- [35] S. C. Cowin and D. H. Hegedus, "Bone remodeling i: Theory of adaptative elasticity," *Journal of Elasticity*, vol. 6, no. 3, pp. 313–326, 1976.
- [36] S. C. Cowin and R. R. Nachlinger, "Bone remodeling iii: uniqueness and stability in adaptive elasticity theory," *Journal of Elasticity*, vol. 8, pp. 285–295, Jul 1978.
- [37] S. C. Cowin, A. M. Sadegh, and G. M. Luo, "An evolutionary wolff's law for trabecular architecture," *Journal of Biomechanical Engineering*, vol. 114, pp. 129–136, Feb 1992.
- [38] D. H. Hegedus and S. C. Cowin, "Bone remodeling ii: small strain adaptive elasticity," *Journal of Elasticity*, vol. 6, pp. 337–352, Oct 1976.
- [39] D. R. Carter, T. E. Orr, and D. P. Fyhrie, "Relationships between femoral loading history and femoral cancellous bone architecture," *Journal of biomechanics*, vol. 22, no. 3, pp. 231–244, 1989.
- [40] D. R. Carter, D. P. Fyhrie, and R. T. Whalen, "Trabecular bone density and loading history: Regulation of connective tissue biology by mechanical energy," *Journal of Biomechanics*, vol. 20, pp. 785–794, jan 1987.
- [41] D. P. Fyhrie and D. R. Carter, "A unifying principle relating stress to trabecular bone morphology," *Journal of orthopaedic research*, vol. 4, pp. 304–317, 1986.
- [42] R. T. Whalen, D. R. Carter, and C. R. Steele, "Influence of physical activity on the regulation of bone density," *Journal of Biomechanics*, vol. 21, pp. 825–837, Jan 1988.
- [43] R. Huiskes, H. Weinans, H. J. Grootenboer, M. Dalstra, B. Fudala, and T. J. Slooff, "Adaptive bone-remodeling theory applied to prosthetic-design analysis," *Journal of Biomechanics*, vol. 20, pp. 1135–1150, jan 1987.

- [44] T. J. Reiter, F. G. Rammerstorfer, and H. J. Bohm, "Numerical algorithm for the simulation of bone remodeling," *American Society of Mechanical Engineers, Bioengineering Division (Publication) BED*, vol. 17, pp. 181–184, 1990.
- [45] T. P. Harrigan and J. J. Hamilton, "Optimality conditions for finite element simulation of adaptive bone remodeling," *International Journal of Solids and Structures*, vol. 29, pp. 2897–2906, Jan 1992.
- [46] T. P. Harrigan and J. J. Hamilton, "An analytical and numerical study of the stability of bone remodelling theories: Dependence on microstructural stimulus," *Journal of Biomechanics*, vol. 25, pp. 477–488, May 1992.
- [47] T. P. Harrigan and J. J. Hamilton, "Finite element simulation of adaptive bone remodelling: A stability criterion and a time stepping method," *International Journal for Numerical Methods in Engineering*, vol. 36, pp. 837–854, Mar 1993.
- [48] J. Belinha, R. M. Natal Jorge, and L. M. J. S. Dinis, "Bone tissue remodelling analysis considering a radial point interpolator meshless method," *Engineering Analysis with Boundary Elements*, vol. 36, pp. 1660–1670, Nov 2012.
- [49] J. Belinha, R. M. N. Jorge, and L. M. Dinis, "A meshless microscale bone tissue trabecular remodelling analysis considering a new anisotropic bone tissue material law," *Computer Methods in Biomechanics and Biomedical Engineering*, vol. 5842, pp. 1–15, jan 2012.
- [50] S. V. Komarova, R. J. Smith, S. J. Dixon, S. M. Sims, and L. M. Wahl, "Mathematical model predicts a critical role for osteoclast autocrine regulation in the control of bone remodeling," *Bone*, vol. 33, pp. 206–215, 2003.
- [51] V. Lemaire, F. L. Tobin, L. D. Greller, C. R. Cho, and L. J. Suva, "Modeling the interactions between osteoblast and osteoclast activities in bone remodeling," *Journal of Theoretical Biology*, vol. 229, pp. 293–309, Aug 2004.
- [52] P. Pivonka, J. Zimak, D. W. Smith, B. S. Gardiner, C. R. Dunstan, N. A. Sims, T. John Martin, and G. R. Mundy, "Theoretical investigation of the role of the rank-rankl-opg system in bone remodeling," *Journal of Theoretical Biology*, vol. 262, pp. 306–316, Jan 2010.

- [53] P. Pivonka, J. Zimak, D. W. Smith, B. S. Gardiner, C. R. Dunstan, N. A. Sims, T. J. Martin, G. R. Mundy, T. John Martin, and G. R. Mundy, "Model structure and control of bone remodeling: A theoretical study," *Bone*, vol. 43, pp. 249–263, Aug 2008.
- [54] M. D. Ryser, N. Nigam, and S. V. Komarova, "Mathematical modeling of spatio-temporal dynamics of a single bone multicellular unit," *Journal of Bone and Mineral Research*, vol. 24, pp. 860–870, May 2009.
- [55] M. J. Martin and J. C. Buckland-Wright, "Sensitivity analysis of a novel mathematical model identifies factors determining bone resorption rates," *Bone*, vol. 35, pp. 918–928, Oct 2004.
- [56] M. A. Savageau, "Biochemical systems analysis: Study of function and design in molecular biology," *Zeitschrift für allgemeine Mikrobiologie*, vol. 5, p. 199, Jan 1976.
- [57] P. Pivonka, J. W. Fernandez, and P. J. Hunter, "Foreword to the special issue on bone and cartilage mechanobiology across the scales," *Biomechanics and Modeling in Mechanobiology*, vol. 15, pp. 5–7, Feb 2016.
- [58] W. Yi, C. Wang, and X. Liu, "A microscale bone remodeling simulation method considering the influence of medicine and the impact of strain on osteoblast cells," *Finite Elements in Analysis and Design*, vol. 104, pp. 16–25, Oct 2015.
- [59] R. Hambli, "Connecting mechanics and bone cell activities in the bone remodeling process: An integrated finite element modeling," *Frontiers in Bioengineering and Biotechnology*, vol. 2, no. 6, pp. 1–12, 2014.
- [60] C. Lerebours, P. R. Buenzli, S. Scheiner, and P. Pivonka, "A multiscale mechanobiological model of bone remodelling predicts site-specific bone loss in the femur during osteoporosis and mechanical disuse," *Biomechanics and Modeling in Mechanobiology*, vol. 15, no. 1, pp. 43–67, 2016.
- [61] E. Lucchinetti, "Composite Models of Bone Properties," in *Bone Mechanics Handbook, Second Edition*, pp. 12–1–12–19, CRC Press, mar 2001.

- [62] A. Barkaoui, B. Tlili, A. Vercher-Martínez, and R. Hambli, “A multiscale modelling of bone ultrastructure elastic proprieties using finite elements simulation and neural network method,” *Computer Methods and Programs in Biomedicine*, vol. 134, pp. 69–78, 2016.
- [63] V. P. Nguyen, M. Stroeve, and L. J. Sluys, “Multiscale Continuous and Discontinuous Modeling of Heterogeneous Materials: a Review on Recent Developments,” *Journal of Multiscale Modelling*, vol. 03, no. 04, pp. 229–270, 2011.
- [64] J. Hazrati Marangalou, K. Ito, and B. van Rietbergen, “A novel approach to estimate trabecular bone anisotropy from stress tensors,” *Biomechanics and Modeling in Mechanobiology*, vol. 14, pp. 39–48, jan 2015.
- [65] R. Moreno, Ö. Smedby, and D. H. Pahr, “Prediction of apparent trabecular bone stiffness through fourth-order fabric tensors,” *Biomechanics and Modeling in Mechanobiology*, vol. 15, pp. 831–844, aug 2016.
- [66] S. C. Cowin, “The relationship between the elasticity tensor and the fabric tensor,” *Mechanics of Materials*, vol. 4, no. 2, pp. 137–147, 1985.
- [67] W. J. Whitehouse, “The quantitative morphology of anisotropic trabecular bone,” *Journal of Microscopy*, vol. 101, no. 2, pp. 153–168, 1974.
- [68] S. C. Cowin and S. B. Doty, *Tissue Mechanics*. Springer Science, 2007.
- [69] K. Mizuno, M. Matsukawa, T. Otani, M. Takada, I. Mano, and T. Tsujimoto, “Effects of structural anisotropy of cancellous bone on speed of ultrasonic fast waves in the bovine femur,” *IEEE Transactions on Ultrasonics, Ferroelectrics, and Frequency Control*, vol. 55, pp. 1480–1487, jul 2008.
- [70] A. Odgaard, “Three-dimensional methods for quantification of cancellous bone architecture,” *Bone*, vol. 20, no. 4, pp. 315–328, 1997.
- [71] P. K. Zysset, “A review of morphology–elasticity relationships in human trabecular bone: theories and experiments,” *Journal of Biomechanics*, vol. 36, pp. 1469–1485, oct 2003.
- [72] J. N. Reddy, *An Introduction to Nonlinear Finite Element Analysis*, vol. 1. Oxford University Press, mar 2004.

- [73] S. S. Bhavikatti, *Finite Element Analysis*. 3rd ed., 2005.
- [74] R. A. Gingold and J. J. Monaghan, "Smooth particle hydrodynamics: theory and application to non-spherical stars," *Monthly Notices of the Royal Astronomical Society*, vol. 181, pp. 375–389, 1977.
- [75] G. R. Liu and Y. T. Gu, "A point interpolation method for two-dimensional solids," *International Journal for Numerical Methods in Engineering*, vol. 50, pp. 937–951, feb 2001.
- [76] Y. T. Liu, G. R. Gu, "Local point interpolation method for stress analysis of two-dimensional solids," *Structural Engineering and Mechanics*, vol. 11, pp. 221–236, feb 2001.
- [77] G. R. Liu and Y. GU, "A Local Radial Point Interpolation Method (LRPIM) for Free Vibration Analyses of 2-D Solids," *Journal of Sound and Vibration*, vol. 246, pp. 29–46, sep 2001.
- [78] L. M. J. S. Dinis, R. M. Natal Jorge, and J. Belinha, "Analysis of 3D solids using the natural neighbour radial point interpolation method," *Computer Methods in Applied Mechanics and Engineering*, vol. 196, pp. 2009–2028, mar 2007.
- [79] T. Liszka and J. Orkisz, "The finite difference method at arbitrary irregular grids and its application in applied mechanics," *Computers and Structures*, vol. 11, no. 1-2, pp. 83–95, 1980.
- [80] B. Nayroles, G. Touzot, and P. Villon, "Generalizing the finite element method: Diffuse approximation and diffuse elements," *Computational Mechanics*, vol. 10, no. 5, pp. 307–318, 1992.
- [81] T. Belytschko, Y. Y. Lu, and L. Gu, "Element-free Galerkin methods," *International Journal*, vol. 37, pp. 229–256, jan 1994.
- [82] S. N. Atluri and T. Zhu, "A new meshless local petrov-galerkin (mlpg) approach in computational mechanics," *Computational Mechanics*, vol. 22, pp. 117–127, Aug 1998.

- [83] J. G. Wang and G. R. Liu, "A point interpolation meshless method based on radial basis functions," *International Journal for Numerical Methods in Engineering*, vol. 54, pp. 1623–1648, aug 2002.
- [84] G. R. Wang, J. G. Liu, "On the optimal shape parameters of radial basis functions used for 2-d meshless methods," *Computer Methods in Applied Mechanics and Engineering*, vol. 191, pp. 2611–2630, mar 2002.
- [85] J. Belinha, L. M. J. S. Dinis, and R. M. N. Jorge, "The natural radial element method," *Int. J. Numer. Methods Eng*, vol. 93, pp. 1286–1313, mar 2013.
- [86] W. K. Liu, S. Jun, and Y. F. Zhang, "Reproducing kernel particle methods," *International Journal for Numerical Methods in Fluids*, vol. 20, pp. 1081–1106, apr 1995.
- [87] J. Belinha, L. M. S. Dinis, and R. M. N. Jorge, "Composite laminated plate analysis using the natural radial element method," *Composite Structures*, vol. 103, pp. 50–67, sep 2013.
- [88] E. Cueto, N. Sukumar, B. Calvo, M. a. Martínez, J. Cegoñino, and M. Doblaré, "Overview and recent advances in natural neighbour galerkin methods," *Archives of Computational Methods in Engineering*, vol. 10, pp. 307–384, dec 2003.
- [89] L. Dinis, R. M. Natal Jorge, and J. Belinha, "A natural neighbour meshless method with a 3D shell-like approach in the dynamic analysis of thin 3D structures," *Thin-Walled Structures*, vol. 49, pp. 185–196, jan 2011.
- [90] L. M. J. S. Dinis, R. M. N. Jorge, and J. Belinha, "A 3D shell-like approach using a natural neighbour meshless method: Isotropic and orthotropic thin structures," *Composite Structures*, vol. 92, no. 5, pp. 1132–1142, 2010.
- [91] G. R. Liu, G. Y. Zhang, Y. Y. Wang, Z. H. Zhong, G. Y. Li, and X. Han, "A nodal integration technique for meshfree radial point interpolation method (NI-RPIM)," *International Journal of Solids and Structures*, vol. 44, pp. 3840–3860, jun 2007.
- [92] X. Zhao, G. R. Liu, K. Y. Dai, Z. H. Zhong, G. Y. Li, and X. Han, "Free-vibration analysis of shells via a linearly conforming radial point interpolation method (LC-RPIM)," *Finite Elements in Analysis and Design*, vol. 45, pp. 917–924, jul 2009.

- [93] G. R. Liu, Y. Jiang, L. Chen, G. Y. Zhang, and Y. W. Zhang, "A singular cell-based smoothed radial point interpolation method for fracture problems," *Computers and Structures*, vol. 89, pp. 1378–1396, jul 2011.
- [94] V. P. Nguyen, T. Rabczuk, S. Bordas, and M. Duflot, "Meshless methods: A review and computer implementation aspects," *Mathematics and Computers in Simulation*, vol. 79, pp. 763–813, dec 2008.
- [95] O. C. Zienkiewicz and R. L. Taylor, *The Finite Element Method*. London: McGraw-Hill, 4th ed., 1994.
- [96] K. J. Bathe and H. Saunders, *Finite Element Procedures in Engineering Analysis*, vol. 106. New Jersey: Prentice-Hall, Inc., 1984.
- [97] R. Sibson, *A Brief Description of Natural Neighbor Interpolation*, pp. 21–36. Wiley, Chichester, 1981.
- [98] G. Voronoi, "Nouvelles applications des paramètres continus à la théorie des formes quadratiques. deuxième mémoire. recherches sur les paralléloèdres primitifs.," *Journal für die Reine und Angewandte Mathematik*, vol. 1908, no. 134, pp. 198–287, 1908.
- [99] B. Delaunay, "Sur la sphère vide. a la memoire de georges voronoï.," *Bulletin de l'Academie des Sciences de l'URSS. Classe des sciences mathematiques et na*, vol. 7, pp. 793–800, 1934.
- [100] R. L. Hardy, "Theory and applications of the multiquadric-biharmonic method 20 years of discovery 1968-1988," *Computers and Mathematics with Applications*, vol. 19, pp. 163–208, jan 1990.
- [101] L. M. J. S. Dinis, R. M. Natal Jorge, and J. Belinha, "Analysis of plates and laminates using the natural neighbour radial point interpolation method," *Engineering Analysis with Boundary Elements*, vol. 32, pp. 267–279, mar 2008.
- [102] M. Golberg, C. Chen, and H. Bowman, "Some recent results and proposals for the use of radial basis functions in the BEM," *Engineering Analysis with Boundary Elements*, vol. 23, pp. 285–296, apr 1999.

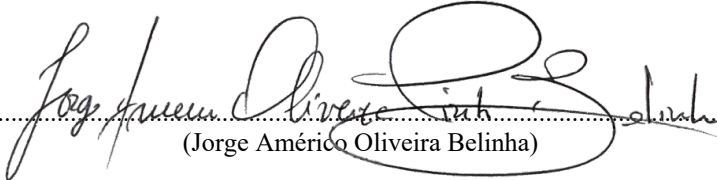
- [103] L. Dinis, R. M. Natal Jorge, and J. Belinha, "Composite Laminated Plates: A 3D Natural Neighbor Radial Point Interpolation Method Approach," *Journal of Sandwich Structures and Materials*, vol. 12, pp. 119–138, mar 2009.
- [104] J. Belinha, L. Dinis, and R. M. N. Jorge, "The natural neighbour radial point interpolation method: dynamic applications," *Engineering Computations*, vol. 26, pp. 911–949, nov 2009.
- [105] L. M. J. S. Dinis, R. M. Natal Jorge, and J. Belinha, "Large deformation applications with the radial natural neighbours interpolators," *CMES - Computer Modeling in Engineering and Sciences*, vol. 44, no. 1, pp. 1–34, 2009.
- [106] L. Dinis, R. M. N. Jorge, and J. Belinha, *The Radial Natural Neighbours Interpolators Extended to Elastoplasticity*, ch. 11, pp. 175–198. Dordrecht: Springer Netherlands, 2009.
- [107] J. Belinha, L. Dinis, and R. N. Jorge, "The meshless methods in the bone tissue remodelling analysis," *Procedia Engineering*, vol. 110, pp. 51–58, 2015.
- [108] F. Lalys, C. Haegelen, J.-C. Ferre, O. El-Ganaoui, and P. Jannin, "Construction and assessment of a 3-T MRI brain template," *NeuroImage*, vol. 49, pp. 345–354, jan 2010.
- [109] Mimics, "Mimics® Medical Image Segmentation for Engineering on Anatomy™."
- [110] T. A. Gruen, G. M. McNeice, and H. C. Amstutz, "'Modes of failure' of cemented stem-type femoral components: a radiographic analysis of loosening.," *Clinical orthopaedics and related research*, pp. 17–27, jun 1979.
- [111] P. Tavakkoli Avval, V. Klika, and H. Bougherara, "Predicting bone remodeling in response to total hip arthroplasty: computational study using mechanobiochemical model.," *Journal of biomechanical engineering*, vol. 136, p. 051002, may 2014.

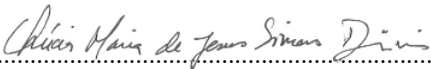
Appendix


Autorização de Compilação

Jorge Américo Oliveira Belinha, Lúcia Maria de Jesus Simas Dinis e Renato Manuel Natal Jorge, na qualidade de coautores do artigo "A new numerical approach to mechanically analyse biological structures" submetido para publicação numa revista internacional, declaram que autorizam a inclusão do mesmo na dissertação de doutoramento do candidato Marco da Costa Marques, intitulada "A Homogenisation Technique for Multiscale Analysis of Bone Tissue Combined With Advanced Discretisation Techniques".

Porto e FEUP, 11 de set. de 19


.....
(Jorge Américo Oliveira Belinha)

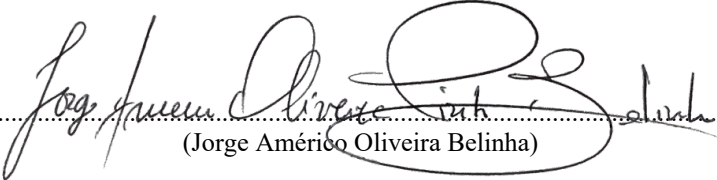

.....
(Lúcia Maria de Jesus Simas Dinis)

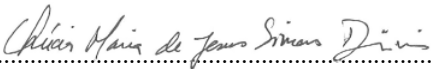

.....
(Renato Manuel Natal Jorge)

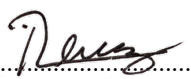
Autorização de Compilação

Jorge Américo Oliveira Belinha, Lúcia Maria de Jesus Simas Dinis e Renato Manuel Natal Jorge, na qualidade de coautores do artigo "A brain impact stress analysis using advanced discretization meshless techniques" submetido para publicação numa revista internacional, declaram que autorizam a inclusão do mesmo na dissertação de doutoramento do candidato Marco da Costa Marques, intitulada "A Homogenisation Technique for Multiscale Analysis of Bone Tissue Combined With Advanced Discretisation Techniques".

Porto e FEUP, 11 de set. de 19


.....
(Jorge Américo Oliveira Belinha)

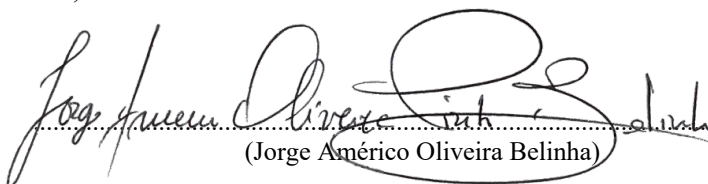

.....
(Lúcia Maria de Jesus Simas Dinis)



.....
(Renato Manuel Natal Jorge)

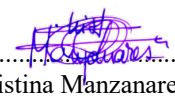
Autorização de Compilação

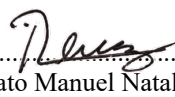
Jorge Américo Oliveira Belinha, António Fonseca Oliveira, Maria Cristina Manzanares Céspedes e Renato Manuel Natal Jorge, na qualidade de coautores do artigo "A multiscale homogenization procedure using the fabric tensor concept" submetido para publicação numa revista internacional, declaram que autorizam a inclusão do mesmo na dissertação de doutoramento do candidato Marco da Costa Marques, intitulada "A Homogenisation Technique for Multiscale Analysis of Bone Tissue Combined With Advanced Discretisation Techniques".

Porto e FEUP, 11 de set. de 19


.....
(Jorge Américo Oliveira Belinha)


.....
(António Fonseca Oliveira)

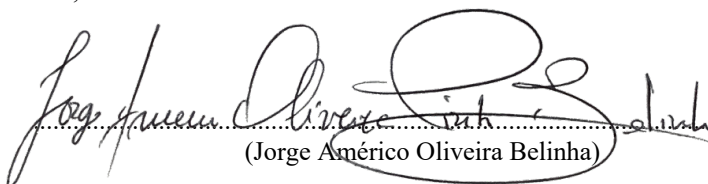

.....
(Maria Cristina Manzanares Céspedes)



.....
(Renato Manuel Natal Jorge)

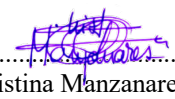
Autorização de Compilação

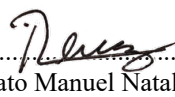
Jorge Américo Oliveira Belinha, António Fonseca Oliveira, Maria Cristina Manzanares Céspedes e Renato Manuel Natal Jorge, na qualidade de coautores do artigo "Combining radial point interpolation meshless method with a new homogenization technique for trabecular bone multiscale structural analyses" submetido para publicação numa revista internacional, declaram que autorizam a inclusão do mesmo na dissertação de doutoramento do candidato Marco da Costa Marques, intitulada "A Homogenisation Technique for Multiscale Analysis of Bone Tissue Combined With Advanced Discretisation Techniques".

Porto e FEUP, 11 de set. de 19


.....
(Jorge Américo Oliveira Belinha)


.....
(António Fonseca Oliveira)

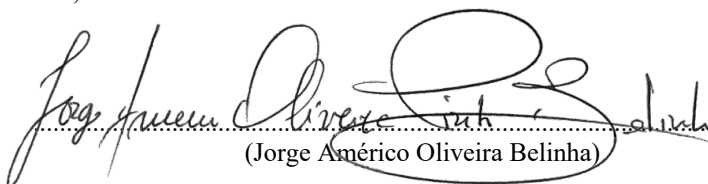

.....
(Maria Cristina Manzanares Céspedes)


.....
(Renato Manuel Natal Jorge)


Autorização de Compilação


Jorge Américo Oliveira Belinha, António Fonseca Oliveira, Maria Cristina Manzanares Céspedes e Renato Manuel Natal Jorge, na qualidade de coautores do artigo "A multiscale homogenization procedure combining the fabric tensor with a natural neighbour meshless method" submetido para publicação numa revista internacional, declaram que autorizam a inclusão do mesmo na dissertação de doutoramento do candidato Marco da Costa Marques, intitulada "A Homogenisation Technique for Multiscale Analysis of Bone Tissue Combined With Advanced Discretisation Techniques".

Porto e FEUP, 11 de set. de 19


.....
(Jorge Américo Oliveira Belinha)


.....
(António Fonseca Oliveira)

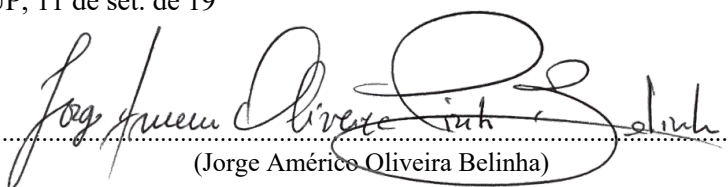

.....
(Maria Cristina Manzanares Céspedes)


.....
(Renato Manuel Natal Jorge)


Autorização de Compilação


Jorge Américo Oliveira Belinha, António Fonseca Oliveira, Maria Cristina Manzanares Céspedes e Renato Manuel Natal Jorge, na qualidade de coautores do artigo "A 3D trabecular bone homogenization technique" submetido para publicação numa revista internacional, declaram que autorizam a inclusão do mesmo na dissertação de doutoramento do candidato Marco da Costa Marques, intitulada "A Homogenisation Technique for Multiscale Analysis of Bone Tissue Combined With Advanced Discretisation Techniques".

Porto e FEUP, 11 de set. de 19


.....
(Jorge Américo Oliveira Belinha)


.....
(António Fonseca Oliveira)

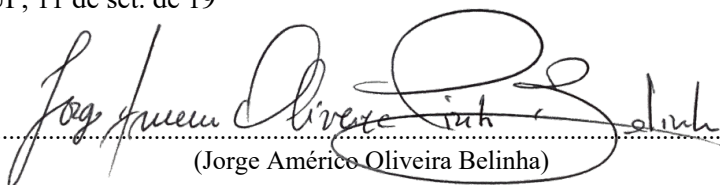

.....
(Maria Cristina Manzanares Céspedes)


.....
(Renato Manuel Natal Jorge)


Autorização de Compilação


Jorge Américo Oliveira Belinha, António Fonseca Oliveira, Maria Cristina Manzanares Céspedes e Renato Manuel Natal Jorge, na qualidade de coautores do artigo "Application of an enhanced homogenisation technique to the structural multiscale analysis of a femur bone" submetido para publicação numa revista internacional, declaram que autorizam a inclusão do mesmo na dissertação de doutoramento do candidato Marco da Costa Marques, intitulada "A Homogenisation Technique for Multiscale Analysis of Bone Tissue Combined With Advanced Discretisation Techniques".

Porto e FEUP, 11 de set. de 19


.....
(Jorge Américo Oliveira Belinha)


.....
(António Fonseca Oliveira)

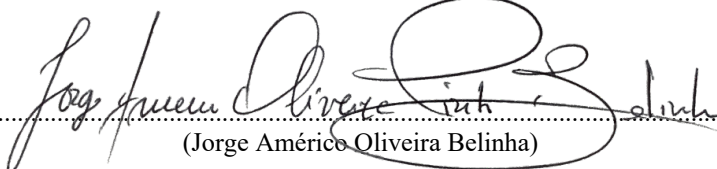

.....
(Maria Cristina Manzanares Céspedes)

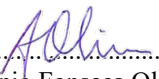

.....
(Renato Manuel Natal Jorge)

Autorização de Compilação

Jorge Américo Oliveira Belinha, António Fonseca Oliveira e Renato Manuel Natal Jorge, na qualidade de coautores do capítulo de livro "Meshless, Bone Remodelling and Bone Regeneration Modelling" submetido para publicação numa editora internacional, declaram que autorizam a inclusão do mesmo na dissertação de doutoramento do candidato Marco da Costa Marques, intitulada "A Homogenisation Technique for Multiscale Analysis of Bone Tissue Combined With Advanced Discretisation Techniques".

Porto e FEUP, 11 de set. de 19


.....
(Jorge Américo Oliveira Belinha)

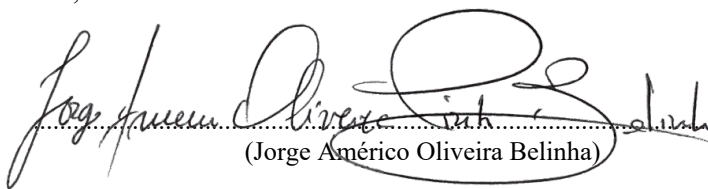

.....
(António Fonseca Oliveira)



.....
(Renato Manuel Natal Jorge)


Autorização de Compilação

Jorge Américo Oliveira Belinha, António Fonseca Oliveira e Renato Manuel Natal Jorge, na qualidade de coautores do capítulo de livro "Determination of the Anisotropic Mechanical Properties of Bone Tissue Using a Homogenization Technique Combined With Meshless Methods" submetido para publicação numa editora internacional, declaram que autorizam a inclusão do mesmo na dissertação de doutoramento do candidato Marco da Costa Marques, intitulada "A Homogenisation Technique for Multiscale Analysis of Bone Tissue Combined With Advanced Discretisation Techniques".

Porto e FEUP, 11 de set. de 19


.....
(Jorge Américo Oliveira Belinha)


.....
(António Fonseca Oliveira)


.....
(Renato Manuel Natal Jorge)